Microscopy and spectroscopy on model catalysts in gas environments

Wenzel, S.

Citation

Wenzel, S. (2021, September 16). *Microscopy and spectroscopy on model catalysts in gas environments*. Retrieved from https://hdl.handle.net/1887/3210401

Author: Wenzel, S.
Title: Microscopy and spectroscopy on model catalysts in gas environments
Issue Date: 2021-09-16

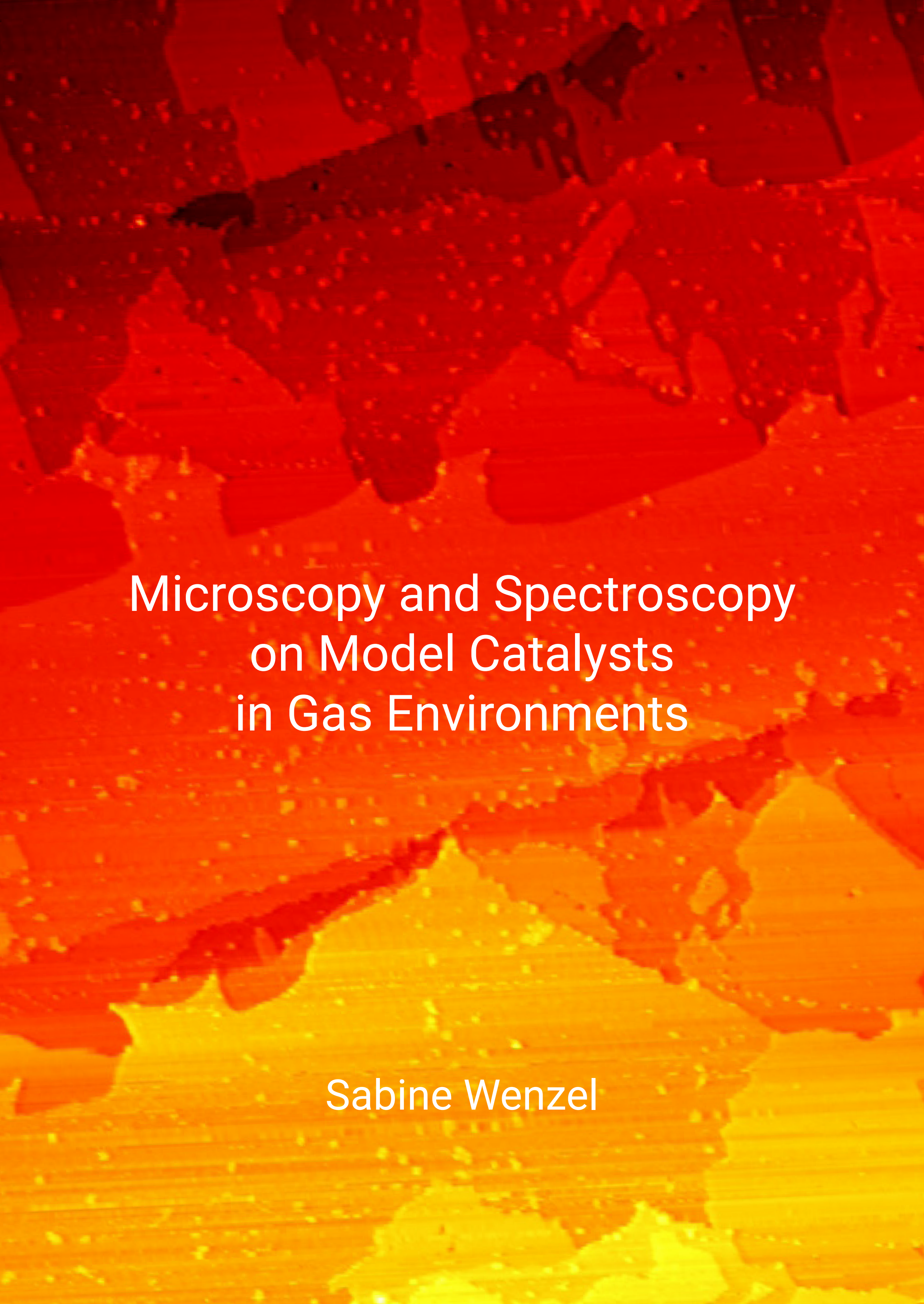

Microscopy and Spectroscopy on Model Catalysts in Gas Environments

Sabine Wenzel

Microscopy and Spectroscopy on Model Catalysts in Gas Environments

Proefschrift

ter verkrijging van
de graad van doctor aan de Universiteit Leiden,
op gezag van rector magnificus prof.dr.ir. H. Bijl,
volgens besluit van het college voor promoties
te verdedigen op donderdag 16 september 2021
klokke 12.30 uur

door

Sabine Wenzel

geboren te Darmstadt, Duitsland
in 1992

Promotor:	Dr. I.M.N. Groot	Universiteit Leiden
	Prof.dr. M.T.M. Koper	Universiteit Leiden
Co-promotor:	Dr. L.B.F. Juurlink	Universiteit Leiden
Promotiecommissie:	Dr. T.V. de Bocarmé	Université libre de Bruxelles
	Prof.dr. E. Lundgren	Lunds Universitet
	Dr. R.V. Mom	Universiteit Leiden
	Prof.dr.ir. T.H. Oosterkamp	Universiteit Leiden
	Prof.dr. H.S. Overkleeft	Universiteit Leiden
	Prof.dr. P. Rudolf	Rijksuniversiteit Groningen

The research presented in this thesis is financed by the Dutch Research Council (NWO), BASF Nederland B.V., SABIC Global Technologies B.V., and Sasol Technology (Pty) Ltd. in line with a Catalytic C1 Chemistry grant [731.015.604].

An electronic version of this thesis can be found at `openaccess.leidenuniv.nl`.

The cover of this book exemplifies the rich structures that can form on a metal (front) and an oxide (back) surface under the influence of gases.

ISBN: 978-94-6423-371-1

Contents

Chapter 1

Introduction

1.1 Catalysis

Some of the most urgent challenges of our time, as defined by the United Nations [1], are the supply of clean and affordable energy, the reduction of pollution and waste on land, in air, and in water, counteracting climate change, and producing enough food for the growing world population. In all of these areas catalysis can and is playing a role: Refining fossil fuels and increasing the cleanliness of the products, which are used for transportation as well as the chemical industry, relies heavily on catalysts [2]. This has not changed with the search for more sustainable energy sources [3]. The use of solar and wind energy relies on more efficient energy-storage methods like chemical storage, which gives the need for catalytic conversion of chemicals. A hydrogen economy would not only need catalysts for the hydrogen production [4], but they are also an integral part of retrieving the energy in fuel cells. Additionally, catalysis for CO_2 conversion is being researched extensively [5]. In the effort to reduce pollution, catalysts can convert harmful substances into less harmful ones after or before they are released into the environment [6], with the most well-known example being the 3-way catalyst in combustion engine vehicles [7]. The use of catalysts for the production of fine chemicals, including pharmaceuticals [8], reduces the amount of energy needed and can prevent unwanted side products. Last, food production has increased significantly due to the catalytic production of fertilizer [9] and depends on enzymes for food processing [10]. Given this vast range of applications, it is not surprising that catalysts come in various forms. One distinguishes the fields of homogeneous catalysis, heterogeneous catalysis including electrochemistry, and biocatalysis [11,12]. Catalysts can be organic like the enzymes in your body, molecules and complexes, or surfaces; they can contain metals or oxides, and can even be made from waste [13] or consist of single atoms [14]. The activity of some catalysts is induced by photons [15] or plasma [16]. The general definition of catalysis is the same in all these fields: Without being a reactant or product itself, the catalyst reduces the barrier for the reaction and thus increases the reaction rate, makes the reaction less energy-consuming, and/or more selective to a specific reactant or product [12].

1.2 Surface Science: Atomic-Level Understanding

This thesis focuses on heterogeneous catalysts, in particular solid surfaces catalyzing gas-phase reactions. In this case the reactant(s) usually adsorb on the surface, possibly dissociate, and react, followed by the desorption of the product(s). In contrast to this Langmuir-Hinschelwood mechanism, one of the reactants can also react directly from the gas phase without prior adsorption in an Eley-Rideal mechanism [17] or atoms from the catalyst can be removed and replaced again during the reaction via a Mars-van Krevelen mechanism [18]. In any of the three cases the so-called catalytic cycle is closed when the reaction has taken place and the catalyst has returned to its initial state [11].

Generally, it is clear that research of catalysts can improve their performance and therefore make their application more cost-effective and energy-efficient. Surface science in particular aims at fundamentally understanding the origin of the catalytic activity by studying the interaction of molecules with surfaces on the atomic level. This includes adsorption, diffusion, and dissociation behavior, as well as the reaction with other (adsorbed) molecules. Atomic-level studies are facilitated on simplified model systems under well-controlled conditions as well as in computational chemistry [19]. Certain techniques such as temperature-programmed desorption [20], molecular beam studies [17], and electron diffraction (see Section 2.5) inherently require ultra-high vacuum environments, whereas other techniques like X-ray photoelectron spectroscopy (see Section 2.4) simply take significantly less technical effort when performed in vacuum and on conductive samples. Atomic-scale imaging with scanning tunneling microscopy (see Section 2.3) is easiest applied on atomically flat and conductive surfaces such as metal single crystals. The results that such conventional surface science achieves are vast and a necessary piece of the puzzle that is understanding the catalytic process in its whole. Therefore, I wish to emphasize the importance of such research, before moving on to motivating an additional direction within surface science in the following sections.

1.3 Complex Model Catalysts: Bridging the Materials Gap

The difference between flat, single-crystalline surfaces studied in conventional surface science and industrially used powder catalysts, often consisting of metal particles and oxide supports, including many different possible structures, is what we call the materials gap [21]. Ideally the most stable face of a single crystal consists of large, flat terraces. However, often low-coordinated surface sites like steps, kinks, and defects can be significantly more active for interactions with gas-phase molecules than the terrace sites [22]. Chapter 5 of this thesis exemplifies the use of the most closed-packed face of a metal single crystal, Co(0001), which is, however, expected to have a significant number of steps and defects due to limitations in the preparation method. The effects of low-coordinated sites can be studied more systematically on stepped single-crystal faces, especially by comparing their behavior to the closed-packed ones [22], which is also possible by computational methods [23]. Recent progress has also been made in continuously varying the step density over a large range by studying curved single crystals [24].

Oxide materials relevant for catalysis can be investigated in the form of thin oxide films deposited onto metal single crystals [25]. These are additionally relevant for certain other applications [26]. Due to the conductivity of the metal substrate underneath, thin films can still be studied with the same techniques as metal single crystals. However, the structure of deposited films depends on the lattice mismatch and the interaction with the substrate, such that it can differ significantly from the bulk structure [27–29]. Additionally, an influence of the substrate on the electronic structure of the oxide and thus its interaction with gases cannot be excluded [25,29]. This can be avoided by directly using bulk oxide single crystals [30]. We do this in Chapter 3 of this thesis with $ZnO(10\bar{1}0)$, where we also mention certain challenges associated with its use.

The world of single-crystal-based model catalysts can be vastly expanded by the deposition of various metal [31], oxide [29], and/or sulfide [32] nanoparticles onto the single-crystal surface. By thus combining the different components that are contained in industrial catalysts, the interface region between them can be studied. Often the oxide 'support' is not merely a template keeping the active metal nanoparticles in place but rather an active component of the catalyst influencing its activity, selectivity, and/or poisoning behavior [31]. So-called strong metal-support interactions can lead to substantially different geometrical and electronic structures in the interface region [33]. In Chapter 4 of this thesis we investigate a complex model catalyst consisting of a metal single crystal with oxide nanoparticles on top, $TiO_2/Au(111)$. Such a so-called inverse model catalyst can more easily be studied with methods requiring conductivity. Directly comparing an inverse model catalyst to its non-inverse counterpart, nanoparticles of the metal on a single crystal of the oxide, can shed light on the influence of nanoparticle morphology, different crystal faces, and electronic structure on the activity [34,35].

1.4 In Situ Studies: Bridging the Pressure Gap

Another disparity between conventional surface science and realistic applications is the so-called pressure gap [21], which refers to the pressure difference between vacuum studies (in 10^{-11} mbar to 10^{-3} mbar) and industrial catalysis at at least atmospheric pressures up to even hundreds of bar [36]. As the interaction of molecules with catalyst surfaces but also the structure of the surfaces itself can strongly depend on the absolute pressure, efforts have been made to expand surface-science techniques to also be applicable at near-ambient to ambient gas pressures, the so-called in situ approach [37]. When, additionally, the products of the catalytic reaction are detected in the gas phase, one can speak of an operando technique [21].

Ambient-pressure imaging of surfaces has been achieved using optical microscopy [38], transmission electron microscopy [39], X-ray microscopy [40], scanning tunneling microscopy [41–44], and atomic force microscopy [45], which is more suited for the study of oxide samples. The so-called ReactorSTM [44], which is used in Chapters 3 and 4 of this thesis, incorporates a small-volume flow-reactor cell into a vacuum chamber. In this way the gas flow and pressure can be regulated precisely and a swift change between vacuum and ambient conditions of up to 6 bar gas pressure and 600 K surface temperature is possible. As such the reactor microscope can show the structure of the active surface and shed light on reaction mechanisms for a variety of catalysts and reactions [46–48].

X-ray absorption techniques can give spectroscopic information and unravel local electronic structure in situ [49], whereas in situ surface X-ray diffraction can determine the structure of the surface during the reaction [50]. The latter can be combined with laser-induced fluorescence probing the gas distribution above the catalytically active surface [51]. Reaction intermediates and products can be identified with infrared and UV-VIS absorption techniques, like vibrational and Raman spectroscopy, which are applied in situ as well [52,53].

A particularly challenging but also particularly useful technique to apply at elevated pressures is X-ray photoelectron spectroscopy. Particularly useful because adsorption behavior of molecules as well as chemical states of the catalyst material can strongly depend on the gas pressure. Particularly challenging because the technique relies on the detection of electrons, which can only travel short distances in situ. Nonetheless, near-ambient pressure X-ray photoelectron spectroscopy has been made available to a large number of catalysis researchers [54], especially through user facilities. Chapter 5 of this thesis presents an example of a near-ambient pressure X-ray photoelectron spectroscopy study conducted using synchrotron X-rays.

Apart from those techniques which are widely used now, new techniques are being adapted to in situ use as shown in proof-of-principle studies. For example synchrotron X-ray assisted scanning tunneling microscopy combines local structural with local spectroscopic information [55]. Simultaneous non-contact atomic force microscopy and scanning tunneling microscopy images corrugation at the same time as electronic structure [56]. Additionally, there is considerable effort made in expanding the use of X-ray photoelectron spectroscopy from near-ambient to fully ambient pressures [57,58]. The list of in situ techniques mentioned here is most likely not complete.

As we will see in all three systems investigated in this thesis, in situ studies on complex model catalysts do not only allow for the observation of new structures and behaviors, but also bring along with them a new set of challenges caused by low concentrations of impurities in materials and gases. Before diving into the experimental results in Chapters 3 to 5, the interested reader can find a detailed explanation of the surface-science techniques used, in vacuum as well as in situ, in the following chapter.

Chapter 2

Experimental Techniques

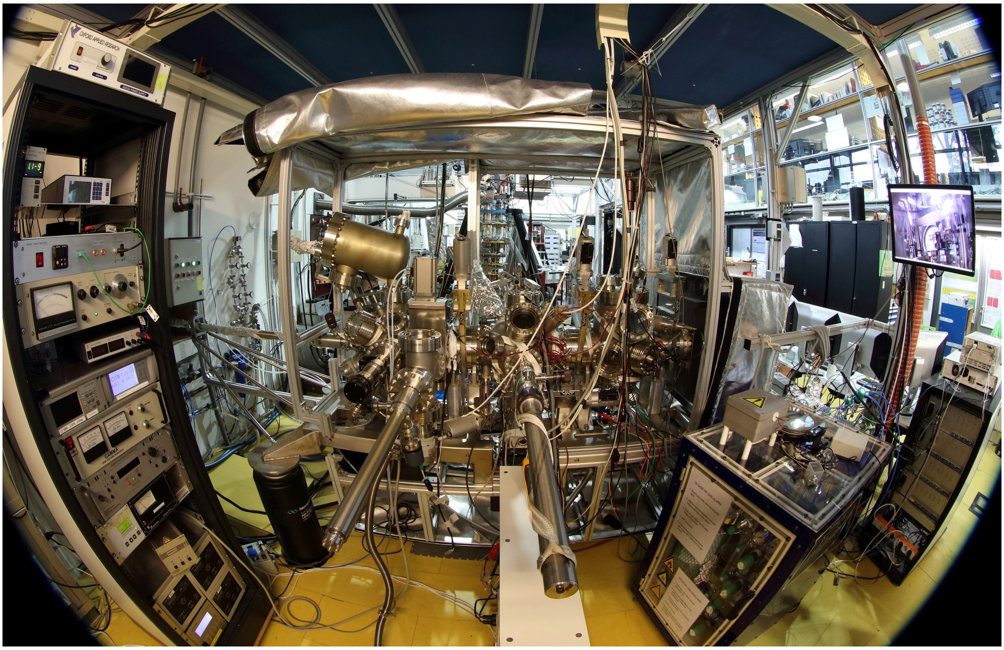

Figure 2.1: Photo of the ReactorSTM setup showing (from left to right) various electronics, the vacuum chamber including the X-ray photoelectron spectroscopy part, the preparation part, and the scanning tunneling microscopy part, the gas delivery system for the flow reactor cell, and the control electronics for the microscope. Photo credit Klaus Wenzel.

2.1 Setups

2.1.1 The ReactorSTM

The measurements presented in Chapters 3 and 4 were conducted on the so-called ReactorSTM at Leiden University, The Netherlands, which is shown in Figure 2.1. This setup is an ultra-high vacuum chamber, in which single-crystal-based samples are prepared and investigated. Hereby, the main component is a scanning tunneling microscope within a flow reactor cell, such that it can image surfaces at ultra-high vacuum pressures as well as in up to 6 bar of gases. This is complemented by vacuum techniques within the same setup: low-energy electron diffraction (LEED), and Auger electron spectroscopy (AES) as well as X-ray photoelectron spectroscopy (XPS). This chapter provides theoretical and technical background necessary for the techniques used.

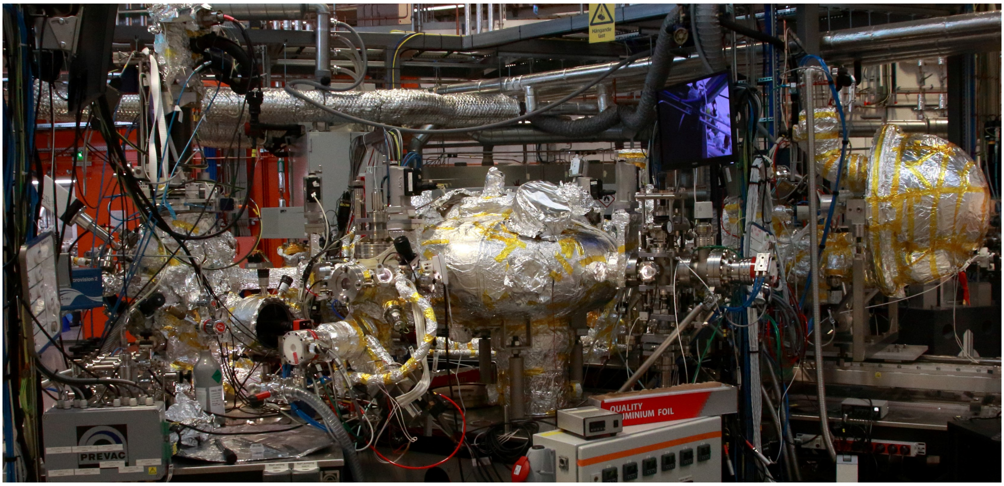

Figure 2.2: Photo of the NAP-XPS endstation of the HIPPIE beamline at MaxIV showing the preparation chamber on the left, a transport chamber in the middle, and the electron analyzer for X-ray photoelectron spectroscopy on the right.

2.1.2 Synchrotron NAP-XPS

The measurements presented in Chapter 5 were mainly conducted at the HIPPIE beamline of MaxIV, Lund, Sweden (see Figure 2.2) and some were conducted at beamline 9.3.2 of the Advanced Light Source, Berkeley, USA. In both cases the endstation consists of a vacuum chamber for sample preparation and synchrotron X-ray photoelectron spectroscopy can be conducted in vacuum as well as in the mbar range of gases. This technique is explained in Section 2.4.

2.2 Ultra-high Vacuum and Gas Handling

Vacuum as well as the use of gas require specialized techniques for creating, maintaining, and monitoring a vacuum, measuring pressures in all ranges, and creating flows of gas. Information on the basic techniques described in this section can be found in fundamental surface-science literature [20,59] and vacuum technology books [60], as well as on manufacturer websites.

2.2.1 Materials

In order to reach ultra-high vacuum the materials inside the chamber cannot have a high vapor pressure, be porous, or contaminated with organic molecules. Additionally, all materials need to be temperature resistant to at least 150 °C as the whole chamber is heated in order to reduce the water background (see following section). Parts which are close to a sample at elevated temperatures might have to be made of materials resistant to significantly higher temperatures. The main chamber is usually constructed of stainless steel and copper seals for connecting different parts. Filaments and other high-temperature parts can for example be made from tungsten, molybdenum, or tantalum. Ceramics as alumina or sapphire are used for electrically isolating parts.

Parts that come in contact with gases, such as gas lines, valves, and reactor parts can be made from stainless steel for a number of standard gases. However, if gases are corrosive, specialized materials such as gold-coated steel or Hastelloy C have to be used. Additionally, the construction materials should be inert for the reactions to be studied.

2.2.2 Vacuum Pumps

Depending on the pressure range, different types of pumps are used. So-called rough pumps like rotary vane pumps, dry scroll pumps, or membrane pumps can reach a rough vacuum down to a range of 10^{-3} mbar. These are used as pre-pumps for high-vacuum pumps as well as for pumping gases when emptying a reactor or using a reactor through which the gas is constantly flowing.

Turbo molecular pumps, which produce a pressure gradient by rotating blades, can reach the ultra-high vacuum range of down to 10^{-10} mbar and require a rough pump downstream. For applications that require low mechanical noise so-called ionization pumps are useful as they do not have any moving parts or exhaust connections. Ionization pumps ionize and trap the molecules and atoms they pump and can only be used once the 10^{-7} mbar range has been reached with a turbo molecular pump. Independent of the pump that is used, vacuum chambers can only reach ultra-high vacuum in a reasonable time frame when they are heated to at least 100 °C after evacuating the air. During this so-called baking, water adsorbed on the inside of the chamber can desorb and be pumped.

2.2.3 Pressure Gauges

Vacuum pressures in the range from 10^{-4} to 10^{-11} mbar can be measured by ionization gauges. In general these create free electrons which ionize the gas molecules. These are in turn collected creating a current that is a measure for the pressure. If the free electrons are produced using a hot filament (hot filament or Bayard-Alpert gauge) this can cause for example oxygen dissociation as well as the deposition of contaminants from the filament material onto samples. Therefore, so-called cold cathode or Penning gauges can be a more suitable choice. Here the free electrons are produced in a self-supporting discharge which starts from a cathode at room temperature and is sustained by secondary free electrons created when the ionized gas molecules impinge on the cathode.

Rough vacuum is mostly monitored with so-called Pirani gauges, which make use of the fact that the electrical resistance of a filament is dependent on the amount of heat loss to the surrounding gas environment.

Whereas all pressure gauges described so far measure gas-type dependently, mechanical pressure gauges can measure the pressure independent of the type of gas and directly as force per area. An example is the baratron gauge, which can be used in the intermediate range from 10^{-4} mbar to atmospheric pressures. Here the pressure-dependent position of a membrane is measured as a change in capacitance. Standard mechanical manometers measure pressure with respect to the surrounding atmosphere by detecting the movement or deformation of a solid piece or liquid and displaying it in an analog way. These are used at atmospheric pressures and above like in gas supply lines and bottles.

Precise digital read-out of pressures over a large range can be achieved using piezoresistive pressure sensors, in which the pressure-dependent deformation of a piezoresistive material is measured as a change in its electrical resistance. These are combined with an automatic valve and feedback system in so-called back pressure controllers, which can stabilize the pressure in flow reactors to a chosen set-point.

2.2.4 Gas Supplies

For the use of gas at low pressures inside a vacuum chamber so-called leak valves can be used. These separate the chamber from the atmospheric pressure gas line by a soft material seal pressed against a sealing surface. By decreasing the force against the seal the amount of gas that leaks into the chamber can be increased. The desired pressure and the type of gas determine which vacuum pumps can be used on the chamber while filled with gas.

For a controlled supply of larger amounts of gas to reactors so-called mass flow controllers can be used. These determine the flow by measuring the transport of heat by the gas and are thus gas-type dependent. A feedback controls a valve inside the controller to allow for the desired flow.

2.2.5 Gas Analysis

The residual gas in a vacuum chamber can be monitored with a quadrupole mass spectrometer (QMS). Gas molecules are ionized by free electrons and then accelerated by a fixed voltage. This results in an ion velocity dependent on the charge-to-mass ratio. The quadrupole itself consists of four parallel rods. The same oscillating voltage is applied to opposite rods with different sign for the two pairs of rods. This leads the ions onto an oscillating path and depending on the voltage only one specific charge-to-mass ratio reaches the detector at the end of the rods whereas all other ions hit the center or the outside wall of the quadrupole. By varying the voltage all desired charge-to-mass ratios can be measured.

A QMS can also be used to measure the reaction mixture or products from a reactor if a small amount of the gas is let into a vacuum chamber with a QMS installed. It can only be operated at pressures up to 10^{-6} mbar. However, the background of the vacuum chamber itself can disturb such gas measurements. A more suitable method for directly analyzing a gas mixture is gas chromatography, which will not be explained here.

2.2.6 Sample Preparation

Controlled surface-science studies in ultra-high vacuum are often done on bulk single-crystal samples. A specific surface face can for example be prepared by cleaving the material in a vacuum chamber or by cutting and polishing in air. Subsequent electrochemical etching and/or ion sputtering in ultra-high vacuum removes contaminants from the material. The cleanliness of the surface can be monitored with different methods in UHV. The indicators used in this work, in the order of increasing sensitivity, are sharpness of the low-energy electron diffraction pattern (see Section 2.5), detection of other materials using spectroscopy (see Section 2.4), and the visibility of foreign atoms in scanning tunneling microscopy images (see Section 2.3).

Sputtering and Annealing

The samples used in this thesis are prepared by sputtering and annealing. The sputtering gun produces free electrons in a filament, which are then trapped in a cylindrical grid. When the vacuum chamber is filled with an inert gas such as argon on the order of 10^{-6} mbar, the free electrons ionize argon atoms. The argon ions are in turn accelerated and focused onto the sample by electrostatic lenses. When impinging on the sample, the positively charged argon ions remove the uppermost layers of atoms of the sample material together with contaminants. As this process roughens the surface it has to be annealed to a temperature of about two thirds of the melting temperature, which flattens the surface again. Heating in ultra-high vacuum can easily be achieved radiatively with a filament behind the sample. The heating power can be increased with so-called e-beam heating where free electrons are accelerated from the filament to the sample. This can either be realized by applying a positive voltage to the sample or by applying a negative voltage to the filament while the sample is grounded. From the 10^{-4} mbar range of gases on, especially in atmospheric and higher pressures, other heating methods have to be applied. Examples are resistive heaters from ceramic materials in direct contact with the sample and heating by exposure to laser light. The temperature of the sample is monitored using so-called thermocouples, two materials whose electrical behavior depends differently on the temperature. When both are in contact with the sample, a voltage difference can be detected at their other end (at room temperature) as a measure for the temperature of the sample. During annealing, contaminants from the bulk of the sample segregate to the surface. With repeated cycles of sputtering and annealing the density of contaminants on the surface and up to a certain depth into the bulk is reduced over time.

Physical Vapor Deposition

Other metals, oxides, and sulfides can be deposited onto a single-crystal substrate via physical vapor deposition using for example a so-called e-beam evaporator. A rod of the desired material is heated using a filament and a positive high voltage on the rod. Once the material starts to sublime, it can be deposited onto the sample in vacuum or gas background.

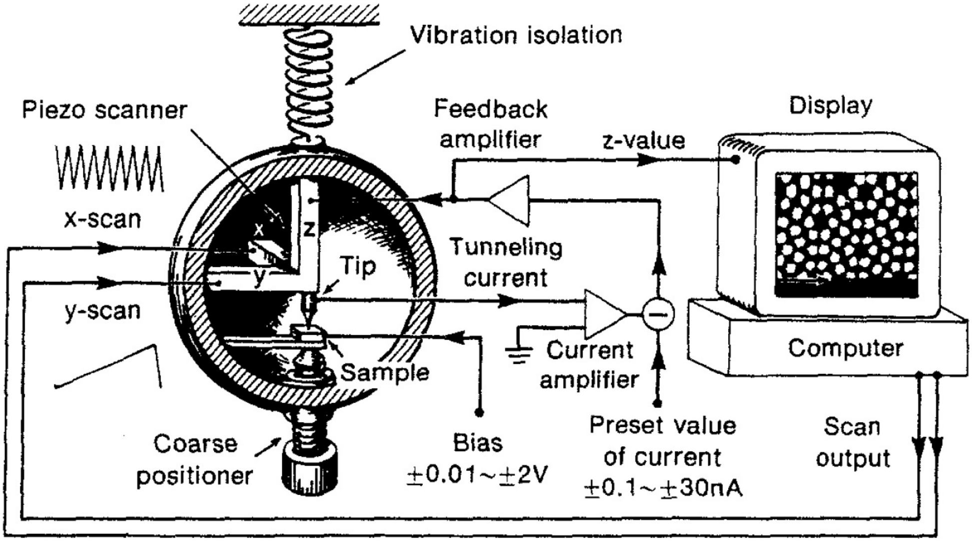

Figure 2.3: Schematic of a typical scanning tunneling microscopy setup. Figure reprinted from Ref. [61].

2.3 Scanning Tunneling Microscopy

Scanning tunneling microscopy, as invented by Binning and Rohrer in 1982 [62,63], allows for atomically resolved imaging of surfaces in vacuum as well as in gases and liquids. The following sections introduce the basic principle and components of a scanning tunneling microscope (STM) based on standard literature [20,61]. Figure 2.3 gives an overview of these components.

2.3.1 General Physical Principle

The scanning tunneling microscope makes use of the principle of electron tunneling. In the quantum mechanical description, the position of an electron is not known exactly but described by a wave function that can be understood as the probability for the electron to be in certain positions. These wave functions partially reach into classically forbidden areas where the potential is higher than the energy of the electron. It follows that there is a non-zero probability for an electron to cross such a potential barrier. This probability decreases exponentially with the width of the potential barrier. This is used in a scanning tunneling microscope where an atomically sharp tip is brought as close to the sample as a few Å. While applying a so-called bias voltage between tip and sample, electrons can tunnel through the vacuum (gas or liquid) in between them, which can be measured as a so-called tunneling current. As this current is dependent on the distance between tip and sample, it can be used as a measure for height changes on the surface while the tip moves across the surface. However, one has to keep in mind that the tunneling current is determined by the local density of electron states and thus not only dependent on the distance between tip and sample but also on the local electronic structure. This can have significant influence on the interpretation of STM data, especially when (partially) isolating compounds are present on the sample surface. When the bias voltage on the sample is negative, the STM image shows the occupied electronic states in the surface (filled-state scanning). A positive bias voltage on the other hand is used to image the unoccupied electronic states (empty-state scanning).

2.3.2 Positioning system

A crucial part of every scanning tunneling microscope is the positioning system as shown in Figure 2.3. First, the tip and sample need to be brought into tunneling distance with a coarse positioning system. Then the tip needs to be able to move in all three directions in small increments on the Å scale. This can be achieved with three independent piezoelectric motors. These are made from materials which expand and contract depending on the voltage that is applied across them. The piezoelectric motors which move parallel to the surface can be used to move to a certain position on

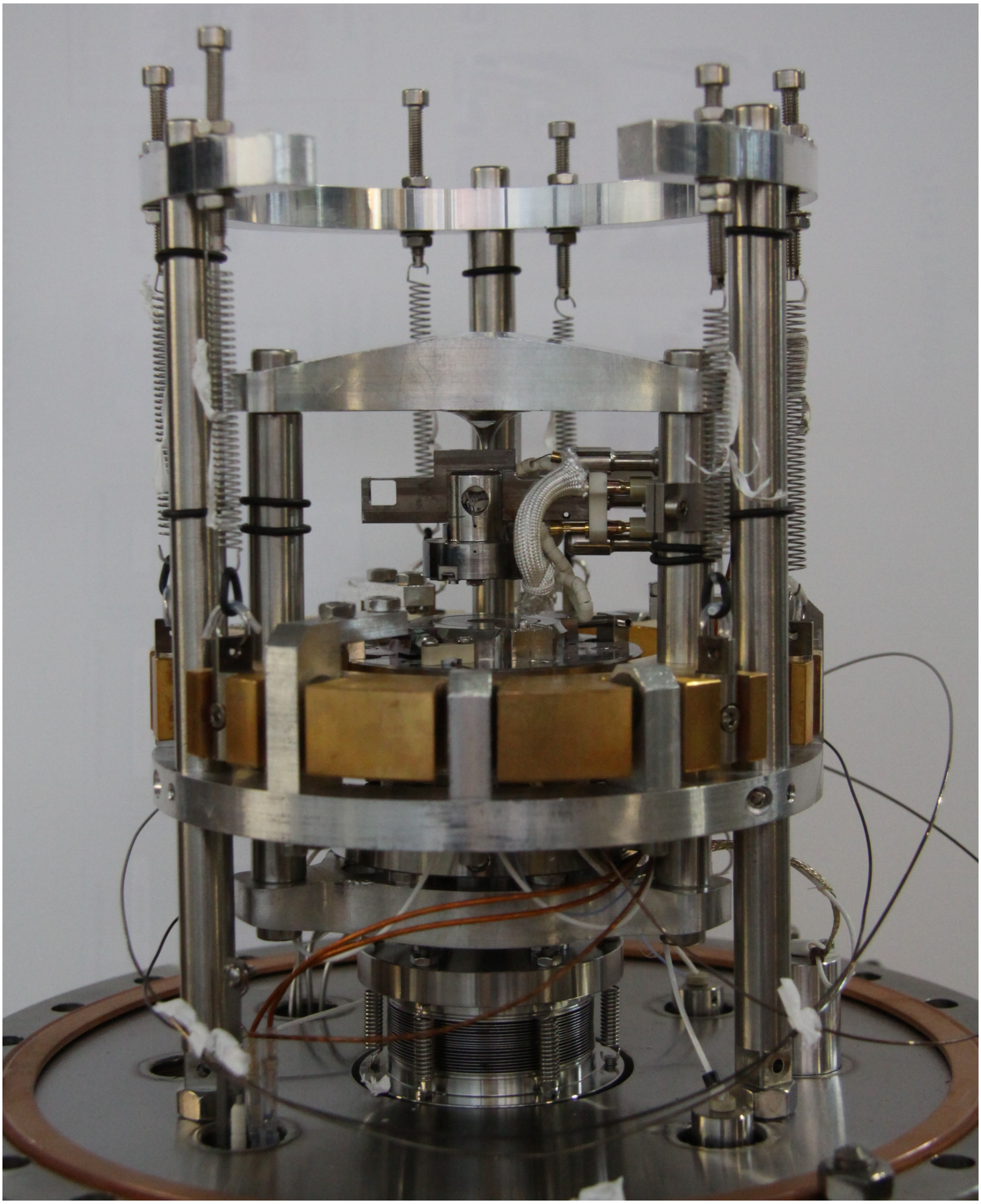

Figure 2.4: Photo of the STM part of the ReactorSTM setup showing the eddy current damping system with the sample holder in the center. The sample (not visible) is facing down.

the surface. During scanning, one direction (x in this thesis) oscillates quickly while the other (y in this thesis) is changed gradually. This constitutes a scanning motion over the surface allowing the recording of two-dimensional images. Finally, the piezo that moves the tip normal to the sample surface (z in this thesis) is needed to move into a suited tunneling distance. In constant-current mode (see Section 2.3.3) the z motor additionally moves while scanning over the surface.

2.3.3 Scanning Modes and Feedback Circuit

On sufficiently flat samples, scanning tunneling microscopes can be used in the constant-height mode. In this case the tip is scanning across the surface at a constant height while the tunneling current is recorded and used as a measure for the corrugation of the surface. While this allows for fast scanning it is not suited for more corrugated surfaces, on which the risk of contact between tip and sample is too high in the constant-height mode. Instead the constant-current mode is used. In this case a feedback circuit is used that moves the z-position of the tip in such a way that the tunneling current stays at a fixed set-point value. The error between the measured tunneling current and the set-point functions as the input for the feedback circuit. The feedback circuit then calculates the necessary change to the z-position as a function of the error itself (proportional) as well as the integrated error over a specific time (integral). Choosing the right parameters for the proportional and integral gain, the response time and accuracy of the feedback circuit are optimized. This is necessary in order to limit the possible scanning speed as little as possible.

2.3.4 Vibration Damping and Electrical Interference

As the positioning of the tip and the distance between tip and sample need to be precise and stable on the Å scale, scanning tunneling microscopes need to be isolated from mechanical movements. In the microscope used in this thesis this is done in multiple stages. First, the floor underneath the setup is disconnected from the floor around it. Second, the setup is mounted on pressurized air legs. And last, the microscope itself is suspended from soft springs within the setup (see Figure 2.4). Fixed magnets next to the suspended part slow down any movements of the copper base of the microscope via eddy current damping. As tunneling currents on the order of pA have to be measured by the STM electronics, they have to be properly shielded from electronic interference as well. A separate physical ground connection is crucial. It can be necessary to decouple the STM electronics from other electronics on the same experimental setup, turn other electronics off, and use differential cables for the tunneling current signal.

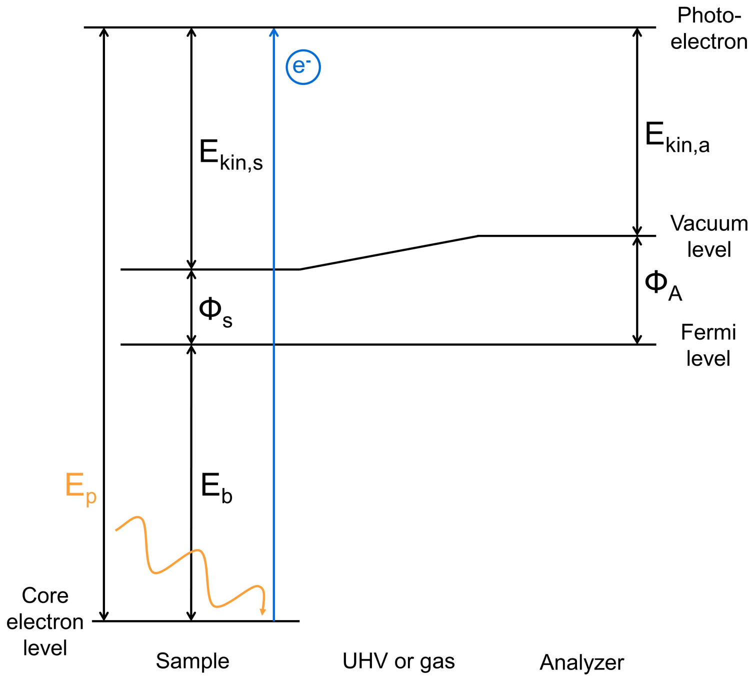

Figure 2.5: Illustration of the energy levels involved in emission and detection of X-ray-induced photoelectrons.

2.3.5 In Situ Scanning Tunneling Microscopy

Scanning tunneling microscopy can in general be used in situ without significant technical effort. However, the gas or liquid does interact with the tunneling electrons as well as the tip and influences the scanning behavior and resolution. The unique feature of the in situ microscope used in this thesis [44], is that the in situ reactor is incorporated into an ultra-high vacuum chamber. This does not only allow for controlled sample preparation in UHV but also for imaging in UHV before and after in situ measurements without exposing the sample to air in between.

2.4 X-ray Photoelectron Spectroscopy

X-ray photoelectron spectroscopy (XPS) identifies the elemental composition of surfaces as well as chemical states. The technique is introduced in general surface-science literature such as Ref. [20] and detailed information can for example be found in Ref. [64]. Originally a UHV technique, XPS is currently also applied in the mbar range of gases and bar range of liquids.

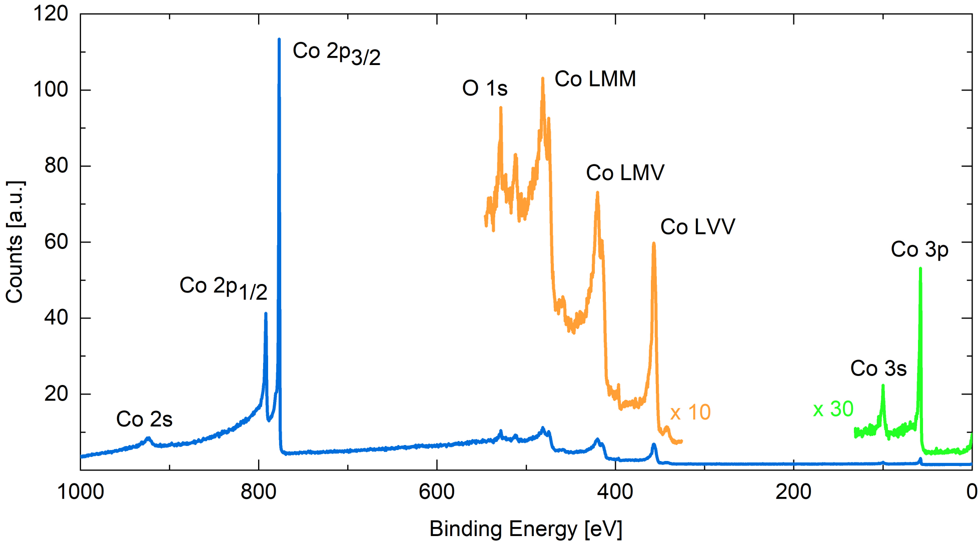

Figure 2.6: Survey X-ray photoelectron spectrum of a Co(0001) surface taken in UHV at 220 °C with a photon energy of 1130 eV. The different peaks are identified using Ref. [65]. Details see text.

2.4.1 General Physical Principle

X-ray photoelectron spectroscopy makes use of the photoelectric effect, which is the ejection of electrons from materials when irradiated with photons. As illustrated in Figure 2.5, the initial energy of the photon E_p is hereby split up into the binding energy of the electron in the material E_b, the work function of the sample material Φ_s, and the remaining kinetic energy of the electron $E_\mathrm{kin,s}$ according to $E_\mathrm{p} = E_\mathrm{b} + \Phi_\mathrm{s} + E_\mathrm{kin,s}$. Depending on the work function Φ_a of the analyzer, the vacuum level close to the analyzer differs from the vacuum level close to the sample by $\Phi_\mathrm{a} - \Phi_\mathrm{s}$. The analyzer thus measures a kinetic energy $E_\mathrm{kin,a} = E_\mathrm{kin,s} - (\Phi_\mathrm{a} - \Phi_\mathrm{s}) = E_\mathrm{p} - E_\mathrm{b} - \Phi_\mathrm{a}$. As the photon energy E_p is known, a material with a peak of known binding energy E_b or the Fermi edge of a material can be used to determine Φ_a and thus calibrate the binding energy axis. In this way the measured kinetic energy spectrum can directly be converted into a measured binding energy spectrum.

2.4.2 Components of XPS Spectra

An X-ray photoelectron spectrum consists of multiple structures. First, the core level peaks of each element which is sufficiently abundant in the sample are visible. The binding energy of a core electron depends on the shell $n = 1,\ 2,\ 3,\ \ldots$, the angular momentum $l = 0,\ 1,\ 2,\ 3, ...$, referred to as s, p, d, f, ..., and the total angular momentum (which includes the electron spin) $j = 1/2,\ 3/2,\ 5/2,\ ...$. The energy levels with the same angular momentum l but different spin ($s = +\ 1/2$ or $-\ 1/2$) have a fixed occupancy ratio and energy difference. Therefore, the XPS peaks of such a so-called doublet, for example $2\mathrm{p}_{3/2}$ and $2\mathrm{p}_{1/2}$, have a fixed separation in energy as well as peak-area ratio. An example of such a doublet with an energy spacing of 15 eV can be seen in the survey spectrum of cobalt displayed in Figure 2.6. Apart from the Co 2p doublet the Co 2s, Co 3s, and Co 3p core level peaks are visible. Additionally, some adsorbed oxygen on the cobalt surface causes an O 1s contribution. In general, the exact position of a core level peak depends on the chemical environment the atom is in.

If an X-ray gun without monochromator is used, additional satellite X-ray energies are emitted, which lead to satellite peaks in the XPS spectrum. Similarly, synchrotron X-rays are accompanied by higher harmonics, photon energies which are multiples of the main photon energy, and cause additional (significantly less intense) XPS peaks.

Additionally, the shape of XPS spectra is determined by different loss processes, through which the emitted photoelectrons can lose a part of their energy before leaving the sample material and being detected: First, due to inelastic scattering of photoelectrons the background on the high binding-energy side of a peak is higher than on the low binding-energy side, which can be seen in the survey spectrum in Figure 2.6. This can be taken into account by using the so-called Shirley background subtraction. Second, photoelectrons can also excite so-called bulk as well as surface plasmons, oscillations of the conduction band electrons in metals. This leads to distinct plasmon loss peaks on the order of 10 eV above the main photoelectron peak with possible higher harmonics. Third, the atom can remain in an excited state when the photoelectron is emitted leaving it with a few eV lower energy forming a so-called shake-up peak. Shake-off features appear when the photoelectron loses energy through interaction with valence electrons. In metals with a high electron density close to the Fermi edge such interactions can excite electrons into empty states above the Fermi edge. This causes a tail on the high binding-energy side of the photoelectric peak instead of discrete shake-off losses. The resulting asymmetric peak shape can be described using specific asymmetric line shapes and asymmetry parameters from literature. The Co 2p doublet in Figure 2.6 contains both an asymmetric main peak caused by shake-off losses as well as discrete plasmon losses as can be seen in a detailed fit in Figure 5.1 in Section 5.2.2. Last, if an atom has unpaired electrons in the outer shell, an unpaired core electron produced by photoelectron emission can couple with the unpaired outer shell electron in a number of different ways resulting in different photoelectron energies. These are visible as so-called multiplets in the XPS spectrum.

In XPS spectra (broader) Auger peaks are visible as well. When the core hole left in an energy level n_a after photoelectron emission is filled with an electron from a higher energy level n_b, energy is released. This energy can cause another electron from an energy level n_c to be emitted from the material. This so-called Auger electron causes a peak in the spectrum denoted as $n_a n_b n_c$. Here the nomenclature $n = 1, 2, 3, ...$ is replaced by $n =$ K, L, M, ..., V with V for valence electrons. In the cobalt survey (see Figure 2.6) the Auger peaks Co LMM, LMV and LVV, each consisting of multiple peaks caused by the sublevels in each shell, are visible. The kinetic energy of Auger electrons is element specific and independent of the initial photon energy. Depending on the X-ray source Auger peaks thus appear at different binding energies in the XPS spectrum.

2.4.3 X-ray Sources

In conventional lab X-ray guns, electrons from a filament are accelerated into an anode material. Depending on the material one specific wavelength of photons is emitted. Common are the aluminum K_α line at 1486.6 eV and the magnesium K_α line at 1253.6 eV. Additionally, satellite peaks as well as bremsstrahlung are produced. A monochromator can be used to select only a narrow width from the spectrum around the primary line and thus improve the energy resolution of the instrument.

In synchrotron X-ray sources, photons are emitted from electrons which are kept on a circular path by a magnetic field. Undulators are used to select a specific photon energy. By tuning the photon energy, different probing depths into the material can be achieved. Compared to X-ray guns, synchrotrons produce a significantly larger amount of photons per time and area as described by the so-called brilliance. This allows for a lower detection limit.

2.4.4 Electron Analyzer

The most common type of electron analyzer used in X-ray photoelectron spectroscopy is the concentric hemispherical analyzer. First, an electrostatic lens focuses photoelectrons emitted from the sample into the analyzer. Additionally, it decelerates all electrons by the same amount such that those with the kinetic energy $E_{\mathrm{kin,a}}$ to be detected are left with the so-called pass energy. Second, two concentric hemispheres with voltages V_1 and V_2 act as a hemispherical capacitor and bring the electrons onto a circular path. As the radius of the motion depends on the kinetic energy of the electrons they are separated spatially. The voltage difference $V_2 - V_1$ is chosen such that those electrons with the pass energy hit the detector area and their count is a measure for the amount of photoelectrons with $E_{\mathrm{kin,a}}$. While increasing the deceleration by the input lens over time, the spectrum is measured from low to high kinetic energy, thus high to low binding energy. The lower the pass energy is chosen, the better the energy resolution of the analyzer. However, a lower pass energy results in a lower overall signal as well.

2.4.5 NAP-XPS

In recent years XPS systems for use in the mbar range of gases have been developed, see for example Ref. [66], which allow for in situ spectroscopy studies of model catalysts. The main challenges are that the electron analyzer can only be operated in vacuum below 10^{-6} mbar as well as the short mean free path of electrons in the gas. Therefore, the most popular design is a differentially pumped system with multiple turbo molecular pumps where the pressure is decreased in stages between the near-ambient pressure region and the electron analyzer. By placing the nozzle between the near-ambient pressure area and the first pumped stage as close as possible to the sample, as many electrons as possible are collected. However, this is limited by the ability of the X-rays to still reach the probed sample area as well as the pressure drop close to the nozzle. Overall, this results in an optimal sample-nozzle distance of roughly 1 to 1.5 times the nozzle diameter. The nozzle diameter can be optimized depending on the requirements for signal strength and gas pressure. In sufficiently large gas pressure, electron attenuation by the gas is pressure dependent and might have to be taken into account during data analysis. Additionally, near-ambient pressure XPS allows for the detection of so-called gas-phase peaks which stem from photoelectrons emitted directly from the gas molecules. As opposed to peaks stemming from the sample, gas-phase peaks shift with the work function Φ_s of the sample. This shift can be used for direct work function measurements [67,68] and thus indicate changes in the overall oxidation state of the sample.

2.5 Low-Energy Electron Diffraction

Low-energy electron diffraction (LEED) is a standard surface-science technique used in ultra-high vacuum in order to determine the structure of crystalline surfaces as well as ordered adsorption structures. Detailed information can be found in general literature such as Ref. [20].

2.5.1 General Physical Principle

The principle of low-energy electron diffraction can conveniently be described in the wave description of quantum mechanics. Electrons with an energy between 30 eV and

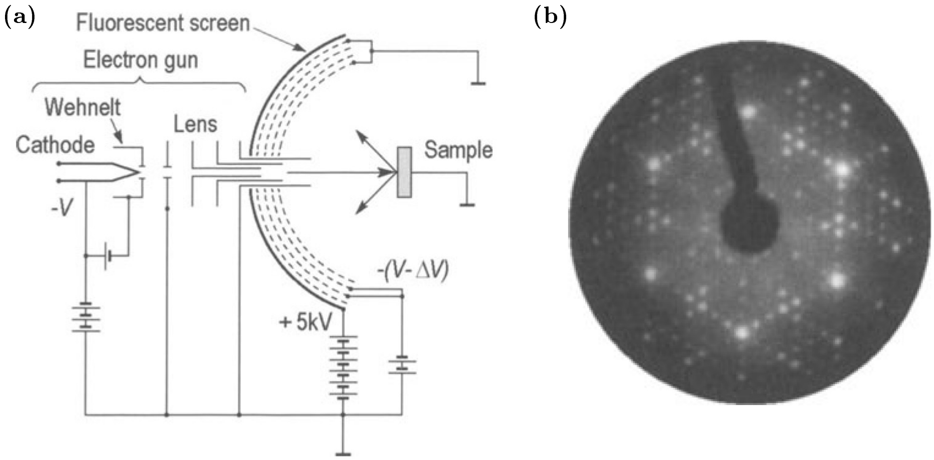

Figure 2.7: (a) Schematic of a LEED setup and (b) typical LEED measurement showing the Si(111) 2x1 reconstruction. Figure reprinted from Ref. [20] and adjusted.

200 eV are waves with a de Broglie wavelength of one to two Å. As this is slightly shorter than the atom-to-atom distance in typical crystalline surfaces, the electrons diffract as on a regular grid and constructively interfere in diffraction spots at a certain distance from the sample. The pattern of diffraction spots is then an image of the crystalline surface structure in reciprocal space. Thus, the inverse of unit cell lengths can be measured in the LEED pattern relative to the inverse of a known unit cell length. In this way the unit cell of an adsorbed super-structure relative to the unit cell of the substrate can be determined more accurately than using microscopy. An example is shown in Figure 2.7(b) where a unit cell seven times as large as the substrate unit cell is observed.

2.5.2 Components

The general components for LEED, as shown in Figure 2.7(a), are an electron gun, four hemispherical electrostatic grids with the sample at their center, and a hemispherical fluorescent screen outside of the grids. In detail, the cathode filament in the electron gun produces free electrons. These are collimated by a Wehnelt cylinder and accelerated to the desired energy by an electrostatic lens. This is achieved by holding the cathode filament on a negative potential with respect to the lens, the sample, and the first grid, which are grounded. When impinging on the sample, not all electrons are scattered elastically as described above but can be scattered inelastically as well. The second and third grid are held on a negative potential in order to prevent the inelastically scattered electrons from reaching the screen and causing a background. The fourth grid is again grounded in order to shield the other grids from the high voltage on the fluorescent screen. This is needed to accelerate the electrons into the screen with enough energy to cause fluorescence at the position of impingement. The LEED pattern on the fluorescent screen can be observed through a viewport of the UHV chamber using any conventional camera.

Chapter 3

Stability of ZnO($\mathbf{10\bar{1}0}$) in Moderate Pressures of Water

3.1 Introduction

Global warming and the depletion of natural resources are among the greatest and most urgent challenges humankind is currently facing. There is an obvious need for alternative methods of transportation and energy production. Renewable energy sources like wind and solar power however are time and weather dependent and thus require simultaneous advances in energy-storage techniques. Methanol is interesting as an energy-storage material. It can be produced from renewable sources [69], is biodegradable [70], and, being liquid at room temperature [71], it can be stored more easily and safely than hydrogen. In order to harvest the energy, methanol can be converted to hydrogen via the methanol steam reforming reaction:

$$CH_3OH + H_2O \rightarrow 3\ H_2 + CO_2 \tag{3.1}$$

Advantages of methanol with respect to other reforming feedstocks are the high H-to-C ratio and a reaction temperature as low as 250 °C [72]. Carbon monoxide forms as a side product to the methanol steam reforming reaction [73]. This is the main challenge in converting the hydrogen further to electricity using a fuel cell. The platinum anode of fuel cells is poisoned by a few parts per million of CO [74]. The requirement for a viable methanol steam reforming catalyst is thus a high selectivity towards CO_2 instead of CO. The industrially used catalyst for methanol synthesis Cu-ZnO/Al_2O_3 shows significant activity for methanol steam reforming and has been researched extensively [72,75,76]. Although there is ample evidence regarding the nature of strong metal-support interactions between copper and zinc oxide [72,77,78], the exact mechanism of the methanol steam reforming remains under debate.

Zinc oxide alone is active itself and relevant for the CO_2 selectivity of the methanol steam reforming catalyst [79,80]. Studies on zinc oxide single crystals of different faces are aiming at understanding its role at the atomic level. The interaction of ZnO($10\bar{1}0$) with methanol [81–83], water [84,85], atomic hydrogen [86], CO [87,88], and CO_2 [89,90] has been studied extensively under ultra-high vacuum conditions. Among these studies are microscopy measurements as well as diffraction, desorption spectroscopy, and theoretical studies. Spectroscopy measurements on the interaction with water have been conducted under near-ambient pressure conditions [91]. However, to our knowledge, there is no microscopy study showing the surface under these conditions. The ReactorSTM setup [44] allows for combining controlled ultra-high vacuum preparation with nanometer-scale imaging in the mbar range of water. In the following we characterize the ZnO($10\bar{1}0$) surface in ultra-high vacuum (Section 3.3.1) and present ex situ as well as in situ imaging of ZnO($10\bar{1}0$) in moderate pressures of water (Sections 3.3.2 and 3.3.4), investigate the role of surface hydroxylation (Section 3.3.3) and give preliminary results on the influence of a hydrogen environment (Section 3.3.5).

3.2 Materials and Methods

3.2.1 The ReactorSTM

The experimental setup has been described in detail by Herbschleb et al. [44]. In short, the scanning tunneling microscope (STM) can be used in ultra-high vacuum (base pressure $< 10^{-9}$ mbar) as well as in up to 6 bar of gases. This is possible in a flow reactor cell of about 0.05 ml volume, which is closed off from the rest of the vacuum chamber by the sample, the STM body, and a Kalrez seal. The video-rate control electronics were described by Rost et al. [92] and the control software is Camera 6.1. [93]. A cut platinum iridium wire (Pt90/Ir10, 0.25 mm) is used for the STM tip. During a scan on a cleaned Au(111) single crystal the tip can be prepared by tip pulsing and the distance and height are calibrated. The STM images are processed in WSxM [94].

Complementary techniques available in the same setup are a low-energy electron diffraction (LEED) and Auger electron spectroscopy (AES) system with 4-grid analyzer (Omicron SpectaLEED with NG LEED S control unit and DATAuger software) and X-ray photoelectron spectroscopy (XPS) with a VG Microtech dual anode X-ray source and a Clam 2 analyzer. For the use of these techniques the ReactorSTM setup consists of multiple chambers with different measurement stations and the sample is fixed to a holder which can be moved between them while staying in UHV. The holder allows for heating with a filament behind the sample as well as e-beam heating induced by a positive voltage directly on the sample. To enable this e-beam heating for oxide samples and to protect them from uneven heating from the filament a metal plate is placed underneath the sample. It is electrically connected to a ring-shaped plate holding the crystal from the top. Tungsten was chosen for sufficient heat conductivity of these plates [95]. They are directly connected to the high voltage connection. Additionally, this connection functions as the ground connection during argon sputtering, LEED/Auger, and X-ray photoelectron spectroscopy, as well as the bias voltage connection for scanning tunneling microscopy. A K-type thermocouple consisting of two 0.125 mm thick wires is spot-welded to the top plate. The temperature read-out for oxide samples is made as accurate as possible by heating up and cooling down slowly (at maximum 1 K/s). Additionally, this ensures that the crystal is not damaged due to uneven heating. In general it has to be noted that the temperature read-out in the ReactorSTM setup has an off-set due to junctions of other materials within the thermocouple connections, which are needed for technical reasons. The off-set of the temperature read-out was thoroughly investigated in [96] and leads to an underestimation of the annealing temperature used for zinc oxide in this thesis by about 120 K.

The ZnO($10\bar{1}0$) single crystal was purchased from SPL.

3.2.2 Water Content of Gases in the ReactorSTM

The reactor volume inside the ReactorSTM can be filled with up to 6 bar of gases via capillaries originating from a dedicated gas mixing system, which is built in-house. Downstream of the reactor the gases can be analyzed using a quadrupole mass spectrometer (Stanford Research Systems RGA100). For this purpose a Vacgen LVM series leak valve is adjusted in-house in order to leak a part of the line content into a separate UHV chamber (base pressure 5×10^{-9} mbar) where the mass spectrometer is located. The gases used here are argon 5.0 from Westfalen [97] and hydrogen 5.0 from Air Liquide [98], both with a water content below 3 volume parts per million. In order to determine the amount of water that reaches the sample, the gas line was filled with 1 bar of argon or hydrogen, respectively, with a leak of 10^{-6} mbar into the mass spectrometer chamber in order to measure the argon, hydrogen, and water signals. The measured backgrounds in the spectrometer chamber (with the leak valve closed) are subtracted from the measurements. Relative sensitivity factors for ionization and fractioning are approximated using Ref. [99]. This results in a measured ratio of water-to-argon partial pressure of $(5.0 \pm 0.3) \times 10^{-3}$ in 1 bar argon and water-to-hydrogen partial pressure of $(2.7 \pm 0.3) \times 10^{-3}$ in 1 bar hydrogen. The error of $\pm\ 0.3 \times 10^{-3}$ was estimated by repeating the same argon measurement multiple times and with different argon flows. A source of systematic overestimation of the amount of water could be that the leak rate through the leak valve increases with increasing mass [100]. However, this difference is likely not larger than one order of magnitude. Thus, we estimate the amount of water in 1 bar of argon or hydrogen to be on the order of 1 mbar. As this is orders of magnitude above the amount that is contained in the gas bottles, the majority of the water must originate from other parts of the gas line and the amount will be roughly the same for all gases used in this experimental setup. Although the majority of the gas lines are flushed with inert gas and heated to at least 90 °C before every use of the gas supply system, some parts cannot be cleaned in this manner. First, the temperature in areas with sensitive electronic equipment such as mass flow controllers cannot surpass 65 °C. Second, the high-pressure parts of the gas lines right after the gas bottles (up to 200 bar) cannot be heated and flushed properly as the gas flow is limited to the 10 ml/min range by the mass flow controllers. This could be improved in the future by installing additional connections between these high-pressure parts and the pump such that they can be flushed repeatedly with a high flow. Due to the requirements for mechanical stability and pressure stability for the in situ STM setup a cold trap to reduce the water content reaching the reactor is not suited. The installation of catalytic water traps into the existing gas system has not been successful so far.

3.2.3 XPS Fitting

The X-ray photoelectron O 1s peaks were fitted using CasaXPS 2.3.19. A zinc Auger peak with a tail towards high binding energies partly overlaps with the oxygen peak such that the background on its low binding-energy side appears too high and higher than on the high binding-energy side. The widely used Shirley background subtraction models the influence of inelastically scattered photoelectrons, which leads to a background that is higher on the high binding-energy side instead. Thus, a Shirley background is not appropriate here and a linear background was chosen. As the background on the low binding-energy side is overestimated, the O 1s peak stemming from the ZnO itself, which we will refer to as the bulk oxygen peak, is likely underestimated in comparison to any other O 1s peaks which are shifted to higher binding energies. We identify a peak at + 1.5 eV with respect to the bulk peak as adsorbed OH and a peak with a shift of + 3.5 eV as molecularly adsorbed water on top of the hydroxylated surface [101]. The shifts of these peaks were fixed during fitting and the full width half maximum of all peaks was constrained. As the bulk O 1s peak shows a larger full width half maximum than the Zn $2p_{3/2}$ peak, the width is not determined by instrumental parameters, but mainly by the chemical states. Therefore, the constraint for the OH and H_2O peaks was chosen larger (maximally 3.5 eV) than the constraint for the bulk peak (maximally 3 eV). Gaussian-Lorentzian product functions with a ratio of 1:1 gave the most satisfactory fit.

Following the procedure described in Ref. [86] the bulk oxygen peak was fixed to 530.4 eV in order to compensate for overall shifts of the measured binding energy. The result is in agreement with calibration of the energy using the Zn $2p_{3/2}$ peak or the Au 4f peak of a Au(111) single crystal to within 0.5 eV. Significant charging of the ZnO can thus be excluded.

The relative peak areas of the OH and the H_2O peaks, A_{OH}/A_{total} and A_{H_2O}/A_{total} respectively, with $A_{total} = A_{bulk} + A_{OH} + A_{H_2O}$, are used as a measure for the amount of hydroxylation and adsorbed molecular water. Additionally, they can be compared to an estimation of the relative peak area for one monolayer according to the Lambert-Beer absorption law approximation [101,102]. We are using $(A_{OH}/A_{total})|_{1ML} = 1 - \exp(-t/\lambda)$ with the thickness of one monolayer of $t = 0.26$ nm [91] and the inelastic mean free path of $\lambda = 1.9$ nm estimated using the TPP-2M formula in the NIST database [103] for an electron kinetic energy of 957 eV, which corresponds to the O 1s binding energy of 530 eV probed using an X-ray energy of 1487 eV (aluminum K_α).

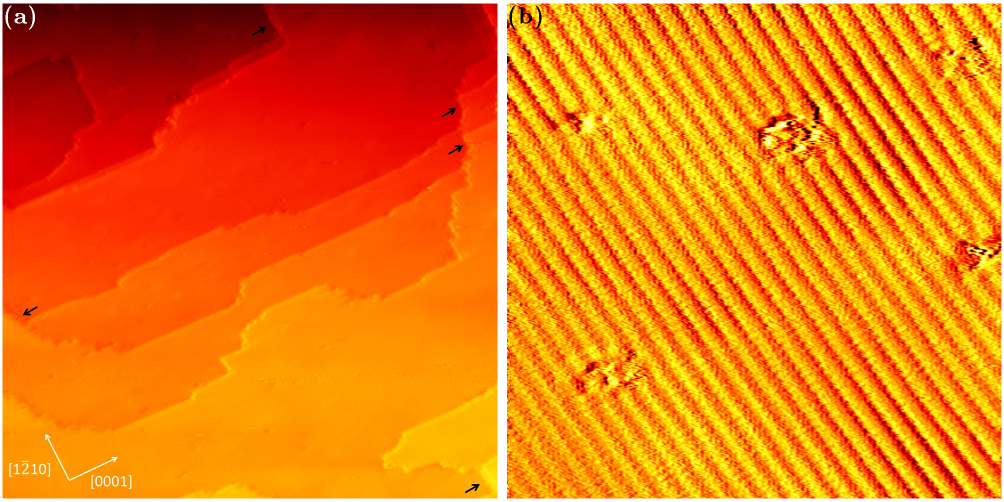

Figure 3.1: (a) 80 nm x 80 nm STM image of the as-prepared ZnO(10$\bar{1}$0) surface taken at 400 K with + 3 V and 50 pA. The plane filter image was merged with its derivative. Black arrows mark double steps parallel to the [1$\bar{2}$10] direction. (b) 17 nm x 17 nm STM image of the same surface taken at 400 K with + 2.5 V and 50 pA. The plane filter image was merged with its derivative in a ratio of 2:1.

3.3 Results and Discussion

3.3.1 As-prepared ZnO(10$\bar{1}$0) in UHV

The ZnO(10$\bar{1}$0) surface was prepared by cycles of 20 min sputtering in $1 \cdot 10^{-6}$ mbar of argon with an acceleration voltage of 1.4 kV resulting in a sample current of 4 μA on a surface area of 0.5 cm^2 followed by 20 min of annealing to 795 K in ultra-high vacuum. More details about the preparation and imaging in UHV can be found in the supplemental information (Section 3.5.1). Figure 3.1 shows the ZnO(10$\bar{1}$0) surface at 400 K after about 100 of these cleaning cycles. 10-nm to 40-nm-wide flat terraces are visible in the large-scale image in (a) with two types of step edges orthogonal to each other. The step heights in this image measure as (0.30 ± 0.04) nm which is in agreement with the value of 0.281 nm expected from the crystal structure [104]. In the smaller-scale image in Figure 3.1(b) regular parallel lines are visible. Their distance, averaged over measurements on multiple images, is (0.59 ± 0.09) nm, which can be identified as the size of the unit cell in the [0001] direction by comparison to the value of 0.521 nm based on the crystal structure. A schematic of the ZnO(10$\bar{1}$0) surface can be found in the supplemental information (Figure 3.15). The higher lines can be attributed to the Zn surface atoms [105] whereas the oxygen atoms in between appear lower in STM. On

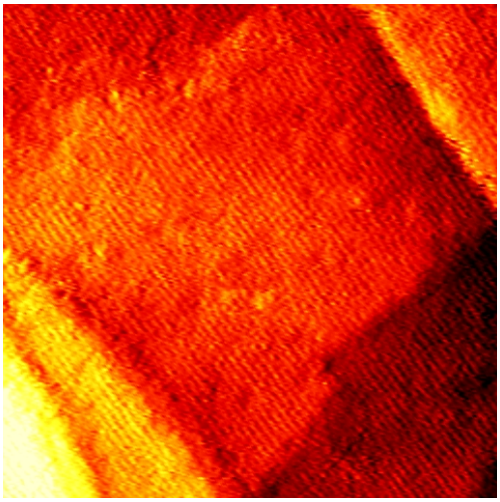

Figure 3.2: 40 nm x 40 nm STM image of the as-prepared ZnO(10$\bar{1}$0) surface taken at room temperature with + 4 V and 50 pA. The plane filter image was merged with its derivative for better visibility of the Zn lines.

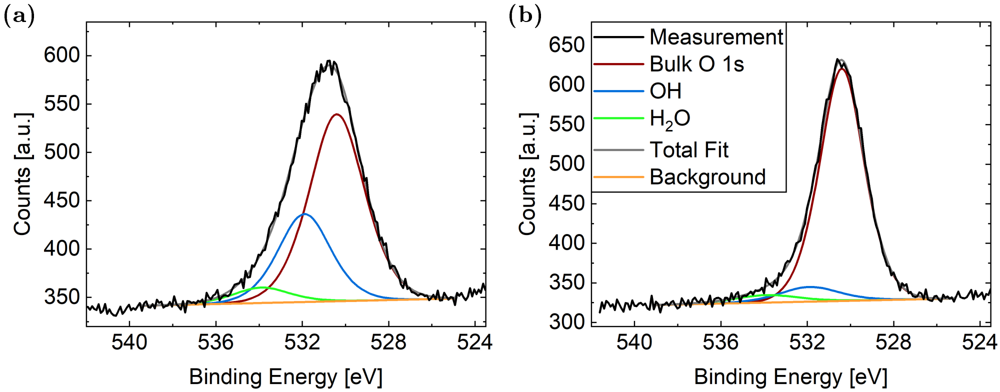

Figure 3.3: O 1s spectra of the as-prepared ZnO(10$\bar{1}$0) taken at (a) 300 K and (b) 400 K. A linear background was subtracted and the fitted peaks are Gaussian-Lorentzian product functions with a ratio of 1:1. The details of the fitting procedure are described in the Materials and Methods Section 3.2.3.

the basis of the lines of Zn atoms, the orientation of the sample can be identified as indicated by the arrows overlaid on the image in Figure 3.1(a). The Zn lines in Figure 3.1(b) are interrupted in five positions, which can be identified as surface vacancies. These are investigated in more detail in the supplemental information (Section 3.5.2). The larger-scale color variations in this image are likely due to the incorporation of argon, see the supplemental information (Section 3.5.3).

At room temperature the resolution on ZnO($10\bar{1}0$) is generally lower than at 400 K in our scanning tunneling microscope. However, the Zn lines can still be visible as shown in Figure 3.2. Figure 3.3 is a comparison between the O 1s X-ray photoelectron peaks at room temperature and 400 K. The fitting procedure is explained in Section 3.2.3. Apart from the O 1s peak of bulk ZnO at 530.4 eV [106], two additional peaks, adsorbed OH and H_2O, are necessary for a satisfactory fit. In the following we use the ratio of the areas underneath the OH and H_2O peaks with the total O 1s peak as a measure for the amount of hydroxylation and molecularly adsorbed water, respectively. For the OH peak these relative areas are 0.29 at room temperature and 0.07 at 400 K, whereas the relative area of the H_2O peak is 0.05 at room temperature and 0.04 at 400 K. The amount of hydroxylation at 400 K is thus only 24 % of the amount of hydroxylation at 300 K. Heinhold et al. measure the relative OH area to decrease to roughly 70 % when increasing the temperature from 300 K to 400 K (estimated from Figure 4.(a) in Ref. [101]). Their coverage only falls below a monolayer above roughly 670 K. Using the same Lambert-Beer law approximation (see Section 3.2.3) a monolayer of OH would correspond to a relative OH peak area of 0.13 here. This estimates the coverage at 400 K to be about 50 % of a monolayer. The discrepancies between the measurements done here and the results of Heinhold et al. could stem from the difference in preparation method of the ZnO($10\bar{1}0$) surface. A more comparable preparation method was used by Newberg et al. [91]. Near-ambient pressure XPS allowed for their measurements in a significantly higher pressure regime on the order of 10^{-1} mbar of water. Although the surface is saturated with OH below 550 K under these conditions, no molecularly adsorbed water was observed in their measurements. In general, discrepancies between the measurement done here and other literature could stem from a partly overlapping Zn Auger peak with the O 1s peak, which, as described in Section 3.2.3, leads to an underestimation of the bulk ZnO oxygen peak and thus an overestimation of the OH and H_2O relative peak areas. This could explain why a relative OH peak area significantly above the value estimated for one full monolayer was measured for 300 K, although one monolayer is identified as the saturation coverage in Ref. [91]. Thus, no accurate coverage values can be given here. However, the photoelectron spectroscopy measurements have shown that more (partly dissociated) water is present on the surface at 300 K in comparison to 400 K.

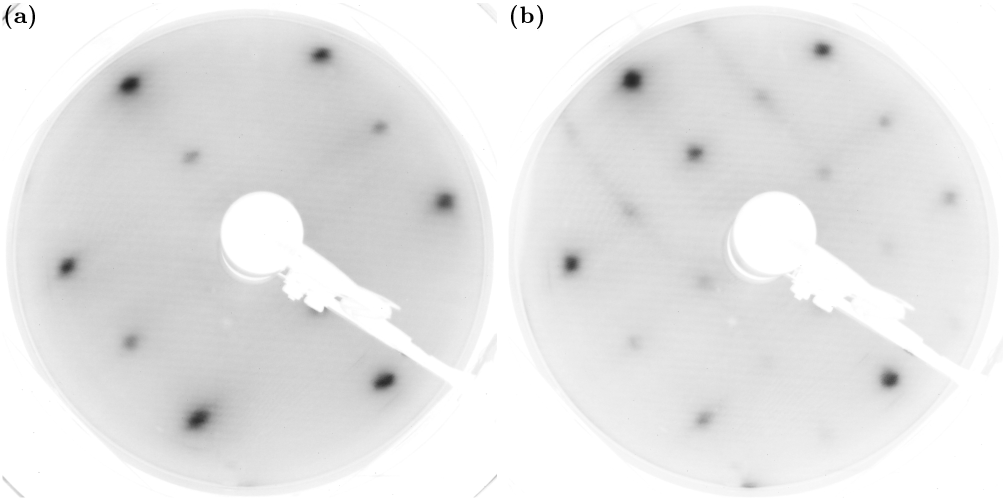

Figure 3.4: Low-energy electron diffraction pattern of ZnO(10$\bar{1}$0) at (a) 400 K compared to (b) room temperature taken at 52.1 eV electron energy.

The first water layer on ZnO(10$\bar{1}$0) can be mobile and locally switch between a molecular and a half-dissociated layer as observed with scanning tunneling microscopy by Dulub et al. [84]. This can account for the more challenging scanning observed here at room temperature in comparison to 400 K despite the ability of water to increase the conductivity of ZnO [107]. However, the areas of the H_2O and OH peaks in XPS at room temperature do not show the same amount of molecularly adsorbed water and dissociated water but merely 18 % as much H_2O as OH. Following Ref. [101] it can be argued that the water molecules in the first adsorption layer, which adsorb with their oxygen atom on the zinc surface atoms, do have strong hydrogen bonds with the neighboring surface oxygen atom, also in the case that this does not lead to dissociation. Therefore, the non-dissociated water in the first layer might rather contribute to the OH peak than the H_2O peak and it is not possible to distinguish between the molecularly adsorbed and the half-dissociated first layer using XPS. However, the half-dissociated layer can be seen in low-energy electron diffraction. Figure 3.4 shows the comparison of low-energy electron diffraction patterns on the ZnO(10$\bar{1}$0) surface at room temperature and 400 K, respectively. Whereas the same rectangular unit cell of the substrate is visible in both patters, the room temperature LEED shows an additional 2x1 overlayer. This confirms the presence of the half-dissociated layer, which has been calculated to be the most stable structure in ultra-high vacuum [108,109].

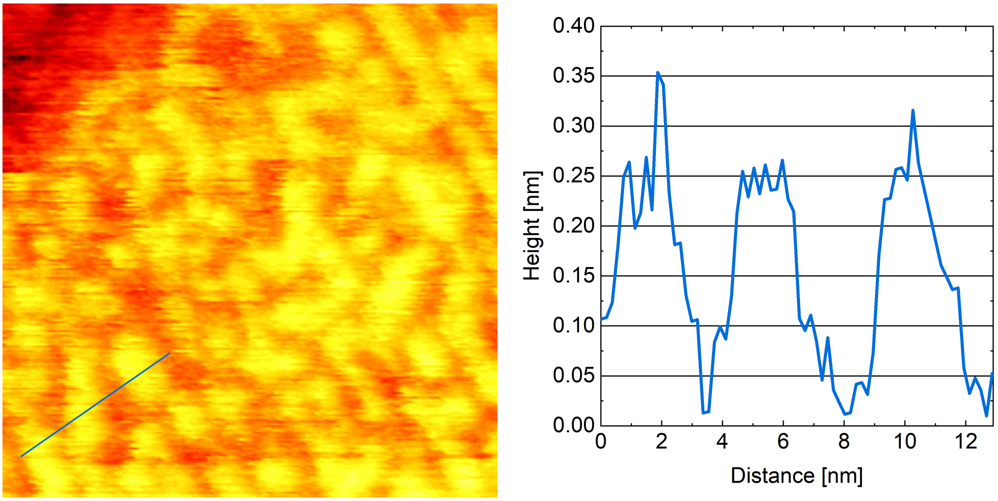

Figure 3.5: 35 nm x 35 nm STM image of ZnO(10$\bar{1}$0) after 10 min in roughly 1 mbar of water at room temperature with the corresponding height profile. The image is taken in UHV at room temperature with + 3 V and 50 pA. Including the initial filling of the reactor up to 1 bar of argon carrier gas the total exposure to the water flow is roughly 19 min (see experiment II in Figure 3.9).

3.3.2 Rough Phase of ZnO(10$\bar{1}$0)

Figure 3.5 and the larger-scale overview in Figure 3.6 show the ZnO(10$\bar{1}$0) surface after exposure to roughly 1 mbar of water for 10 min. The corresponding height profile on the right side of Figure 3.5 shows a height difference between the terrace and the newly formed structure of between 0.23 nm and 0.33 nm. Although the accuracy of this value is limited by the ability of the tip to follow the rapid height changes, the measured height difference is in agreement with the step height of ZnO(10$\bar{1}$0) suggesting that the surface has roughened. This is confirmed by the stability of this phase in ultra-high vacuum for several days as well as the ability of the surface to flatten out again when annealing, as shown in Figure 3.7. After 10 min annealing at 795 K there is some local roughness left, which does however not cover the whole terrace anymore. At the same time medium-sized holes, one step height lower than the original terraces, appear, which are evidence of the rearrangement taking place during annealing. These holes are still present after a total of 20 min annealing and even larger ones exist as they merge during the rearrangement. The local roughness is gone completely after 20 min of annealing. In order to remove all medium-sized holes and restore the flatness of the as-prepared sample (see Figure 3.1(a)) annealing for a total of 2 hours is necessary.

The overview image of the rough surface in Figure 3.6 allows for an estimation of the

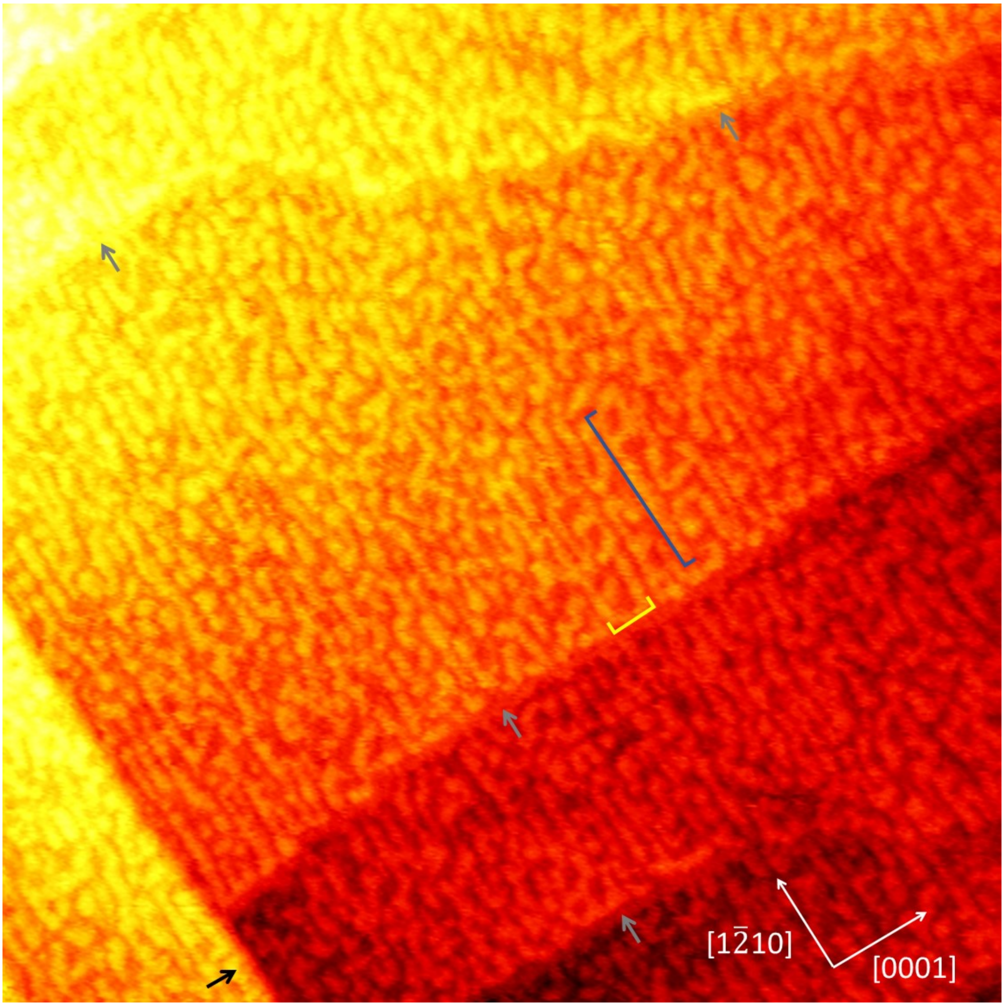

Figure 3.6: 150 nm x 150 nm STM image of ZnO(10$\bar{1}$0) after 10 min in 1 mbar of water at room temperature. The image is taken in UHV at room temperature with + 3 V and 50 pA. For better visibility of the steps as well as the structure on the terraces the plane filter image was merged with its derivative at a ratio of 2:1. Examples of areas with the same height are marked with a blue line parallel to the [1$\bar{2}$10] direction and a yellow line parallel to the [0001] direction. A black arrow marks a (000$\bar{1}$)-type double step. Grey arrows mark (1$\bar{2}$10)-type steps accompanied by a 2-nm-wide area without height differences.

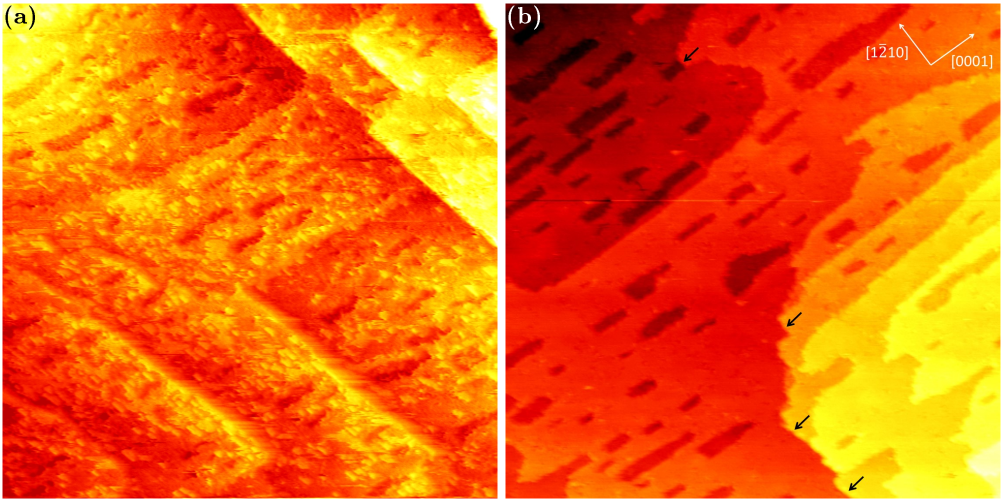

Figure 3.7: 150 nm x 150 nm STM images of ZnO(10$\bar{1}$0) after 10 min in 1 mbar of water at room temperature and subsequent annealing at 795 K for (a) 10 min and (b) 20 min. The images were taken at 400 K with + 3 V and 50 pA. Although step edges are clearly visible by eye in (a), the different terraces could not be properly identified using the local plane filter in WSxM. This could be due to the inhomogeneity on the terraces. For better visibility of the remaining small-scale roughness the image was merged with its derivative at a ratio of 2:1. Black arrows in (b) mark double steps parallel to the [1$\bar{2}$10] direction.

typical size of areas with the same height. In the [0001] direction the size is between 2 and 4 nm with some longer areas up to 7 nm mostly near the step edges. An example is marked with a yellow line. In the [1$\bar{2}$10] direction, however, the areas with the same height are up to 26 nm long. An example is marked with a blue line. This suggests that there is a clear favor for the formation of (0001)- or (000$\bar{1}$)-type steps, which are parallel to the [1$\bar{2}$10] direction, in comparison to the formation of (1$\bar{2}$10)-type steps, which are orthogonal to the [1$\bar{2}$10] direction. The original (1$\bar{2}$10)-type step edges in Figure 3.6 show a roughly 2-nm-wide area without height difference as indicated by the grey arrows. This suggests that, although a large part of the terraces is elevated by one step height, double steps of this type are unfavored. On as-prepared surfaces with a large step density double steps of both types are present (see for example Figure 1(a) in Ref. [110] and Figure 1(a) in Ref. [105]). However, on surfaces with lower step density we have observed more double steps in the parallel direction than the (1$\bar{2}$10) type. Examples of these double steps are marked with black arrows in Figures 3.1(a), 3.6, and 3.7(b). The (1$\bar{2}$10)-type steps and double steps being unfavored suggests a lower stability of the (1$\bar{2}$10) face compared to the (0001) or (000$\bar{1}$) faces of ZnO. Although theory [111] suggests the opposite, (1$\bar{2}$10) is the least stable of the low-index faces according to experimental data [112]. This is confirmed by STM measurements showing that the $(1\bar{2}10)$-type step edge is the most active site for nucleation during the deposition of Cu on ZnO$(10\bar{1}0)$ [110].

Although the probability of formation of the two different types of steps and double steps during the roughening process in water can be motivated by the stability of the corresponding face, the total ratio of the two different types of single steps on the as-prepared surface does not agree with this difference in stability. The ratio of step types varies significantly with scanning position and in comparison to different publications as it additionally depends on other factors like the preparation procedure and initial miscut of the single crystal.

3.3.3 Hydroxylation and Adsorbed Water

Table 3.1: Relative OH peak areas for different exposure times, flows of water, and exposure temperatures in comparison to the as-prepared sample (in the first column) including XPS measurements taken at 400 K as well as at 300 K.

Exposure Time [min]	-	10	10	10	240
Flow [ml/min]	-	1	2	1	1
Exposure Temperature [K]	-	300	300	400	400
Relative OH peak area at 400 K	0.07	0.04	0.12	0.08	0.06
Relative OH peak area at 300 K	0.29	0.12	0.18	0.12	0.15

Table 3.2: Relative H_2O peak areas for different exposure times, flows of water, and exposure temperatures in comparison to the as-prepared sample (in the first column) including XPS measurements taken at 400 K as well as at 300 K.

Exposure Time [min]	-	10	10	10	240
Flow [ml/min]	-	1	2	1	1
Exposure Temperature [K]	-	300	300	400	400
Relative H_2O peak area at 400 K	0.04	0.1	0.12	0.16	0.14
Relative H_2O peak area at 300 K	0.05	0.08	0.09	0.13	0.09

X-ray photoelectron spectroscopy measurements of the O 1s peak have been taken after exposure to argon. As explained in the supplemental information (Section 3.5.4), the ZnO$(10\bar{1}0)$ surface has to be heated to 400 K in order to remove it from the reactor. Therefore, every XPS measurement was first done at this temperature and once more after cooling down to 300 K. The relative areas of the OH as well as H_2O

peaks, calculated as described in Section 3.2.3, are used as a measure for the amount of hydroxylation and molecularly adsorbed water, respectively. By comparing multiple measurements taken after the same exposure (data not shown) the accuracy of the relative peak areas can be roughly estimated as ± 0.05. This value is taken into account in the following when interpreting the relative peak areas presented in Tables 3.1 and 3.2 for different exposures. Comparing all values taken at 400 K to the as-prepared surface at 400 K, the exposure does not increase the hydroxylation to a detectable amount. Letting the surface cool down to 300 K, the amount of hydroxylation increases for every measurement, however it does not reach the level measured on the clean sample at 300 K. This could be due to a longer waiting time before taking the XPS spectra on the clean sample, which indicates that the hydroxylation increases over time in UHV. An increase in the H_2O relative peak area is detected right after the exposure in the measurements taken at 400 K compared to the clean sample at the same temperature. A part of this molecularly adsorbed water has desorbed when the XPS is measured at 300 K as can be seen in a decrease in the relative peak areas for all measurements. As the desorption of water cannot be caused by the decrease in temperature, this effect can only be attributed to the longer time passed since the end of the exposure. Given the accuracy of the relative peak areas of ± 0.05 the values measured at 300 K after exposure are comparable with the as-prepared surface. Thus, the desorption of the molecularly adsorbed water after the exposure proceeds faster than the increase of hydroxylation in UHV.

As the rough phase is stable in UHV at 300 K as well as 400 K, it can be concluded that, although the formation is induced by water, the presence of the rough phase is not directly correlated to the amount of hydroxylation and molecularly adsorbed water left on the surface after the end of the water exposure. This is additional evidence that the rough phase consists of zinc and oxygen atoms from the surface itself.

3.3.4 Roughening Process

Figure 3.8 shows the structural change of ZnO(10$\bar{1}$0) in 1 bar of argon containing roughly 1 mbar of water. (A quantification of the water content is presented in Section 3.2.2.) The roughening process starts at multiple positions on the terrace and the surface is completely roughened 7.4 min afterwards. In comparison to the ex situ image in Figure 3.5, the in situ images presented here show horizontal streaks and the shapes can be distorted. In general, the presence of gas can disturb the tunneling electrons. Sample drift under the high pressure as well as the clear mobility of surface atoms during the structural change further disturb the imaging in this case.

Figure 3.9 compares two different measurements of the formation of the rough phase where different flows of carrier gas were used. Colored areas indicate the time from the

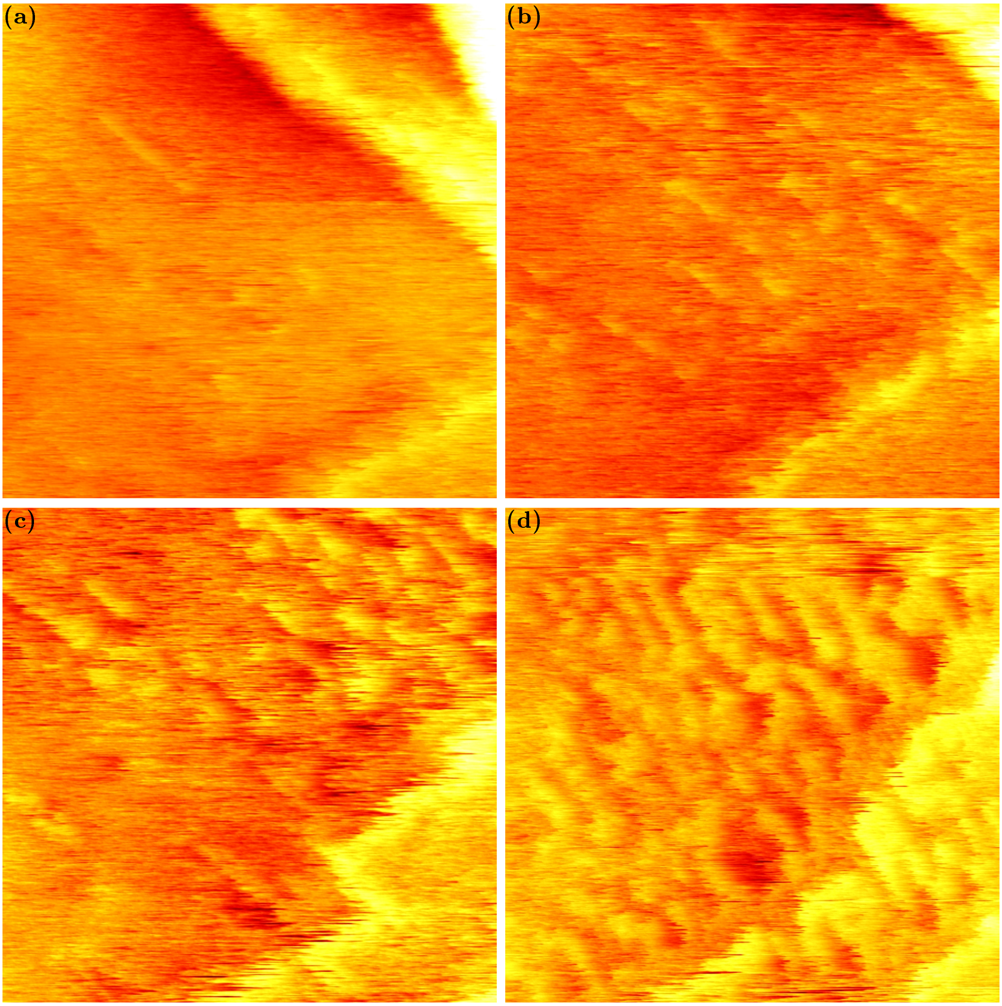

Figure 3.8: 35 nm x 35 nm STM images of ZnO($10\bar{1}0$) in roughly 1 mbar of water at room temperature taken with + 2 V and 50 pA. The images were taken (a) 13.0 min, (b) 14.2 min, (c) 16.7 min, and (d) 20.4 min after starting the flow of gas.

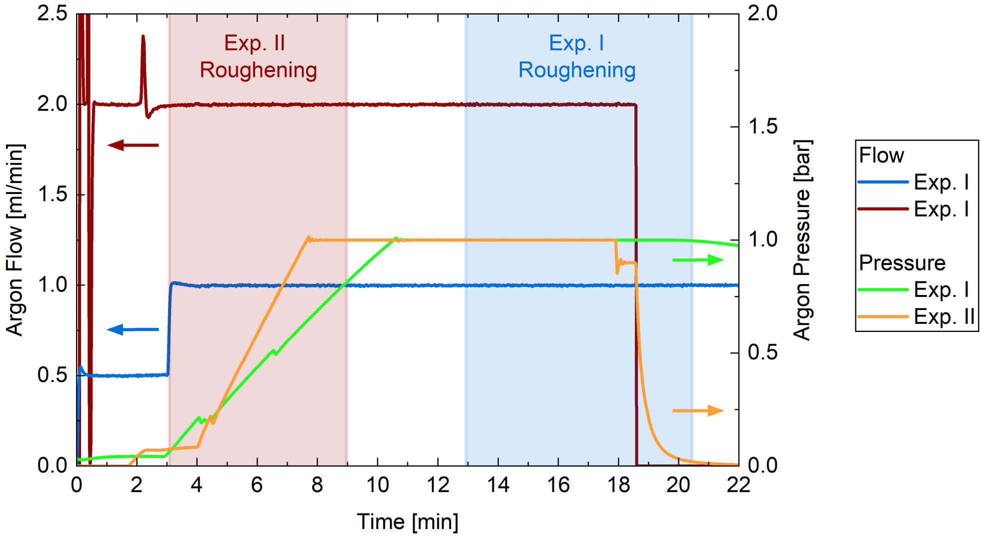

Figure 3.9: Flow and pressure curves of two different exposures to up to 1 bar of wet argon. The colored areas indicate the roughening of the ZnO($10\bar{1}0$) as observed in STM. Experiment I corresponds to the STM images shown in Figure 3.8. The higher peaks seen at the beginning of the flow are caused by a pressure build-up that is released when opening the mass flow controller. Another peak in the flow of experiment II after 2 min is likely due to a necessary adjustment of the argon pressure in the gas line leading to the mass flow controller.

moment where the roughening can first be seen, like in Figure 3.8(a), until the point where the terraces are fully roughened, like in Figure 3.8(d). With an argon flow of up to 1 ml/min (experiment I) the roughening only starts when 1 bar has been reached after 13 min of flow and a total of 11 ml of gas passing by the sample. In contrast, when an argon flow of 2 ml/min is used (experiment II), the roughening starts significantly earlier, at 0.075 bar after 3 min of flow and a total of 6 ml of gas passing by the sample. This total amount of gas is likely underestimated in experiment II due to the initial high flow peaks before stabilizing to the desired flow as seen in Figure 3.9. Additionally, the scanning velocity in these measurements was chosen such that each STM image takes slightly more than one minute. This limits the accuracy in determining when the roughening starts and when it fills the whole terrace, respectively, and thus for the total amounts of flown gas calculated here. Still the clearly faster onset of formation with larger flow even at a significantly lower pressure suggests that the water pressure is not the main factor that allows for the roughening of the surface to begin and a pressure of less than 1 mbar of water would be sufficient. The time from the onset of roughening until the terrace is fully roughened is shorter as well using the larger flow.

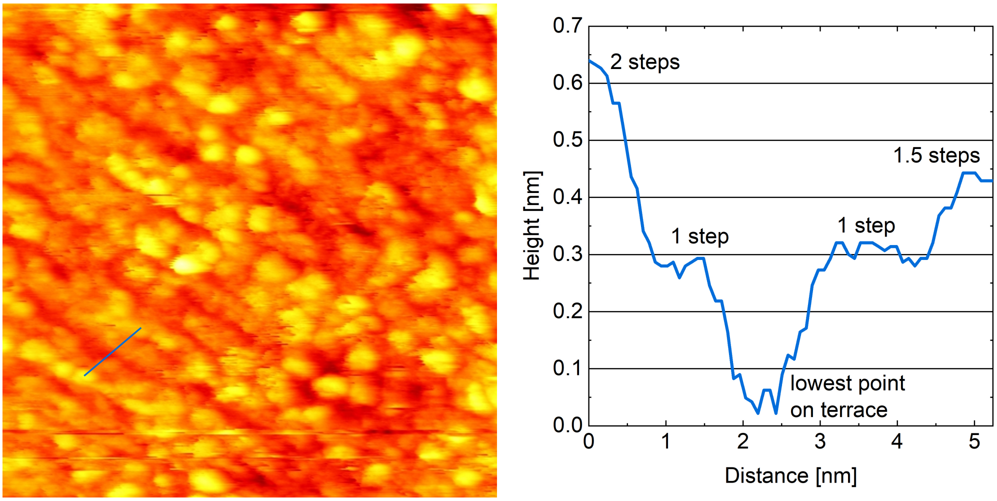

Figure 3.10: 35 nm x 35 nm STM image of ZnO$(10\bar{1}0)$ after 4 h in 1 mbar of water at 400 K with the corresponding height profile indicated in blue. The image is taken in UHV at room temperature with + 4 V and 50 pA.

In experiment II it takes 5.8 min and a total amount of 11 ml of gas and with the lower flow 7.4 min, but only a total amount of 7.5 ml of gas. Thus, the speed of formation increases less than linearly with the flow. It is possible that, once a sufficient amount of water for the onset of the roughening has been supplied to the surface, the higher pressure in experiment I does lead to a more efficient use of the flown gas.

Under prolonged exposure the ZnO$(10\bar{1}0)$ roughens more severely. Figure 3.10 shows an STM image after 4 h in roughly 1 mbar of water. (For technical reasons this exposure was done at 400 K surface temperature.) As can be seen in the corresponding height profile, the height difference on one terrace can be twice the step height of ZnO$(10\bar{1}0)$. Areas with a height difference of about 1.5 times the step height with respect to the lowest point on the terrace are observed as well. As explained in Section 3.5.2, one step consists of two layers of ZnO dimers allowing for the observation of steps with about half the height when the topmost layer is missing. Apart from height differences that correspond to full or half steps, smaller height variations on the small terraces can be seen in Figure 3.10. This suggests that the density of smaller vacancies increases as well. If they for example consist of only one missing dimer, they might not be resolved completely and therefore appear less deep than half the step height. Additionally, the surface could become increasingly amorphous with longer exposure and more severe restructuring. As vacancies can interact more strongly with water [113], the speed of the roughening process could increase over time.

Overall, we thus observe a restructuring of the ZnO$(10\bar{1}0)$ surface which must stem from an interaction with water that is significantly different from the interaction that leads to the ordered adsorption structures observed in UHV [84]. Theoretical studies on the interaction of ZnO(10$\bar{1}$0) with water confirm that the 2x1 half-dissociated monolayer (with one dissociated and one molecular water molecule per two ZnO(10$\bar{1}$0) unit cells) is the most stable structure in UHV [109,113,114]. However, the structure changes significantly when adding more water as investigated in detail by Kenmoe et al. [109]. When exactly two monolayers of water are present, they observe a double layer to be the most stable, which does not leave any dangling bonds for adsorption of additional water molecules. Thus, from three monolayers on the structure is significantly different again: One layer, the so-called contact layer, is adsorbed on the surface in an ordered fashion while all additional water molecules are adsorbed in a "liquid-like film", which is more amorphous and can move between a number of different configurations. This picture of the water adsorption suggests that from three monolayers on the structure of the contact layer on the ZnO(10$\bar{1}$0) surface does not change significantly when adding more water. This could account for our observation that the roughening does not primarily depend on the exact pressure in the 0.1 to 1 mbar regime investigated here. The dependence on the gas flow, however, could stem from the amount of water molecules that need to pass through the reactor before at least three monolayers are adsorbed and the contact layer is present. The contact layer differs from the 2x1 monolayer in structure and can contain more water molecules, whereas the ratio of dissociated and non-dissociated molecules is comparable [109,114]. Tocci et al. [114] show that the properties of the contact layer lead to a significant increase in proton exchange to and from the surface in comparison to the 2x1 monolayer. Additionally, proton exchange between the dissociated and non-dissociated water molecules in the first layer, which is not possible in the 2x1 monolayer, occurs frequently in the contact layer. This proton mobility could be responsible for allowing a restructuring of the ZnO(10$\bar{1}$0) surface. A restructuring of the polar (0001) face of ZnO under the influence of water has been observed previously by Önsten et al. [115], showing that water and/or proton mobility can induce mobility of zinc and oxygen atoms or the ZnO dimer. They observe a severe roughening of ZnO(0001) after a deposition of 20 L of water, which is explained as an interaction with hydrogen atoms from dissociated water as hydrogen is known to be able to reconstruct this face of ZnO. However, on the ZnO(10$\bar{1}$0) face, although some vacancies are formed, no severe restructuring due to atomic hydrogen has been reported so far. An ordered 1x1 H overlayer is observed in UHV [105]. Interestingly, before the (0001) surface roughens, the observations of Önsten et al. first show an increase in the size of the (0001) terraces under exposure to smaller amounts of water (up to 5 L). Thus, water itself, without a significant amount of leftover H atoms, might in turn stabilize the (0001) face. This could explain the formation of (0001)-type steps

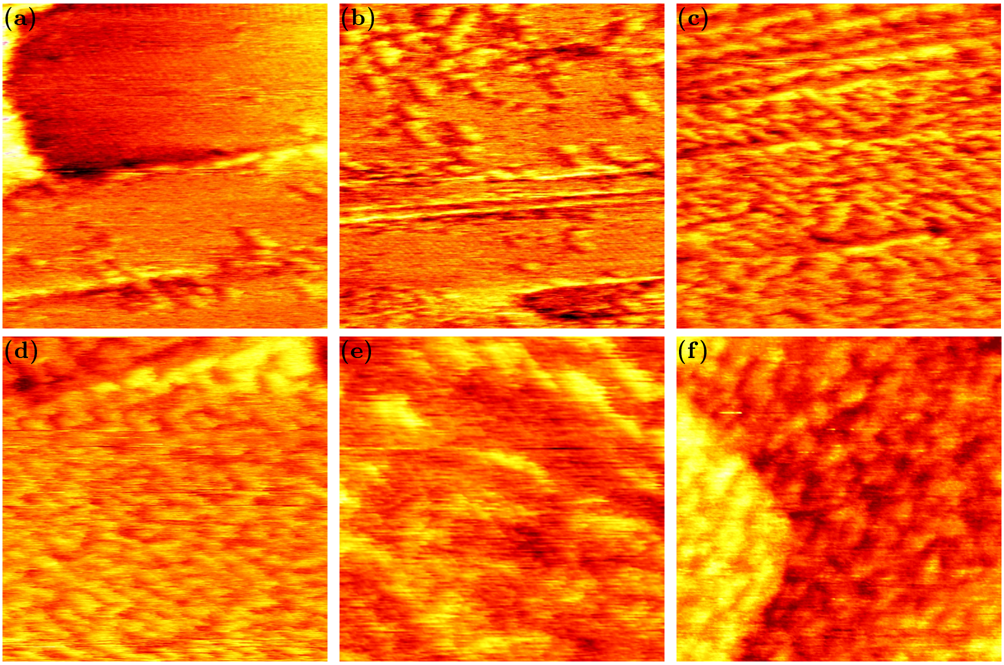

Figure 3.11: 35 nm x 35 nm STM images of ZnO(10$\bar{1}$0) in flow of wet hydrogen at room temperature taken after (a) 6.4 min of flow (reactor filled to 0.2 bar), (b) 7.5 min of flow (reactor filled to 0.3 bar), (c) 10.8 min of flow (reactor filled to 0.7 bar), (d) 12 min of flow (reactor filled to 0.8 bar), (e) 20 min of flow (reactor filled to 1 bar), and (f) after the end of the exposure in UHV. The total exposure, consisting of the filling of the reactor as well as 10 min at 1 bar, is 23 min. The images are taken with (a)-(e) + 2.5 V and (f) + 3 V, and 50 pA.

observed here on ZnO(10$\bar{1}$0) during the restructuring under the influence of water. As shown in Section 3.3.2, the formation of the (0001)- and (000$\bar{1}$)-type steps is favored over the formation of (1$\bar{2}$10)-type steps. The difference in stability of the different faces and step types, as observed in UHV [110,112], might thus be more severe in moderate pressures of water.

3.3.5 Roughening in Hydrogen Environment

Figure 3.11 shows the structural change of ZnO(10$\bar{1}$0) under a flow of hydrogen which contains a comparable amount of water as the argon used in the sections above. (A quantification of the water content is presented in Section 3.2.2.) The same roughening process as in argon is observed in Figure 3.11(a) to (c). As can be seen in the flow and pressure curves in Figure 3.12, the roughening begins after 6.4 min of flow when

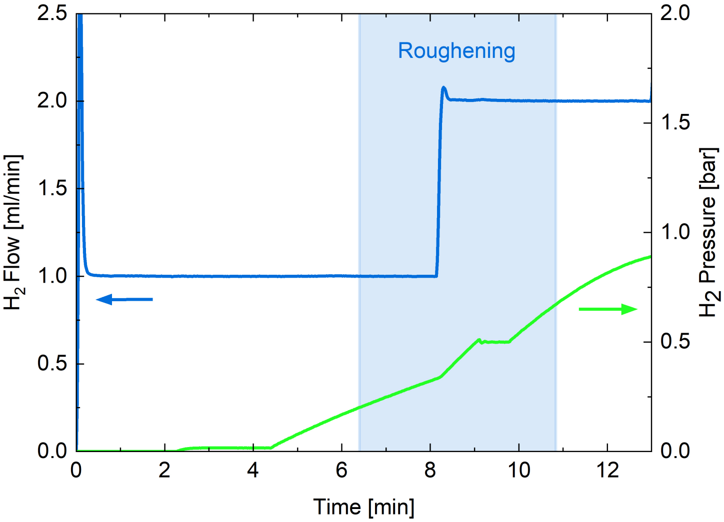

Figure 3.12: Flow and pressure curves of the exposure to up to 1 bar of wet hydrogen. The colored area indicates the roughening of the ZnO as observed in the STM images of which examples are shown in Figure 3.11. The higher peak seen at the beginning of the flow is caused by a pressure build-up that is released when opening the mass flow controller.

the reactor is filled to 0.2 bar of hydrogen. The total amount of gas flown is likely larger than 6.4 ml due to the larger peak of flow during the initial stabilization of the flow. Taking this into account the moment of onset of roughening is in agreement with those observed for water in argon in Section 3.3.4, especially with experiment II. The duration of the roughening process is 4.4 min with a total amount of 7.1 ml of gas. This is comparable to the amount of gas needed in argon in experiment I, although the reactor was filled to a lower pressure when using hydrogen. For this measurement the same sources of inaccuracies as mentioned above (see Section 3.3.4) hold. Overall, the initial roughening in hydrogen environment proceeds in a comparable way as without hydrogen such that we can suggest that the interaction with water proceeds via the same underlying mechanism. It can thus be assumed that ZnO(10$\bar{1}$0) is not covered with hydrogen atoms. The known 1x1 overlayer of H atoms [105] has been calculated to passivate the ZnO(10$\bar{1}$0) surface for adsorption and dissociation of water molecules [113] and would thus prevent the strong interaction with water we see here. This suggests that the nonpolar face does not dissociate hydrogen (to a significant extent) in the 1 bar regime at room temperature. The same has been calculated for UHV conditions where only the polar faces dissociate hydrogen [116]. This could, however, allow for H$_2$ dissociation at the (0001)- and (000$\bar{1}$)-type step edges of ZnO(10$\bar{1}$0). We do observe additional structural changes on the ZnO($10\bar{1}0$) surface after the whole terrace has roughened. The size of areas which are not interrupted by steps increases again over time as is visible when comparing Figure 3.11(e) to Figure 3.11(d). As the density of step edges increases during the initial roughening from Figure 3.11(a) to Figure 3.11(c), the dissociation at the polar-type steps could lead to more dissociated hydrogen, which in turn destabilizes the (0001) face [115]. This could lead to the ZnO($10\bar{1}0$) partially flattening out again. However, after more time has passed a larger step density can be observed again as shown in Figure 3.11(f). Overall, this describes a competition of two effects, the formation of steps due to water and the destabilization of these steps due to H_2, which would account for the continued changes in shape. Which of the two processes dominates likely depends on the exact ratio of H_2 and H_2O partial pressures. For technical reasons the surface is exposed to a rough vacuum on the order of 0.1 mbar for a couple of minutes before the flow of hydrogen gas can be initiated. It can thus be assumed that it is saturated with the first monolayer of water at the beginning of the hydrogen exposure, which could explain why the initial roughening is similar to the case without hydrogen.

3.4 Conclusions and Outlook

The use of a ZnO($10\bar{1}0$) single crystal in the ReactorSTM setup is technically feasible but practically challenging for a number of reasons. A preparation procedure using sputtering and annealing which leads to a sufficient cleanliness and flatness has been found. However, extended use in ultra-high vacuum and repeated preparation leads to a loss of conductivity of the crystal and to the incorporation of argon. These limitations are especially challenging for use in high-pressure experiments as intense re-preparation of the sample is usually necessary after exposure to gases in the reactor. The loss of conductivity does not only technically impede STM measurements, but also allows for the formation of large vacancy densities, which can be highly active and strongly influence results. In order to allow for future measurements where repeated preparation is necessary, we recommend a systematic study of hydrogen exposure at elevated temperatures, such that a preparation step which counteracts the loss of conductivity can be incorporated into the preparation procedure. This would allow for more comparable and less time-consuming studies of ZnO($10\bar{1}0$) in the ReactorSTM setup.

We have presented evidence for a significant roughening of the ZnO($10\bar{1}0$) surface in the mbar range of water, which proceeds within the first 10 min and is dependent on the total amount of water supplied to the surface. The formation of different step types during the roughening has been discussed on the basis of their stability in UHV as well as in water background. Preliminary measurements of this roughening in hydrogen background suggest that a second process is taking place. Distinguishing the two processes, for example by imaging the surface in dried hydrogen, and understanding their exact balance would be interesting from a fundamental point of view. However, for practical applications the water content in air as well as in industrially used gases is likely higher than in the mbar range, especially during reactions where water is a reactant or product. Thus, it can be assumed that the water content would be high enough for ZnO($10\bar{1}0$) to be present only in the rough phase at room temperature independent of the hydrogen partial pressure. This limits the applicability of UHV studies on ZnO($10\bar{1}0$) at room temperature as a model for methanol steam reforming catalysts as well as other ZnO devices. Additionally, the roughening could have influence on the interpretation of data taken at room temperature under elevated water pressures, such as near-ambient pressure XPS, where the surface is not imaged and assumed to be flat ZnO($10\bar{1}0$). However, in order to evaluate the significance of our findings it is crucial to investigate the influence of temperature on the roughening process. Such an influence is likely, since the interaction of ZnO($10\bar{1}0$) with the water background in UHV changes when heating up from room temperature to only 400 K (see Section 3.3.1). A study in the range of 500 K surface temperature would be most relevant for catalytic applications.

3.5 Supplemental Information

3.5.1 Preparation and STM of ZnO($10\bar{1}0$)

A commonly used technique for the preparation of single-crystal surfaces is cycles of argon ion sputtering and annealing in ultra-high vacuum. Additionally, metal samples are frequently annealed in oxygen background in order to react away surface carbon as well as bring other metal impurities to the surface and oxidize them. While there is no concrete evidence as to whether this would be possible or not for oxide samples in general, ZnO($10\bar{1}0$) is prepared without oxygen annealing in the literature. We have observed a significant increase in the roughness of the sample after oxygen annealing (data not shown), which prevents an estimation of the effect on the cleanliness and requires long annealing in ultra-high vacuum afterwards, thus resulting in an inefficient cleaning process. After increasing the annealing temperature until the crystal became sufficiently flat, the final cleaning recipe was chosen as 20 min sputtering in $1{\cdot}10^{-6}$ mbar of argon with an acceleration voltage of 1.4 kV resulting in a sample current of 4 μA on a surface area of 0.5 cm^2 followed by 20 min of annealing to 795 K in ultra-high vacuum. In the last cycle before imaging the surface the annealing temperature was decreased to 794 K in order to prevent contaminants which are present in the bulk from reaching the surface.

Most STM images shown in this chapter are taken at voltages significantly lower than the bandgap of ZnO at 3.4 eV [117]. Atomic-resolution images of ZnO($10\bar{1}0$) are generally taken at bias voltages of around 2 V or less [105,112,118]. An increase in resolution with decreasing voltage can easily be understood for conductive samples as a lower voltage at constant tunneling current results in the tip moving over the surface at closer proximity. However, the fact that ZnO is sufficiently conductive for scanning tunneling microscopy at all is not entirely understood. For the more commonly used TiO_2 single crystals the conductivity is increased by slightly reducing the material through annealing in ultra-high vacuum, which leads to oxygen vacancies in the surface [119,120]. This method has been proven ineffective for ZnO. A probable cause is that, as density functional theory has shown [121], oxygen vacancies on ZnO($10\bar{1}0$) are unlikely. They might be observed in small coverages only at temperatures above 1000 K and in the absence of O_2 [122]. In comparison, ZnO dimer vacancies show a significantly lower formation energy [121], suggesting that the zinc atom leaves the surface together with the oxygen atom in most cases. Additionally, it has been calculated that, even if present, oxygen vacancies would not contribute to n-type conductivity [123]. There is evidence, however, that hydrogen impurities are donors that contribute to the conductivity of ZnO. These can easily be incorporated during the production of single crystals [123,124].

Although the ZnO($10\bar{1}0$) single crystal was sufficiently conductive for high-resolution imaging in the beginning, we have observed a decrease in scanning resolution with prolonged use of the crystal and repeated preparation in UHV. It was not suitable for high-pressure scanning tunneling microscopy anymore after a total of about 300 cleaning cycles. In order to evaluate the stability of the H impurities contributing to the conductivity it is necessary to distinguish between two different types of impurities, which have been observed and described in detail by Janotti et al. [123] and Shi et al. [124]. The first type of hydrogen impurity, a hydrogen atom bound to a bulk oxygen atom, referred to as OH-type, is only stable up to around 420 K. The second type of hydrogen impurity is a hydrogen atom that replaces an oxygen atom. This so-called substitutional hydrogen is believed to be the main one present in samples which have been cooled down slowly during preparation or stored at room temperature for a long time. It is stable up to higher temperatures of about 770 K. This suggests that repeated preparation of ZnO($10\bar{1}0$) according to the recipe used throughout this work could deplete the sample of the substitutional as well as the OH-type hydrogen, thus decreasing the conductivity. Annealing zinc oxide in ambient pressures of molecular hydrogen to 1000 K can reintroduce hydrogen impurities of both types depending on the cooling process. It is unlikely that this could be done with a single crystal while preserving its structure and flatness. We have observed an improved scanning resolution after ex-

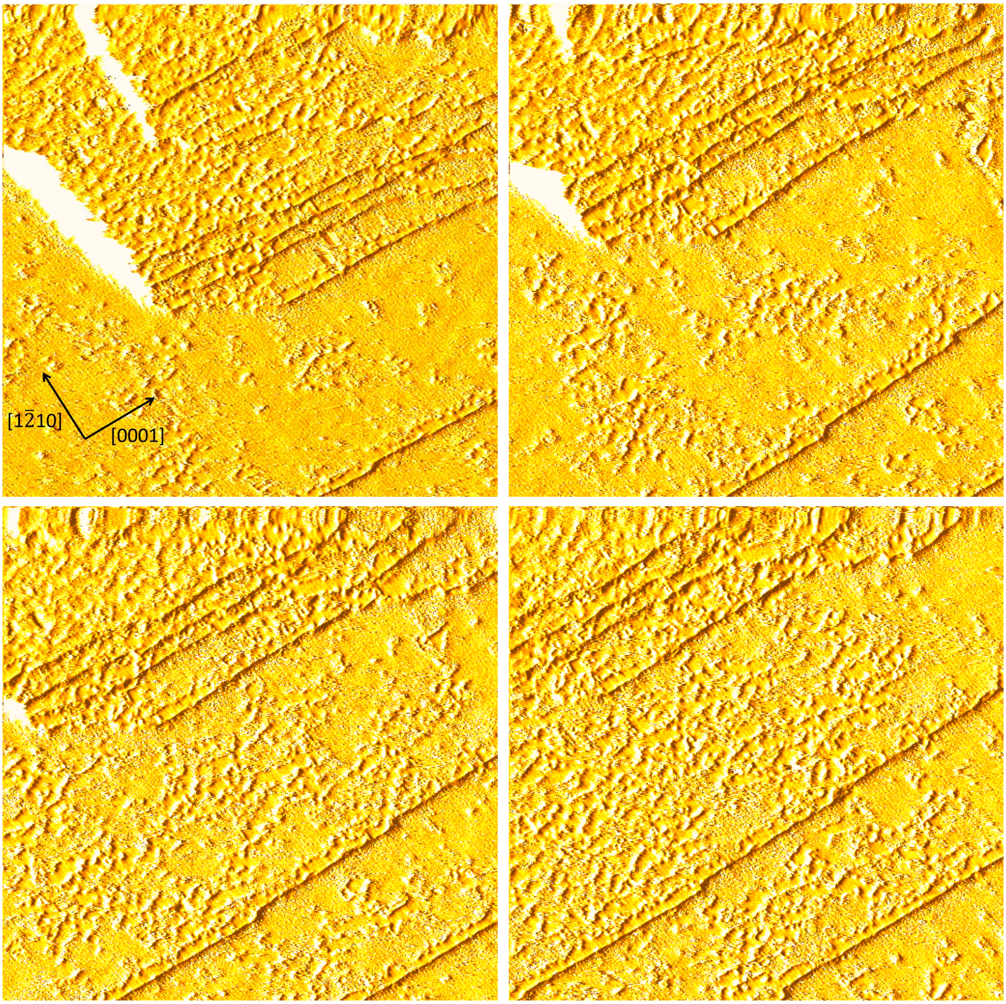

Figure 3.13: Consecutive 80 nm x 80 nm STM images of the as-prepared ZnO(10$\bar{1}$0) surface after roughly 160 cleaning cycles taken at 400 K with + 2.5 V and 50 pA. A derivative of the images is shown here in order to make the pits on all the terraces in the image visible at once.

posure to $1{\cdot}10^{-6}$ mbar of H_2 in the UHV chamber at a surface temperature of 400 K. As the increase in resolution was short-lived, however, it is possible that an adsorption structure of hydrogen or a functionalized tip resulted in sharper images rather than the conductivity of the sample itself recovering. It has been shown that adsorption of atomic hydrogen metallizes the surface [105,107,125]. However, the dissociation of molecular hydrogen has only been observed on the polar faces and not on the $(10\bar{1}0)$ face of ZnO [116]. The effect of low pressures of hydrogen on the resolution has not been investigated systematically here and it is generally difficult to identify one factor alone as the reason for a sudden increase in resolution as there are a large number of factors that play a role in the resolution of an STM. It has been observed previously that prolonged storage in air can recover the conductivity of zinc oxide samples [126]. This is currently the only reliable method we are aware of, although it has not been investigated how and how fast hydrogen can incorporate into zinc oxide in air at room temperature.

3.5.2 Tip-induced Vacancy Formation

Figure 3.13 shows multiple STM images taken in UHV at 400 K on the as-prepared $ZnO(10\bar{1}0)$ surface. The images are taken consecutively at roughly the same position such that the same roughly 30-nm-wide terrace can be identified in all of them. During scanning the density of pits on the terrace increases until it becomes more homogeneously covered with them. The sample drifts to the upper left corner which brings not previously scanned areas with a small vacancy density into the frame from the lower right corner. In additional images (not shown here) the scan size at the same position was increased resulting in the observation of areas of low pit density around the previously scanned area with high density. This is clear evidence that the scanning itself is the cause for the formation of these pits.

A zoom-in of the fourth scan as well as a corresponding height profile can be seen in Figure 3.14. Again a step height of around 0.3 nm is measured (as in Section 3.3.1) while the pits seen on the lower terrace have a depth between 0.1 and 0.15 nm. This is in agreement with one layer of ZnO missing. As the $ZnO(10\bar{1}0)$ step is a double layer of these ZnO dimers, the vacancies are not a step height deep but can have less than half that depth, as has been observed in Ref. [84]. This is illustrated in Figure 3.15.

The larger-resolution image in Figure 3.16 shows that the Zn lines stay intact in between the vacancies. The smallest vacancies, marked with a blue circle, can be identified as a vacancy of one dimer when comparing to simulated STM images based on density functional theory from Ref. [121]. However, most vacancies in this image have already become larger and must consist of several missing dimers. At this stage they can appear longer in parallel or orthogonal direction with respect to the Zn lines. However,

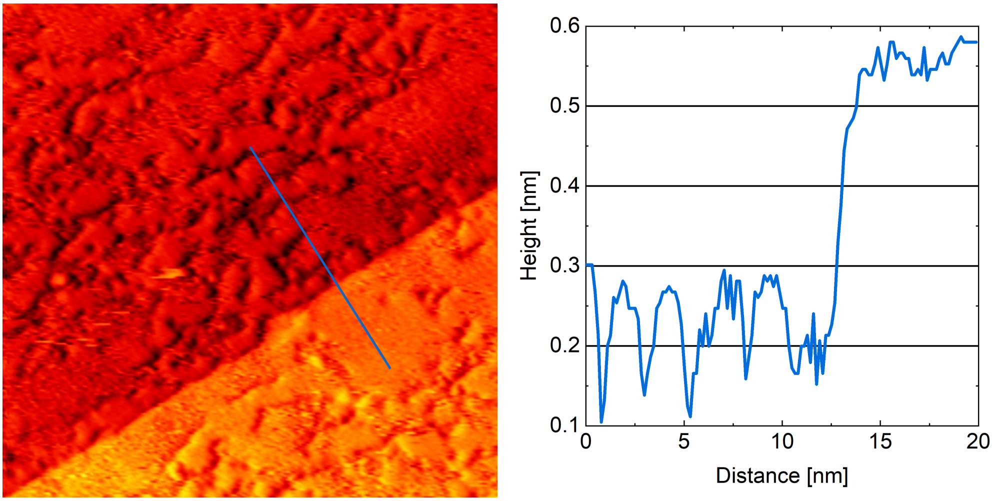

Figure 3.14: 40 nm x 40 nm zoom of the last image in Figure 3.13 with the corresponding height profile indicated in blue. For better visibility of the pits the image is a plane filter merged with its derivative, whereas the height profile is taken at a most common normal plane filter.

during longer scanning, where the vacancies connect to a network as seen in Figures 3.13 and 3.14, they are more often connected in the direction perpendicular to the Zn lines. This suggests that the vacancy growth is favored in the [0001] direction at this stage. As the resolved Zn lines in Figure 3.16 run diagonally from the upper left to the lower right corner of the image, the fast scanning direction of the STM tip (horizontally in all images shown) is at an angle of about 45° with respect to the [0001] as well as the [1$\bar{2}$10] direction. It is thus unlikely that the movement of the tip is the main reason for the preferred direction of the vacancy lines along one direction.

When scanning at bias voltages between 2 V and 3 V, a terrace is covered with vacancies within five to eight scans on the same position. However, when scanning with the same tip speed but bias voltages of 4 V or higher a terrace is already covered with vacancies in the first image taken (data not shown). Although the tip is farther away from the surface, a higher bias voltage also leads to a higher charge on the ZnO surface. The apparent difference between the behavior at 3 V and 4 V could be related to the bandgap of ZnO at 3.4 V [117]. It is thus likely that electronic effects play a role in the removal of the ZnO dimers. However, although the bias voltage is applied to the whole surface, areas without vacancies can be found when moving to an area that was not scanned previously. Thus, the charge alone is not sufficient to create the vacancies. It is rather the (local) tunneling current or a combination of charge effect and mechanical interaction with the tip that is responsible for removing ZnO dimers from the surface.

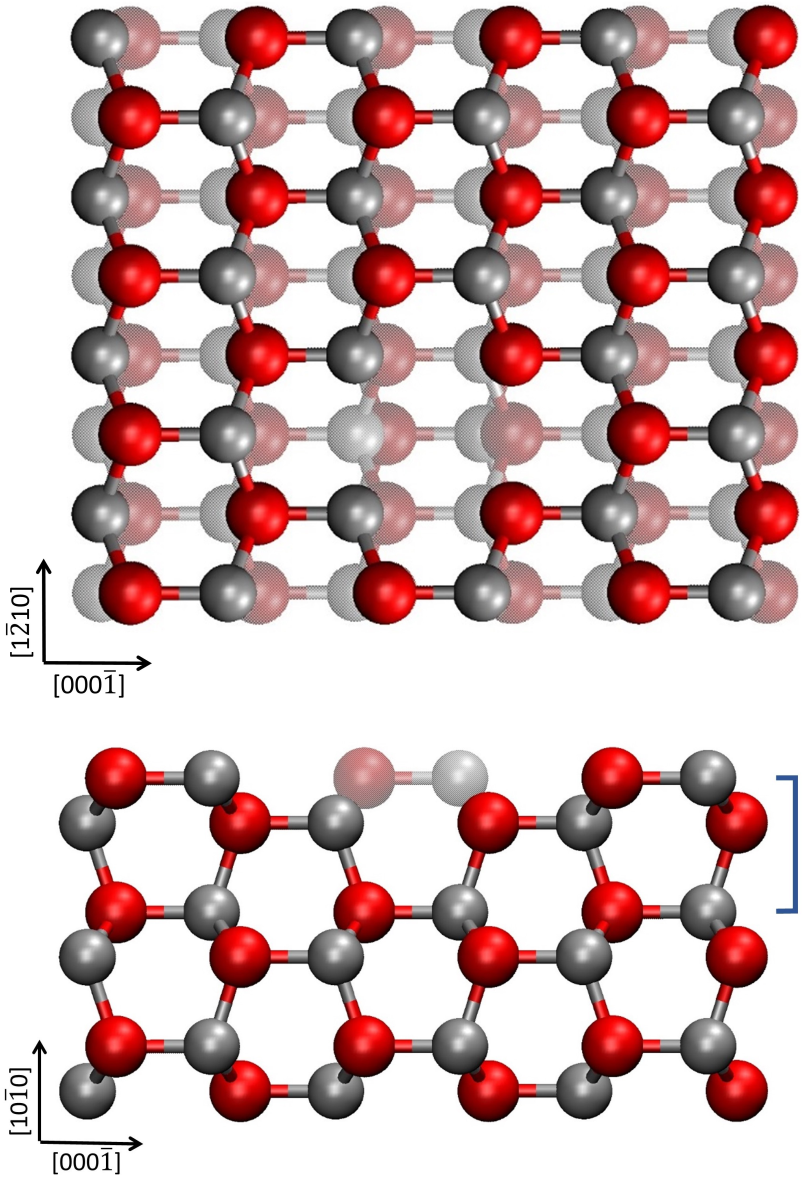

Figure 3.15: Top view (top) and side view (bottom) of a schematic representation of the ZnO($10\bar{1}0$) surface with one dimer vacancy. Zinc atoms are grey and oxygen atoms red. Atoms in transparent colors are further away from the viewer. The blue line indicates one step height of ZnO($10\bar{1}0$).

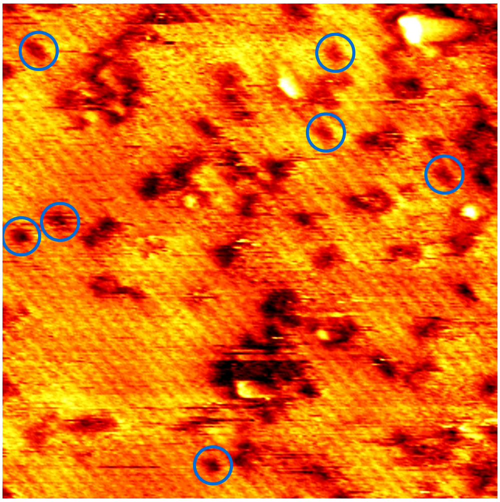

Figure 3.16: 20 nm x 20 nm STM image of ZnO(10$\bar{1}$0) after roughly 160 cleaning cycles taken at 400 K with + 2.5 V and 50 pA. The image has been merged with its derivative for better visibility of the Zn lines.

The same tunneling current and voltages up to 4 V were used in the images in Figures 3.1 and 3.2. Nevertheless, a significantly smaller amount of vacancies is visible in these images, which were taken after less cleaning cycles. In light of the loss of conductivity with repeated preparation described in Section 3.5.1 it is possible that the conductivity was already lower to some extent in the images taken in Figures 3.13 to 3.16, allowing the tip to move closer at all voltages. This suggests that the proximity of the tip is relevant for the vacancy formation and the tunneling current alone is not sufficient. As the mechanism responsible for the conductivity of zinc oxide is not completely understood however, it cannot be excluded that the loss of conductivity is directly related to the underlying electronic effect which enables the vacancy formation. In images taken after even more cleaning cycles, like shown in Sections 3.3.2 and 3.3.4, the formation of vacancies is not observed anymore. These high-pressure scans cannot be directly compared to the scans shown here however, as a number of other processes could be taking place under the influence of gases. Adsorbates can increase the conductivity and thus the tip-sample distance. Additionally, the resolution on the terraces, for example in Figure 3.8(a), is significantly lower, such that a small vacancy density might be present but not visible in the images. Additionally, the roughening observed at these pressures starts as soon as the gas is introduced, diminishing the resolution on the small ZnO(10$\bar{1}$0) patches which are left between the steps.

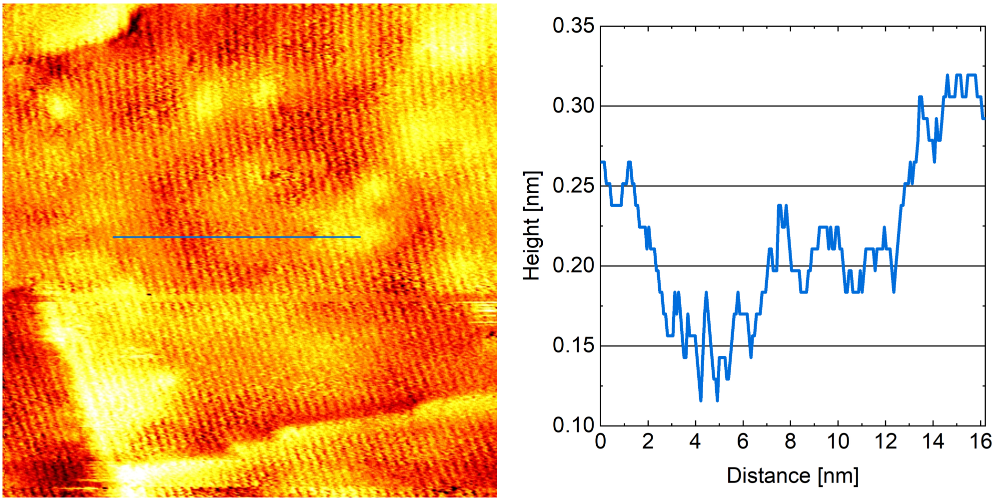

Figure 3.17: 20 nm x 20 nm STM image of the as-prepared ZnO(10$\bar{1}$0) surface after more than 300 cleaning cycles taken at 400 K with + 3 V and 50 pA including the corresponding height profile indicated in blue. For better visibility of the Zn lines the image is a plane filter merged with its derivative in a ratio of 2:1, whereas the height profile is taken at a most common normal plane filter.

3.5.3 Incorporation of Argon

In the high-resolution image obtained after about 100 cleaning cycles shown in Figure 3.1(b), brighter and darker areas of about 6 nm diameter can be seen overlaid on the Zn lines. This larger-scale corrugation increases with repeated preparation. It is seen again in Figure 3.16 after about 160 cleaning cycles and more clearly in an image taken after more than 300 cleaning cycles as shown in Figure 3.17. As the Zn lines are not interrupted, the height variances must stem from a subsurface structure. The height profile in Figure 3.17 shows that after more than 300 cleaning cycles the height variation has different levels and is on the order of 0.1 nm. Areas with the same height level can extend up to tens of nanometers. The onset of such a structure is visible in an STM image of ZnO(10$\bar{1}$0) in Figure 4(a) in Ref. [118], where it was not investigated further. Shi et al. observe comparable structures on ZnO(10$\bar{1}$0) that they identify as subsurface defects [87,89].

It is likely that the height variations observed here are due to the incorporation of argon ions while sputtering during the surface preparation (see Section 3.5.1). Such subsurface ions or so-called argon bubbles have been observed previously with STM on a number of single-crystalline surfaces. Among these are O-ZnO(000$\bar{1}$) [118], Co(0001) [127], Ru(0001) [128], Al(111) [129], and PtSi on Si(100) [130]. The last example shows that argon bubbles can reach diameters of up to the order of a hundred nanometers. This suggests that the dimensions observed here are not unrealistic, although the significantly higher argon acceleration voltage of 20 to 160 kV used in Ref. [130] could facilitate the incorporation and growth of the bubbles. The shape difference between the round argon bubbles observed in the literature on other materials and the network of more irregular height variations in Figure 3.17 could stem from argon bubbles merging over time with increasing incorporation. In comparison to ZnO(10$\bar{1}$0) imaged in Ref. [118], the images presented here are taken after significantly more sputtering and annealing (hundreds instead of tens of cycles), which can explain the more severe height variations observed. Additionally, the higher argon acceleration voltage chosen here (1.4 kV instead of 1 kV in Ref. [118]) could influence the severity and speed of the argon incorporation.

Although the surface layer of the material is not interrupted by argon bubbles, they are known to change the properties of the surface to an extent that can influence its interaction with gases [128,129]. This suggests that argon bubbles have to be taken into account when interpreting measurements on single-crystal model catalysts.

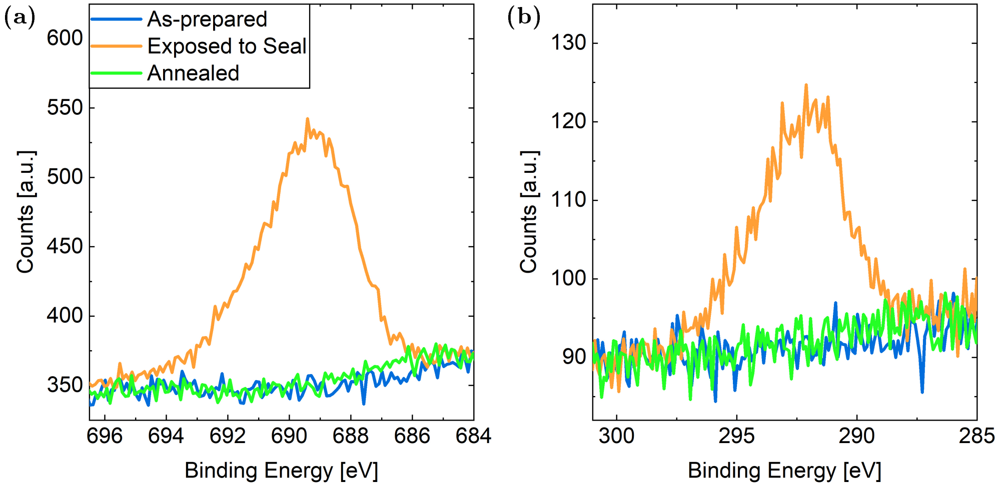

Figure 3.18: (a) F 1s peak and (b) C 1s peak of ZnO(10$\bar{1}$0) taken at room temperature. The as-prepared surface is compared to the same surface after exposure to the reactor seal as well as after an additional annealing step.

3.5.4 Influence of the Reactor Seal

As explained in Section 3.2.1, the reactor is sealed off from the UHV chamber with a Kalrez seal directly on the sample. Although the area of the sample probed by STM is sufficiently far away from the area touched by the seal (on the order of millimeters), residues from the seal need to be removed in order to prevent migration to the probed area. The X-ray photoelectron spectroscope used here probes a lager area of the surface and can thus detect fluorine and carbon residues from the seal. As can be seen in Figure 3.18, no carbon or fluorine is detectable on the as-prepared ZnO($10\bar{1}0$). After exposure to the seal for 3 hours at RT, while keeping the sample in ultra-high vacuum, carbon as well as fluorine are visible in XPS. Annealing the surface to 794 K for one hour removes these residues.

The behavior of the Kalrez seal is temperature-dependent. With increasing temperature the seal between the high-pressure side and the vacuum side generally improves as can be observed in terms of the leak rate into the ultra-high vacuum chamber. Additionally, an elevated temperature facilitates removing the seal from the sample after a high-pressure STM measurement. In order to keep the forces on the sample as small as possible and prevent damage to the specialized oxide sample holder, the seal needs to be removed from the ZnO($10\bar{1}0$) crystal at 400 K surface temperature. This needs to be taken into account when interpreting measurements taken in UHV after removal of the seal including UHV STM, spectroscopy, and diffraction data.

Chapter 4

Gold Oxide Formation on TiO_2/Au(111) during CO Oxidation

4.1 Introduction

Whereas conventional power plants can be turned on and off as needed, the energy output of wind and solar plants varies with the weather and the time of day. Therefore, the transition to sustainable energy sources requires the development of efficient energy-storage methods. A viable option is to store the energy in the form of chemicals such as methanol. As a liquid at room temperature [71], methanol is simple to store and it is biodegradable [70]. In comparison to other hydrocarbons, methanol has the highest hydrogen-to-carbon ratio. The energy stored in the form of methanol can be harvested by converting it to hydrogen via methanol steam reforming [72,76]. However, for the use in fuel cells this hydrogen needs to be free from carbon monoxide, a byproduct of methanol steam reforming, to prevent poisoning of the fuel-cell anode [74]. In Section 3.1 of this thesis we mention the strong research effort to improve the selectivity of methanol steam reforming catalysts towards CO_2 instead of CO. An alternative solution is removing the traces of CO over a second catalyst via preferential CO oxidation, which takes place in the hydrogen environment without oxidation of the H_2:

$$2\ CO + O_2 \rightarrow 2\ CO_2 \tag{4.1}$$

$$2\ H_2 + O_2 \not\rightarrow 2\ H_2O \tag{4.2}$$

Compared to conventional CO oxidation catalysts such as platinum and palladium, gold-based catalysts are more suited for this application, since they are more selective for the oxidation of CO instead of H_2 at low temperatures [131–133]. Gold-based catalysts have shown CO oxidation activity at temperatures as low as room temperature [134]. They are thus additionally interesting for improving the 3-way car catalyst, which is currently not efficiently oxidizing CO during the cold start-up of the car [135]. There has been research into the catalytic activity of gold nanoparticles deposited on oxide supports for more than 30 years [136–141]. Inverse model catalysts of oxide particles on metal single crystals are widely applied as well due to the ease of controlled preparation and application of surface-science techniques, especially in ultra-high vacuum [29,141,142]. On Au(111) single crystals various oxide nanoparticles have been prepared. Among these are CeO_2 [143], MoO_3 [144], MgO [145], CoO [146], Fe_2O_3 [147], and TiO_2 [148]. However, inverse model catalysts on gold single crystals are not only a useful research tool but can also show even higher CO oxidation activities than their non-inverse counterparts as suggested by Palomino et al. [34]. In their study, TiO_2/Au(111) showed the highest activity of all tested catalysts. For inverted as well as non-inverted catalysts it is clear that the active site lies in the interface region between support and particles [149–151] and metal-support interactions have been observed [34,152,153]. However, the exact oxidation state of gold during the reaction remains under debate. The oxidation of gold is believed to not be possible from molecular oxygen [154–156] and more specifically under CO oxidation conditions [157]. There is evidence that a gold oxide prepared with ozone would be less active than metallic gold [158]. However, other work has suggested that oxidized gold is the active species during CO oxidation [159,160]. Additionally, there is evidence that water can promote the CO oxidation reaction [161–163] and could even make the oxide support unnecessary [164].

The challenges in investigating the presence of a gold oxide with spectroscopy techniques are the low signals stemming from small amounts of surface oxides as well as the influence of exposing the sample to air and thus water between the reaction and the characterization as is necessary in many laboratories. However, crystalline surface oxides can be detected via atomically resolved microscopy as well [96,165–167].

Our in situ scanning tunneling microscope allows for the imaging of the support and the full inverse model catalyst under reaction conditions. In this chapter we present evidence for the presence of a gold oxide on Au(111) after exposure to oxygen (Section 4.3.1) and differentiate between the influence of the water background in the reactor (Section 4.3.2), the CO in the reaction mixture (Section 4.3.3), the TiO_2 nanoparticles (Section 4.3.4), and finally contaminants on the gold substrate (Section 4.3.5). In the outlook in Section 4.4 we give a suggestion on how the presence of the gold oxide on this model catalyst could be confirmed using spectroscopy.

4.2 Materials and Methods

4.2.1 Sample Preparation

The Au(111) single crystal was purchased from SPL and prepared with cycles of argon ion sputtering at 1 kV to 1.4 kV acceleration voltage and annealing to between 800 K and 850 K in UHV. Whenever carbon particles were visible in the STM, the crystal was additionally annealed in $1 \cdot 10^{-6}$ mbar of O_2 to between 750 K and 800 K until the carbon was removed. This was followed by at least ten cycles without annealing in oxygen before running an experiment.

For the preparation of the TiO_2/Au(111) model catalyst titanium was deposited onto the clean, metallic Au(111) using an e-beam evaporator from Oxford Applied Research. The deposition was performed in an oxygen background of $1 \cdot 10^{-6}$ mbar at room temperature. Subsequently the crystal was annealed to 850 K in $5 \cdot 10^{-6}$ mbar of O_2 for 20 min and cooled down in the same oxygen pressure until below 500 K. To exclude any influence from titanium residue or alloying of titanium with gold the experiments in Sections 4.3.1 to 4.3.3 and 4.3.5 were performed on a crystal that had not been exposed to titanium whereas another crystal was used solely for the experiments on TiO_2/Au(111).

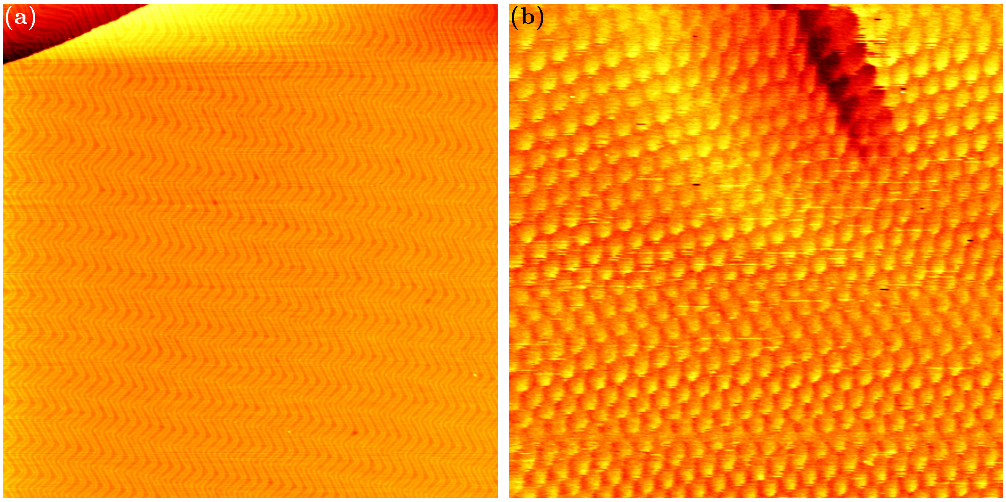

Figure 4.1: (a) 300 nm x 300 nm STM image of the as-prepared Au(111) surface and (b) 10 nm x 10 nm STM image of the same surface with atomic resolution. Both images are taken in UHV at room temperature with − 1 V and 50 pA.

4.2.2 The ReactorSTM

As described in more detail in Section 3.2.1 and in Ref. [44], the ReactorSTM setup allows for scanning tunneling microscopy in ultra-high vacuum as well as in up to 6 bar of gases and at up to 600 K. Without leaving the vacuum chamber the sample can be moved between preparation, STM, LEED/Auger, and XPS.

4.2.3 Gases

The amount of water in our gas system was measured for 1 bar Ar and 1 bar O_2 with a result on the order of 1 mbar of water. Section 3.2.2 describes the measurement process and that the water background in our system is likely independent of which gases are used. In the following we have used Ar 5.0 from Westfalen [97], O_2 5.0 from Westfalen [168], and CO 4.7 from Air Liquide [169]. The CO contains less than 5 ppm of O_2.

4.3 Results and Discussion

4.3.1 Gold Oxide on Au(111)

Figure 4.1(a) shows an overview of the as-prepared Au(111) surface with the well-known herringbone reconstruction visible as brighter lines with straight sections as well as so-called elbows. The hexagonal unit cell of Au(111) can be seen in the zoomed-in image

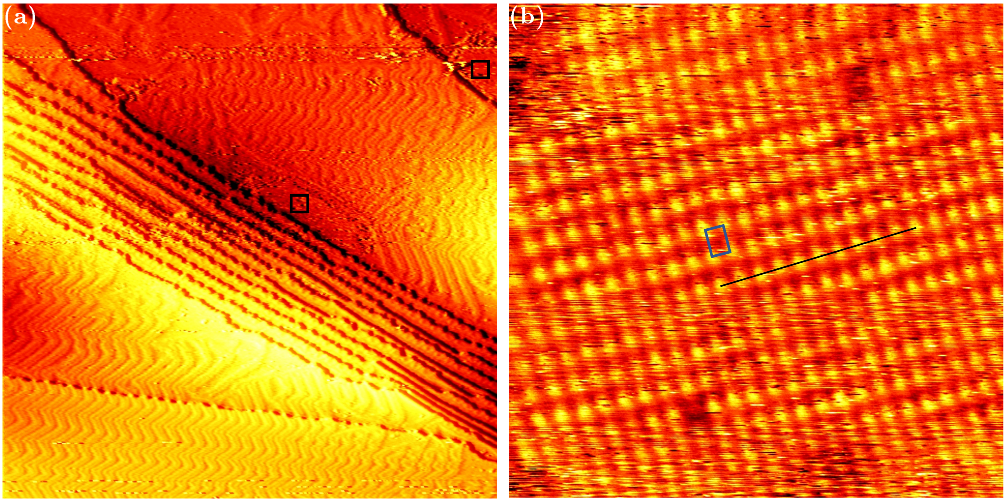

Figure 4.2: (a) 300 nm x 300 nm STM image of Au(111) after exposure to 0.8 bar O_2 at room temperature for 1 h. For better visibility of the structure next to the step edges (marked with black squares) the image is merged with its derivative in a ratio of 1:15. (b) 10 nm x 10 nm STM image of the newly formed structure indicating the rectangular unit cell in blue. Following the black line deviations from the unit cell can be seen, which are discussed in the supplemental information (Section 4.5.2). Both images are taken in UHV at room temperature with − 1 V and 50 pA.

in Figure 4.1(b) including part of a herringbone in the upper right corner.

After exposing this surface to 0.8 bar O_2 at room temperature for 1 h, the herringbone is still present on most part of the terraces (see Figure 4.2(a)). Additionally, islands of another structure with a height of about (0.09 ± 0.02) nm are visible on step edges as marked with black squares. An area as large as the square (10 nm x 10 nm) is shown close up in Figure 4.2(b). Averaging over tens of STM images the size of the unit cell is determined to be (0.50 ± 0.07) nm in the longer direction and (0.37 ± 0.03) nm in the shorter direction with the standard deviations as error. As shown in the supplemental information (Section 4.5.1), the same unit cell is observed when the Au(111) surface is exposed to atomic oxygen before the exposure to atmospheric oxygen pressures. Additionally, it has been observed in STM by Min et al. after exposing Au(111) to ozone (see Figure 9 in Ref. [165]). Overall, this allows for identifying the islands as surface gold oxide. When using atomic oxygen, the oxide can also grow on the terraces (see Figure 4.12(b) in the supplemental information) as opposed to only at step edges as in Figure 4.2. This allows for the observation of three different orientations of the oxide unit cell as is to be expected for a rectangular structure on top of the hexagonal Au(111) substrate. The presence of the unit cell seen in STM is additionally evidenced by a

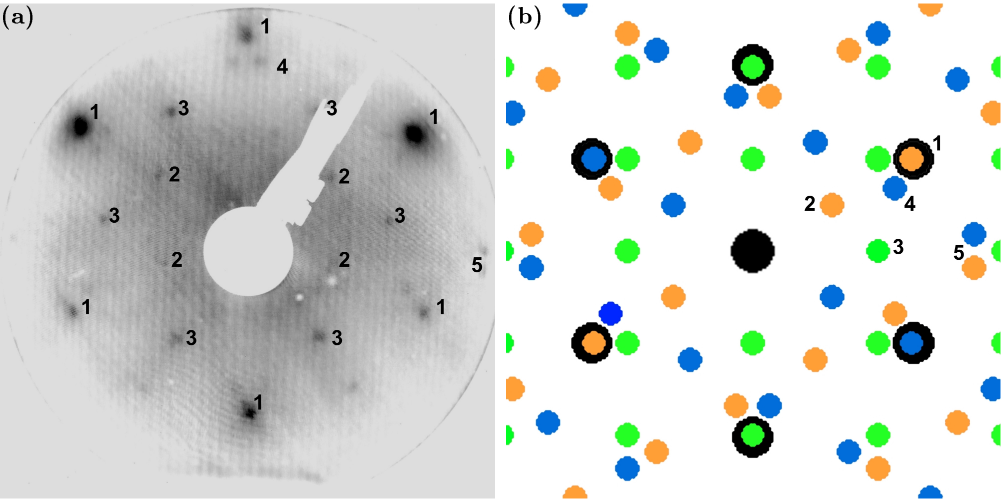

Figure 4.3: (a) LEED image taken of Au(111) after O_2 exposure (78 eV electron energy). Measurement done by Dajo Boden, Leiden Institute of Chemistry. (b) Simulated LEED image based on the unit cell measured in STM including the Au(111) substrate in black and the three different possible orientations of the oxide overlayer in blue, orange, and green. Corresponding spots in (a) and (b) are marked with numbers 1 to 5. The simulated LEED image is made using LEEDpat [170].

LEED measurement as seen in Figure 4.3(a). This is in agreement with the simulated LEED image of the unit cell in Figure 4.3(b) and shows all three different orientations. Additional details on the unit cell of the gold oxide and a model for the structure of the oxide is given in the supplemental information (Section 4.5.2).

Although we can detect the presence of oxygen on the surface with XPS (data not shown), the surface sensitivity of our lab setup is not large enough to distinguish between adsorbed atomic oxygen and gold oxide (for details see Section 4.4). Note that in order to observe the unit cell in LEED and the presence of oxygen in XPS a higher coverage of the gold oxide is needed, which can only be achieved on contaminated samples in the presence of CO as described in Section 4.3.5.

4.3.2 The Role of Water

The theoretical dissociation barriers of O_2 on the Au(111) terraces of 2.23 eV and on the Au(111) step edge of 1.16 eV [171] suggest that O_2 dissociation even on the step edge is unlikely in pure O_2. To test whether water could deliver the necessary atomic oxygen, the as-prepared Au(111) was exposed to 0.8 bar argon for 1 h and thus the

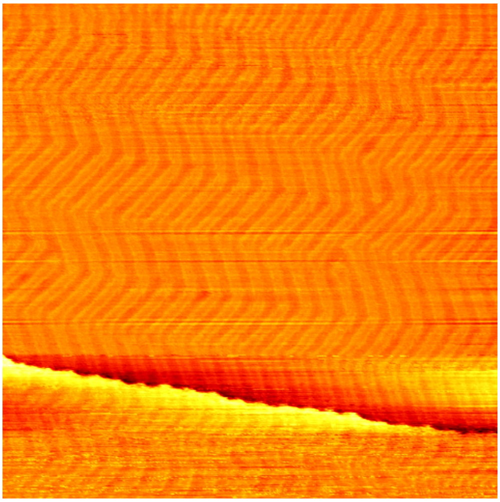

Figure 4.4: 150 nm x 150 nm STM image of the as-prepared Au(111) surface after 1 h in 0.8 bar argon, containing roughly 1 mbar of water, at room temperature. The image is taken in UHV at room temperature with − 1 V and 50 pA.

same amount of water as was present during the O_2 exposure. No oxide islands could be found after this water exposure and the herringbone reconstruction stayed intact as can be seen in Figure 4.4. Water alone does thus not cause the formation of gold oxide, which can be understood on the hands of theoretical dissociation barriers as well: Whereas the dissociation barrier of H_2O is somewhat lower than the barrier of O_2 on the terraces with 1.80 eV [172], it is slightly higher than the barrier of O_2 at the step edges with 1.33 eV [173]. However, Liu et al. [174] have shown that the presence of water reduces the dissociation barrier of oxygen on the steps of Au(111). With two water molecules per oxygen molecule the barrier is already reduced to 0.54 eV and with a larger amount of water molecules the barrier can be as low as 0.15 eV. Given that our gas mixtures contain on the order of 1 mbar of water, it is probable that this water-assisted dissociation of molecular oxygen on the Au(111) steps supplies the first atomic oxygen from which the gold oxide can start growing. However, only one island per 320 nm x 320 nm is present on average after 1 h of oxygen exposure showing that this is still a rare event. Once an island of gold oxide exists, it is believed to be able to dissociate more O_2 from the gas phase [165,175] allowing the islands to keep growing away from the step. In situ images of the formation of gold oxide are shown in the supplemental information (Section 4.5.3).

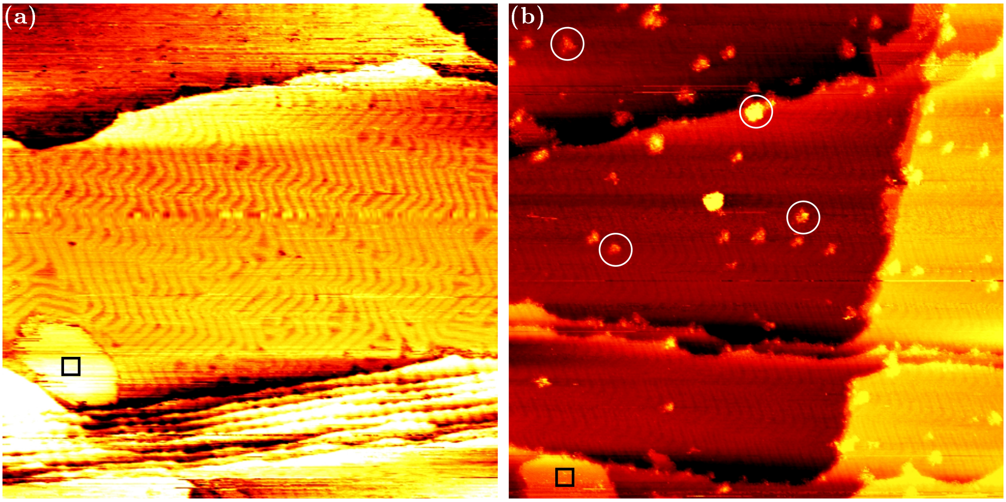

Figure 4.5: 300 nm x 300 nm STM images of Au(111) (a) after 1 h in 1 bar of 4 O_2 + 1 CO and (b) after 1 h in 0.2 bar CO, respectively. The images are taken in UHV at room temperature with (a) $-$ 1 V and (b) $-$ 1.5 V, and 50 pA. Black squares mark islands of gold oxide. White circles mark structures which likely consist of carbon.

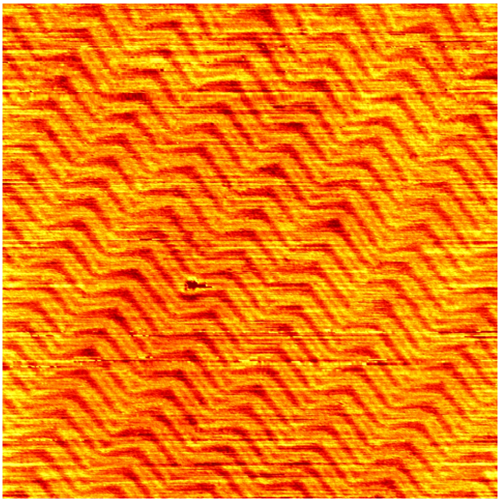

Figure 4.6: 150 nm x 150 nm STM image of Au(111) after 88 min of exposure to increasing CO pressure followed by 13 min at 1 bar. The image is taken in 1 bar CO at room temperature with $-$ 1 V and 50 pA. Horizontal lines caused by a disturbed STM tip have been removed.

4.3.3 The Influence of CO

Figures 4.5(a) and (b) show Au(111) after exposure to CO oxidation conditions (1 bar 4 O_2 + 1 CO) and 0.2 bar CO for 1 h, respectively. Comparing several images of these measurements with the images of the sample exposed to oxygen only (see Figure 4.2(a)), the number and size of the gold oxide islands are comparable. This indicates no promoting or inhibiting influence by the CO on the oxidation of clean Au(111). There is no evidence in the literature that CO itself dissociates on Au(111) and adsorption is only possible at the steps [176–178]. However, after exposure to only CO, additional structures with roughly round shapes can be observed as bright spots on the terraces in Figure 4.5(b) marked with white circles. As discussed in more detail in the supplemental information (Section 4.5.4), these are likely carbon structures, but whether they stem from the CO itself or from contaminants in the gas bottle is unclear. As most of these structures are observed on the terraces and not in proximity to the oxide islands, any relevance for the formation of the oxide can be deemed unlikely. As suggested above (see Section 4.3.2), the first O_2 dissociation initiating the growth of an oxide island is a rare event. Therefore, it is reasonable that the 10^{-3} mbar range of O_2 present in 0.2 bar CO (see Section 4.2.3) is sufficient to produce a roughly comparable number of islands as in 0.8 bar O_2. However, it could be expected that the self-catalyzed growth of existing islands from O_2 would proceed more slowly here. We cannot find conclusive evidence for this when comparing average sizes of islands for multiple images after exposure to the different gas compositions. Thus it is likely that, in the pressure range studied here, the amount of O_2 in the gas phase is not the limiting factor for the growth speed.

Figure 4.5(b) additionally clearly shows that the herringbone reconstruction is still intact after CO exposure. This is further confirmed in Figure 4.6 showing an in situ image of the Au(111) in 1 bar CO after 12.7 min at this pressure with the herringbone intact. This contradicts Piccolo et al. [179] observing a complete lifting of the herringbone in 333 mbar CO, which is not reversible when returning to UHV. We comment further on this in Section 4.3.5.

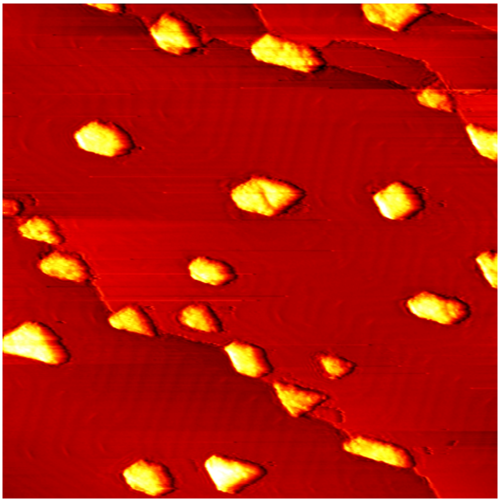

Figure 4.7: 110 nm x 110 nm STM image of the as-prepared TiO_2/Au(111) taken in UHV at room temperature with + 3 V and 50 pA. In order for the particles and the herringbone to be visible simultaneously the image was flattened and merged with its derivative.

4.3.4 Gold Oxide on TiO_2/Au(111)

Figures 4.7 and 4.8(a) show the as-prepared TiO_2/Au(111) model catalyst. The nanoparticles are roughly between 5 nm and 15 nm wide and show an apparent height between 0.6 nm and 1.9 nm in the STM. Triangular, hexagonal, and more elongated shapes can be recognized suggesting a crystalline structure. In general, the TiO_2 nanoparticles are in agreement with those prepared by Biener et al. [148]. A more detailed analysis can be found in Ref. [180].

In Figure 4.8 the as-prepared TiO_2/Au(111) surface is compared to the same surface after exposure to O_2, CO oxidation conditions, and CO, respectively. Under all conditions, islands of gold oxide are formed at step edges as marked with a black square. The amount of gold oxide is comparable to the amount seen when exposing only the Au(111) substrate as presented in Sections 4.3.1 and 4.3.3. Specifically, no oxide islands are observed on the terraces despite the presence of the TiO_2 nanoparticles suggesting that no spillover of atomic oxygen from the titania to the gold substrate takes place. Studies on TiO_2 single crystals suggest that dissociation of molecular oxygen is possible at oxygen vacancies in the titania at room temperature [181]. Additionally, the dissociation is increasingly more likely with higher vacancy density [182]. If oxygen dissociation takes place on the titania in our case, the resulting oxygen atoms might thus rather remain on the nanoparticles curing vacancies instead of spilling over to the gold substrate.

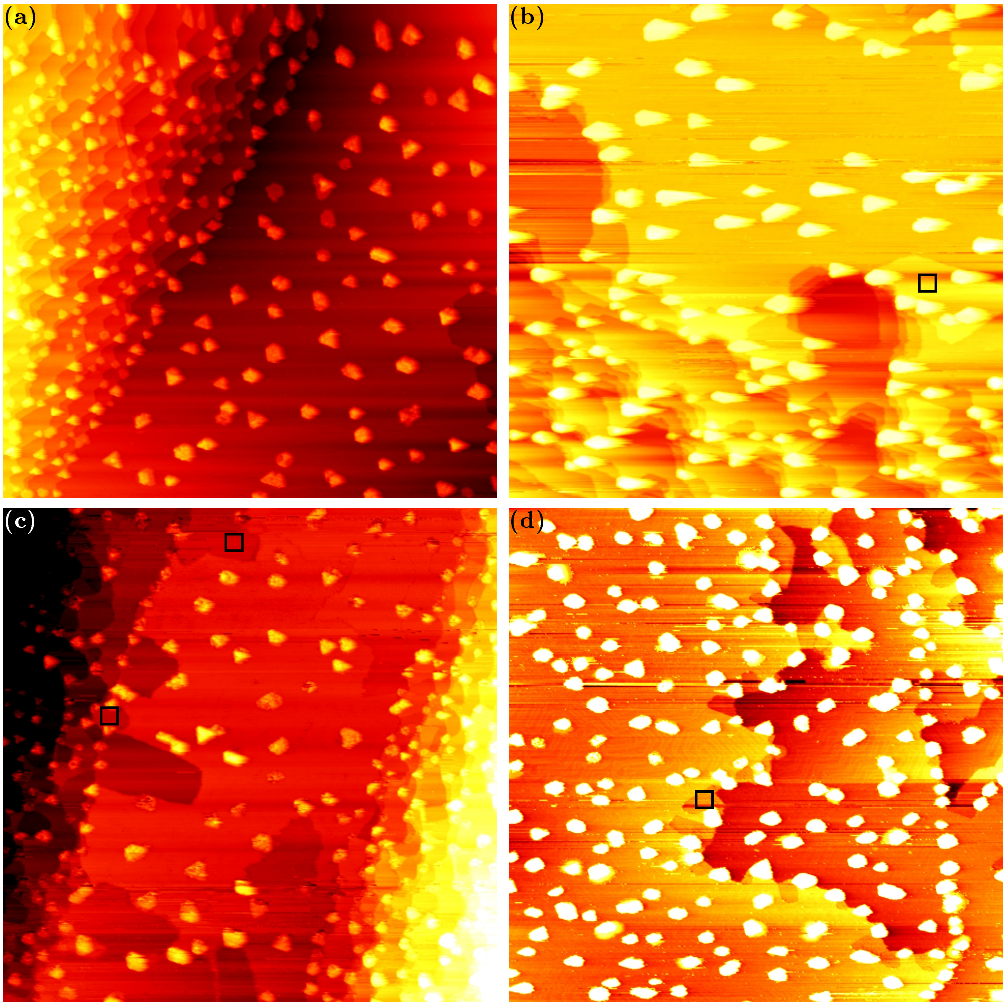

Figure 4.8: 300 nm x 300 nm STM images of TiO_2/Au(111) (a) as-prepared, (b) after 1 h in 0.8 bar O_2, (c) after 1 h in 1 bar of 4 O_2 + 1 CO, and (d) after 1 h in 0.2 bar CO, respectively. All images are taken in UHV at room temperature with + 3 V and 50 pA. Black squares mark islands of gold oxide. The size of the squares corresponds to the size of the atomic-resolution image of the gold oxide in Figure 4.2(b).

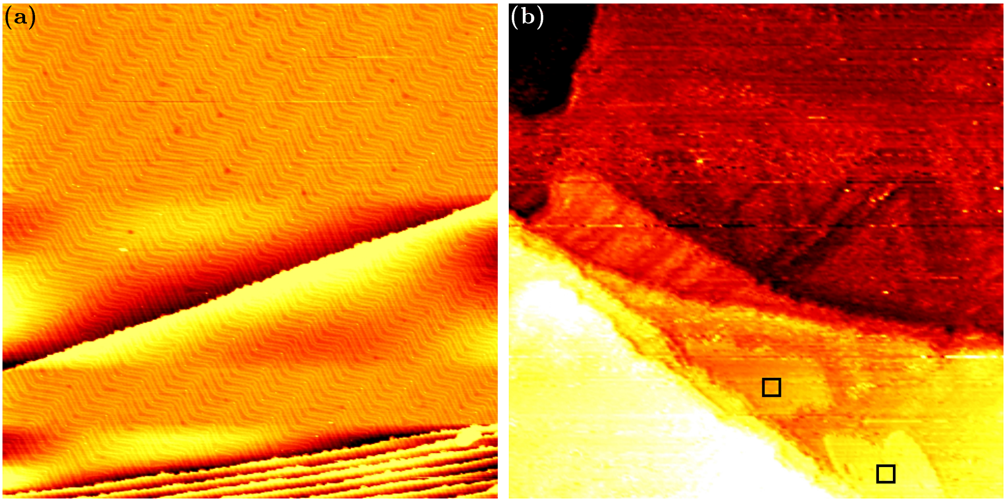

Figure 4.9: 300 nm x 300 nm STM images of contaminated Au(111) (a) as-prepared and (b) after 1 h in 0.8 bar O_2. The images are taken in UHV at room temperature with (a) − 2 V and (b) − 1.5 V, and 50 pA. Black squares mark islands of gold oxide.

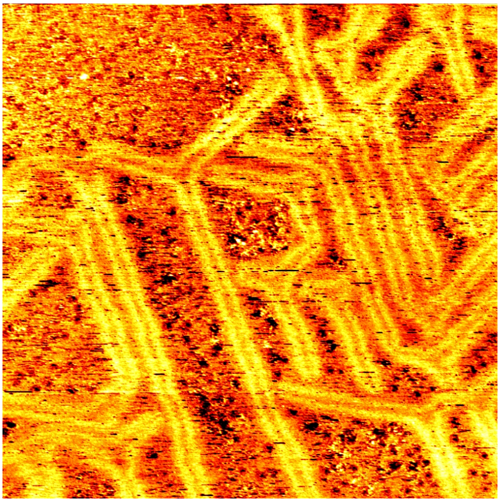

Figure 4.10: 120 nm x 120 nm STM image of a terrace of contaminated Au(111) after 1 h in 0.8 bar O_2. The image is taken in UHV at room temperature with + 1.5 V and 50 pA.

4.3.5 Sensitivity to the Cleanliness of the Substrate

Figure 4.9(a) shows the Au(111) substrate in a contaminated state, which is present when a newly purchased single crystal has been submitted to less cleaning cycles than needed to fully clean the crystal (as in Figure 4.1). Bright spots on elbows of the herringbone as well as darker spots in between the reconstruction lines are visible on the contaminated gold. Carbon as well as other metals are typical candidates for these contaminants. However, the amount present on the surface is not sufficient to allow for a spectroscopic characterization with the methods available in the ReactorSTM setup (XPS and AES). Additionally, this means that the amount of contamination cannot be quantified precisely and repeated preparation of this surface will lead to deviations in the amount and nature of contaminants present. However, general trends can be observed compared to the clean gold when exposing a contaminated surface to the same gas environments.

Figure 4.9(b) shows that the exposure to 0.8 bar O_2 leads to a comparable number and size of gold oxide islands as on the clean gold in Figure 4.2(a). However, most of the terrace does not show the herringbone reconstruction anymore. This can be seen more clearly in Figure 4.10. Areas which appear amorphous (meaning that no atomic resolution could be achieved) are separated by single lines of herringbone. This suggests a mobility of the surface gold atoms during O_2 exposure. A restructuring of Au(111) can be expected from literature under exposure to atomic oxygen (or ozone) [183,184] as well as in O_2 at elevated temperatures [185–187]. As the amount of gold oxide is comparable to the case of clean gold, the presence of significantly more atomic oxygen is unlikely. It is more probable that the contaminants promote the restructuring by O_2 similar to the effect of an elevated temperature. For the case of oxygen exposure we have not been able to achieve the necessary resolution in situ to determine whether the herringbone on clean gold is lifted as well but recovers when returning to UHV. Thus it remains unclear whether the contaminants are the cause of the changes on the terrace or whether they only prevent them from being reversible.

When CO is present in the gas mixture (Figure 4.11(a) and (b)), the number of gold oxide islands can be higher than on clean gold and oxide islands which are not connected to a step edge are observed. This suggests that the contaminants form sites on the step edges as well as on the terraces where oxygen can dissociate aided by CO (and possibly by water) more readily than on clean gold. It is possible that these dissociation sites are the contaminants themselves, low-coordinated Au atoms caused by the contaminant, or a combination of both. Other metals are known to dissociate O_2 directly [156]. However, density functional theory calculations suggest that the presence of CO hampers the O_2 dissociation on Pd and Pt single crystals [188,189]. Silver is the most likely bulk contaminant in the gold single crystal according to the analysis provided by

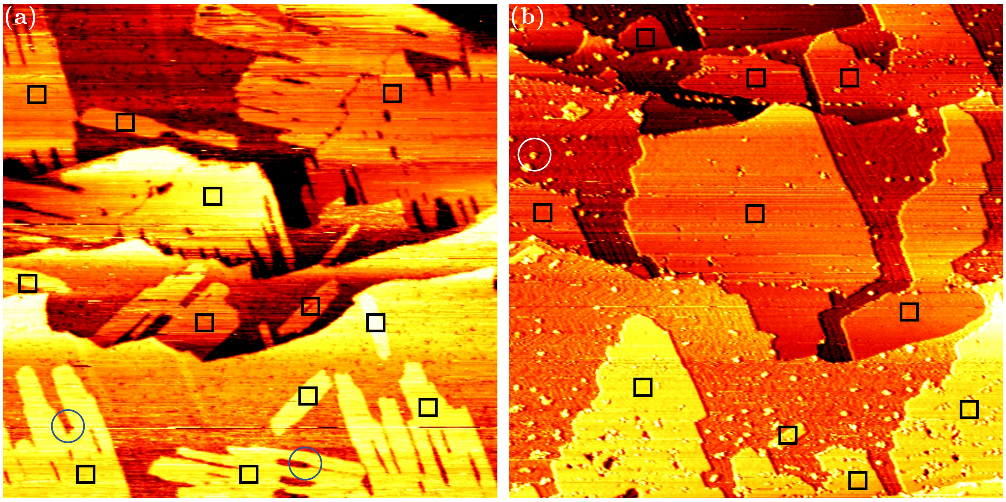

Figure 4.11: 300 nm x 300 nm STM images of contaminated Au(111) (a) after 1 h in 1 bar of 4 O_2 + 1 CO and (b) after 1 h in 0.2 bar CO, respectively. The images are taken in UHV at room temperature with (a) -1.5 V and (b) -1 V, and 50 pA. Black squares mark islands of gold oxide and blue circles mark a certain type of contaminants that blocks the growth of islands. A white circle marks a structure which likely consist of carbon. For better visibility of the herringbone on the terraces the image in (b) is merged with its derivative in a ratio of 1:2.

the supplier. Although Ag(111) is inert for O_2 dissociation, low-coordinated Ag sites might easily split O_2 [156]. Carbon as a possible contaminant is a less likely candidate for O_2 dissociation [190,191]. As described in detail in the supplemental information (Section 4.5.4), we identify carbon structures on the surface after CO exposure (see also area marked with a white circle in Figure 4.11(b)). That many of these areas are observed on the terraces without gold oxide islands connected to them confirms that carbon is likely not responsible for the promotion of gold oxide formation observed in Figure 4.11(a) and (b).

We do not only observe more gold oxide islands, but a single island can also grow larger than on clean gold during the same exposure time. As we identify the O_2 dissociation on already oxidized gold as responsible for this in Section 4.3.2, we have to conclude here that the dissociation promoted by contaminants is more efficient than the self-catalyzed growth or that the latter is promoted by the contaminants as well.

In Figure 4.11(a) blue circles mark positions where it can be seen that contaminants, possibly of a different nature, are able to block the growth of the oxide islands as well, which leads to more irregular shapes. As a common contaminant that is known to form pinning sites on Au(111) and does not promote O_2 dissociation, it is likely that this

contaminant is carbon.
Apart from the gold oxide islands, the terraces of the gold substrate are influenced as well. Similar to after oxygen exposure, a lifting of the herringbone is observed with only a few lines left after exposure to the reaction mixture. As this suggests that the surface atoms of gold are mobile during the exposure, it is possible that it aids in the formation of sites of low-coordinated gold atoms and/or contaminants where stronger O_2 dissociation takes place. As the herringbone is not lifted after exposure to pure CO (Figure 4.11(b)), the more complete lifting of the herringbone in the mixture (Figure 4.11(a)) compared to O_2 exposure (Figure 4.9(b)) cannot be interpreted as a sign of a promotion by CO. However, as explained above, a deviation in the exact amount of contaminants could likely cause the more complete lifting in the mixture. Although the contaminants seem to promote the restructuring of the herringbone in O_2, they are not sufficient to lead to a loss of herringbone in CO in our case. Thus, the presence of the type of contaminants observed here cannot explain the discrepancy stated in Section 4.3.3 where no lifting of the herringbone in CO is observed despite evidence to the contrary in the literature [179].

4.4 Conclusions and Outlook

We have presented evidence for the formation of surface gold oxide on TiO_2/Au(111) model catalysts under exposure to O_2, CO, or a mixture of both at atmospheric pressures. The formation is likely enabled by water in all gas mixtures and can be strongly promoted by CO when contaminants are present on the Au(111) substrate. Taking into account that under industrial conditions the same or more water is present and the gold is less pure, it is reasonable to assume that gold oxide could be formed during the reaction on a realistic catalyst. As we do not see any influence of titania on the gold oxide formation, it is unlikely that the transfer of atomic oxygen from one to the other is a possible step in the CO oxidation mechanism. Assuming that our conclusion about the role of water is correct, our observations cannot confirm that titania and water have interchangeable roles as suggested in Ref. [164]. Additional evidence for the role of water in the formation of gold oxide should be collected by exposing all as-prepared surfaces studied here to dried gases. Reducing the water content in our gas delivery system has not been successful so far for technical reasons. Although we have observed the presence of oxygen in XPS and the crystalline structure in STM which has the same unit cell as gold oxide, this does not yet confirm that gold is in a non-metallic oxidation state during the reaction as proposed in Ref. [159]. The presence of oxidized gold in a spectroscopic gold signal would be the only direct evidence that an oxidized gold species is present during the reaction and thus

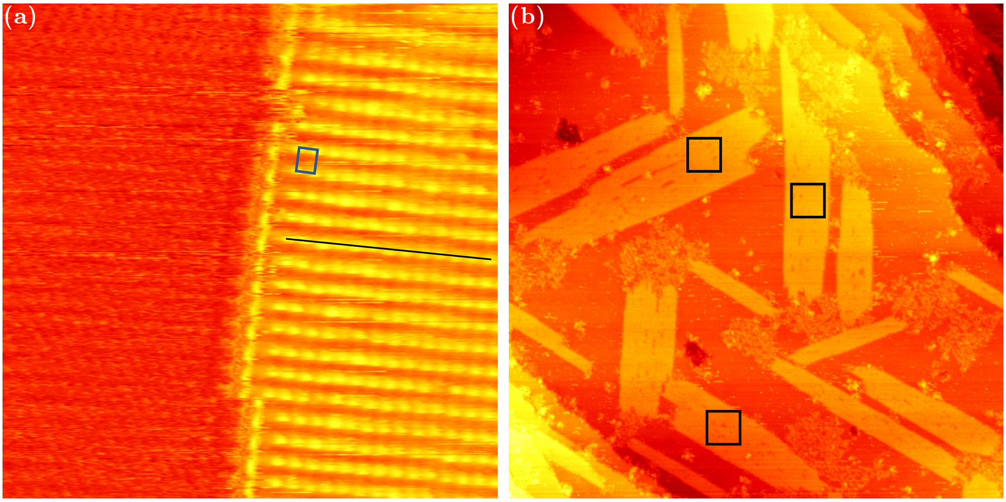

Figure 4.12: (a) 10 nm x 10 nm STM image of O/Au(111) prepared using a hot tungsten filament in oxygen background and subsequently exposed to 1 bar O_2 for several hours. The rectangular unit cell of gold oxide is marked in blue. Following the black line, deviations from the unit cell can be seen, which are discussed in Section 4.5.2. (b) 140 nm x 140 nm STM image of the same surface showing the three possible orientations of gold oxide islands marked with black squares of 10 nm x 10 nm. The images are taken in UHV at room temperature with (a) + 0.3 V and 140 pA, and (b) + 1 V and 80 pA.

confirm that a real gold oxide and not just an adsorbed oxygen species has been observed here. As the coverage of the surface oxide is limited to less than a monolayer, a highly surface-sensitive measurement is needed to distinguish the oxidized gold peak from the bulk metallic gold peak stemming from the substrate. This could be achieved using synchrotron XPS. As atomic oxygen or ozone is necessary to form the oxide in UHV, studying its formation under CO oxidation conditions will require near-ambient pressure XPS.

4.5 Supplemental Information

4.5.1 Gold Oxide Formed from Atomic Oxygen

For comparison to the surfaces studied above, one gold sample was oxidized in O_2 after depositing a seed of atomic oxygen. In this case a tungsten filament facing the surface was turned on in an oxygen background on the order of $1{\cdot}10^{-5}$ mbar for 75 min before exposure to atmospheric pressures of O_2. As shown in Figure 4.12(a), this leads to the formation of the same structure as described in Section 4.3.1 as evidenced by the same

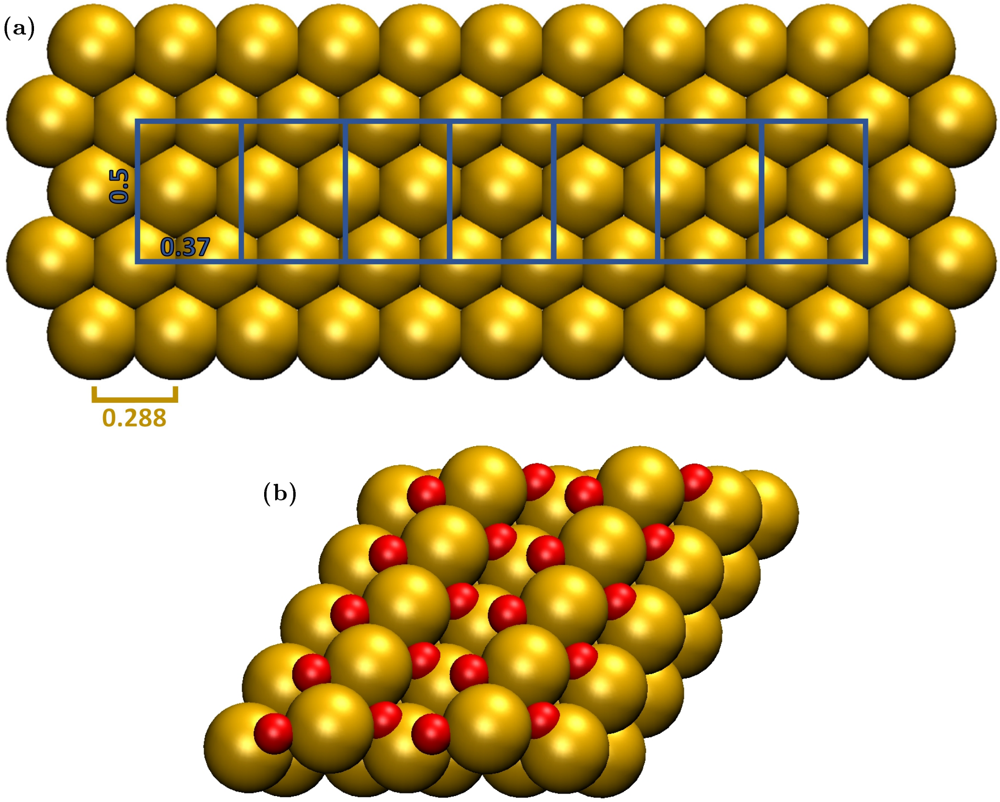

Figure 4.13: (a) Comparison of the measured gold oxide unit cell to the unit cell of the Au(111) substrate. Lengths in nm. (b) Proposed structure of the surface gold oxide showing gold atoms in gold and oxygen atoms in red.

rectangular unit cell. In the larger overview in Figure 4.12(b), it can be seen that the use of an atomic oxygen seed allows for the growth of gold oxide islands which are not connected to a step. In this case, the three possible orientations of the rectangular gold oxide unit cell on top of the hexagonal unit cell of the gold substrate can be seen.

4.5.2 Structure of the Gold Oxide

On a larger scale, the crystalline gold oxide shows slight deviations from the unit cell measured in Section 4.3.1: When following the black lines drawn in Figures 4.2(b) and 4.12(a) parallel to the short side of the gold oxide unit cell, it can be seen that the brightest spots are not always centered on this line but some appear slightly above or below the line. This can be explained by comparing the measured gold oxide unit cell to the unit cell of the Au(111) substrate as is done in Figure 4.13(a). The long side of the measured oxide unit cell of (0.50 ± 0.07) nm agrees with the shortest distance between two gold atoms in the vertical direction in 4.13(a). However, the short side of the measured oxide unit cell of (0.37 ± 0.03) nm does not match with the substrate unit cell. This indicates that the actual unit cell of the gold oxide including the Au(111) substrate is larger and contains the measured 0.5 nm x 0.37 nm unit cell multiple times. Figure 4.13(a) shows that a reasonable agreement with the substrate can be achieved when the actual gold oxide unit cell is at least seven times as long as the measured gold oxide unit cell.

Despite the actual unit cell not being known unambiguously, we want to offer a rough idea of the structure that the gold oxide could have. Inspired by similar surface oxide structures on Pt(111) [192,193] this structure is given in Figure 4.13(b). Rows of gold atoms (gold) are lifted out of the surface with oxygen atoms (red) on either side.

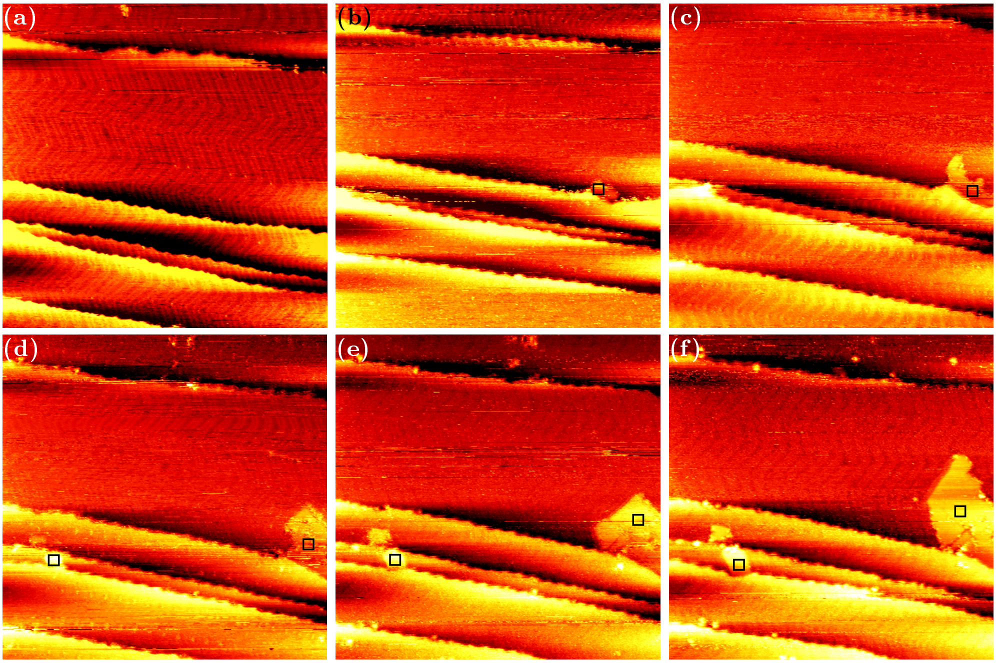

Figure 4.14: 160 nm x 160 nm STM images of Au(111) in 0.2 bar CO at (a) 0 min, (b) 2.2 min, (c) 4.8 min, (d) 13.1 min, (e) 17.5 min, and (f) 24.1 min since the start of the exposure. All images are taken with − 1 V and 50 pA. No more than five horizontal lines were removed from each of the images. A global plane filter which does not reflect the step edges correctly was chosen because it allows for a clearer visibility of the herringbone as well as the gold oxide island on the largest terrace in the image. Islands of gold oxide are marked with a black square of 5 nm x 5 nm.

4.5.3 Formation of the Gold Oxide

Figure 4.14 shows the formation of a gold oxide island on Au(111) in 0.2 bar CO. Upon introducing the gas to the reactor the gold oxide (marked with black squares) starts to grow almost immediately, starting from the step edge. The island on the lower right grows primarily in the direction towards the upper left corner of the images whereas it does not grow significantly in the orthogonal direction anymore from (d) on. In most cases where no step edges or nanoparticles limit the available space, we observe gold oxide islands which are longer parallel to the long side of the rectangular unit cell, which indicates a preferred growth direction.

The growth seen from Figure 4.14(a) to (f) takes place within 24 min. It would be interesting to see whether this growth speed is limited by the low oxygen pressure present here or by other factors. Unfortunately, observing the formation in situ was so far only possible in pure CO and not when significant amounts of oxygen are present. We attribute this to a different interaction of the gases with the tip of the scanning tunneling microscope. Whereas the CO can surely adsorb on the platinum iridium tip it does not seem to influence the imaging too much. On the other hand, oxygen might oxidize the tip and roughen it which could explain a strongly diminished resolution observed here. Images taken in O_2 often show that multiple points on the tip tunnel at the same time.

4.5.4 Carbon Structures after CO Exposure

On clean as well as contaminated Au(111), structures form during CO exposure which are not present after exposure to the reaction mixture. The first of these structures is marked with white circles in Figures 4.5(b) and 4.11(b). It can be seen over the entire terrace suggesting that it is unrelated to the formation of the gold oxide islands. Taking a closer look in Figure 4.15, regular lines are visible in this structure. It strongly resembles the carbon film on Pt(111) observed by Starr et al. (Figure 1(c) in Ref. [194]). We measure the line-to-line distance in their image as 0.33 nm, which is the graphite layer distance [195] and thus supports the interpretation of Starr et al. that their film consists of small graphite domains. In contrast, the line-to-line distance in our structure is (0.51 ± 0.02) nm, as concluded from averaging over multiple images. The height with respect to the gold substrate appears between 0.06 nm and 0.15 nm in the STM. As can be seen in the height profile in Figure 4.15, multiple layers of the smallest height of 0.06 nm seem to be present. The line-to-line distance we measure agrees with the line-to-line distance of diamond(100)-2x1 [196,197]. The measured layer thickness is somewhat lower than the step height of diamond(100)-2x1, which is 0.089 nm as calculated from the crystal structure [198] and observed in Ref. [196]. However, the

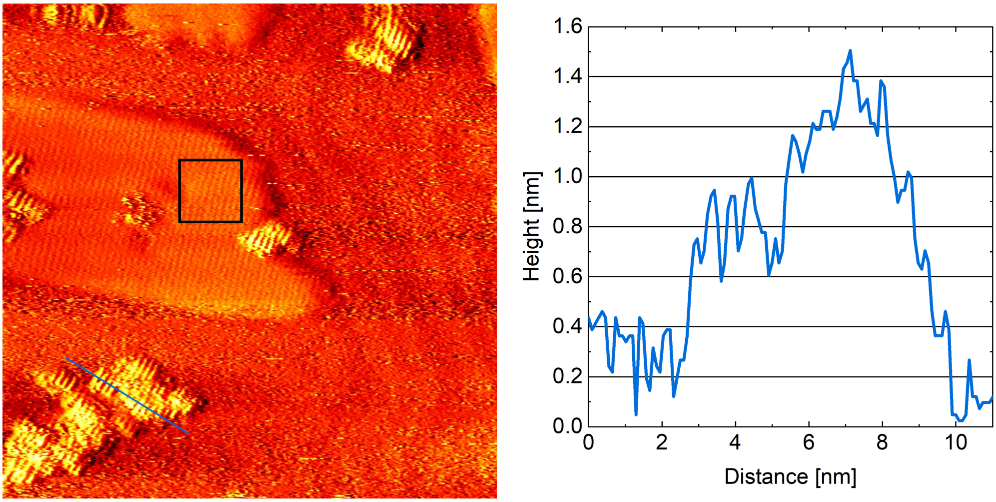

Figure 4.15: 40 nm x 40 nm STM image of contaminated Au(111) after exposure to 0.2 bar CO for 1 h. The image is taken in UHV at room temperature with − 1 V and 50 pA. For better visibility of all structures the image was merged with its derivative. A black square of 5 nm x 5 nm marks a gold oxide island. Another structure formed appears yellow. A height profile through one of these is drawn on the right and is indicated by the blue line in the STM image.

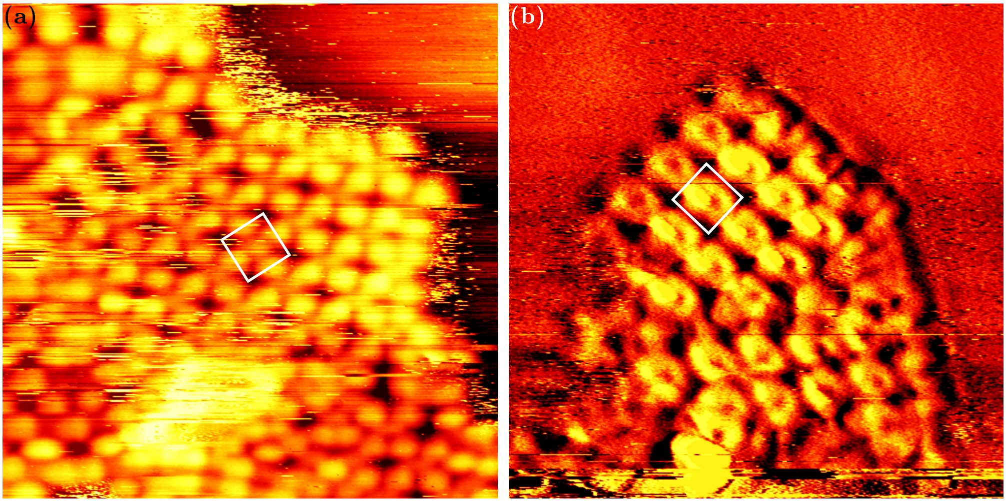

Figure 4.16: 10 nm x 10 nm STM images of the second structure observed after CO exposure showing the two different appearances in (a) and (b). The unit cell is marked with a white square. The images are taken in UHV at room temperature with (a) − 1 V and (b) − 1.5 V, and 50 pA. For better visibility of the details inside the unit cell the image in (b) is merged with its derivative in a ratio of 4:1.

height could be underestimated in our STM, especially as the structure is likely not completely conductive [199]. There is some evidence that on Au(111) diamond should rather grow as the diamond(111) orientation [200,201]. On the other hand, theory suggests that diamond(111) does not interact strongly with gold [202], which could allow for other orientations to grow as well. Overall, we have to conclude that further investigation is needed to unambiguously identify this structure.

As to the origin of the carbon, direct dissociation of adsorbed CO can be excluded as the atomic oxygen would form gold oxide next to every carbon structure. However, dissociation via another route which does not leave atomic oxygen on the surface cannot be excluded. Additionally, the hydrocarbon background from the CO bottle could cause the deposition of carbon. A clear conclusion cannot be reached without further research into the formation of the structure, which could be done by intentionally exposing the clean Au(111) surface to different sources of carbon.

The second structure observed is shown in Figure 4.16. It can appear in two different shapes in the STM (shown in (a) and (b)), which have the same squared unit cell with a length of (0.99 ± 0.02) nm in both directions (see white squares in Figure 4.16), as concluded from averaging over multiple images. This structure is only found connected to a step edge, suggesting that it is formed via a different mechanism than the first structure. However, an adsorption structure of CO itself can be excluded as it should not be stable in UHV at room temperature for several hours [176–179]. No similar adsorption structures on Au(111) could be found in the literature. Westenfelder at al. [203] have grown gold carbide layers on a graphene sheet decorated with gold nanoparticles. They exhibit an fcc(100) structure in which the quadratic unit cell has a length of (0.335 ± 0.01) nm in both directions. Taking the standard deviations into account the length of the unit cell measured here is in agreement with three times the length of this gold carbide unit cell. Westenfelder et al. imaged the carbide layers with transmission electron microscopy, in which the carbon atoms might not be visible between the gold atoms. As both gold and carbon are visible in STM, the larger unit cell measured here could be due to variations in the location of the carbon atoms. However, this would disagree with the three possible structures that Westenfelder at al. propose for the gold carbide. As it preferentially grows on the Au(111) facet of gold nanoparticles, the carbide would likely be stable on a Au(111) single crystal surface. However, it is formed at temperatures close to the melting point of gold in Ref. [203] such that it is unclear whether a formation via the same mechanism would be possible at room temperature. Overall, more investigation is needed for a clear identification of the structure observed here. Specifically, the dependence on bias voltage in STM and the elemental composition in spectroscopy should be studied. Observing the formation in CO at higher temperatures as well as studying the thermal stability of the structure in UHV would allow for a more conclusive comparison to the gold carbide observed in Ref. [203].

As both structures observed here do not form in the same partial pressure of CO when O_2 is present as well, the oxygen is either able to suppress the formation or remove the structure after formation. Further experiments are needed to clarify this. Additionally, the water content in the CO used here could play a role, which should be investigated by using dried CO.

Chapter 5

Spectroscopy of Co(0001) during Fischer-Tropsch Synthesis

5.1 Introduction

The urgent need for sustainable means of transportation is obvious and reflected in increasingly strict regulations [204]. For certain applications such as in aviation and maritime shipping, the use of electrical motors will not be feasible in the near future. Here a sustainable solution, which does not require new infrastructure and vehicles, is the use of synthetic Fischer-Tropsch fuels. During Fischer-Tropsch synthesis (FTS) syngas, a mixture of H_2 and CO, is converted into long-chain hydrocarbons [205]. The syngas can stem from natural gas, oil, or renewable feedstocks such as biomass. Additionally, there is a strong research effort [206,207] to enable capture and conversion of CO_2 for the production of syngas, thereby closing the carbon cycle. The synthetic production of fuels cannot only reduce CO_2 emissions compared to conventional fuels, but the resulting fuel is cleaner as well, leading to less CO, NO_x, SO_x, and particulate matter emission than conventional diesel [208,209].

Fischer-Tropsch catalysis on a large industrial scale has been demonstrated [210,211]. Typical conditions for so-called low-temperature FTS are 30 bar gas pressure and 200 °C to 240 °C catalyst temperature [212]. Compared to iron-based catalysts, cobalt supported on various oxide supports shows higher activity and selectivity to linear alkanes [213–215]. However, cobalt catalysts are prone to multiple deactivation mechanisms, which are being researched intensively [216,217]. Among these are carbon deposition [218,219], sulfur deposition [220,221], and the oxidation of the cobalt [222–225]. Whereas there seems to be a consensus in this literature that cobalt oxide is not active, the ability of cobalt to oxidize under Fischer-Tropsch conditions has been doubted.

As oxidation states are highly sensitive to gas pressure and composition, in situ spectroscopy studies are indispensable. The use of near-ambient pressure X-ray photoelectron spectroscopy for the study of late transition metal catalysts has been reviewed recently [66]. Wu et al. [226] have used this technique to determine that, at pressures on the order of 0.1 mbar, CO reduces an oxidized cobalt foil at lower temperatures than hydrogen. In a reaction mixture of 1 CO + 1 H_2 the surface stayed metallic at temperatures above 225 °C suggesting that an oxidation of the foil by (background or product) water does not take place under these conditions. Additionally, they have observed carbide formation from CO at temperatures as low as 57 °C. However, it has been shown that the oxidation behavior of cobalt can depend significantly on the crystallinity, structure, and support of the cobalt sample used [227,228]. This suggests that studies on single crystals are a small but relevant contribution to completely understanding the oxidation behavior of cobalt. Kizilkaya et al. [229] find that H_2 more readily removes oxygen from Co(0001) than CO. Although this suggests the opposite behavior of Co(0001) compared to Co foil [226], the significantly different pressure regime of 10^{-5} mbar used in Ref. [229] compared to the mbar range used in Ref. [226] could be responsible as well.

Combining the use of a single crystal with higher gas pressures, we performed near-ambient pressure X-ray photoelectron spectroscopy on a Co(0001) model catalyst. In the following we report on the cleanliness of the as-prepared crystal in UHV (Section 5.3.1), investigate the role of background water for the oxidation of Co(0001) in 0.25 mbar H_2 (Section 5.3.2), and compare this to the behavior in 0.25 mbar CO (Section 5.3.3). Using a theoretical model to convert measured intensities to coverages on the Co(0001) surface, we quantify the amount of surface area covered by adsorbed oxygen, different carbon species, and sulfur in H_2 (Section 5.3.4), CO (Section 5.3.5), and reaction conditions with a H_2-to-CO-ratio of 2:1 and 4:1 (Section 5.3.6).

5.2 Materials and Methods

5.2.1 Setup and Sample Preparation

The measurements presented in this chapter were performed at beamline 9.3.2 [230] of the Advanced Light Source, Berkeley and at the HIPPIE beamline [231] of Max IV Laboratory, Lund. The higher flux available at MaxIV allowed for resolving a larger number of carbon and oxygen species as exemplified in the following section. Whereas the gas exposure at ALS was realized by filling a vacuum chamber via one leak valve for each gas, the HIPPIE beamline at MaxIV uses a high-pressure cell (similar to the one described in Ref. [232]), allowing for more precise setting of flows and pressures as well as faster changes in gas composition. At the ALS we used hydrogen of purity 6.0 and CO of purity 3.0 whereas H_2 4.7 and CO 3.7 were available at MaxIV. A liquid nitrogen trap was used on the hydrogen line for most of the measurements presented here. Independent of the use of the trap, the water content was below the detection limit of QMS measurements performed at MaxIV. The effects of the different gas purities and the trap are investigated in Section 5.3.2. Table 5.1 shows the water and oxygen background expected in the different bottles.

Table 5.1: Expected level of contaminants in the different gas bottles that were used [233–236]. As the values for H_2 4.7 could not be found, they are estimated as the values for H_2 5.0.

Gas	Purity	Supplier	H_2O Content [ppm]	O_2 Content [ppm]
H_2	6.0	Praxair	≤ 0.5	≤ 0.1
H_2	4.7	Air Liquide	≤ 3	≤ 2
CO	3.0	Praxair	≤ 10	≤ 10
CO	3.7	Air Liquide	< 5	< 10

The Co(0001) single crystals were purchased from SPL. They were prepared by cycles of argon ion sputtering with 1 kV acceleration voltage and subsequent annealing to 590 K in UHV. The annealing temperature is limited by the phase transition from an hcp to an fcc crystal structure [237]. To additionally prevent contaminants in the bulk from reaching the surface the annealing temperature is 5 K to 10 K lower in the last cleaning cycle and the sample is kept at maximally 573 K or 300 °C during all experiments.

5.2.2 Resolved Species and Peak Fitting

The binding energy axis of the oxygen, carbon, and sulfur spectra was calibrated according to the metallic Co $3p_{3/2}$ peak at 59.3 eV [238] measured after every change of the photon energy. After applying this calibration, detected peaks which deviate less than ± 0.1 eV between different measurement conditions are identified as being the same species. All peak fits are done in CasaXPS 2.3.19 [239] using a Shirley background. The Co 3p peak is fitted using a metallic peak consisting of an asymmetric main peak of the shape LA(1.1,1.5,3) as well as a plasmon loss peak of shape GL(30) fixed at + 3 eV and 12.2 % peak area with respect to the main peak. Both these peaks were used for the $3p_{3/2}$ as well as the $3p_{1/2}$ part of the doublet with a fixed doublet splitting of 1.2 eV. Due to limited literature on Co 3p peak positions and fitting [238,240], this method is based on the fitting of the Co 2p peak as described below and was adjusted until a satisfactory fit for the metallic surface was found. However, for all measurement sets where the Co 3p peak was used this shape was sufficient for a satisfactory fit such that no cobalt oxide contribution needs to be considered here and only the total area underneath the metallic Co 3p doublet is relevant for the further analysis. The Co 2p peak was fitted with a main metallic peak at 778 eV of asymmetric shape LA(1,2.25,3) and two plasmon loss peaks of shape GL(30) fixed at + 3 eV and + 5 eV and 6.4 % and 2.1 % peak area with respect to the main peak, respectively. This is based on the Co 2p fitting presented in Refs. [226,241] and adjusted until a satisfactory fit for a measurement on metallic cobalt is reached. Additionally, four oxidized peaks of shape GL(40) at positions + 1.8 eV, + 4.1 eV, + 7.8 eV, and + 10 eV with respect to the metallic main peak are necessary for some measurements (see Section 5.3.2). As both CoO and Co_3O_4 cause a number of Co 2p contributions in the same binding energy region [241], an exact identification is complex. However, CoO has been identified on Co(0001) using in situ SXRD [242] under similar conditions as used here, which is thus the more likely candidate. Figure 5.1 shows an example fit where both metallic and oxidized cobalt are present.

For the O 1s measurements taken at the ALS, we identified oxygen peaks at 529.7 eV as adsorbed atomic oxygen O(ad), 530.8 eV as adsorbed hydroxyls OH(ad), and 532.1 eV

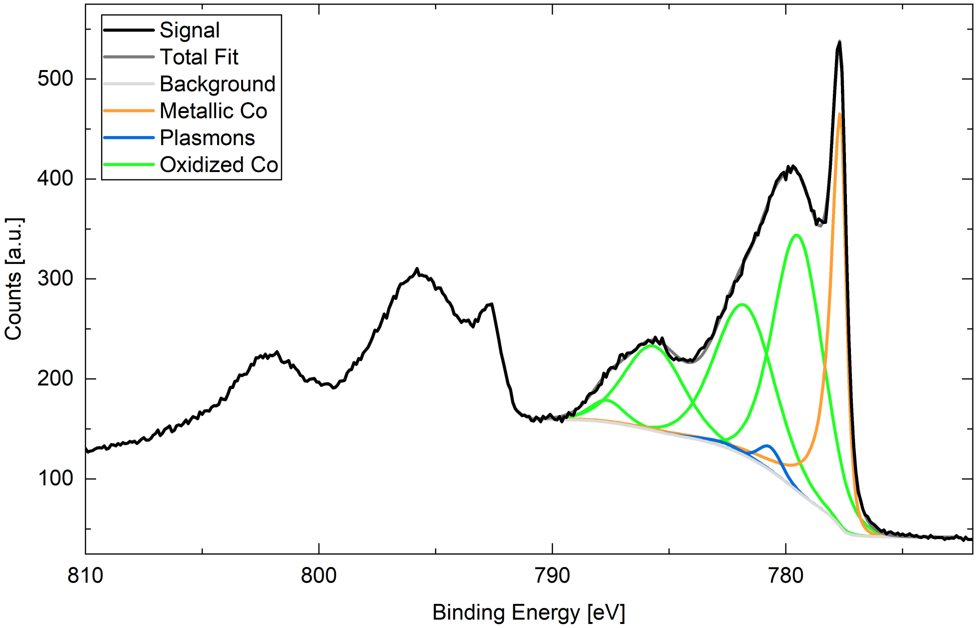

Figure 5.1: Co 2p area measured on Co(0001) in 0.25 mbar H_2 at 220 °C surface temperature showing all peaks necessary for a satisfactory fit of the 3/2 part of the doublet. This surface is partially oxidized, which was likely caused by a temporary technical problem with the liquid nitrogen trap that was used on the hydrogen line. For details about the oxidation behavior of Co(0001) in H_2 see Section 5.3.2.

as adsorbed carbon monoxide CO(ad) by comparison with relative positions given in literature [226,241,243]. These are fitted with line shapes of GL(50) and GL(70) (only adsorbed CO) and fixed binding energy distances. In the same manner [226,243] we identify carbon peaks as carbide or carbon atoms C at 283.5 eV, hydrocarbons C_xH_y at 284.9 eV, and adsorbed carbon monoxide CO(ad) at 286.0 eV in the C 1s peak. The hydrocarbon contribution shifts to 285.6 eV only in UHV, which might indicate that a different type of hydrocarbon is predominantly present here compared to reaction conditions.

In the measurements done at MaxIV a larger number of species can be resolved in the C 1s peaks. An example fit with all necessary peaks is shown in Figure 5.2. The adsorbed CO is split up into four contributions: Two peaks at + 2.69 eV and + 1.50 eV with respect to the main CO(ad) peak can be identified as adsorbed CO in the presence of adsorbed atomic oxygen as they appear in agreement with the appearance of O(ad) in the O 1s signal. The main CO(ad) peak at 286.0 eV is best fitted with a slightly asymmetric LA(1.8,2.5,0) shape. Additionally, a small contribution at − 0.65 eV from the

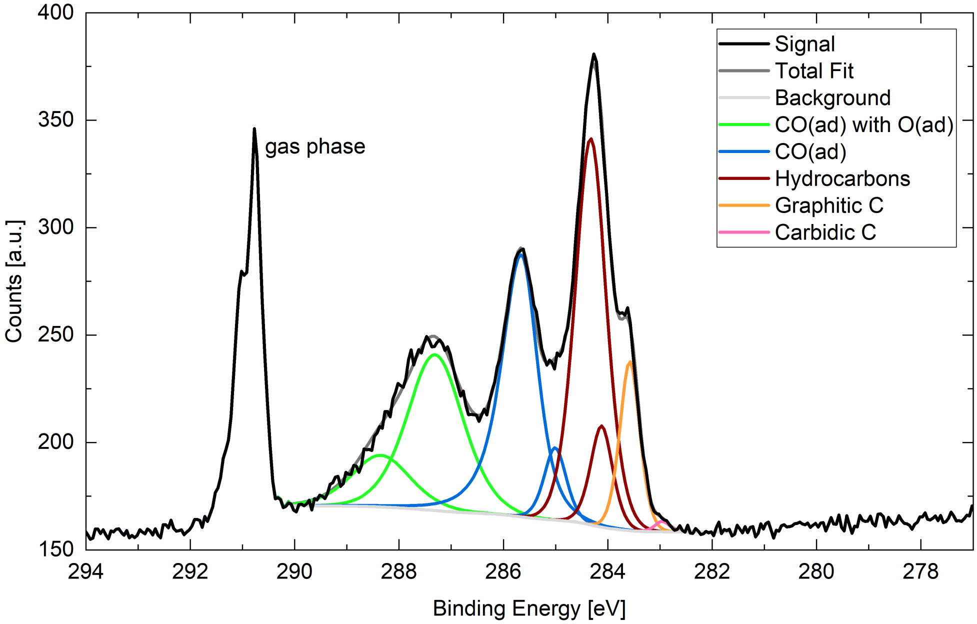

Figure 5.2: C 1s area measured on Co(0001) in 0.25 mbar CO at 190 °C surface temperature showing all peaks necessary for a satisfactory fit.

main CO(ad) peak could stem from a different adsorption site on the surface [244,245] compared to the main CO peak, but cannot be unambiguously identified on the basis of current literature or our measurements. The hydrocarbon peak is split up into two contributions at a distance of 0.2 eV from each other. It is likely that a number of different hydrocarbons are present, such that these two different peaks are necessary for a satisfactory fit. In comparison with literature [246–248] the carbide/atomic carbon contribution is split into a graphitic carbon/multiple carbon atom contribution at 283.9 eV and a carbidic/single carbon atom contribution at − 0.37 eV with respect to the first. All C 1s peaks (except the main CO(ad) peak) were fitted satisfactorily with a GL(50) shape. The relative binding energy positions of all contributions are fixed and the FWHM is restricted to the same value for every measurement of the same peak for consistency.

As in the C 1s peak, the adsorbed CO contribution to the O 1s peak is split into two parts (with and without co-adsorbed O, respectively) with a binding energy difference of 0.65 eV to each other. This can be seen in the example fits in Figure 5.3 where (a) some or (b) all of the adsorbed carbon is influenced by the adsorbed oxygen. In some conditions one additional small contribution to the O 1s signal is detected at − 1.7 eV with respect to the O(ad) contribution. It might stem from a different O

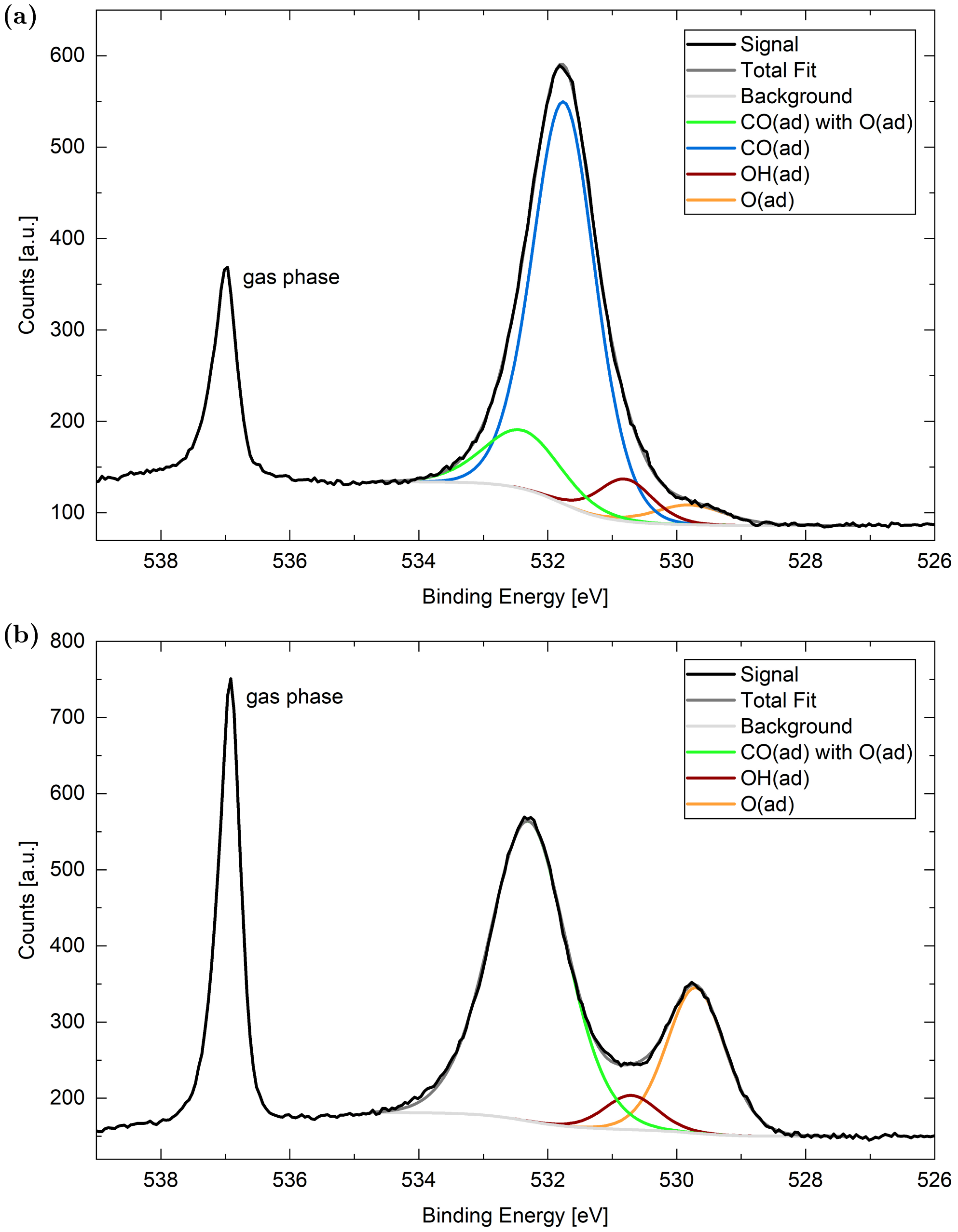

Figure 5.3: O 1s area measured on Co(0001) in 0.25 mbar CO at (a) 220 °C or (b) at 120 °C surface temperature showing the peaks necessary for a satisfactory fit.

adsorption site or a co-adsorbate, but cannot be unambiguously identified on the basis of current literature and our measurements. The area underneath this peak is therefore added to the adsorbed oxygen peak area. The adsorbed CO contribution in the O 1s signal can overlay with a contribution caused by molecularly adsorbed H_2O. As the exact binding energy position of the adsorbed water might vary significantly depending on co-adsorbates, the oxidation state of the cobalt, and the amount of water [226,241,249], the CO and the H_2O contribution cannot be easily distinguished during peak fitting. However, on clean Co(0001) as well as on O(ad)/Co(0001) in UHV at all investigated temperatures, it can be expected that water, if it adsorbs, adsorbs dissociatively [249,250]. Therefore, the CO contribution in the O 1s signal of sets of measurements taken in UHV can be clearly identified without overlay with any signal stemming from molecular water. By comparing this CO contribution in the O 1s signal to the CO contribution in the C 1s signal from the same set of measurements we thus have a measure to evaluate whether molecular water is present on the surface. In most conditions investigated here, the ratio of the two different CO contributions is comparable to the ratio in UHV such that no molecularly adsorbed water needs to be taken into account during the analysis. One exception are measurements on an oxidized Co(0001) surface presented in Sections 5.3.2 and 5.3.4.

As no different sulfur species are resolved, the area under the S 2p peak can be determined from only the background subtraction in CasaXPS without a detailed fit. Last, when potassium was detectable, the K 2p peak partially overlapped with a second harmonic peak of the Co $2p_{3/2}$ such that a proper fit of both at the same time was necessary to determine the area underneath the K 2p doublet. GL(20) shapes with a doublet splitting of + 2.7 eV were then used for the K 2p contribution.

5.2.3 Converting Peak Areas to Coverages

Model

To convert the measured peak ares into surface coverages of all adsorbates, a mathematical description of the measured intensities is needed. In the straight line approximation [251], which only takes inelastic scattering of electrons into account, we first describe a homogeneous sample of a material i. In this case the amount of photoelectrons produced by a specific orbital of species i in a depth δ and detected outside the surface is

$$I_i(\delta) = \phi \sigma_i W_i N_i P \cdot e^{-\delta/\lambda_i} \equiv k_i \cdot e^{-\delta/\lambda_i} \tag{5.1}$$

with the photon flux $\phi(E_p)$ at photon energy E_p, the cross section $\sigma_i(E_p)$ and asymmetry parameter W_i of the probed orbital of species i for the same photon energy, the number of atoms of species i per volume N_i, the spectrometer efficiency $P(E_{kin})$ for

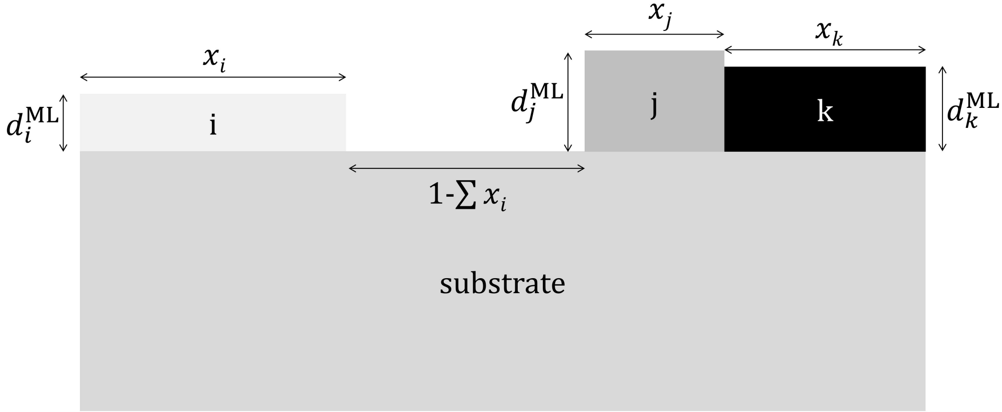

Figure 5.4: Illustration of the model assumed for coverage calculations. Explanation see text.

detection of electrons with the kinetic energy E_{kin}, and the inelastic mean free path $\lambda_i(E_{kin})$ of the same electrons in material i.
Integrating Equation 5.1 over a homogeneous, clean, and macroscopically thick ($\delta \to \infty$) cobalt substrate results in the total contribution from the specific orbital and thus the area under the measured peak of

$$I_{\mathrm{Co}}^{\mathrm{sub}} = k_{\mathrm{Co}}\lambda_{\mathrm{Co}}. \tag{5.2}$$

Figure 5.4 illustrates how this is extended to include different adsorbed species. For an adsorbate i covering an area x_i, with $0 \leq x_i \leq 1$, Equation 5.1 has to be integrated over the thickness of the first monolayer d_i^{ML} resulting in

$$I_i^{\mathrm{ad}} = x_i \cdot k_i\lambda_i \left(1 - e^{-d_i^{\mathrm{ML}}/\lambda_i}\right). \tag{5.3}$$

For a part of the cobalt substrate which is covered with an adsorbate i the substrate intensity given in Equation 5.2 is attenuated due to the adsorbate by a factor of $e^{-d_i^{\mathrm{ML}}/\lambda_i}$. On the other hand, the area $1-\sum_i x_i$ of the cobalt follows Equation 5.2 without attenuation. Notice that this is only valid if all possible adsorbates i are taken into account. The total cobalt signal is then

$$\begin{aligned} I_{\mathrm{Co}} &= k_{\mathrm{Co}}\lambda_{\mathrm{Co}} \cdot \left(\left(1 - \sum_i x_i\right) + \sum_i x_i \cdot e^{-d_i^{\mathrm{ML}}/\lambda_i}\right) && (5.4)\\ &= k_{\mathrm{Co}}\lambda_{\mathrm{Co}} \cdot \left(1 - x_j \sum_i (x_i/x_j) \cdot \left(1 - e^{-d_i^{\mathrm{ML}}/\lambda_i}\right)\right) && (5.5) \end{aligned}$$

where the second notation is simply for the purpose of convenience for the following steps. With the above equations we can express the ratio of intensities of two different adsorbates I_i/I_j as well as the ratio of the intensity of an adsorbate and the cobalt substrate I_i/I_{Co} and subsequently solve for the following equations.

$$\frac{x_i}{x_j} = \frac{I_i}{I_j}\frac{k_j\lambda_j}{k_i\lambda_i}\frac{\left(1-e^{-d_j^{\mathrm{ML}}/\lambda_j}\right)}{\left(1-e^{-d_i^{\mathrm{ML}}/\lambda_i}\right)} \tag{5.6}$$

$$x_j = \left(\frac{I_{\mathrm{Co}}}{I_j}\frac{k_j\lambda_j}{k_{\mathrm{Co}}\lambda_{\mathrm{Co}}}\left(1-e^{-d_j^{\mathrm{ML}}/\lambda_j}\right)+\sum_i (x_i/x_j)\cdot\left(1-e^{-d_i^{\mathrm{ML}}/\lambda_i}\right)\right)^{-1} \tag{5.7}$$

We have found it most convenient to first calculate x_i/x_j for all x_i and one specific adsorbate j using Equation 5.6, then calculating the x_j from I_{Co}/I_j and all (x_i/x_j) using Equation 5.7, and finally getting all other x_i as $x_i = (x_i/x_j)\cdot x_j$.

Multiple Layers

One complication in applying this model in our scientific case is that over time the overlayer of one of the adsorbed materials, the hydrocarbons, can become thicker than one monolayer under specific conditions (see Section 5.5.1). This introduces another unknown, the height of that hydrocarbon overlayer. To take this into account the sum of all coverages $\sum_i x_i$ is monitored. Once the result would be larger than 1 the equations as above do not hold anymore and the calculation needs to be adjusted slightly. For this the coverage of an adsorbate for which the measured intensity does not significantly change over time (anymore) in these conditions, we used oxygen or sulfur, is fixed to the last calculated value. All other coverages are calculated as above and the coverage x_{hc} of the hydrocarbons is then $1-\sum_{i\neq \mathrm{hc}} x_i$. Now the ratio of the oxygen or sulfur and the hydrocarbon intensities can be used to calculate the height D_{hc} and thus number of monolayers of the hydrocarbons as

$$D_{\mathrm{hc}}/d_{\mathrm{hc}}^{\mathrm{ML}}. \tag{5.8}$$

We finally plot the corresponding number of monolayers that were present if it were the only adsorbate on the surface $X_{\mathrm{hc}} \equiv x_{\mathrm{hc}}\cdot D_{\mathrm{hc}}/d_{\mathrm{hc}}^{\mathrm{ML}}$. As this procedure assumes that all of the hydrocarbons are layered to the same height D_{hc} on only one specific fraction x_{hc} of the substrate surface area, this model is limited and can easily become inaccurate, especially for large coverages. The manner in which the hydrocarbons grow, layer-by-layer or three-dimensional growth as well as potentially on top of other adsorbates, is unknown and neglected here.

In the case of the oxidation in H_2 at temperatures below 220 °C (see Section 5.3.2) the model results in (oxygen) coverage values large than 1 as well. As here not only the adsorbate O(ad) is present in multiple layers but a cobalt oxide is growing, the model cannot be extended in a similar fashion and the situation would require a more complex model making assumptions about the fashion in which this oxide grows, which is outside the scope of this thesis. Therefore, the results of our model for this case are intentionally reported only as relative coverages of the different adsorbed species instead of absolute coverages and can only be discussed in a qualitative manner.

Estimating Parameters

The photon flux $\phi(E_p)$ was recorded during the measurements after every change of the photon energy (ALS) or read from a pre-recorded flux curve (MaxIV). The cross sections $\sigma_i(E_p)$ of Co 2p, Co 3p, O 1s, C 1s, and S 2p for the specific photon energies were determined using Ref. [252] and are displayed in Table 5.2. The asymmetry parameters W_i are equal to 1 as the setups used here adhere to the "magic angle" in XPS [64]. As only ratios of intensities measured in the same geometry and at the same electron kinetic energy are compared, the spectrometer efficiency $P(E_{kin})$ does not need to be known. The inelastic mean free path was calculated according to the TTP-2M equation with the help of the NIST Database 71 Version 2.1 [253]. For the bulk cobalt metal the mean free path can be taken directly from the database. For all adsorbates the calculation requires an estimation of the mass density m_i, the number of valence electrons V of the material (contributing to electron loss), and a rough estimate of the bandgap E_g of the material. A recommendation for the choice of V is given in the manual to the NIST Database [253]. For estimation of the mass density, the number of atoms per volume N_i, and the thickness of one monolayer d_i^{ML} we distinguish two different cases.

Most measurements shown in this thesis are of the first case, in which less than a monolayer of an adsorbate is expected. Then the structure likely differs significantly from any bulk structure of the adsorbate and the crystal structure of the Co(0001) substrate thus needs to be taken into account. In this case the topmost cobalt layer has to be included in the calculation of λ and thus contributes to the mass density, the valence electrons, and the bandgap. Theory supplies values for the Co-O distance for adsorbed O and OH [254], Co-C distance for adsorbed C [255], and the Co-S distance for sulfur [256], which are used to estimate the monolayer thicknesses. Together with the cobalt crystal structure [257] these are used to calculate the mass density and number of probed atoms per volume geometrically. The rough bandgap estimations were done using literature values for cobalt oxide [258] as well as different sulfides and carbides [259]. For the case of CO, the measurement of the C 1s signal as well as the O 1s signal are available to include into the model. Based on theory literature [260] we assume an upright adsorption with the carbon atoms towards the surface and use the Co-C as well as the C-O distance for the layer thicknesses. These are used separately

Table 5.2: Estimated parameters for the calculation of coverages. Explanation and sources see text.

Species	Peak	E_p [eV]	σ [Mbarn]	d^{ML} [nm]	N [(nm)$^{-3}$]	m [g·(cm)$^{-3}$]	V	E_{g} [eV]	λ [nm]
O	O 1s	730	0.2551	0.18	99.8	5.89	15	2.5	0.685
OH	O 1s	730	0.2551	0.20	92.5	5.75	16	2.5	0.697
CO	O 1s	730	0.2551	0.12	152.7	5.27	19	3	0.709
CO	C 1s	480	0.2987	0.18	103.0	5.27	19	3	0.709
C	C 1s	480	0.2987	0.21	87.3	5.2	13	3	0.299
C_xH_y ($<$ 1 ML)	C 1s	480	0.2987	0.34	50.4	1.19	86	14.5	2.278
C_xH_y (bulk)	C 1s	480	0.2987	0.34	32.5	0.76	86	14.5	2.371
S	S 2p	365	1.2080	0.16	114.6	57.6	15	3	0.592
Co	Co 3p	260	0.7197	0.21	90.1	8.8	9		0.544
Co	Co 2p	980	0.7651	0.21	90.1	8.8	9		0.544

for the calculation of N for the O 1s signal and the C 1s signal. The CO contribution in the C 1s signal is additionally calibrated to take the attenuation by the oxygen atoms on top into account. Thus, the measured intensities are divided by a factor of $\exp(-d^{\mathrm{ML}}_{(\mathrm{O\ of\ CO})}/\lambda_{\mathrm{CO}})$. However, the thickness of the whole CO molecule $d_{\mathrm{CO}} = d_{(\mathrm{C\ of\ CO})} + d_{(\mathrm{O\ of\ CO})}$ is then taken into account for the calculation of m and λ as well as the attenuation of the cobalt signal in the area covered with CO. The adsorbed hydrocarbons are a more complex case as a large number of different molecules could be present. Navarro et al. [47] investigated the Co(0001) surface using in situ scanning tunneling microscopy during FTS under similar conditions as studied here. The main product length detected on the surface was 14 carbon atoms with each molecule taking up an area of 1.8 nm by 0.46 nm and an apparent overlayer height of 0.11 nm. However, the height can be underestimated in the STM due to limited conductivity. Graphene already has a higher thickness of 0.21 nm on Co(0001) as determined by DFT [255] similar to the thickness of benzene on Co(0001) of 0.22 nm [261]. We choose a more generous estimate of 0.34 nm on the hands of the layer thickness of graphite [195]. Using the surface area taken up by one molecule and the height estimate we can again calculate m and N.

In the second case, when significantly more than a monolayer of a certain adsorbate is expected to be present, it is likely that the structure is similar to the structure the adsorbate has when it is present in bulk. This is the case for adsorbed hydrocarbons in some measurements under the conditions described in Section 5.5.1. Then literature values for E_{g} [262] and m [263] of $C_{14}H_{30}$ can be used to calculate the number of probed atoms per volume N. In this case the thickness of one monolayer is thus not needed for the calculation of N, but can be used in the last step of the calculation in Equation 5.8 in order to convert the resulting total overlayer thickness into a number of layers. We choose the same estimate of 0.34 nm as described for the first case above.

Test and Calibration

When applying this model to a series of measurements it became clear that it is not complete. A rough estimate of peak areas from a cobalt survey spectrum measured at 1130 eV photon energy shows that the order of magnitude of the Co 3p, Co 3s, and Co 4s peaks does agree with the literature values of the cross sections confirming the validity of the general approach of our model as well as the literature values. In contrast, the peak area of the Co 2p peak in the survey is at least an order of magnitude higher than expected from the cross section. This estimate was done without taking the different probing depths for the different peaks into account. As Co 2p has the highest binding energy, the probing depth is lowest such that the discrepancy should be even larger. This agrees with the discrepancy of a factor of about 50 that results from fitting detailed Co 2p and Co 3p peaks taken at the same probing depth with an electron kinetic energy of 200 eV. This value was obtained by averaging over 20 different measurements taken on different days. From these observations the following can be excluded as causes for the discrepancy: repeated changing of slits being irreproducible, the flux curve for the different photon energies being imprecise, and the same slit setting leading to varying attenuation depending on the photon energy. It is likely that the crystalline structure of the substrate, which is not taken into account in our model at all, could have a strong influence on the production of photoelectrons and the complex loss processes in the material. Investigating this further is out of the scope of this thesis.

However, it follows that the coverage model has to be complemented by experimental calibration factors for the different peaks which are measured. First, we calibrate the ratio of the O 1s and the Co 2p (or Co 3p) signal such that the adsorbed oxygen contribution in UHV corresponds to the 0.25 monolayer coverage expected when assuming maximum coverage with the 2x2 overlayer on Co(0001) [229]. The calibration factor was determined from the cleanest as-prepared sample measured in UHV. A second as clean sample measured on a different day, resulted in a calibration factor deviating from the first by 1 %, which evidences that this calibration method is reproducible. The measurements used were done at 220 °C. But, as we will show in Section 5.3.1, the measured signal of adsorbed oxygen in UHV is not temperature dependent between 140 °C and 300 °C.

Second, the C 1s to O 1s signal ratio is calibrated such that the two different CO coverages, calculated from the carbon and the oxygen signal respectively, are in agreement. This calibration factor is an average over at least 20 different measurement sets in different gas and temperature conditions. However, as explained in Section 5.2.2, the CO contribution to the O 1s signal cannot be clearly determined from measurements where molecularly adsorbed water is present on the surface. These are therefore not taken into account for the calculation of this calibration factor. In all other gas compositions the calculated ratio of the CO contributions in C 1s and O 1s roughly agrees with the ratio in UHV. Therefore, the resulting calibration factor we have used is free from the possible influence by the contribution from molecularly adsorbed water.

Third, the coverage of species calculated from peaks for which there is no calibration measurement, S 2p in our case, should be merely seen as an estimate of the order of magnitude and used for relative comparison of the coverage in different situations or changes over time rather than as an absolute value.

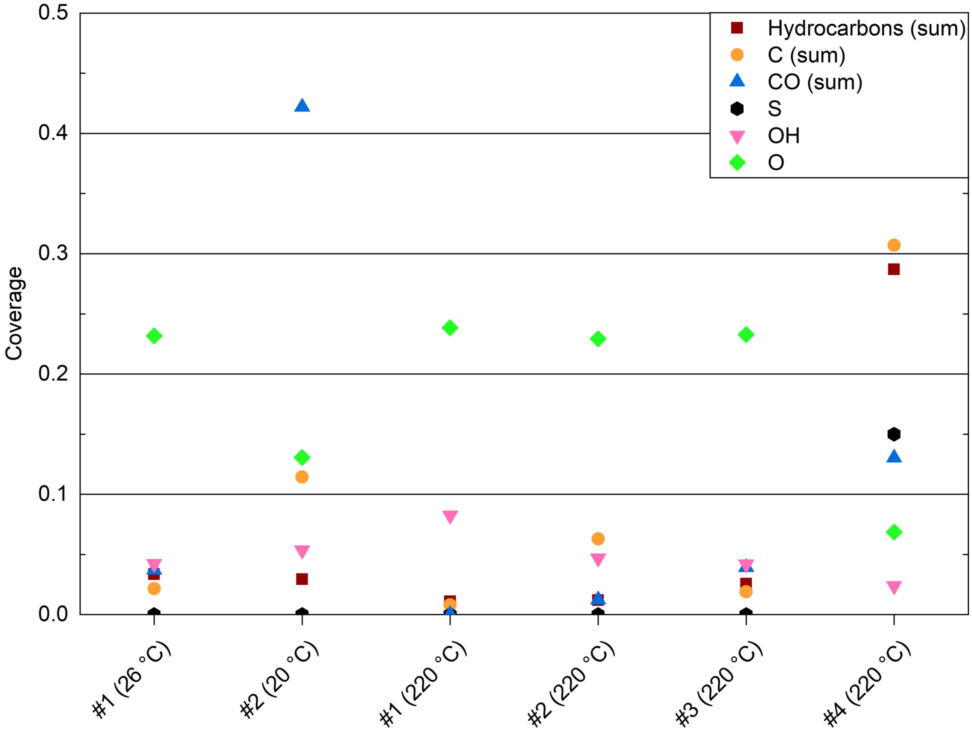

Figure 5.5: Coverages of all measured adsorbed species on four different as-prepared Co(0001) samples in UHV at roughly room temperature or 220 °C. For a better overview the different carbon, hydrocarbon, and adsorbed CO peaks are summed up to one coverage each here and are only displayed in detail in the supplemental information.

5.3 Results and Discussion

5.3.1 As-prepared Co(0001) in UHV

Figure 5.5 displays the calculated coverages comparing multiple as-prepared samples in UHV at room temperature and at 220 °C. On average the oxidized contribution in the Co 3p or Co 2p peaks measured in UHV is 3 % of the total depth of cobalt probed. The O contribution in the O 1s signal is thus mainly due to adsorbed atomic oxygen on metallic cobalt in UHV. At room temperature it is noticeable that sample # 1 has a coverage of adsorbed oxygen of 0.23, whereas sample # 2 only has 0.13. On the other hand, sample # 2 shows more adsorbed CO, 0.42 compared to 0.04 CO on sample # 1, which leaves less adsorption sites for the oxygen. As both water and CO are common background gases in UHV and known to adsorb on Co(0001) at room temperature

[245], in the case of water dissociatively forming adsorbed O [249], it is likely that the coverages can differ depending on the exact composition of the UHV background. Whereas sample # 1 was measured in a freshly baked UHV chamber, sample # 2 was measured after CO had been used in the high-pressure cell, thus in an increased CO background, although the pressure had recovered to the 10^{-9} mbar range. Figure 5.20(a) in the supplemental information indicates that an increased CO adsorption at the expense of adsorbed O (sample # 2 at 20 °C and sample # 4 at 220 °C) is mainly detected as an increase in the peak identified as CO without co-adsorbed O rather than the peak associated with CO co-adsorbed with O, therefore confirming the validity of the peak fitting method. However, the separation of the two peaks is not accurate enough for a quantitative comparison with the O coverage, especially at low total CO coverages.

Under heating to 220 °C most of the adsorbed CO desorbs also in the high CO background. At this temperature the CO coverage is between 0 and 0.04 on samples # 1 to # 3, whereas the O coverage remains at 0.23 to 0.24. The OH coverage, which likely stems from the H_2O dissociation as well, lies between 0.04 and 0.08. Carbon and hydrocarbon contaminants cover maximally 0.06 and 0.03 of the surface, respectively, for samples # 1 to # 3. Hereby, the detailed peak fitting (see Figure 5.20(b) in the supplemental information) shows that carbon is mainly present as carbidic carbon. In most samples the carbidic peak represents at least 95 % of the summed-up C peak area in UHV with one exception (67 % carbidic C and 33 % graphitic C on sample # 3). On the other hand, the two different types of hydrocarbons do not show a clear trend in UHV as both can represent between 0 % and 100 % of the total hydrocarbons (see Figure 5.20(c) in the supplemental information).

Sample # 4 is more contaminated compared to samples # 1 to # 3. It shows 0.29 coverage with hydrocarbons and 0.31 coverage with atomic carbon. At the same time a higher coverage with CO (0.13) is possible in this state, which can either be related to the other co-adsorbates or this surface is rougher than the other samples, which would leave more low-coordinated surface atoms, steps and kinks, for the CO adsorption. The Co(0001) terraces are expected to be free from CO above roughly 130 °C in UHV [245]. Obviously, a sample like sample # 4 has to be subjected to more sputtering and annealing before performing any experiments.

No sulfur was detected on the other samples after preparation in UHV. On one as-prepared sample traces of potassium could be detected. By a rough comparison of the K 2p signal to the C 1s signal and the respective photon cross sections at 480 eV photon energy, the potassium coverage was estimated to be on the order of 0.001 at 20 °C and increasing to an order of 0.01 when heating to 300 °C. Therefore, the potassium was not included in the coverage model applied here. The temperature dependence

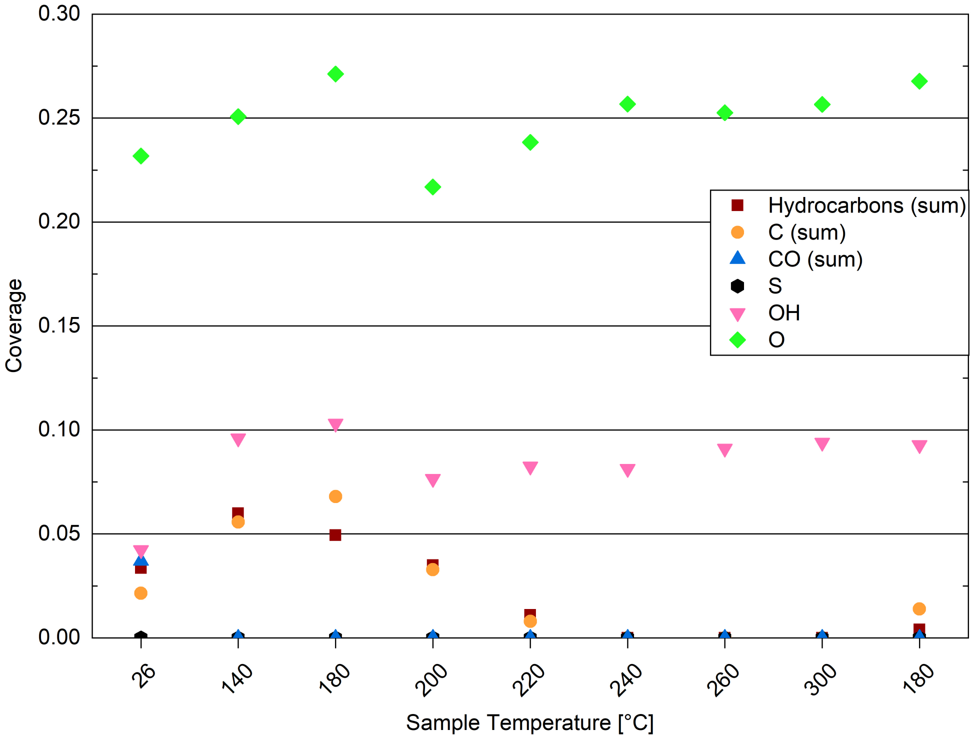

Figure 5.6: Coverages of all adsorbed species on one as-prepared sample in UHV (sample # 1) at different temperatures. Details see text.

suggests that the potassium is present in the bulk of the cobalt crystal and can reach the surface upon heating. The manufacturer excludes their starting material, as well as processing materials and tools as the source of the potassium. However, it could stem from polymer materials inside the vacuum chamber [264]. On the as-prepared samples used for the measurements in Sections 5.3.2 to 5.3.6 the potassium was below the detection limit. These were subjected to at least 100 more cleaning cycles.

Figure 5.6 shows the temperature dependence of the UHV characterization of sample # 1. In the whole probed range from room temperature to 300 °C the adsorbed oxygen remains at a coverage of 0.25 ± 0.04. From this we generously estimate a maximal uncertainty of ± 0.05 for all calculated coverages in the following sections. The temperature stability suggests that the adsorbed oxygen might be stable under the annealing to 317 °C during the sample preparation. This is in agreement with temperature-programmed desorption experiments by Xu et al. [249], in which the adsorbed oxygen formed by water dissociation was stable until at least 350 °C. In the measurements presented here the adsorbed OH coverage remains between 0.075 and 0.1 upon heating to 300 °C as well. A lower value of 0.04 is only measured at room temperature where more CO is present on the surface possibly blocking the adsorption sites. The CO has desorbed from 140 °C on, which is in agreement with temperature-programmed desorption reported in the literature (see Figure S1 in Ref. [245]). The surface area covered with hydrocarbons from the UHV background seems to increase upon heating to 140 °C, which might be due to outgassing of parts of the sample holder during this first heating in the analysis chamber. Upon further heating the hydrocarbons desorb and are not detectable from 240 °C on. Cooling down again to 180 °C, a coverage of 0.01 with hydrocarbons adsorbs again.

The atomic carbon coverage increases from 0.02 to 0.07 when heating to 180 °C and decreases again upon further heating until it is not detectable anymore from 240 °C on. This is somewhat surprising as the dissolution of carbon in cobalt is only expected at significantly higher temperatures where cobalt carbide can be formed [265]. Theory suggests that carbon atoms can easily diffuse below the topmost surface layer of Co(0001), whereas they are unlikely to diffuse deeper into the bulk unless Co vacancies are present [266]. Carbon atoms right below the topmost surface layer should still be detectable in our case as we probe the two to three topmost layers of the cobalt crystal. This is estimated by comparing the inelastic mean free path of 0.544 nm at 200 eV electron kinetic energy (see Section 5.2.3) to the layer thickness of Co(0001) of 0.21 nm (calculated from the crystal structure [257]). However, the existence of vacancies is likely on a Co(0001) surface, especially as the annealing temperature is limited, such that the dissolution to lower layers cannot be excluded as an explanation for not detecting the carbon at these temperatures. Cooling down to 180 °C a carbon coverage of 0.01 resurfaces, which is an order of magnitude less than the 0.14 that was present at 140 °C before heating up. In general, it is clear that keeping the surface at an elevated temperature (between 220 °C and 260 °C) in UHV and when introducing gases can increase the surface cleanliness and keep the surface free from CO, carbon, and hydrocarbons.

5.3.2 Oxidation of Co(0001) in Hydrogen

Figure 5.7 compares the change in the O 1s signal measured at MaxIV while introducing (a) wet and (b) dried hydrogen, respectively, both at 220 °C surface temperature. Both samples show some adsorbed oxygen when starting from UHV as discussed in detail in the previous section. When introducing the wet hydrogen, the oxygen signal strongly increases, whereas the dried hydrogen removes the adsorbed oxygen from the as-prepared sample. The horizontal reference lines in Figure 5.7(b) show that the adsorbed oxygen can already be removed before actually starting the flow of 3.8 ml/min

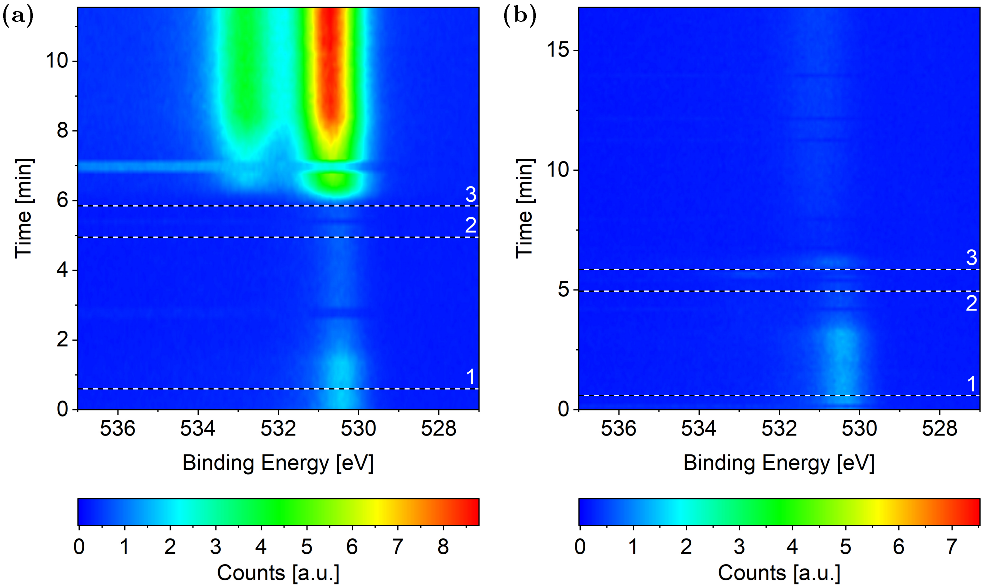

Figure 5.7: O 1s area measured on Co(0001) over time while introducing (a) wet and (b) dried H_2, respectively, both at 220 °C. The black and white reference lines mark (1) the closing of the near-ambient pressure cell, (2) the enabling of the mass flow controller, (3) and the start of the flow of H_2 (details see text). All scans in each map were normalized to have the same background level. In (a) two consecutive scans at around 7 min as well as around 3 min do not agree with the scans before and after. Such faulty scans can be caused by mechanical movements on the machine, for example when closing the cell door, or when the detector does not move to the correct energy range in time (meaning that the delay time between different peaks is not chosen long enough). In (b) such faulty scans might be present at 0 min and around 6 min.

H_2 (at the time of reference line 3). When closing the cell door (at reference line 1) the volume is not pumped via the analysis chamber anymore such that the composition of the vacuum background can change. Subsequently, the gas lines are opened to the cell (no reference line) such that the background composition can be influenced by the background in the gas lines as well. Additionally, when the mass flow controller is enabled (at reference line 2), meaning a valve between the mass flow controller and the gas lines to the cell is opened, some gas could easily enter the cell as mass flow controllers might not be completely leak-tight when closed. These complications in knowing the exact gas composition at every point in time could also explain why it appears that the adsorbed oxygen on the as-prepared sample is (partially) removed in Figure 5.7(a) before it strongly increases in the flow of wet H_2.

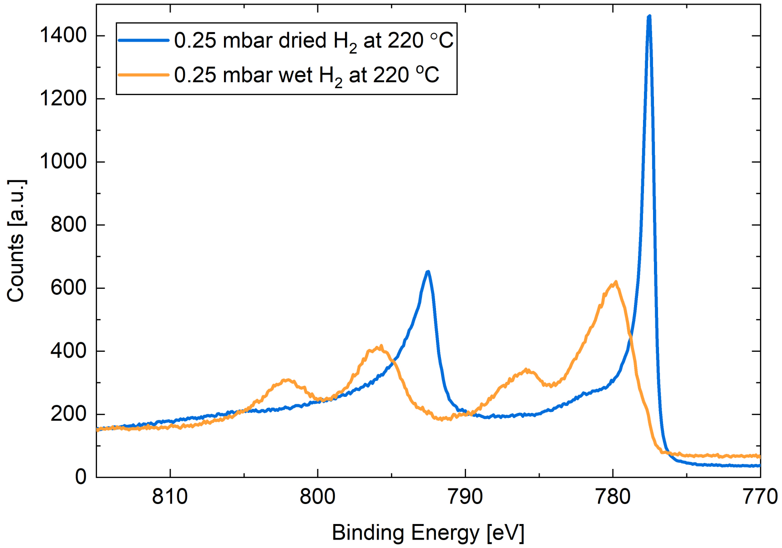

Figure 5.8: Co 2p area measured on Co(0001) after roughly 30 min in 0.25 mbar dried H_2 (blue) compared to after roughly 10 min in wet H_2 (orange), both introduced at 220 °C. The latter spectrum was only measured shortly after CO was added to the gas composition. However, as will be shown in Section 5.3.3, the presence of CO does not oxidize the cobalt surface, such that this measurement can still be used to estimate the extent of oxidation caused by wet H_2.

Apart from the adsorbed oxygen or oxide signal at 530.4 eV, a second contribution is visible in Figure 5.7(a). The binding energy is roughly the one we have identified as the binding energy of CO co-adsorbed with O. However, in this case there is no measurable carbon signal at the time of the last spectrum of the map, such that the same peak needs to be identified as molecularly adsorbed water (see Section 5.2.2). If the water dissociates, the binding energy of the resulting adsorbed OH would lie between the adsorbed O or oxide and the adsorbed H_2O, such that it might not be clearly resolved as a distinct peak in Figure 5.7(a). A detailed fit of the last spectrum in the map results in 29 % of the oxygen signal stemming from adsorbed water and merely 2 % from adsorbed OH. Thus, the water is mainly adsorbed molecularly in this case. As shown in the following paragraph, the cobalt is oxidized here, which explains why it is inactive for water dissociation [249].

The Co 2p peaks displayed in Figure 5.8 suggest that the probed depth of the cobalt sample is almost completely oxidized by the wet hydrogen. 98 % of the peak area in a detailed fit is the oxidized contribution. The strong contribution in the O 1s signal can thus be identified as mainly stemming from cobalt oxide instead of adsorbed atomic

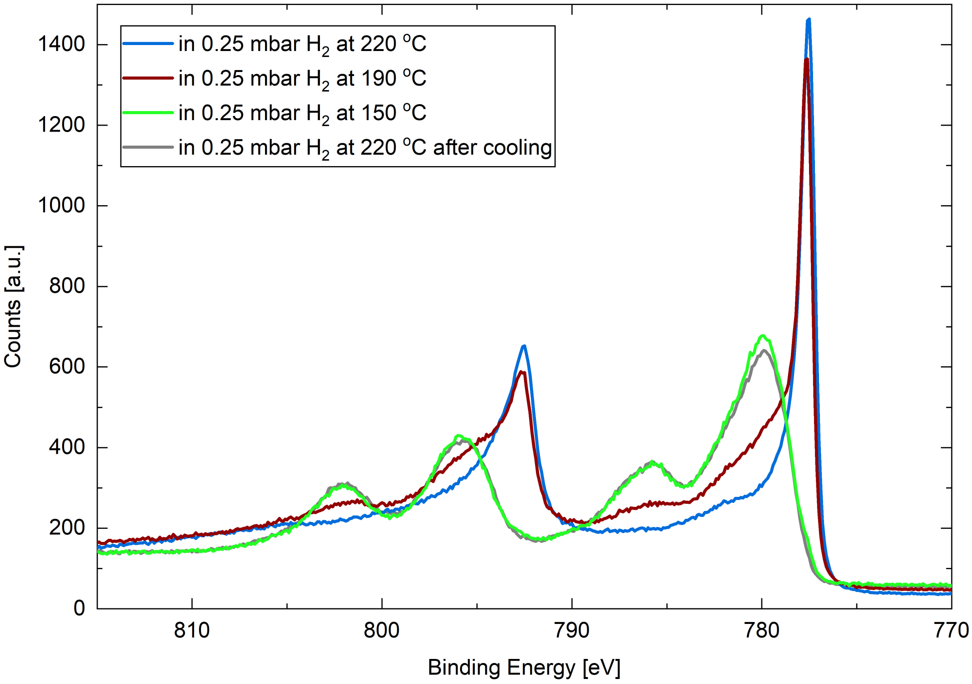

Figure 5.9: Co 2p areas measured on Co(0001) in 0.25 mbar dried H_2 at 220 °C, 190 °C, and 150 °C, as well as after subsequent heating to 220 °C.

oxygen in this case. In comparison, the surface stays mostly metallic in the dried hydrogen. The detailed fit shows 9 % oxidized contribution in the Co 2p peaks, which is not more than the maximum measured on an as-prepared sample in UHV.

While the dried hydrogen keeps the cobalt surface metallic in 0.25 mbar at 220 °C, it does oxidize upon reduction of the temperature. Figure 5.9 shows the Co 2p area in 0.25 mbar dried H_2 under cooling down from 220 °C to 190 °C and 150 °C, as well as under subsequently increasing the temperature to 220 °C again. The sample was kept at every temperature for about 1 h. Within this time frame a partial oxidation at 190 °C is clearly visible in the Co 2p area (red curve). A detailed fit identifies 38 % of the probed depth measured as oxidized cobalt. While staying in these conditions, the O 1s area was measured twice with a time difference of 26 min, over which no change is measurable (data not shown). Thus, the full oxidation measured at 150 °C another 29 min later (green curve) is likely actually caused by this decreased temperature and would have not taken place at 190 °C, at least not within this time frame.

Figure 5.9 additionally displays the Co 2p area after increasing the temperature of the oxidized surface from 150 °C to 220 °C (grey curve), where it is not reduced within

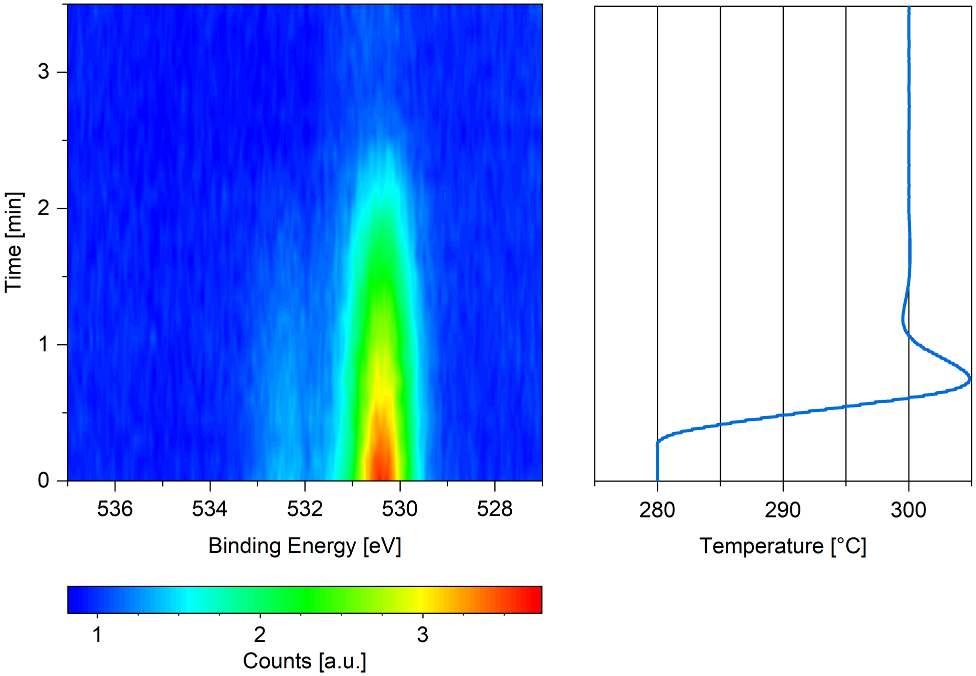

Figure 5.10: O 1s area measured on previously oxidized Co(0001) in 0.25 mbar dried H_2 while increasing the temperature from 280 °C to 300 °C with the corresponding temperature graph.

1 h and two measurements of the O 1s area with a time difference of 36 min do not show any change. This suggests that the reduction is kinetically limited in the time frame investigated here. Upon further increasing of the temperature the sample is reduced within 2 min above 280 °C. This is evidenced by the change of the O 1s signal displayed next to the sample temperature in Figure 5.10. A 90 % metallic contribution was subsequently measured in the Co 2p area at 300 °C. However, the increase of the temperature from 220 °C to 280 °C, over which no significant change in the O 1s area was visible, took place within only 15 min, leaving the possibility that a lower temperature might have been sufficient for reduction over the course of hours.

In measurements taken at the ALS in purer H_2 (see Table 5.1) as well as using a liquid nitrogen trap the cobalt stayed completely metallic at 180 °C (data not shown). However, lower temperatures were not tested in this case and a possible disagreement between the temperature read-out in the two different systems is not unlikely. This can be caused by different positioning of thermocouples with respect to the sample, different thicknesses of the thermocouples, as well as different distances between the sample and other materials picking up the thermocouple signal. Therefore, this is no

clear evidence that the initial purity of the gas in the bottle has an influence. However, the difference between wet and dried hydrogen used at MaxIV is clearly evidencing at least some influence of the water background on the oxidation behavior in hydrogen.
As hydrogen adsorbed on the terraces of Co(0001) is more stable than on the steps and defects [267,268], these lower-coordinated Co sites could be free for dissociative H_2O adsorption as soon as the temperature is low enough in the specific H_2O partial pressure. DFT calculations by Ma et al. [269] suggest that the adsorption of H_2O is significantly easier on the steps than on the terraces, whereas the dissociation is only slightly enhanced in comparison. Once some H_2O has dissociated, the resulting adsorbed O can strongly promote further H_2O dissociation on the terrace [249,270] and even more so on the steps [269]. The oxidized CoO/Co(0001) terraces are not active for further water dissociation [249], such that a limited growth of only one layer of oxide could be expected. However, to our knowledge there are no similar studies regarding the water dissociation on the steps and defects of oxidized cobalt. As the measurements presented here probe between two and three layers of the single crystal, which appear fully oxidized, we cannot directly confirm or exclude a limited growth.
Under vacuum pressures, where hydrogen has been shown to remove adsorbed oxygen from Co(0001) from roughly 180 °C on [229] and no oxidation caused by H_2 has been reported, the background water pressure could be significantly lower leading to less water adsorption and dissociation. The same study finds that a higher temperature is needed for H_2 to remove adsorbed oxygen from defective Co(0001) compared to the Co(0001) terraces, which confirms that it is less effective at the low-coordinated sites.
The oxidation observed here in the mbar range has been observed previously by Groot et al. [242] in ambient-pressure surface X-ray diffraction on Co(0001) showing the formation of crystalline CoO in 1 bar H_2 when decreasing the temperature from 220 °C to 180 °C. Interestingly, although these studies were done without any drying of the gas (purity of the hydrogen between 4.5 and 5), the surface stayed metallic at 220 °C and reduced again when increasing the temperature to 220 °C after the oxidation. These observations indicate a more efficient reduction in 1 bar wet H_2 compared to 0.25 mbar dried H_2. The difference in total pressure might lead to a larger hydrogen coverage at the same temperature, thus more efficiently preventing the adsorption and dissociation of water and removing the oxygen atoms. Especially, the reduction when returning to 220 °C indicates that it is less kinetically limited at higher pressure compared to our measurements. In a pressure of 0.2 mbar H_2, Papaefthimiou et al. [228] have reduced an oxidized Co(0001) surface at about 250 °C, which is the same range as our result taking the usual inaccuracies of temperature measurements into account. Additionally, our measurements agree with the results of Wu et al. [226] on polycrystalline cobalt foil. In roughly 0.13 mbar (100 mTorr) H_2 they observe

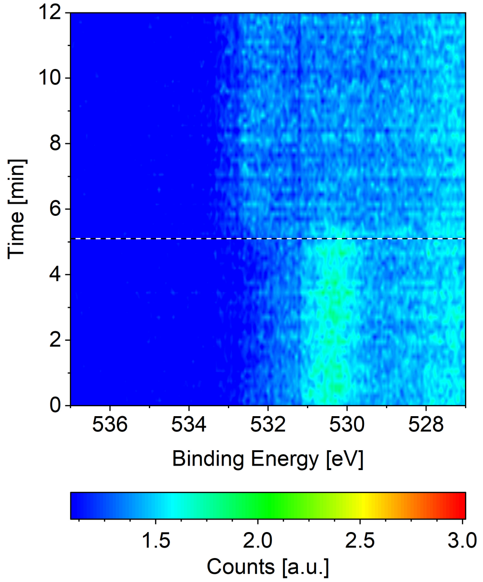

Figure 5.11: O 1s area measured on Co(0001) over time while introducing CO at 220 °C. The black and white reference line marks the start of the flow of 1.9 ml/min CO.

oxidation below 185 °C and the reduction between 200 °C and 290 °C indicating that the difference in structure between the single-crystalline and the polycrystalline sample might not have a significant influence on the oxidation behavior in this pressure range of hydrogen. Lukashuk et al. [271] have observed the reduction of a Co_3O_4 powder in 0.4 mbar H_2 starting from 250 °C on as well. In contrast, Turczyniak et al. [227] observe a complete reduction of Co_3O_4 nanopowder in 0.2 mbar H_2 only at 350 °C. This confirms that the complex structure of nanoparticles and powders, which can consist of numerous different types of cobalt sites, not even taking possible supports into account, can still lead to significantly different results compared to studies on crystalline samples. In general, the above considerations suggest that low-coordinated cobalt atoms are more prone to the oxidation by water in a hydrogen environment and that the water partial pressure as well as the total hydrogen pressure play a significant role.

5.3.3 Metallic Co(0001) in CO

Figure 5.11 displays the change of the O 1s signal on Co(0001) while introducing CO into the near-ambient pressure cell at 220 °C surface temperature. The adsorbed oxygen on the as-prepared sample is efficiently removed as soon as the CO is introduced

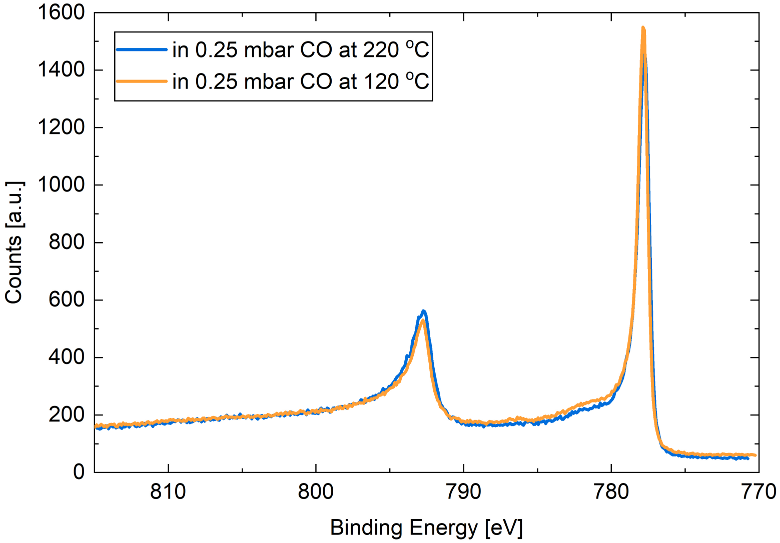

Figure 5.12: Co 2p areas measured on Co(0001) in 0.25 mbar CO at 220 °C and 120 °C.

(see horizontal reference line). At the same time the adsorbed CO signal appears at higher binding energy, albeit not yet to a strong extent compared to the adsorbed O on the as-prepared sample (see Section 5.3.5 for a quantitative analysis of the adsorbed species in 0.25 mbar CO).

The Co 2p signals displayed in Figure 5.12 confirm that the cobalt stays mainly metallic in 0.25 mbar CO at 220 °C (0.5 % oxidized contribution in the fit). This is is still the case when decreasing the temperature to 120 °C (4 % oxidized contribution in the fit). Thus, although the CO contains a similar amount of water (see Table 5.1) and is not additionally dried, it is significantly more efficient at keeping the Co(0001) metallic compared to dried H_2 at the same total pressure. This is especially surprising as the CO is expected to dissociate on defect sites starting from around 60 °C on [272]. Thus, at least part of the resulting adsorbed atomic oxygen (see Section 5.3.5) desorbs as CO_2 without oxidizing the cobalt.

These results are in agreement with the measurements of Wu et al. [226] on cobalt foil, which stays metallic even at room temperature in roughly 0.13 mbar CO. Additionally, they measure the reduction of CoO/Co(0001) by CO between 150 °C and 200 °C again indicating a kinetic limitation as well as the more efficient reduction by CO compared to H_2 at the same total pressure. Co_3O_4 powder has also been shown to start reducing in 0.15 mbar CO from 150 °C on, at lower temperatures than in 0.4 mbar H_2 [271]. In UHV studies, Kizilkaya et al. [229] observe the opposite behavior as $2 \cdot 10^{-5}$ mbar H_2 removes adsorbed oxygen from Co(0001) at 177 °C, whereas CO in the same pressure range does not remove it even at 357 °C. In these conditions a coverage of at most 0.33 monolayers of CO and mainly on the top sites can be expected (estimated from Figure 8 in Ref. [245]). Based on the same reference, a coverage between 0.33 and 0.5 monolayers can be expected on the top as well as the hollow sites in all pressure and temperature conditions studied here (as well as industrial FTS conditions). As the top sites would be the most stable position for H_2O as well [254,270], a specific minimal coverage with CO, thus minimal CO pressure at a specific temperature, could be needed for sufficient site blocking to prevent the oxidation. Combined TPD and DFT studies by Jiawei et al. [250] suggest that the adsorption of CO is significantly stronger than the adsorption of H_2O such that the CO could adsorb preferentially when both are present in the gas phase. They also find that the co-adsorption of CO stabilizes the adsorption of H_2O via hydrogen bonds. As molecularly adsorbed water can form two of those hydrogen bonds whereas OH could only form one, this might hinder dissociation of the adsorbed water.

As water preferentially adsorbs on the steps compared to on the Co(0001) terrace [269], the steps might be more relevant than the different terrace sites here. In contrast to H_2 (see Section 5.3.2), CO shows a comparable adsorption on stepped surfaces as on Co(0001) [273]. Thus, the blocking of step sites by the CO at the investigated pressures is possible. At the same time the dissociation of CO has been shown to be facilitated at the steps of Co(0001) compared to the terrace [272] and to not be hindered by an increasing CO coverage [274]. The dissociation could lead to additional blocking of the step edges by the resulting atomic carbon. As will be shown in Section 5.3.5, carbon species can be detected on the Co(0001) surface in CO at all investigated temperatures. Although the carbon atoms could diffuse on the terraces [266], they are more stable at the steps [218].

However, at even higher pressures, Groot et al. [242] observe the formation of CoO on Co(0001) in CO (purity 4.5 to 5) at temperatures up to 260 °C and no reduction up to 340 °C. In this case the total water pressure is higher such that the preferential adsorption of CO might be insufficient to block all sites for the H_2O dissociation. However, in their study the total water pressure in both gases should be comparable and can thus likely not completely explain the significantly more efficient reduction they observe in H_2 compared to CO, which is in contrast to our results in the mbar range.

In general, the above suggested site blocking effect preventing oxidation could lead to a different result depending on the exact water content as well as the exact manner and order of introducing the CO and the oxidizing agent (O_2, H_2O, or wet H_2), which can further complicate the comparison of different studies in the literature.

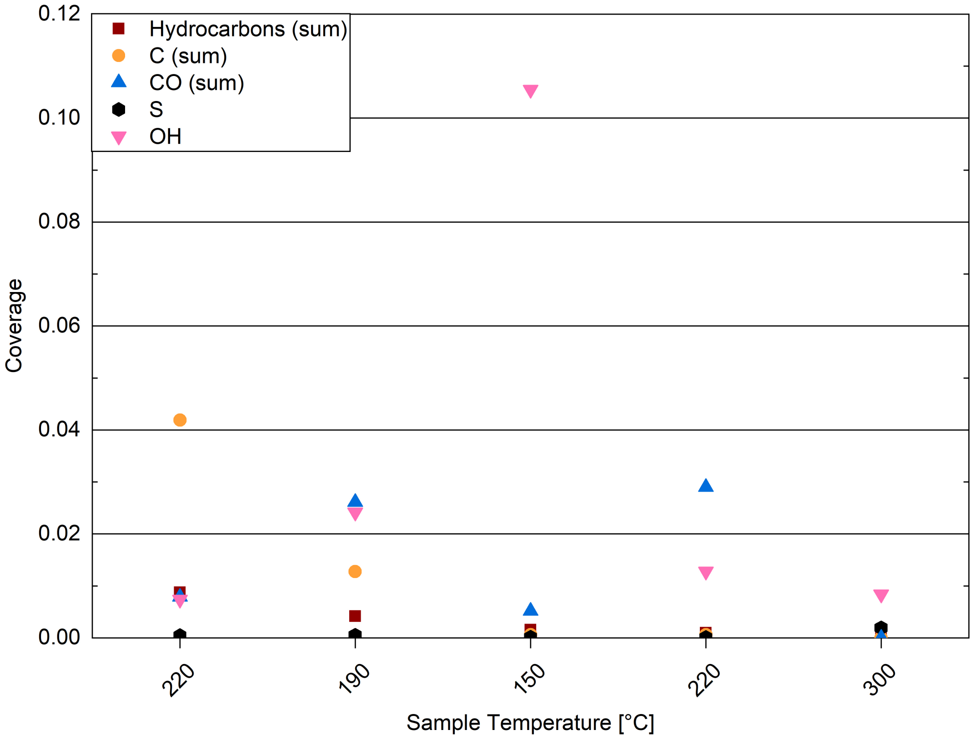

Figure 5.13: Coverages of adsorbed carbon species, OH, and sulfur on the Co(0001) surface in 0.25 mbar dried H_2 at different temperatures cooling down from 220 °C to 150 °C and subsequently heating up to 300 °C. For clarity the different carbon, hydrocarbon, and adsorbed CO peaks are summed up to one coverage each here and the detailed results are only displayed in the supplemental information. As explained in the text, the coverages can only be interpreted relatively to each other instead of absolutely in this case.

5.3.4 Adsorbed Species on Co(0001) in Hydrogen

Figure 5.13 displays the coverages of the adsorbed carbon species, OH, and sulfur on Co(0001) in 0.25 mbar dried H_2 at different temperatures. As explained in Section 5.2.3, the model to calculate these coverages does not take the oxidation of the surface (see Section 5.3.2) into account such that the resulting values can only be discussed as relative coverages with respect to each other here and are not absolute coverage values. As shown in Section 5.3.1, all as-prepared samples show some carbon. Here we start out with a carbon coverage of 0.04. It can clearly be seen that in time in H_2 the carbon is removed from the surface. This can be expected from around 150 °C surface temperature on [226]. Whereas the atomic C signal in the first measurement at 220 °C consists of 23 % graphitic carbon and 77 % carbidic carbon, only carbidic carbon is left in all subsequent measurements (see Figure 5.21(a) in the supplemental information), suggesting that the graphitic carbon is removed first.

Interestingly, the hydrocarbons are removed as well while reducing the temperature from 220 °C to 150 °C (see Figure 5.13). As they can already be present on the as-prepared sample from the UHV background (see Section 5.3.1), the removal might not be related to the cooling but simply happen over time in H_2. On the other hand, hydrocarbons can stem from the hydrogen bottle. In this case it could be expected that more adsorb at lower temperatures. However, if that type of hydrocarbon needs to dissociate in a certain way to stick on the surface, they might only be present at higher temperatures. This is unlikely as they do not re-appear after heating to 300 °C. The two types of hydrocarbons differentiated in the fit do not show a clear trend (see Figure 5.21(b) in the supplemental information). In all investigated conditions the hydrocarbon signal is small with less than 0.01, which can lead to inaccuracies in such a detailed analysis.

The presence of some adsorbed CO is generally not surprising as there is a CO background in the UHV chamber as well as in the gas lines after previous uses of CO in the cell. However, no clear trend with temperature in H_2 can be recognized in Figure 5.13 except that no CO is adsorbed on the metallic Co(0001) at 300 °C. The difference between the other temperature steps, especially comparing the two different sets of measurements at 220 °C while cooling down and heating up again, could be explained on the basis of how much Co(0001) or CoO/Co(0001) is covered with other adsorbates (C, hydrocarbons, OH, and O) and how much is thus free for CO adsorption. The distinction between CO alone and CO co-adsorbed with O in the detailed fit (see Figure 5.21(c) in the supplemental information) shows that mainly the latter is present in those sets of measurements where the cobalt is oxidized. Thus, the binding energy of CO on CoO/Co(0001) is shifted as well and contributes to the peak that was identified as CO with co-adsorbed O. Therefore, it is not possible to use the position of the CO peak as an indication for the presence of adsorbed O on top of the CoO. However, the adsorbed OH, which also originates from dissociated water, is increased at these temperatures as well (see Figure 5.13). As the adsorbed oxygen contribution to the O 1s peak cannot be distinguished from the cobalt oxide, the presence of adsorbed oxygen on top of the oxide cannot be confirmed in a direct measurement. Whereas co-adsorbed oxygen would already reduce the probability for CO adsorption and CO dissociation [275], cobalt oxides favor CO oxidation over CO dissociation to such an extent that they are even investigated as CO oxidation catalysts [276].

Over the course of more than 7 h in 0.25 mbar H_2, a small amount of sulfur is adsorbed on the surface (0.002 in the last set of measurements at 300 °C), which likely stems

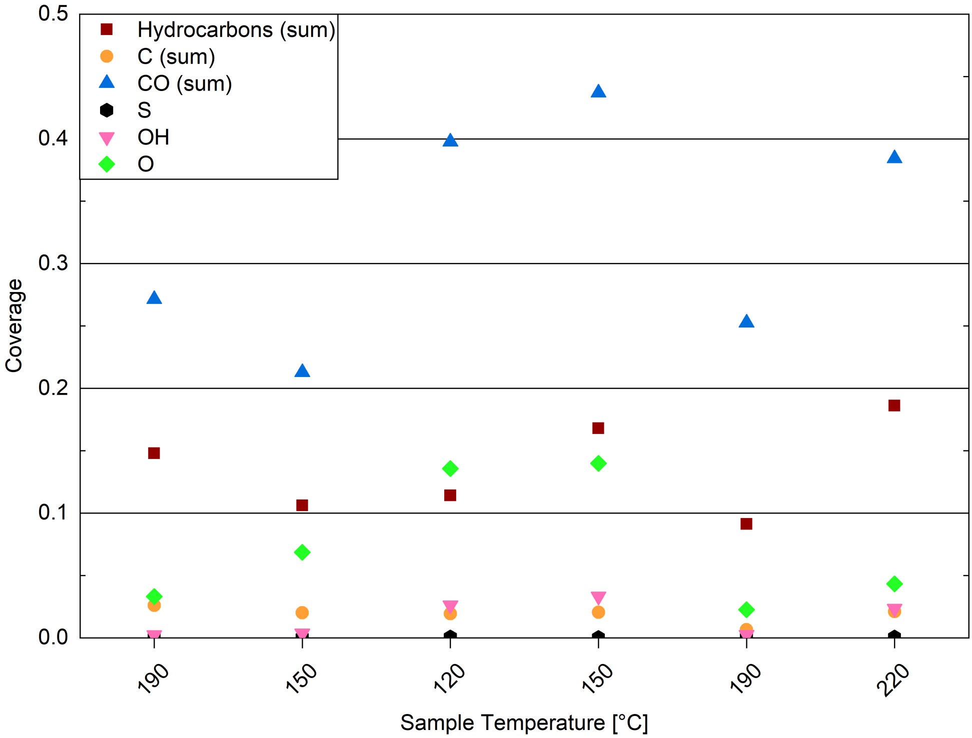

Figure 5.14: Coverages of adsorbed carbon species, oxygen species, and sulfur on the Co(0001) surface in 0.25 mbar CO at different temperatures cooling down from 190 °C to 120 °C and subsequently heating up to 220 °C. For clarity the different carbon, hydrocarbon, and adsorbed CO peaks are summed up to one coverage each here and are only displayed in detail in the supplemental information.

from contaminants in the hydrogen bottle.

5.3.5 Adsorbed Species on Co(0001) in CO

Figure 5.14 displays the calculated coverages of the adsorbed species on Co(0001) in 0.25 mbar CO at different temperatures. With a maximum coverage below 0.15, less oxygen than on the as-prepared sample in UHV is present. This confirms the removal of adsorbed oxygen by CO described in Section 5.3.3. Still, a trend to increasing oxygen coverage with decreasing temperature is observed. Adsorbed OH, although significantly less than O (as in UHV as well as in H_2), follows the same trend confirming that again both likely stem from dissociation of background water. Additionally, this confirms that O from CO dissociation at defect sites is mostly removed as CO_2 as expected from literature [226,245].

The range of CO coverages measured (between 0.21 and 0.44) is slightly lower than the expected range between 0.33 to 0.5 monolayers (see Figure 8 in Ref. [245]). However, taking into account how much surface area is in total occupied by other species, the CO coverage on the bare part of the surface area can be calculated as between 0.27 and 0.68. This estimate does not take possible interactions between the different adsorbates as well as changes over time (see below) into account.

The CO coverage shown in Figure 5.14, which is calculated based on the C 1s spectra, is not generally higher at lower temperatures. Figure 5.22(a) in the supplemental information compares these CO coverages to the CO coverages calculated from the O 1s spectra. Whereas the latter is generally higher at lower temperatures, the C 1s spectrum shows more adsorbed CO in the first measurement at 190 °C as well as after heating up to 220 °C again. As the C 1s spectra are measured right after changing the temperature and the O 1s spectra roughly 18 min later, this could be related to a carbon and/or hydrocarbon built-up over time, which is especially expected at the temperatures active for FTS (as well as beam-induced reaction, see Section 5.5.1). Thus, although no change in the carbon signal can be detected on the time scale of the C 1s measurement, it could be detected indirectly as less surface area is free for CO, OH, and O adsorption once the O 1s spectrum is measured.

The CO in the O 1s spectrum, the CO in the C 1s spectrum, as well as the adsorbed O and OH show a (slightly) higher coverage after heating to 150 °C compared to their coverage at 120 °C. As this trend is the same in the C 1s and the O 1s spectrum, it cannot be caused by the time difference between the two measurements (as the effect explained in the previous paragraph). However, an increase in any adsorbate towards the end of a set of measurements can cause an inaccuracy in all coverages at once as the Co 2p signal (which is measured at the end of the set) is then underestimated. All calculated coverages, which are roughly inverse proportional to the measured Co 2p intensity (see Equation 5.7 in Section 5.2.3), are thus overestimated at the same time. Taken the estimated inaccuracy of ± 0.05 for all coverages into account, the CO and O coverages at 120 °C and subsequent increase to 150 °C are overall comparable. Comparing the coverages at 150 °C before and after the cooling to 120 °C, a hysteresis between adsorption and desorption can thus be observed.

As explained in Section 5.2.2, two peaks are associated with adsorbed CO (without co-adsorbed O) in the C 1s signal, a main higher binding-energy peak as well as a lower binding-energy peak that was tentatively identified as a second, less stable adsorption site on the Co(0001) terrace. At all temperatures investigated here, most of the CO (without co-adsorbed O) is located at the most stable site (between 83 % and 88 %) confirming this identification. Compared to the phase diagram for CO adsorption by

Weststrate et al. (Figure 8 in Ref. [245]), it is likely that the most stable site is the top site, whereas the second observed one is the hollow site. As the coverage of CO (without co-adsorbed O) does not change significantly with the different temperatures investigated here (see Figure 5.22(b) in the supplemental information), a constant ratio of the two different adsorption sites is not surprising. Instead the change in CO adsorption with temperature is detected mainly in the peak identified as CO with co-adsorbed O (agreeing with the change in adsorbed O). This CO with co-adsorbed O consists of two peaks in the detailed C 1s fit as well. Here, the lower binding energy one is dominant (thus likely the most stable site) and accounts for between 71 % and 83 % of the CO co-adsorbed with O. Thus, although the total CO coverage varies in a range from 0.21 to 0.44 depending on the temperature (see Figure 5.14), the distribution over the different adsorption sites remains comparable for CO both with and without co-adsorbed O.

The change of the amount of adsorbed hydrocarbons with temperature appears somewhat correlated to the amount of adsorbed CO. If all hydrocarbons stemmed from the CO bottle, one could expect that the adsorbed amount is simply correlated to the temperature like the adsorbed O or to the free space on the surface, which can be estimated from the total amount of all other adsorbates. In this case more adsorbed hydrocarbons could be expected after decreasing the temperature to 150 °C. On the other hand, a larger hydrocarbon coverage at higher temperatures from 190 °C on could be expected if the hydrocarbons are formed through reaction of the adsorbed CO with background hydrogen. The distinction between two different hydrocarbon peaks in the detailed fit (see Figure 5.22(c)) shows that one type is increased at higher temperatures (type I) and might thus be the hydrocarbons that are produced by reaction with background H_2, whereas the other type (type II) is adsorbed more at lower temperatures and could stem from the background in the CO bottle.

The absolute atomic carbon coverage is not significant with values between 0.007 and 0.021, such that the change with temperature is within the estimated inaccuracy of the calculated coverages. Although CO dissociation, which can be expected from 60 °C on [272], could leave carbon behind, the amount of carbon is in the same range as on the as-prepared sample in UHV (see Section 5.3.1). Thus, it cannot be related to CO dissociation unambiguously. However, in contrast to the UHV measurements, the detailed fit (see Figure 5.22(d) in the supplemental information) suggests that the carbon is mainly present as graphitic carbon, whereas a smaller amount of carbidic carbon that appears when decreasing the temperature to 150 °C is not visible anymore after increasing it to 190 °C again. The carbidic carbon can diffuse into the bulk, although we have observed that only from higher temperatures on in UHV (see Section 5.3.1). It is more likely that carbon is removed by reaction with background H_2 from 190 °C

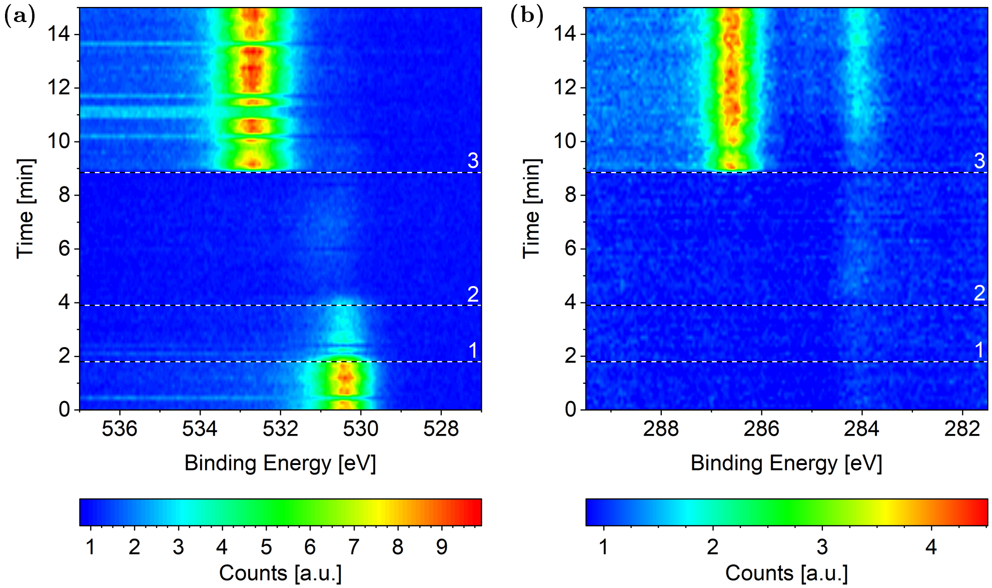

Figure 5.15: Change of the (a) O 1s and (b) C 1s signals measured on Co(0001) over time while introducing the reaction mixture of 4 H_2 + 1 CO at 220 °C. The three black and white reference lines mark (1) the moment the mass flow controllers are connected to the cell, (2) the start of the flow of 4.4 ml/min H_2, (3) and the start of the flow of 1.1 ml/min CO. All consecutive spectra have been normalized to the background level at low binding energy. Some faulty measurements caused by an insufficient delay between the different scans are visible as horizontal lines in (a).

on (see Section 5.3.4). Interestingly, the graphitic carbon seems to be present in larger amounts at higher temperatures. This could be due to a higher rate of CO dissociation or also be related to the decrease in carbidic carbon at those temperatures. If some carbidic carbon would become graphitic, it might not lead to a net change in the total carbon coverage. The graphitic carbon could then be more resistant to removal by the low background pressures of H_2 (details see following section).

The sulfur coverage detected after a total of more than 17 h in 0.25 mbar CO is less than 0.001.

5.3.6 Adsorbed Species on Metallic Co(0001) during FTS

Starting from the as-prepared Co(0001) in UHV the reaction mixture was introduced by first starting the flow of dried H_2 and, once all adsorbed oxygen has been removed, starting the additional flow of CO. This can be seen in Figure 5.15(a) in the form of the removal of O and the subsequent adsorption of CO at higher binding energy.

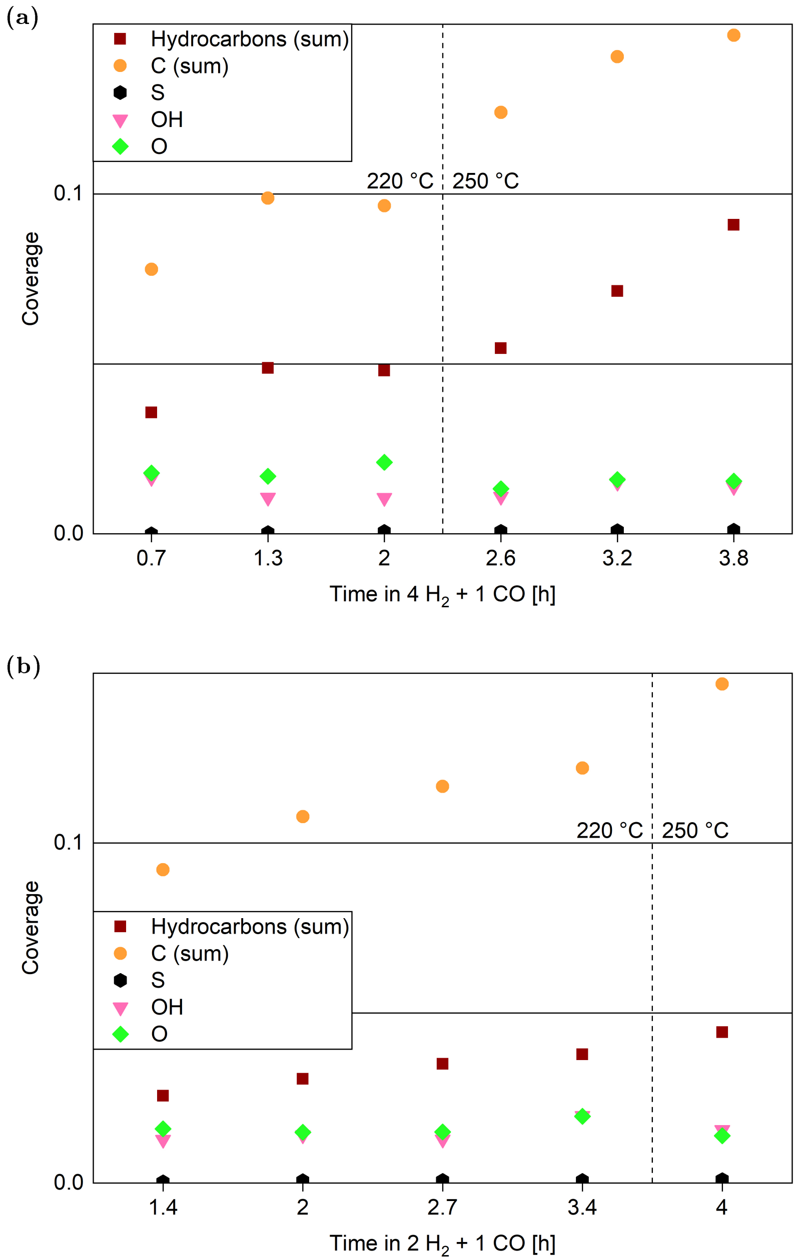

Figure 5.16: Coverages of carbon species, oxygen species, and sulfur on Co(0001) in 0.25 mbar (a) 4 H_2 + 1 CO and (b) 2 H_2 + 1 CO. The temperature is increased from 220 °C to 250 °C at the dotted, vertical reference line. For clarity the different atomic carbon and hydrocarbon peaks are summed up to one coverage each here and are only displayed in detail in the supplemental information.

The removal of oxygen seems to start already before setting the hydrogen flow. At reference line 1 the mass flow controllers are connected to the cell by opening certain valves. This can easily cause a partial reduction by background gas from the lines or small amounts of H_2 or CO leaking through the mass flow controllers. Right after the start of the CO flow the adsorbed CO as well as carbon and some hydrocarbons can be seen in the change of the C 1s signal in Figure 5.15(b). Additionally, a small amount of adsorbed OH and some carbon or hydrocarbon species could be suspected in H_2 (between reference line 2 and reference line 3). However, these are not significant compared to the background level.

As the cobalt stayed metallic in 0.25 mbar dried H_2 (see Section 5.3.2) as well as 0.25 mbar CO (see Section 5.3.3) at 220 °C, it could be expected that it also stays metallic in a mixture of the two gases at the same total pressure and temperature. This is confirmed by an oxidized contribution to the Co 2p fit of at most 3 % during up to 3 h in a 4:1- or a 2:1-ratio of H_2 to CO at 220 °C. At 250 °C the same value is measured. Thus, the additional water produced in the Fischer-Tropsch reaction is not sufficient to oxidize the surface under these conditions.

Figure 5.16 displays the coverages of the adsorbed species on Co(0001) at the two different gas ratios. In line with the removal of oxygen described above, the O coverage stays between 0.015 and 0.02 for both gas ratios at 220 °C, and is only slightly lower with a maximum of 0.016 at 250 °C. The OH coverage is comparable with values between 0.01 and 0.02. These values are on the same order of magnitude as on the metallic surface in 0.25 mbar CO at 220 °C. As shown in Section 5.3.5, the O coverage can still be an order of magnitude higher upon decreasing the temperature while the surface stays metallic. In UHV the O coverage is even higher with 0.25 ± 0.05 without oxidizing the surface (see Section 5.3.1). However, in 0.25 mbar dried H_2 the surface did oxidize at lower temperatures (see Section 5.3.2). In the two reaction mixtures lower temperatures were not investigated here. However, the observation that the surface is metallic at 220 °C is in rough agreement with the reduction of oxidized cobalt foil seen from 225 °C on in 0.1 mbar 1 H_2 + 1 CO [226], as well as the reduction of CoO/Co(0001) observed in 1 bar 1 H_2 + 1 CO above 220 °C [242]. As mentioned above, the complexity of catalysts, supports, and promoters can strongly influence the oxidation and catalytic behavior. This is evidenced by observations of positive as well as negative effects of water on the activity and selectivity of different cobalt-based catalysts [277–279]. Overall, the poisoning by oxidation is believed to not play a large role for industrial Fischer-Tropsch synthesis as it can easily be prevented under realistic conditions [222].

Figure 5.17 displays the CO coverage in the reaction mixture (compared to the other adsorbed species). The absolute value of CO coverage lying between 0.44 and 0.53

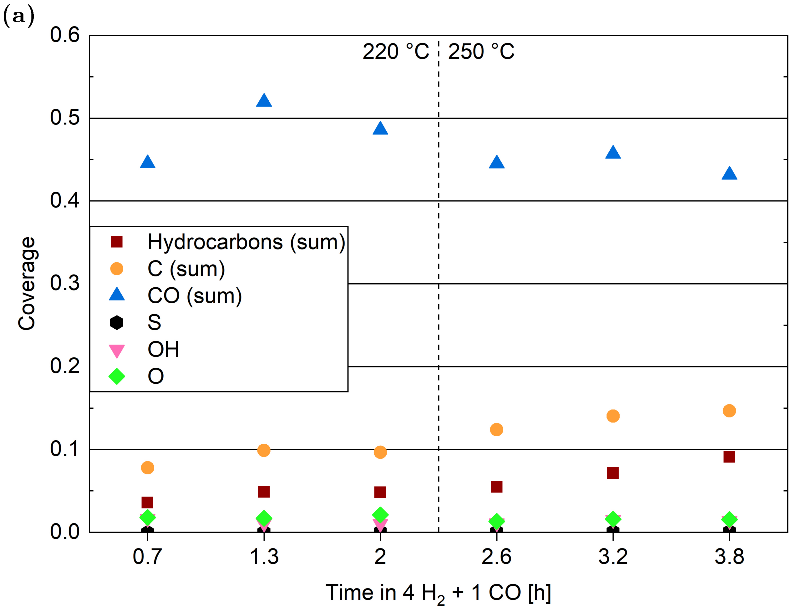

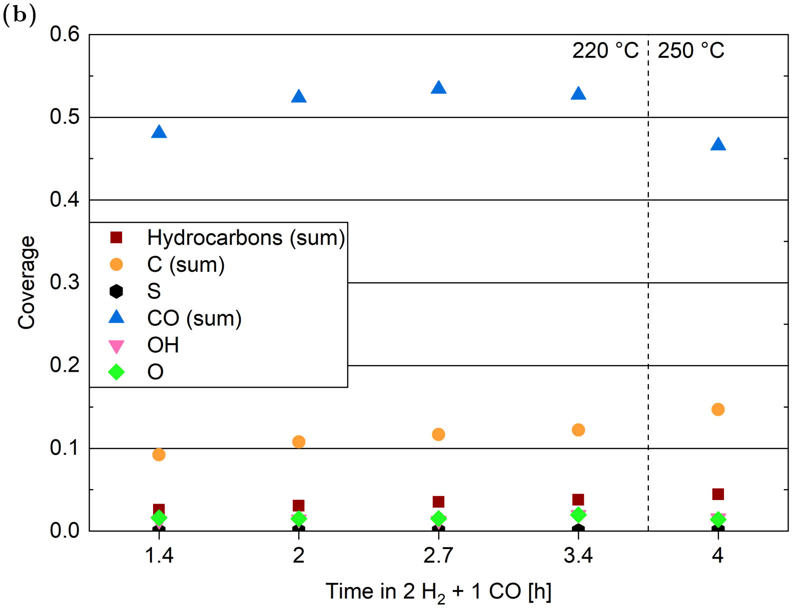

Figure 5.17: Coverage of CO on Co(0001) in 0.25 mbar (a) 4 H_2 + 1 CO and (b) 2 H_2 + 1 CO. The temperature is increased from 220 °C to 250 °C at the dotted, vertical reference line. For clarity the sum of the different CO peaks is shown here and the results are only displayed in detail in the supplemental information. For comparison the coverages of all other adsorbed species from Figure 5.16 are plotted again.

seems somewhat higher in reaction conditions compared to 0.25 mbar CO at 220 °C (see Figure 5.14 in Section 5.3.5). However, less other species are adsorbed here. The coverage on the bare part of the surface is comparable for both gas mixtures and lies between 0.52 and 0.63 at 220 °C. Thus, this is not significantly different from the value of 0.53 measured in 0.25 mbar CO at 220 °C. A trend to smaller absolute CO coverages in the reaction mixtures at 250 °C compared to 220 °C is not significant and can be explained by the increase of other carbon species. The CO coverage on the bare part of the surface is calculated to be between 0.59 and 0.60 at 250 °C and is thus in the same range as at 220 °C. These results are roughly in agreement with the expected CO coverage of 0.5 during the reaction [245] and confirm that it does not strongly depend on the CO partial pressure or the temperature under the conditions investigated here. As only a small amount of adsorbed O is detected in reaction conditions, it is not surprising that the adsorbed CO is mainly found in the peaks associated with CO without co-adsorbed O (see Figure 5.23(a) in the supplemental information). The two different peaks associated with adsorbed CO without co-adsorbed O further show that between 93 % and 97 % of the CO is adsorbed in the most stable site, which is likely the top site. Thus, although the absolute coverage in reaction conditions is comparable to in CO (see Section 5.3.5), a somewhat higher fraction of it is in the top site. This might be related to the smaller amount of other adsorbates, which allows more CO to sit in the preferred position.

The atomic carbon coverage during the reaction is displayed in Figure 5.16. Although an increasing trend is visible at 220 °C, the C coverage stays between 0.08 and 0.12 over a time of 3 h at this temperature. In the first measurement in time the C coverage is already significantly more than in H_2 or CO at 220 °C suggesting that it is caused by the Fischer-Tropsch reaction. Taking the different time axes in Figure 5.16(a) and Figure 5.16(b) into account, the carbon deposition is not faster in 2 H_2 + 1 CO than in 4 H_2 + 1 CO suggesting that the removal of C is not limited by the exact H_2 partial pressure in this pressure range. Although there seems to be a jump in the C coverage when increasing the temperature to 250 °C, the further C deposition at this temperature (measured only in 4 H_2 + 1 CO) does not clearly display a larger rate than at 220 °C. Thus, any increase in the rate of CO dissociation with increased temperature seems to be compensated by a faster C removal by H_2. These observations seem to be in contrast to magnetometer studies on an industrial catalyst where the rate of carbide formation, although deemed insignificant in general, was found to decrease with an increased H_2-to-CO-ratio as well as with increased temperature [280]. However, a direct comparison of such literature to our experiments is not justified given the use of a single crystal, the lower pressure range, and significantly shorter time frame investigated here. It is especially unclear whether the C deposition would keep increasing linearly over time, thus covering the whole surface after on the order of tens of hours, or whether it would saturate at a certain coverage in an equilibrium between deposition and removal. Generally, only specific polymeric, graphitic, and bulk carbides are deemed a poison to the catalyst [216,219,246], whereas all surface carbon that is hydrogenated at FT gas ratios and temperatures can be considered a reaction intermediate. Figure 5.23(b) in the supplemental information shows that, although both carbidic and graphitic carbon follow a similar trend in time, most adsorbed C is carbidic. However, our results in Section 5.3.4 show that both forms of carbon detected here could be removed by exposure to 0.25 mbar H_2 and are thus likely not carbon species responsible for significant catalyst poisoning.

Starting out with an absolute value of 0.04 and 0.03 at 220 °C respectively, in both reaction mixtures there are more hydrocarbons adsorbed than in UHV and H_2, but they are in the same order of magnitude as in 0.25 mbar CO (see Section 5.3.5). However, the absolute hydrocarbon coverage is higher in 4 H_2 + 1 CO than in 2 H_2 + 1 CO, thus scaling inversely with the CO partial pressure. This can for example be seen by comparing the measurement after 2 h at 220 °C and the first measurement at 250 °C for the two different gas ratios in Figure 5.16. Thus, it can be excluded that all hydrocarbons stem from the background of the CO gas. Additionally, the hydrocarbon coverages follow roughly the same trend over time as the C coverage including a stronger increase after increasing the temperature indicating that at least part of the hydrocarbons could stem from the same reaction process as the carbon. Under industrial conditions on cobalt catalysts a higher H_2-to-CO-ratio has a positive effect on the turnover for short products and switches to a negative effect on the turnover for longer products from a length of roughly 15 carbon atoms on [281]. This can be explained by a decreased chain growth probability α in the Anderson-Schulz-Flory chain-growth model [282] with increasing H_2-to-CO-ratio. On Co(0001), the Fischer-Tropsch product distribution decreases exponentially from methane to longer chains with mainly C_1 to C_4 products detected at atmospheric pressures [243,283]. Therefore, mainly methanation is measured on Co(0001) in the mbar range [127]. The methane turnover on Co(0001) does increase with increasing H_2-to-CO-ratio [284,285]. Thus, mainly shorter products can be assumed here and a higher activity in 4 H_2 + 1 CO compared to 2 H_2 + 1 CO is likely. However, even if it is the main product, methane will likely not stay adsorbed on the Co(0001) surface [286] and is thus likely not the species detected by XPS. In contrast, it can be expected that the adsorption strength of the products increases roughly linearly with the chain length [287,288], which results in an exponential increase in the residence time on the surface. Based on this assumption Navarro et al. [47] have modeled the adsorption of products on Co(0001) over time. Their result that a chain length of at least 15 carbon atoms is needed to reach a significant coverage on the surface agrees well with the length they find experimentally. As our experiments are done at lower pressures, it is to be expected that a full coverage with products could only be reached after a significantly longer time than the 30 min Navarro et al. [47] observed in the same temperature range. The sum of the coverages of all adsorbates stays within 0.6 to 0.7 for both reaction mixtures over the time of hours tested here. This confirms that the surface is not fully covered with products and excludes any influence of space limitation on the measured coverages. To shed more light on the nature of the adsorbed hydrocarbons, Figure 5.23(c) in the supplemental information distinguishes the two different peaks contributing to the overall hydrocarbon coverages displayed in Figure 5.16. In both gas ratios the two types show a similar increase over time at 220 °C with the hydrocarbon type labeled II clearly being dominant (at least 70 % of the total hydrocarbon coverage). However, at 250 °C the amount of type I strongly increases over time, whereas type II starts to desorb. If both hydrocarbons were from the reaction, one would have to conclude that the increase of the desorption rate of type II strongly exceeds the increase of the rate of its formation when increasing the temperature from 220 °C to 250 °C, whereas for type I the increase of rate of formation strongly exceeds the increase of the desorption rate when increasing the temperature from 220 °C to 250 °C. As type I is more strongly adsorbed, it would be a longer hydrocarbon than type II in this case. However, the formation of different products shows a comparable temperature dependence on Co(0001) [283], whereas in industrial FTS the product distribution would rather shift to shorter chain lengths with increasing temperature [212]. Therefore, we deem it more likely that the hydrocarbon type II stems from the gas background whereas type I is a reaction product, which agrees with the results of Section 5.3.5. Generally, the deposition of products, although it can poison the catalyst [216], can also be considered part of the initiation phase of the catalyst after which the desorption of subsequent products is facilitated [47].

The sulfur coverage increases to maximally 0.001 within 4 h in the reaction mixture for both gas ratios. Thus, although sulfur is known to easily block CO oxidation on Co(0001) [220,289] as well as more industrially relevant catalysts [221], it is not a significant poison in the conditions and time frame studied here.

5.4 Conclusions and Outlook

Generally, the oxidation behavior of cobalt during FTS depends on a number of factors: the structure of the sample, the water partial pressure, and the H_2-to-CO-ratio. For the case of Co(0001), CO is more efficient at keeping the cobalt metallic compared to H_2 at the same total pressure of 0.25 mbar as measured here by in situ XPS. We have suggested that this behavior can be explained on the basis of the different adsorption and dissociation sites of H_2, CO, and H_2O, respectively. Namely, CO adsorbs equally well on the steps and vacancies as on the terrace sites and is therefore able to block the dissociation of water, which most likely proceeds at low-coordinated sites. In comparison, H_2 prefers the Co(0001) terrace sites for adsorption and can therefore not prevent the H_2O dissociation in this pressure range. Under reaction conditions of 4 H_2 + 1 CO and 2 H_2 + 1 CO at 220 °C to 250 °C the surface stays mainly metallic.

We have developed a theoretical model to convert the measured intensities of all adsorbed species to quantitative coverage values. Comparisons to values expected from literature have confirmed the validity of this model in combination with an experimental calibration.

The high-resolution carbon areas measured at the HIPPIE beamline of MaxIV allow for the distinction of a number of species. In this way it can be seen that at least 70 % of the carbon adsorbed on the surface during the reaction at 220 °C is carbidic and thus a reaction intermediate that can easily be removed by hydrogenation. Additionally, two different hydrocarbon peaks in the fit allowed for the distinction of hydrocarbons adsorbed from the CO gas background and formed by the Fischer-Tropsch reaction.

We plan to further study the effect of the water partial pressure on the oxidation behavior of Co(0001) by recording phase diagrams with and without drying of the gases. At a high-flux beamline this can be done via quick O 1s, C 1s, and Co 2p scans while continuously changing the conditions within a larger range of H_2-to-CO-ratios and temperatures. Additionally, the identification of the different CO adsorption peaks should be confirmed by more detailed studies in a larger CO pressure range from UHV to mbars.

5.5 Supplemental Information

5.5.1 Beam-induced Deposition

Figure 5.18 compares the carbon and hydrocarbon coverage measured over time in the reaction mixture at 220 °C while staying in one position on the surface (thus with strong beam exposure) to measurements where the beam exposure was minimized. To achieve the minimum beam exposure we have moved to a new position on the sample right before every measurement of the carbon area. In this way the influence by the beam is as small as possible and stays constant over time between measurements taken at the same temperature. When comparing two consecutive sweeps of every such carbon area measurement, no difference is detectable, which confirms that the beam-induced deposition does not play a role in the time frame in which the carbon signal is measured. However, as the O 1s and Co 2p areas are measured later in time, they

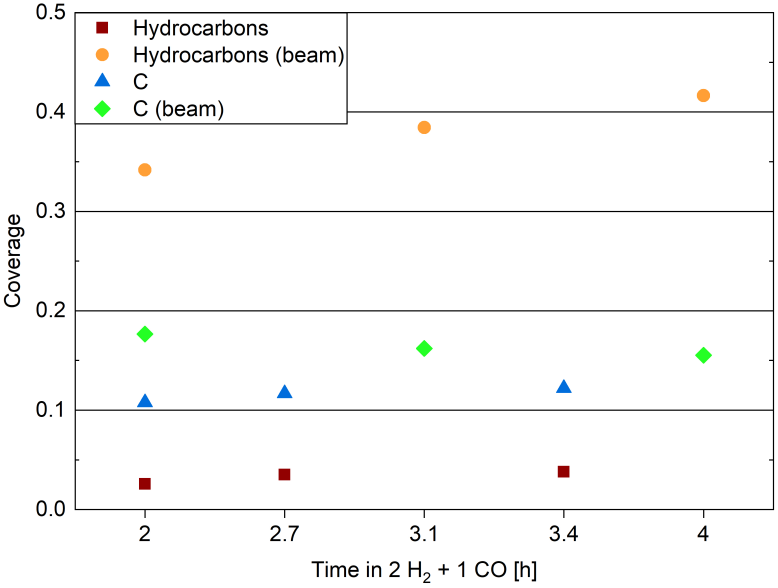

Figure 5.18: Coverages of carbon and hydrocarbons measured on Co(0001) in 0.25 mbar 2 H_2 + 1 CO at 220 °C over time comparing measurements done with strong beam exposure, labeled (beam), to measurements done while minimizing beam exposure as explained in the text.

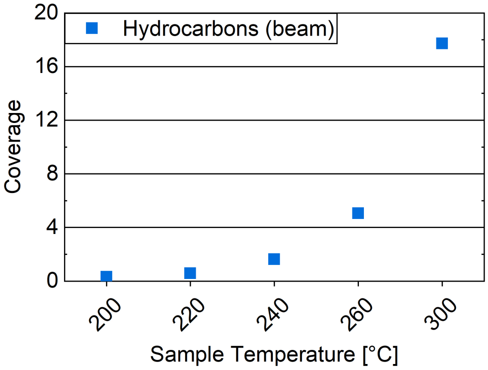

Figure 5.19: Hydrocarbon coverage on Co(0001) measured in 0.25 mbar 2 H_2 + 1 CO at increasing temperature. The sample was held at every temperature step for roughly 2.5 h under continuous beam exposure at the same position. As explained in Section 5.2.3, the coverage values displayed here are calculated as the number of layers that would be present if the hydrocarbons covered the whole surface in the absence of other adsorbates.

could still be slightly influenced by a change in carbon species over time. The same procedure is used for all measurements shown in the previous sections.

In detail, the comparison in Figure 5.18 shows a somewhat higher coverage of C, likely stemming from beam-induced CO dissociation. Subtracting the two values at 2 h results in a maximum beam-induced C coverage of 0.07. However, this difference decreases over time, likely because more surface area gets blocked by hydrocarbons on the surface with strong beam exposure. The detailed fits show that between 69 % and 80 % of the carbon is carbidic on the beam-exposed sample. This is in the same range as on the sample with minimized beam exposure (70 % to 76 %), thus not suggesting any promotion of graphite formation by the beam.

The deposition of hydrocarbons is more strongly increased on the sample with strong beam exposure, roughly by a factor of 10 compared to the sample with minimum exposure. This suggests a beam-induced Fischer-Tropsch reaction. The detailed fits show that all of the beam-induced hydrocarbon is the one labeled here as type I. This is the type identified as a Fischer-Tropsch product of the cobalt-catalyzed reaction in Section 5.3.6. There, it was formed significantly faster at 250 °C compared to at 220 °C. Thus, the beam might practically have a similar effect as an increased temperature. The beam-induced deposition could be observed starting from 220 °C surface temperature on and proceeds faster at higher temperatures. While increasing the temperature from 220 °C to 300 °C in the reaction mixture over a course of roughly 8 h, the hydrocarbon coverage increased exponentially (see Figure 5.19) and reached a total of 18 layers. As explained in Section 5.2.3, at these kind of coverages the model used for the calculations is not accurate and this is thus a rough estimate at best. However, it is clear that the cobalt terraces are completely covered before reaching this amount of hydrocarbons. This additionally suggests that the cobalt surface itself might not be necessary for the beam-induced reaction, although the steps could still be involved. In contrast to type II, the hydrocarbon type I does not seem to desorb in the temperature range investigated here, thus being able to cover the whole surface and making it crucial to minimize the beam exposure.

5.5.2 Detailed Fit Results

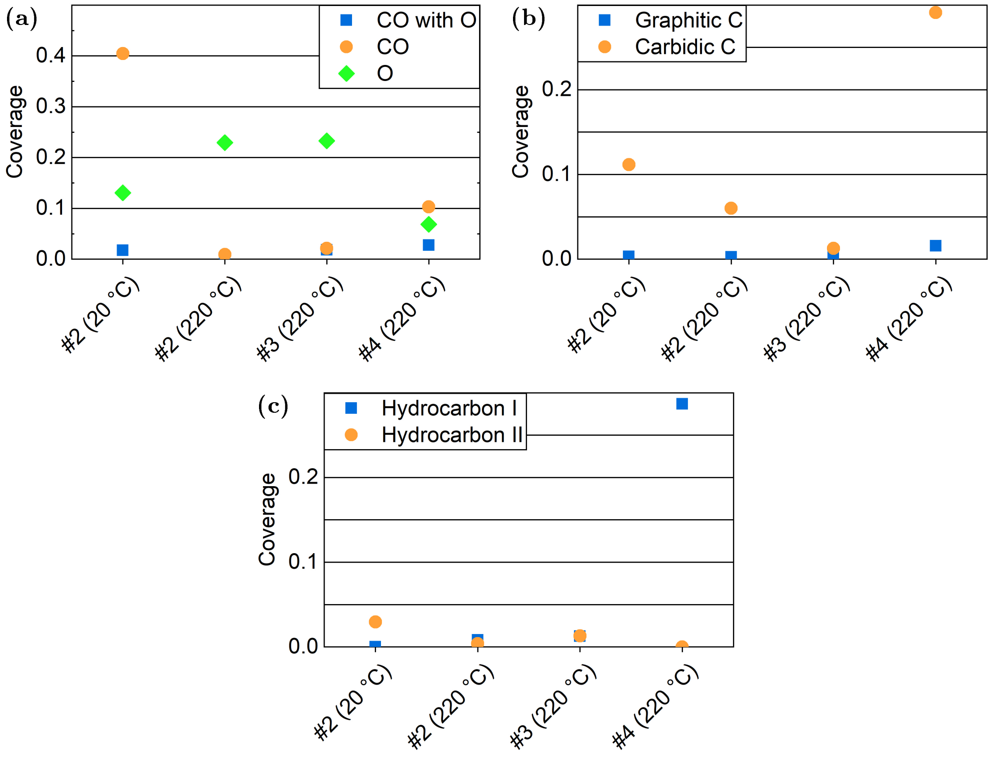

Figure 5.20: Results of the detailed fits of C 1s spectra measured on different as-prepared samples in UHV (a) distinguishing CO alone from CO co-adsorbed with O compared to the O coverage from the O 1s spectra, (b) distinguishing carbidic and graphitic C, and (c) distinguishing two types of hydrocarbons.

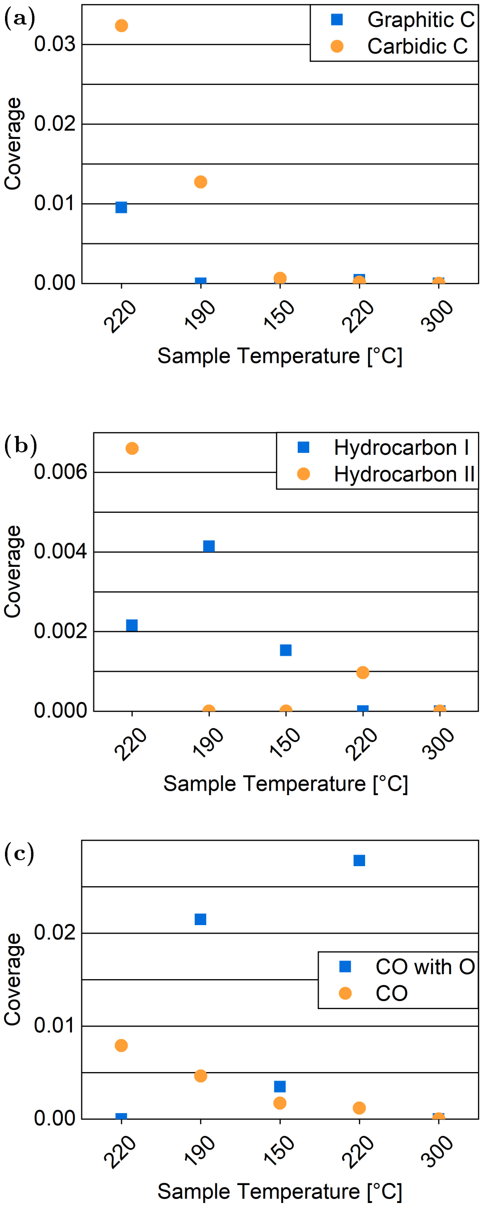

Figure 5.21: Results of the detailed fits of C 1s spectra measured in 0.25 mbar H_2 at different temperatures distinguishing (a) carbidic from graphitic C, (b) two types of hydrocarbons, and (c) CO alone from CO co-adsorbed with O.

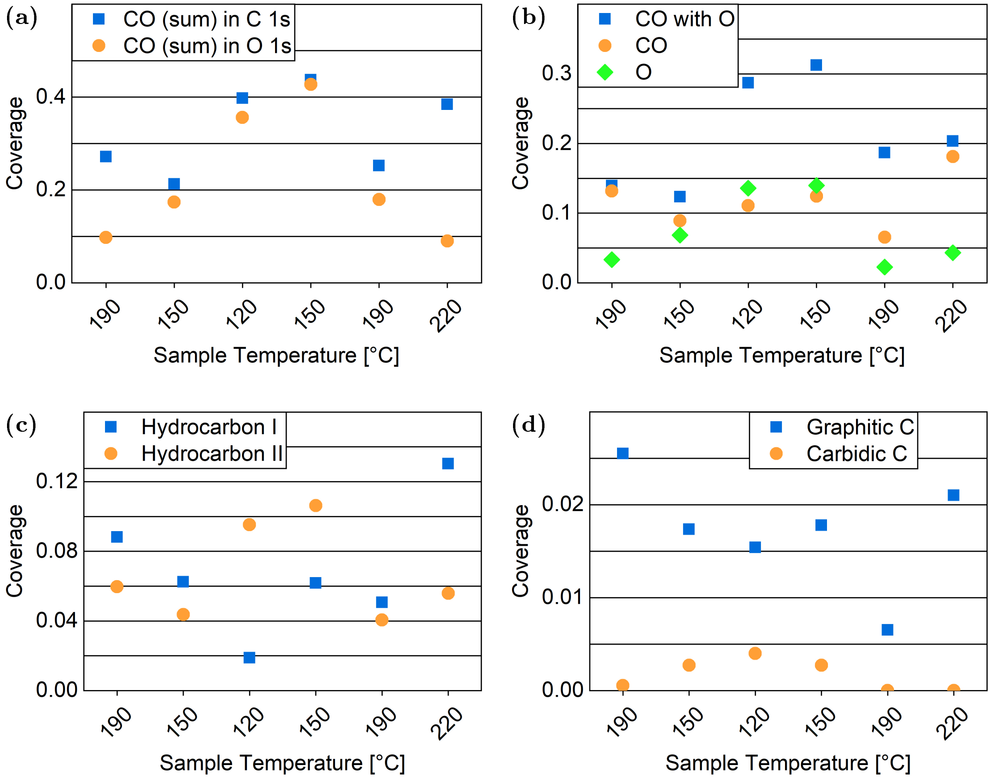

Figure 5.22: Results of the detailed fits of the spectra measured in 0.25 mbar CO at different temperatures (a) comparing the total CO coverage calculated from the C 1s spectra to the total CO coverage calculated from the O 1s spectra, (b) distinguishing CO alone from CO co-adsorbed with O compared to the O coverage, (c) distinguishing two types of hydrocarbons, and (d) distinguishing carbidic from graphitic C.

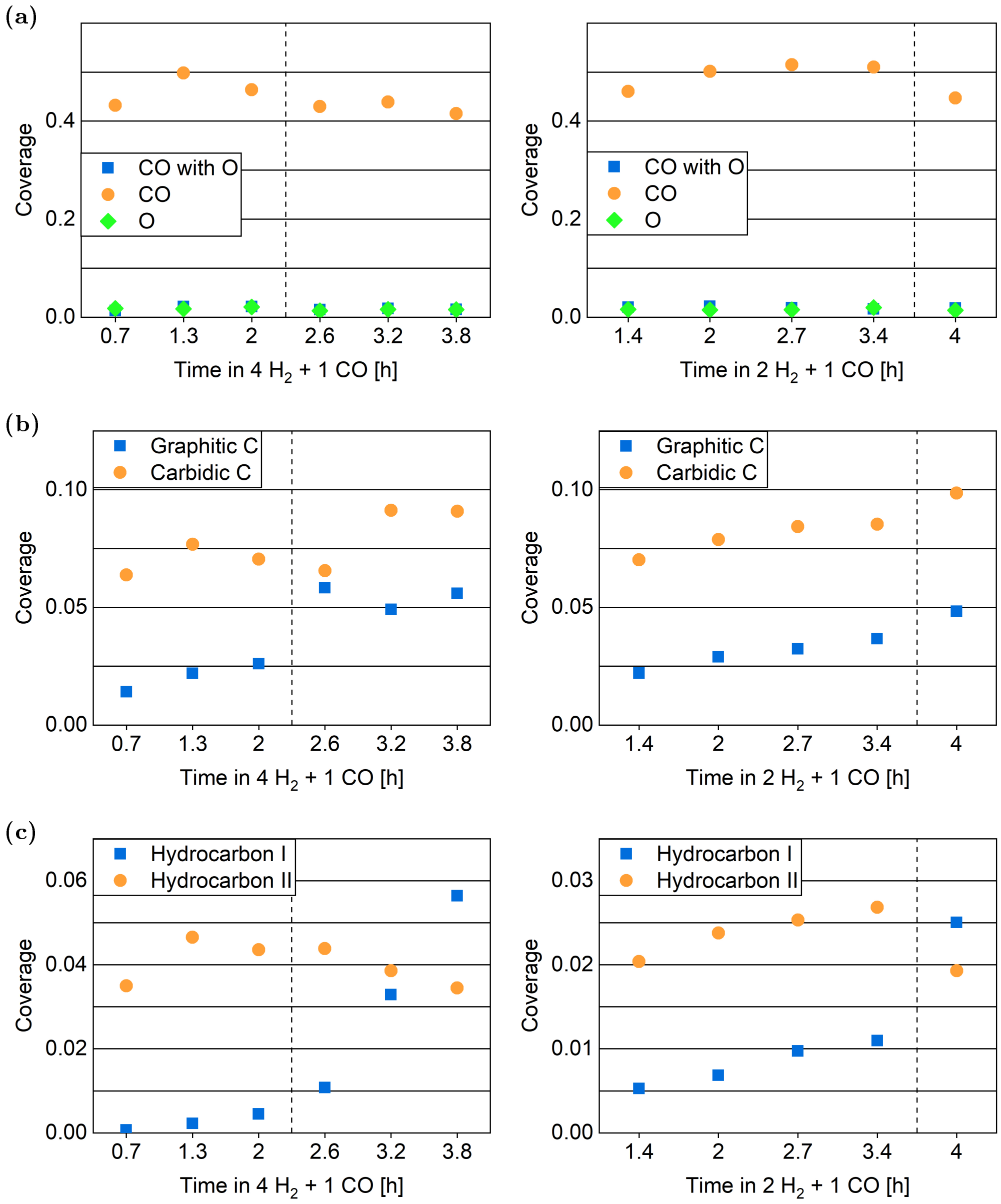

Figure 5.23: Results of the detailed fits of C 1s spectra measured in 0.25 mbar of 4 H_2 + 1 CO (left column) and 2 H_2 + 1 CO (right column) (a) distinguishing CO alone from CO co-adsorbed with O compared to the O coverage from the O 1s spectra, (b) distinguishing carbidic from graphitic C, and (c) distinguishing two types of hydrocarbons. The dashed, vertical lines mark an increase of the temperature from 220 °C to 250 °C.

Chapter 6

Summary and Outlook

Catalyst applications are vast and include the areas of energy supply and sustainability [2–10]. All types of catalysts increase the activity and/or selectivity of a reaction while returning back to their original state themselves [11,12]. Heterogeneous catalysts in particular are solid surfaces that catalyze gas-phase reactions. Surface science aims at understanding how such surfaces catalyze the reaction in detail on the atomic level [20]. Standard surface-science techniques such as microscopy, spectroscopy, and diffraction techniques are easiest applied on flat metal single crystals in ultra-high vacuum. As industrial catalysts function at atmospheric or even significantly higher pressures, one speaks of the pressure gap between research and application [21]. There is considerable effort in bridging this gap by developing various in situ techniques [37]. The ReactorSTM, used in Chapters 3 and 4, is a scanning tunneling microscope inside a flow-reactor cell which is incorporated into an ultra-high vacuum chamber [44]. In this way it combines the controlled preparation and characterization of model catalysts with imaging in atmospheric gas pressures revealing the structure of the catalytic surface during the reaction [46–48]. Near-ambient pressure X-ray photoelectron spectroscopy (NAP-XPS) on the other hand can reveal chemical states of surface atoms as well as adsorbed species during the reaction in the mbar pressure range [54]. In combination with synchrotron X-rays, as used in Chapter 5, this technique allows for high surface sensitivity, energy resolution, as well as swift measurements [230,231]. Apart from the pressure difference, industrially used catalysts also consist of multiple components with complex structures compared to single crystals studied in surface science. In order to bridge this so-called materials gap [21], model catalysts are made increasingly more complex from flat metal single crystals to stepped [22] and curved [24] single crystals, oxide single crystals [30], and metal [31], oxide [29], as well as sulfide [32] nanoparticles on top of the different single crystals. This thesis presents work on a metal single crystal, an oxide single crystal, as well as a complex model catalyst containing nanoparticles.

Chapter 3 presents a first-time use of a ZnO($10\bar{1}0$) single crystal in the ReactorSTM. Zinc oxide is part of the most-studied catalyst for methanol steam reforming, Cu-ZnO/Al_2O_3 [72,75,76]. The use of such a catalyst in hydrogen fuel-cell vehicles could make them safer and more convenient. However, the main challenge is for the catalyst to be highly selective for producing CO_2 instead of the side product CO, for which the zinc oxide could play a significant role [79,80]. Although ZnO($10\bar{1}0$) is a flat single crystal, we mention a number of challenges that come with its use in scanning tunneling microscopy in UHV. Among these are its affinity for H_2O adsorption from the UHV background, the incorporation of argon below the surface, and a loss of conductivity with repeated preparation, which we interpret as a loss of natural hydrogen impurities. Another experimental challenge is the amount of background water in the in situ cell of the ReactorSTM, which we measure in detail in Chapter 3 and relate it to the design of the gas delivery system. This leads to a water pressure on the order of roughly 1 mbar when filling the cell to 1 bar total pressure of any gas. When exposing the $ZnO(10\bar{1}0)$ surface to argon in the ReactorSTM, this water leads to a roughening of the surface in the form of the formation of a large number of additional steps on top of the original terraces. In this process, the formation of (0001)- and $(000\bar{1})$-type steps is favored compared to $(1\bar{2}10)$-type steps, which we interpret to be in contradiction with theoretical but in agreement with experimental literature. Preliminary results on the exposure of $ZnO(10\bar{1}0)$ to wet hydrogen suggest that a stabilizing effect of the terraces might be able to counteract the roughening. As water is a reactant in the methanol steam reforming reaction, it has to be concluded that the $(10\bar{1}0)$ face of zinc oxide might not be stable under reaction conditions and the applicability of UHV studies on $ZnO(10\bar{1}0)$ as a model for the industrial process is rather limited. Although we suggest the use of dried gases to confirm the role of water, as well as studies at temperatures more relevant for the catalytic application, further use of $ZnO(10\bar{1}0)$ in the ReactorSTM would first require systematic trials to improve its preparation method.

In Chapter 4 we move on to studying a more complex, yet inverted, model catalyst, $TiO_2/Au(111)$, which is prepared via physical vapor deposition. Gold-based catalysts, usually applied in the form of gold nanoparticles on different oxide supports, are active for CO oxidation at lower temperatures compared to more conventional catalysts [134]. Therefore, they could reduce CO emissions during the cold start-up of combustion engine vehicles. Additionally, the lower reaction temperature allows for the selective oxidation of CO in H_2 environment over gold-based catalysts [131–133], which can again supply clean hydrogen for fuel-cell vehicles. However, the reaction mechanism including the oxidation state of the gold during the reaction [158–160], the role of the oxide support [34,149–153], as well as the role of water in the gas mixture [161–164] are not unambiguously identified in the current literature. First studying the Au(111) substrate in the ReactorSTM, we observe the formation of gold oxide islands under exposure to atmospheric pressures of oxygen, CO oxidation reaction conditions, or CO alone. The surface oxide can be identified by its unit cell, which is also formed when exposing Au(111) to atomic oxygen. Although the presence of oxygen on the surface can be confirmed with lab-based XPS, the surface sensitivity and energy resolution of synchrotron near-ambient pressure XPS will be necessary for the detection of oxidized gold. As the gold oxide islands observed here are always connected to a step edge of Au(111) and molecular oxygen is unlikely to dissociate by itself [171], we interpret the formation in line with the water-enabled dissociation of O_2 on the step edge of Au(111) as it is suggested from theoretical studies [174]. On the other hand, the presence of contaminants on the gold surface can strongly promote the gold oxide formation even on the terraces. As background water as well as contaminants in the gold are likely present on industrial catalysts under realistic reaction conditions, it can be concluded that the presence of the oxide is likely as well. However, certain reaction studies in literature disagree on whether this would promote or rather poison the reaction [158–160]. Additionally, the exposure of TiO_2/Au(111) to CO oxidation reaction conditions in the ReactorSTM has revealed no difference in the gold oxide formation compared to the Au(111) substrate alone. This suggests that, although (defected) TiO_2 might dissociate O_2 [181,182], the resulting atomic oxygen does not end up on the gold substrate. Thus, the atomic oxygen spillover from TiO_2 to Au is not part of the CO oxidation reaction mechanism on TiO_2/Au(111). The ReactorSTM offers a number of opportunities to further study this system: the interaction of Au(111) with CO alone and resulting carbon depositions, the influence of a hydrogen environment on the catalyst structure including the gold oxide formation, and a comparison of TiO_2/Au(111) to its non-inverse counterpart, gold nanoparticles on a TiO_2 single crystal.

Chapter 5 of this thesis focuses on a different in situ technique, near-ambient pressure X-ray photoelectron spectroscopy, performed at Max IV [231] as well as at the ALS [230]. A cobalt single crystal is used as a model for a Fischer-Tropsch synthesis catalyst. This reaction [205] allows for the production of cleaner [208,209], synthetic fuels from syngas, a mixture of H_2 and CO, which can be produced from natural gas, oil, or renewable sources. Cobalt catalysts, although already used industrially [211,212], are investigated in line with a number of deactivation mechanisms [216,217] like oxidation [222–225] and the deposition of carbon, sulfur, and reaction products [218–221]. It is clear from the current state of the literature that the oxidation behavior can strongly depend on the H_2-to-CO ratio, the water partial pressure, as well as the structure of the cobalt sample [227,228]. As one piece to this puzzle, we thus present the first NAP-XPS results measured on Co(0001) during Fischer-Tropsch synthesis at 0.25 mbar total pressure. In this case CO seems to be more efficient at keeping the Co(0001) surface metallic than H_2, especially as the water background is able to oxidize the Co(0001) in H_2 even when a liquid nitrogen trap is used to dry the hydrogen. Although the opposite behavior is reported in lower [229] as well as higher [242] total pressure ranges, these results roughly agree with those on cobalt foil in a similar pressure range [226]. We offer a possible interpretation of the difference between the interaction of CO and H_2 with Co(0001) at different pressures based on their preferred adsorption and dissociation sites compared to water. Relevant for this explanation is that, in experimental studies, a Co(0001) surface cannot be perfectly flat but contains steps and vacancies. However, the picture is not yet complete and we suggest near-ambient pressure studies on Co(0001) in a larger range of gas composition, total pressure, and temperature. Additionally, Chapter 5 presents a model to convert measured spectra into coverages on the Co(0001) surface, which is applied to quantify the adsorbed products as well as poisons during the reaction. Here, detailed carbon spectra can aid in the identification of different carbon species, hydrocarbon products, and CO adsorption sites, which should, however, be confirmed in future studies.

Although this thesis gives examples of model catalysts based on metals and oxides often used to bridge the materials gap, other materials such as alloys are not used as routinely yet. An example would be PdZn, which is a promising catalyst for methanol steam reforming [290]. PdZn can be studied with surface-science techniques when it is formed on top of zinc oxide single crystals after the deposition of palladium [291]. However, in these cases it cannot be excluded that results are influenced by the surrounding elements and the specific structure of the supported alloy. To our knowledge, there is no established method to prepare macroscopic single crystals of alloys when the melting temperatures of the two metals differ as significantly as between palladium and zinc. Currently, such a method is being developed in Leiden. It is based on an existing single-crystal face of the metal with the higher melting point, Pd(111) in the case of PdZn. The zinc is introduced in the form of a Zn rod, which is placed in a hole in the back of the Pd(111) crystal and enclosed with additional palladium. When carefully heating the crystal in ultra-high vacuum, zinc atoms will diffuse through the palladium crystal until they reach the surface. Using a surface-sensitive and spatially resolved spectroscopy technique, the formation of the alloy on the surface can then be studied as a function of the distance from the center. If the original zinc rod has a significantly smaller diameter than the palladium single crystal, the zinc-to-palladium-ratio decreases from the center to the sides of the crystal surface. This gradient could allow for a number of spatially resolved studies, like molecular beam studies and in situ spectroscopy, to shed light on the influence of the zinc-to-palladium-ratio on the catalytic activity. When successful, this method to prepare alloy single crystals could in principle be expanded to many other alloys of which no single crystals are available at the moment.

In general, the results presented in this thesis exemplify how low concentrations of contaminants in the gas phase as well as in sample materials can have a significant effect when moving from UHV to in situ studies in order to bridge the pressure and materials gaps. Often, such effects are suppressed by using very pure materials and gases, which simplifies the interpretation of data. The ReactorSTM used in Chapters 3 and 4 suffers from a large water background. Based on tests done in line with this thesis, we consider a complete redesign of the gas delivery system necessary to allow for proper drying of the gases. However, drying and purifying again reduces the relevance of the obtained results for realistic reaction conditions, which undermines the motivation for in situ surface science. Therefore, we suggest more systematic comparisons of pure compared to non-pure studies, which can be achieved by consciously not drying gases, or intentionally adding water, and for example controllably depositing small amounts of certain contaminants onto clean samples. At the same time the behavior of complex model catalysts can only be understood well if every component is investigated separately before combining them. Additionally, it is crucial to include specific information about the gases, materials, setups, and gas delivery systems in publications to facilitate literature comparisons. The interpretation of data and comparisons of pure and non-pure studies can be especially challenging at user facilities such as those used in Chapter 5 as the user is not too familiar with the design of the gas delivery system and the possible sources of contaminants.

References

[1] `https://www.un.org/sustainabledevelopment/sustainable-development-goals/` accessed on 09.03.2021.

[2] C. Marcilly. “Present status and future trends in catalysis for refining and petrochemicals”. *Journal of Catalysis* 216 (2003), 47–62.

[3] J. R. Rostrup-Nielsen. “Fuels and Energy for the Future: The Role of Catalysis”. *Catalysis Reviews* 46 (2004), 247–270.

[4] R. Chaubey, S. Sahu, O. O. James, and S. Maity. “A review on development of industrial processes and emerging techniques for production of hydrogen from renewable and sustainable sources”. *Renewable and Sustainable Energy Reviews* 23 (2013), 443–462.

[5] J. Ma, N. Sun, X. Zhang, N. Zhao, F. Xiao, W. Wei, and Y. Sun. “A short review of catalysis for CO_2 conversion”. *Catalysis Today* 148 (2009), 221–231.

[6] S. Wacławek, V. V. Padil, and M. Černík. “Major Advances and Challenges in Heterogeneous Catalysis for Environmental Applications: A Review”. *Ecological Chemistry and Engineering S* 25 (2018), 9–34.

[7] S. Rood, S. Eslava, A. Manigrasso, and C. Bannister. “Recent advances in gasoline three-way catalyst formulation: A review”. *J Automobile Engineering* 234 (2020), 936–949.

[8] H.-U. Blaser. “Heterogeneous catalysis for fine chemicals production”. *Catalysis Today* 60 (2000), 161–165.

[9] J. W. Erisman, M. A. Sutton, J. Galloway, Z. Klimont, and W. Winiwarter. “How a century of ammonia synthesis changed the world”. *Nature Geoscience* 1 (2008), 636–639.

[10] M. Bilal and H. M. Iqbal. “State-of-the-art strategies and applied perspectives of enzyme biocatalysis in food sector - current status and future trends”. *Critical Reviews in Food Science and Nutrition* 60 (2020), 2052–2066.

[11] I. Chorkendorff and J. Niemantsverdriet. “Introduction to Catalysis”. In: *Concepts of modern catalysis and kinetics.* 2nd, revised and enlarged. Germany: Wiley-VCH Verlag, 2007.

[12] L. Lefferts, U. Hanefeld, and H. Bitter. “Introduction”. In: *Catalysis An Integrated Approach.* Netherlands Institute of Catalysis, 2016. Chap. 1.

[13] J. A. Bennett, K. Wilson, and A. F. Lee. “Catalytic applications of waste derived materials”. *J. Mater. Chem. A* 4 (2016), 3617–3637.

[14] Z. W. Chen, L. X. Chen, C. C. Yang, and Q. Jiang. “Atomic (single, double, and triple atoms) catalysis: frontiers, opportunities, and challenges”. *J. Mater. Chem. A* 7 (2019), 3492–3515.

[15] A. O. Ibhadon and P. Fitzpatrick. “Heterogeneous photocatalysis: Recent advances and applications”. *Catalysts* 3 (2013), 189–218.

[16] H.-h. Kim, Y. Teramoto, A. Ogata, H. Takagi, and T. Nanba. “Plasma Catalysis for Environmental Treatment and Energy Applications”. *Plasma Chemistry and Plasma Processing* 36 (2016), 45–72.

[17] A. W. Kleyn. “Molecular beams and chemical dynamics at surfaces”. *Chemical Society Reviews* 32 (2003), 87–95.

[18] R. A. v. Santen. “Molecular Heterogeneous Catalysis”. In: *Modern Heterogeneous Catalysis*. John Wiley & Sons, Ltd, 2017. Chap. II.

[19] B. W. Chen, L. Xu, and M. Mavrikakis. “Computational methods in heterogeneous catalysis”. *Chemical Reviews* 121 (2021), 1007–1048.

[20] K. Oura, V. G. Lifshits, A. A. Saranin, A. Zotov, and M. Katayama. *Surface Science. An Introduction*. Springer-Verlag Berlin Heidelberg, 2003.

[21] R. Schlögl. “Heterogeneous catalysis”. *Angewandte Chemie - International Edition* 54 (2015), 3465–3520.

[22] N. Musselwhite and G. A. Somorjai. “Investigations of structure sensitivity in heterogeneous catalysis: From single crystals to monodisperse nanoparticles”. *Topics in Catalysis* 56 (2013), 1277–1283.

[23] J. X. Liu and W. X. Li. “Theoretical study of crystal phase effect in heterogeneous catalysis”. *Wiley Interdisciplinary Reviews: Computational Molecular Science* 6 (2016), 571–583.

[24] S. V. Auras. “Exploring structure dependencies of gas-surface interactions with curved single crystals”. PhD thesis. Leiden University, 2021.

[25] N. Nilius. “Properties of oxide thin films and their adsorption behavior studied by scanning tunneling microscopy and conductance spectroscopy”. *Surface Science Reports* 64 (2009), 595–659.

[26] Ü. Özgür, Y. I. Alivov, C. Liu, A. Teke, M. A. Reshchikov, S. Doğan, V. Avrutin, S. J. Cho, and H. Morkoç. “A comprehensive review of ZnO materials and devices”. *Journal of Applied Physics* 98 (2005), 1–103.

[27] B. H. Liu, J. A. Boscoboinik, Y. Cui, S. Shaikhutdinov, and H. J. Freund. “Stabilization of ultrathin zinc oxide films on metals: Reconstruction versus hydroxylation”. *Journal of Physical Chemistry C* 119 (2015), 7842–7847.

[28] M. M. Biener and C. M. Friend. “Heteroepitaxial growth of novel MoO_3 nanostructures on Au(111)”. *Surface Science* 559 (2004), L173–L179.

[29] J. A. Rodriguez, P. Liu, J. Graciani, S. D. Senanayake, D. C. Grinter, D. Stacchiola, J. Hrbek, and J. Fernández-Sanz. “Inverse Oxide/Metal Catalysts in Fundamental Studies and Practical Applications: A Perspective of Recent Developments”. *Journal of Physical Chemistry Letters* 7 (2016), 2627–2639.

[30] H.-J. Freund, H. Kuhlenbeck, and V. Staemmler. “Oxide surfaces”. *Rep. Prog. Phys.* 59 (1996), 283–347.

[31] J. Libuda and H. J. Freund. “Molecular beam experiments on model catalysts”. *Surface Science Reports* 57 (2005), 157–298.

[32] F. Besenbacher, M. Brorson, B. S. Clausen, S. Helveg, B. Hinnemann, J. Kibsgaard, J. V. Lauritsen, P. G. Moses, J. K. Nørskov, and H. Topsøe. "Recent STM, DFT and HAADF-STEM studies of sulfide-based hydrotreating catalysts: Insight into mechanistic, structural and particle size effects". *Catalysis Today* 130 (2008), 86–96.

[33] I. Ro, J. Resasco, and P. Christopher. "Approaches for Understanding and Controlling Interfacial Effects in Oxide-Supported Metal Catalysts". *ACS Catalysis* 8 (2018), 7368–7387.

[34] R. M. Palomino, R. A. Gutiérrez, Z. Liu, S. Tenney, D. C. Grinter, E. Crumlin, I. Waluyo, P. J. Ramírez, J. A. Rodriguez, and S. D. Senanayake. "Inverse Catalysts for CO Oxidation: Enhanced Oxide-Metal Interactions in MgO/Au(111), CeO_2/Au(111), and TiO_2/Au(111)". *ACS Sustainable Chemistry and Engineering* 5 (2017), 10783–10791.

[35] K. Hayek, M. Fuchs, B. Klötzer, W. Reichl, and G. Rupprechter. "Studies of metal-support interactions with "real" and "inverted" model systems: reactions of CO and small hydrocarbons with hydrogen on noble metals in contact with oxides". *Topics in Catalysis* 13 (2000), 55–66.

[36] L. Lefferts, E. Hensen, and H. Niemantsverdriet. "Heterogeneous Catalysis". In: *Catalysis An Integrated Approach.* Netherlands Institute of Catalysis, 2016. Chap. 2.

[37] J. Frenken and I. Groot, eds. *Operando Research in Heterogeneous Catalysis.* Springer International Publishing Switzerland, 2017.

[38] W. G. Onderwaater, A. Taranovskyy, G. M. Bremmer, G. C. Van Baarle, J. W. Frenken, and I. M. Groot. "From dull to shiny: A novel setup for reflectance difference analysis under catalytic conditions". *Review of Scientific Instruments* 88 (2017), 023704.

[39] M. Xu, S. Dai, P. Tieu, X. Ren, F. Ye, and X. Pan. "In Situ TEM Studies of Catalysts Using Windowed Gas Cells". *Catalysts* 10 (2020), 779.

[40] F. M. de Groot, E. de Smit, M. M. van Schooneveld, L. R. Aramburo, and B. M. Weckhuysen. "In-situ scanning transmission X-ray microscopy of catalytic solids and related nanomaterials". *ChemPhysChem* 11 (2010), 951–962.

[41] E. Laegsgaard, L. Österlund, P. Thostrup, P. B. Rasmussen, I. Stensgaard, and F. Besenbacher. "A high-pressure scanning tunneling microscope". *Review of Scientific Instruments* 72 (2001), 3537–3542.

[42] M. Rößler, P. Geng, and J. Wintterlin. "A high-pressure scanning tunneling microscope for studying heterogeneous catalysis". *Review of Scientific Instruments* 76 (2005), 023705.

[43] F. Tao, D. Tang, M. Salmeron, and G. A. Somorjai. "A new scanning tunneling microscope reactor used for high-pressure and high-temperature catalysis studies". *Review of Scientific Instruments* 79 (2008), 084101.

[44] C. T. Herbschleb, P. C. V. D. Tuijn, S. B. Roobol, V. Navarro, J. W. Bakker, Q. Liu, D. Stoltz, G. Verdoes, M. A. V. Spronsen, M. Bergman, L. Crama, I. Taminiau, A. Ofitserov, G. J. C. V. Baarle, and J. W. M. Frenken. "The ReactorSTM: Atomically resolved scanning tunneling microscopy under high-pressure, high-temperature catalytic reaction conditions". *Review of Scientific Instruments* 85 (2014), 083703.

[45] S. B. Roobol, M. E. Cañas-Ventura, M. Bergman, M. A. Van Spronsen, W. G. Onderwaater, P. C. Van Der Tuijn, R. Koehler, A. Ofitserov, G. J. Van Baarle, and J. W. Frenken. "The ReactorAFM: Non-contact atomic force microscope operating under high-pressure and high-temperature catalytic conditions". *Review of Scientific Instruments* 86 (2015), 033706.

[46] M. A. van Spronsen, J. W. M. Frenken, and I. M. N. Groot. “Observing the oxidation of platinum”. *Nature Communications* 8 (2017), 429.

[47] V. Navarro, M. A. van Spronsen, and J. W. M. Frenken. “In situ observation of self-assembled hydrocarbon Fischer-Tropsch products on a cobalt catalyst”. *Nature Chemistry* 8 (2016), 929–934.

[48] R. V. Mom, J. N. Louwen, J. W. Frenken, and I. M. Groot. “In situ observations of an active MoS_2 model hydrodesulfurization catalyst”. *Nature Communications* 10 (2019), 1–8.

[49] S. Bordiga, E. Groppo, G. Agostini, J. A. Van Bokhoven, and C. Lamberti. “Reactivity of surface species in heterogeneous catalysts probed by in situ X-ray absorption techniques”. *Chemical Reviews* 113 (2013), 1736–1850.

[50] R. Van Rijn, M. D. Ackermann, O. Balmes, T. Dufrane, A. Geluk, H. Gonzalez, H. Isern, E. De Kuyper, L. Petit, V. A. Sole, D. Wermeille, R. Felici, and J. W. Frenken. “Ultrahigh vacuum/high-pressure flow reactor for surface x-ray diffraction and grazing incidence small angle x-ray scattering studies close to conditions for industrial catalysis”. *Review of Scientific Instruments* 81 (2010), 014101.

[51] S. Pfaff, J. Zhou, U. Hejral, J. Gustafson, M. Shipilin, S. Albertin, S. Blomberg, O. Gutowski, A. Dippel, E. Lundgren, and J. Zetterberg. “Combining high-energy X-ray diffraction with Surface Optical Reflectance and Planar Laser Induced Fluorescence for operando catalyst surface characterization”. *Review of Scientific Instruments* 90 (2019), 033703.

[52] E. Stavitski and B. M. Weckhuysen. “Infrared and Raman imaging of heterogeneous catalysts”. *Chemical Society Reviews* 39 (2010), 4615–4625.

[53] J. J. Bravo-Suárez and P. D. Srinivasan. “Design characteristics of in situ and operando ultraviolet-visible and vibrational spectroscopic reaction cells for heterogeneous catalysis”. *Catalysis Reviews - Science and Engineering* 59 (2017), 295–445.

[54] L. Nguyen, F. F. Tao, Y. Tang, J. Dou, and X.-J. Bao. “Understanding Catalyst Surfaces during Catalysis through Near Ambient Pressure X-ray Photoelectron Spectroscopy”. *Chemical Reviews* 119 (2019), 6822–6905.

[55] R. V. Mom, W. G. Onderwaater, M. J. Rost, M. Jankowski, S. Wenzel, L. Jacobse, P. F. Alkemade, V. Vandalon, M. A. van Spronsen, M. van Weeren, B. Crama, P. van der Tuijn, R. Felici, W. M. Kessels, F. Carlà, J. W. Frenken, and I. M. Groot. “Simultaneous scanning tunneling microscopy and synchrotron X-ray measurements in a gas environment”. *Ultramicroscopy* 182 (2017), 233–242.

[56] H. Achour et al. In preparation.

[57] K. Roy, L. Artiglia, and J. A. van Bokhoven. “Ambient Pressure Photoelectron Spectroscopy: Opportunities in Catalysis from Solids to Liquids and Introducing Time Resolution”. *ChemCatChem* 10 (2018), 666–682.

[58] P. Amann, D. Degerman, M. T. Lee, J. D. Alexander, M. Shipilin, H. Y. Wang, F. Cavalca, M. Weston, J. Gladh, M. Blom, M. Björkhage, P. Löfgren, C. Schlueter, P. Loemker, K. Ederer, W. Drube, H. Noei, J. Zehetner, H. Wentzel, J. Åhlund, and A. Nilsson. “A high-pressure x-ray photoelectron spectroscopy instrument for studies of industrially relevant catalytic reactions at pressures of several bars”. *Review of Scientific Instruments* 90 (2019), 103102.

[59] H. Ibach. *Physics of surfaces and interfaces.* Springer-Verlag Berlin Heidelberg, 2006.

[60] B. Suurmeijer, T. Mulder, and J. Verhoeven. *Vacuum Science and Technology.* The High Tech Institute, 2016.

[61] C. J. Chen. *Introduction to Scanning Tunneling Microscopy.* OXFORD UNIVERSITY PRESS, New York, 1993.

[62] G. Binnig and H. Rohrer. "Scanning tunneling microscopy". *Helvetica Physica Acta* 55 (1982), 726–735.

[63] G. Binning, H. Rohrer, C. Gerber, and E. Weibel. "Surface Studies by Scanning Tunneling Microscopy". *Physical Review Letters* 49 (1982), 57–61.

[64] S. Hofmann. *Auger- and X-Ray Photoelectron Spectroscopy in Materials Science. A User-Oriented Guide.* Springer-Verlag Berlin Heidelberg, 2013.

[65] C. Wagner, W. Riggs, L. Davis, and G. Muilenberg (Editor). *Handbook of X-ray Photoelectron Spectroscopy.* Perkin-Elmer Corporation, 1991.

[66] L. Zhong, D. Chen, and S. Zafeiratos. "A mini review of in situ near-ambient pressure XPS studies on non-noble, late transition metal catalysts". *Catalysis Science and Technology* 9 (2019), 3851–3867.

[67] H. Bluhm. "Photoelectron spectroscopy of surfaces under humid conditions". *Journal of Electron Spectroscopy and Related Phenomena* 177 (2010), 71–84.

[68] S. Axnanda, M. Scheele, E. Crumlin, B. Mao, R. Chang, S. Rani, M. Faiz, S. Wang, A. P. Alivisatos, and Z. Liu. "Direct work function measurement by gas phase photoelectron spectroscopy and its application on PbS nanoparticles". *Nano Letters* 13 (2013), 6176–6182.

[69] Q. I. Roode-Gutzmer, D. Kaiser, and M. Bertau. "Renewable Methanol Synthesis". *ChemBioEng Reviews* 6 (2019), 209–236.

[70] J. H. Park and J. K. Park. "Fate of methanol in an anaerobic digester". *Korean Journal of Chemical Engineering* 20 (2003), 509–516.

[71] D. R. Lide. *CRC Handbook of Chemistry and Physics, Internet Version 2005, www.hbcpnetbase.com.* CRC Press, Boca Raton, FL, 2005.

[72] X. Xu, K. Shuai, and B. Xu. "Review on Copper and Palladium Based Catalysts for Methanol Steam Reforming to Produce Hydrogen". *Catalysts* 7 (2017), 183.

[73] B. A. Peppley, J. C. Amphlett, L. M. Kearns, and R. F. Mann. "Methanol–steam reforming on Cu/ZnO/Al_2O_3. Part 1: the reaction network". *Applied Catalysis A: General* 179 (1999), 21–29.

[74] J. Larminie and A. Dicks. *Fuel cell systems explained.* John Wiley & Sons Ltd, Chichester, 2003, 14–16.

[75] S. Sá, H. Silva, L. Brandão, J. M. Sousa, and A. Mendes. "Catalysts for methanol steam reforming-A review". *Applied Catalysis B: Environmental* 99 (2010), 43–57.

[76] A. Iulianelli, P. Ribeirinha, A. Mendes, and A. Basile. "Methanol steam reforming for hydrogen generation via conventional and membrane reactors: A review". *Renewable and Sustainable Energy Reviews* 29 (2014), 355–368.

[77] T. Lunkenbein, J. Schumann, M. Behrens, R. Schlögl, and M. G. Willinger. "Formation of a ZnO Overlayer in Industrial Cu/ZnO/Al_2O_3 Catalysts Induced by Strong Metal-Support Interactions". *Angewandte Chemie - International Edition* 54 (2015), 4544–4548.

[78] J. Wang, S. Funk, and U. Burghaus. “Indications for metal-support interactions: The case of CO_2 adsorption on Cu/ZnO(0001)”. *Catalysis Letters* 103 (2005), 219–223.

[79] H. Lorenz, M. Friedrich, M. Armbrüster, B. Klötzer, and S. Penner. “ZnO is a CO_2-selective steam reforming catalyst”. *Journal of Catalysis* 297 (2013), 151–154.

[80] Y. Matsumura and H. Ishibe. “Suppression of CO by-production in steam reforming of methanol by addition of zinc oxide to silica-supported copper catalyst”. *Journal of Catalysis* 268 (2009), 282–289.

[81] X. Shao, K.-i. Fukui, H. Kondoh, M. Shionoya, and Y. Iwasawa. “STM Study of Surface Species Formed by Methanol Adsorption on Stoichiometric and Reduced ZnO($10\bar{1}0$) Surfaces”. *J. Phys. Chem. C* 113 (2009), 14356–14362.

[82] J. Kiss, D. Langenberg, D. Silber, F. Traeger, L. Jin, H. Qiu, Y. Wang, B. Meyer, and C. Wöll. “Combined theoretical and experimental study on the adsorption of methanol on the ZnO($10\bar{1}0$) surface”. *Journal of Physical Chemistry A* 115 (2011), 7180–7188.

[83] L. Jin and Y. Wang. “Surface chemistry of methanol on different ZnO surfaces studied by vibrational spectroscopy”. *Physical Chemistry Chemical Physics* 19 (2017), 12992–13001.

[84] O. Dulub, B. Meyer, and U. Diebold. “Observation of the dynamical change in a water monolayer adsorbed on a ZnO surface”. *Physical Review Letters* 95 (2005), 1–4.

[85] B. Meyer, D. Marx, O. Dulub, U. Diebold, M. Kunat, D. Langenberg, and C. Wöll. “Partial dissociation of water leads to stable superstructures on the surface of zinc oxide”. *Angewandte Chemie - International Edition* 43 (2004), 6642–6645.

[86] C. Wöll. “The chemistry and physics of zinc oxide surfaces”. *Progress in Surface Science* 82 (2007), 55–120.

[87] Z. Li, H. Shi, H. Yuan, S. Ruan, W. Wang, Z. Li, and X. Shao. “Adsorption and Diffusion of CO on Clean and CO_2-Precovered ZnO($10\bar{1}0$)”. *Journal of Physical Chemistry C* 122 (2018), 8919–8924.

[88] M. Buchholz, X. Yu, C. Yang, S. Heißler, A. Nefedov, Y. Wang, and C. Wöll. “IR-spectroscopy of CO adsorption on mixed-terminated ZnO surfaces”. *Surface Science* 652 (2016), 247–252.

[89] H. Shi, S. Ruan, H. Liu, L. Wang, W. Wang, X. Ren, B. Wang, K. Wu, and X. Shao. “Directional Growth of One-Dimensional CO_2 Chains on ZnO($10\bar{1}0$)”. *Journal of Physical Chemistry C* 120 (2016), 23669–23674.

[90] R. Lindsay and G. Thornton. “Structure of Atomic and Molecular Adsorbates on Low-Miller-Index ZnO Surfaces Using X-ray Absorption Spectroscopy”. *Topics in Catalysis* 18 (2002), 15–19.

[91] J. T. Newberg, C. Goodwin, C. Arble, Y. Khalifa, J. A. Boscoboinik, and S. Rani. “ZnO($10\bar{1}0$) Surface Hydroxylation under Ambient Water Vapor”. *Journal of Physical Chemistry B* 122 (2018), 472–478.

[92] M. J. Rost, L. Crama, P. Schakel, E. van Tol, G. B. E. M. van Velzen-Williams, C. F. Overgauw, H. ter Horst, H. Dekker, B. Okhuijsen, M. Seynen, A. Vijftigschild, P. Han, A. J. Katan, K. Schoots, R. Schumm, W. van Loo, T. H. Oosterkamp, and J. W. M. Frenken. “Scanning probe microscopes go video rate and beyond”. *Review of Scientific Instruments* 76 (2005), 053710.

[93] `https://secure.eld.leidenuniv.nl/~moene/software/camera/Camera/Camera-MainPage.html`.

[94] I. Horcas, R. Fernández, J. M. Gómez-Rodríguez, J. Colchero, J. Gómez-Herrero, and A. M. Baro. “WSXM: A software for scanning probe microscopy and a tool for nanotechnology”. *Review of Scientific Instruments* 78 (2007), 013705.

[95] Design by Mirthe Bergmann and Mahesh Prabhu, Leiden University.

[96] M. A. v. Spronsen. “Oxidation catalysis on Pt and Au : complexity of simple chemistry”. PhD thesis. Leiden University, 2016.

[97] Product information provided by Westfalen: `www.westfalengassen.nl/industriele-gassen/alle-gassen-op-een-rij/applicationdetailviewnl/productdetailviewnl/gas/argon-50-5.html`, accessed on 22.08.2019.

[98] Product information provided by Air Liquide: `specialty.airliquide.co.uk/product/hydrogen-5-0-10/?category=pures`, accessed on 27.11.2019.

[99] Hiden Analytical Application Note 282. *Relative sensitivity: RS measurements of gases.*

[100] J. H. Batey. “Fractionation in gas inlets for PPA calibration”. *Vacuum* 44 (1993), 639–642.

[101] R. Heinhold, S. P. Cooil, D. A. Evans, and M. W. Allen. “Stability of the Surface Electron Accumulation Layers on the Nonpolar ($10\bar{1}0$) and ($11\bar{2}0$) Faces of ZnO”. *The Journal of Physical Chemistry C* 118 (2014), 24575–24582.

[102] Y. Joseph, W. Ranke, and W. Weiss. “Water on FeO(111) and Fe_3O_4(111): Adsorption behavior on different surface terminations”. *Journal of Physical Chemistry B* 104 (2000), 3224–3236.

[103] C. J. Powell and A. Jablonski. *NIST Electron Inelastic-Mean-Free-Path Database, version 1.2.* National Institute of Standards and Technology: Gaithersburg, MD, 2010.

[104] H. Morkoc and U. Özgür. *General Properties of ZnO.* Wiley-VCH Verlag GmbH & Co. KGaA, 2009, 1–2.

[105] X. L. Yin, A. Birkner, K. Hänel, T. Löber, U. Köhler, and C. Wöll. “Adsorption of atomic hydrogen on ZnO($10\bar{1}0$): STM study”. *Physical Chemistry Chemical Physics* 8 (2006), 1477–1481.

[106] J. Moulder and J. Chastain. *Handbook of X-ray Photoelectron Spectroscopy: A Reference Book of Standard Spectra for Identification and Interpretation of XPS Data.* Physical Electronics Division, Perkin-Elmer Corporation, 1992.

[107] K. Ozawa, K. Mase, and D. Walle. “Metallization of ZnO($10\bar{1}0$) by adsorption of hydrogen, methanol, and water: Angle-resolved photoelectron spectroscopy”. *Physical Review B* 81 (2010), 1–6.

[108] B. Meyer, H. Rabaa, and D. Marx. “Water adsorption on ZnO($10\bar{1}0$): From single molecules to partially dissociated monolayers”. *Physical Chemistry Chemical Physics* 8 (2006), 1513–1520.

[109] S. Kenmoe and P. Ulrich Biedermann. “Water aggregation and dissociation on the ZnO($10\bar{1}0$) surface”. *Physical Chemistry Chemical Physics* 19 (2017), 1466–1486.

[110] O. Dulub, L. A. Boatner, and U. Diebold. “STM study of Cu growth on the ZnO($10\bar{1}0$) surface”. *Surface Science* 504 (2002), 271–281.

[111] B. Meyer and D. Marx. “Density-functional study of the structure and stability of ZnO surfaces”. *Physical Review B - Condensed Matter and Materials Physics* 67 (2003), 1–11.

[112] L. Boatner, U. Diebold, and O. Dulub. “STM study of the geometric and electronic structure of ZnO(0001)-Zn, $(000\bar{1})$-O, $(10\bar{1}0)$, and $(11\bar{2}0)$ surfaces”. *Surface Science* 519 (2002), 201–217.

[113] A. Calzolari and A. Catellani. “Water adsorption on nonpolar ZnO$(10\bar{1}0)$ surface: A microscopic understanding”. *Journal of Physical Chemistry C* 113 (2009), 2896–2902.

[114] G. Tocci and A. Michaelides. “Solvent-induced proton hopping at a water-oxide interface”. *Journal of Physical Chemistry Letters* 5 (2014), 474–480.

[115] A. Önsten, D. Stoltz, P. Palmgren, S. Yu, M. Göthelid, and U. O. Karlsson. “Water adsorption on ZnO(0001): Transition from triangular surface structures to a disordered hydroxyl terminated phase”. *Journal of Physical Chemistry C* 114 (2010), 11157–11161.

[116] M. Nyberg, M. A. Nygren, L. G. M. Pettersson, D. H. Gay, and A. L. Rohl. “Hydrogen Dissociation on Reconstructed ZnO Surfaces”. *The Journal of Physical Chemistry* 100 (1996), 9054–9063.

[117] A. Mang, K. Reimann, and S. Rübenacke. “Exciton Binding Energies in ZnO under hydrostatic pressure”. *Solid State Communications* 94 (1995), 251–254.

[118] U. Diebold, L. Vogel, and O. Dulub. “Atomic-scale properties of low-index ZnO surfaces”. *Applied Surface Science* 237 (2004), 336–342.

[119] G. S. Rohrer, V. E. Henrich, and D. A. Bonnell. “Structure of the reduced TiO_2(110) surface determined by scanning tunneling microscopy”. *Science* 250 (1990), 1239–1241.

[120] P. Stone, R. A. Bennett, and M. Bowkery. “Reactive re-oxidation of reduced TiO_2(110) surfaces demonstrated by high temperature STM movies”. *New Journal of Physics* 1 (1999), 8.

[121] R. Kováčik, B. Meyer, and D. Marx. “F centers versus dimer vacancies on ZnO surfaces: Characterization by STM and STS calculations”. *Angewandte Chemie - International Edition* 46 (2007), 4894–4897.

[122] N. R. D’Amico, G. Cantele, and D. Ninno. “First-principles calculations of clean and defected ZnO surfaces”. *Journal of Physical Chemistry C* 116 (2012), 21391–21400.

[123] A. Janotti and C. G. Van De Walle. “Fundamentals of zinc oxide as a semiconductor”. *Reports on Progress in Physics* 72 (2009).

[124] G. A. Shi, M. Stavola, S. J. Pearton, M. Thieme, E. V. Lavrov, and J. Weber. “Hydrogen local modes and shallow donors in ZnO”. *Physical Review B* 72 (2005), 1–8.

[125] J.-C. Deinert, O. Hofmann, M. Meyer, P. Rinke, and J. Stähler. “Local Aspects of Hydrogen-Induced Metallization of the ZnO$(10\bar{1}0)$ Surface”. *Physical Review B* 91 (June 2015), 235313.

[126] Personal communication from Ulrike Diebold, TU Vienna.

[127] M. Ehrensperger and J. Wintterlin. “In situ high-pressure high-temperature scanning tunneling microscopy of a Co(0001) Fischer-Tropsch model catalyst”. *Journal of Catalysis* 319 (2014), 274–282.

[128] M. Gsell, P. Jakob, and D. Menzel. “Effect of substrate strain on adsorption”. *Science* 280 (1998), 717–720.

[129] M. Schmid, W. Hebenstreit, P. Varga, and S. Crampin. “Quantum wells and electron interference phenomena in Al due to subsurface noble gas bubbles”. *Physical Review Letters* 76 (1996), 2298–2301.

[130] Z. L. Liau and T. T. Sheng. "Argon bubble formation in the sputtering of PtSi". *Applied Physics Letters* 32 (1978), 716–718.

[131] N. Bion, F. Epron, M. Moreno, F. Mariño, and D. Duprez. "Preferential oxidation of carbon monoxide in the presence of hydrogen (PROX) over noble metals and transition metal oxides: Advantages and drawbacks". *Topics in Catalysis* 51 (2008), 76–88.

[132] S. Kandoi, A. A. Gokhale, L. C. Grabow, J. A. Dumesic, and M. Mavrikakis. "Why Au and Cu are more selective than Pt for preferential oxidation of CO at low temperature". *Catalysis Letters* 93 (2004), 93–100.

[133] P. Lakshmanan, J. E. Park, and E. D. Park. "Recent Advances in Preferential Oxidation of CO in H_2 Over Gold Catalysts". *Catalysis Surveys from Asia* 18 (2014), 75–88.

[134] M. Haruta. "When gold is not noble: Catalysis by nanoparticles". *Chemical Record* 3 (2003), 75–87.

[135] C. Dardiotis, G. Martini, A. Marotta, and U. Manfredi. "Low-temperature cold-start gaseous emissions of late technology passenger cars". *Applied Energy* 111 (2013), 468–478.

[136] M. Haruta, N. Yamada, T. Kobayashi, and S. Iijima. "Gold catalysts prepared by coprecipitation for low-temperature oxidation of hydrogen and of carbon monoxide". *Journal of Catalysis* 115 (1989), 301–309.

[137] M. Haruta. "Novel catalysis of gold deposited on metal oxides". *Catalysis Surveys from Japan* 1 (1997), 61–73.

[138] R. Meyer, C. Lemire, S. K. Shaikhutdinov, and H. J. Freund. "Surface chemistry of catalysis by gold". *Gold Bulletin* 37 (2004), 72–124.

[139] Y. Chen, P. Crawford, and P. Hu. "Recent advances in understanding CO oxidation on gold nanoparticles using density functional theory". *Catalysis Letters* 119 (2007), 21–28.

[140] Z. Ma and S. Dai. "Development of novel supported gold catalysts: A materials perspective". *Nano Research* 4 (2011), 3–32.

[141] J. Gong. "Structure and surface chemistry of gold-based model catalysts". *Chemical Reviews* 112 (2012), 2987–3054.

[142] J. A. Rodríguez and J. Hrbek. "Inverse oxide/metal catalysts: A versatile approach for activity tests and mechanistic studies". *Surface Science* 604 (2010), 241–244.

[143] S. Ma, J. Rodriguez, and J. Hrbek. "STM study of the growth of cerium oxide nanoparticles on Au(111)". *Surface Science* 602 (2008), 3272–3278.

[144] M. M. Biener, J. Biener, R. Schalek, and C. M. Friend. "Growth of nanocrystalline MoO_3 on Au(111) studied by in situ scanning tunneling microscopy". *Journal of Chemical Physics* 121 (2004), 12010–12016.

[145] S. Benedetti, N. Nilius, P. Torelli, G. Renaud, H. J. Freund, and S. Valeri. "Competition between polar and nonpolar growth of MgO thin films on Au(111)". *Journal of Physical Chemistry C* 115 (2011), 23043–23049.

[146] M. Li and E. I. Altman. "Shape, morphology, and phase transitions during Co oxide growth on Au(111)". *Journal of Physical Chemistry C* 118 (2014), 12706–12716.

[147] X. Deng and C. Matranga. "Selective growth of Fe_2O_3 nanoparticles and islands on Au(111)". *Journal of Physical Chemistry C* 113 (2009), 11104–11109.

[148] J. Biener, E. Farfan-Arribas, M. Biener, C. M. Friend, and R. J. Madix. “Synthesis of TiO_2 nanoparticles on the Au(111) surface”. *Journal of Chemical Physics* 123 (2005), 094705.

[149] J. D. Grunwaldt and A. Baiker. “Gold/titania interfaces and their role in carbon monoxide oxidation”. *Journal of Physical Chemistry B* 103 (1999), 1002–1012.

[150] M. Kotobuki, R. Leppelt, D. A. Hansgen, D. Widmann, and R. J. Behm. “Reactive oxygen on a Au/TiO_2 supported catalyst”. *Journal of Catalysis* 264 (2009), 67–76.

[151] M. Boronat and A. Corma. “Oxygen activation on gold nanoparticles: separating the influence of particle size, particle shape and support interaction”. *Dalton Transactions* 39 (2010), 8538–8546.

[152] J. Y. Park, L. R. Baker, and G. A. Somorjai. “Role of hot electrons and metal - Oxide interfaces in surface chemistry and catalytic reactions”. *Chemical Reviews* 115 (2015), 2781–2817.

[153] J. G. Lee and K. An. “Catalytic CO Oxidation on Nanocatalysts”. *Topics in Catalysis* 61 (2018), 986–1001.

[154] Y. Xu and M. Mavrikakis. “Adsorption and dissociation of O_2 on gold surfaces: Effect of steps and strain”. *Journal of Physical Chemistry B* 107 (2003), 9298–9307.

[155] P. Jiang, S. Porsgaard, F. Borondics, M. Kober, A. Caballero, H. Bluhm, F. Besenbacher, and M. Salmero. “Room-temperature reaction of oxygen with gold: An in situ ambient-pressure x-ray photoelectron spectroscopy investigation”. *Journal of the American Chemical Society* 132 (2010), 2858–2859.

[156] M. M. Montemore, M. A. Van Spronsen, R. J. Madix, and C. M. Friend. “O_2 Activation by Metal Surfaces: Implications for Bonding and Reactivity on Heterogeneous Catalysts”. *Chemical Reviews* 118 (2018), 2816–2862.

[157] N. Weiher, E. Bus, L. Delannoy, C. Louis, D. E. Ramaker, J. T. Miller, and J. A. van Bokhoven. “Structure and oxidation state of gold on different supports under various CO oxidation conditions”. *Journal of Catalysis* 240 (2006), 100–107.

[158] B. K. Min, A. R. Alemozafar, D. Pinnaduwage, X. Deng, and C. M. Friend. “Efficient CO oxidation at low temperature on Au(111)”. *Journal of Physical Chemistry B* 110 (2006), 19833–19838.

[159] A. Y. Klyushin, M. T. Greiner, X. Huang, T. Lunkenbein, X. Li, O. Timpe, M. Friedrich, M. Hävecker, A. Knop-Gericke, and R. Schlögl. “Is Nanostructuring Sufficient to Get Catalytically Active Au?” *ACS Catalysis* 6 (2016), 3372–3380.

[160] J. C. Fierro-Gonzalez and B. C. Gates. “Evidence of active species in CO oxidation catalyzed by highly dispersed supported gold”. *Catalysis Today* 122 (2007), 201–210.

[161] J. Saavedra, T. Whittaker, Z. Chen, C. J. Pursell, R. M. Rioux, and B. D. Chandler. “Controlling activity and selectivity using water in the Au-catalysed preferential oxidation of CO in H_2”. *Nature Chemistry* 8 (2016), 584–589.

[162] T. Fujitani, I. Nakamura, and A. Takahashi. “H_2O Dissociation at the Perimeter Interface between Gold Nanoparticles and TiO_2 Is Crucial for Oxidation of CO”. *ACS Catalysis* 10 (2020), 2517–2521.

[163] H. Y. Su, M. M. Yang, X. H. Bao, and W. X. Li. “The effect of water on the CO oxidation on Ag(111) and Au(111) surfaces: A first-principle study”. *Journal of Physical Chemistry C* 112 (2008), 17303–17310.

[164] F. Kettemann, S. Witte, A. Birnbaum, B. Paul, G. Clavel, N. Pinna, K. Rademann, R. Kraehnert, and J. Polte. “Unifying Concepts in Room-Temperature CO Oxidation with Gold Catalysts”. *ACS Catalysis* 7 (2017), 8247–8254.

[165] B. K. Min, A. R. Alemozafar, M. M. Biener, J. Biener, and C. M. Friend. “Reaction of Au(111) with Sulfur and Oxygen: Scanning Tunneling Microscopic Study”. *Topics in Catalysis* 36 (2005), 77–90.

[166] J. Klikovits, E. Napetschnig, M. Schmid, N. Seriani, O. Dubay, G. Kresse, and P. Varga. “Surface oxides on Pd(111): STM and density functional calculations”. *Physical Review B - Condensed Matter and Materials Physics* 76 (2007), 1–9.

[167] O. Kizilkaya, D. A. Hite, D. M. Zehner, and P. T. Sprunger. “Formation of aluminum oxide thin films on FeAl(110) studied by STM”. *Surface Science* 529 (2003), 223–230.

[168] Product Information provided by Westfalen: `www.westfalengassen.nl/industriele-gassen/alle-gassen-op-een-rij/applicationdetailviewnl/productdetailviewnl/gas/sauerstoff-50`, accessed on 24.07.2020.

[169] Product Information provided by Air Liquide: `specialty.airliquide.co.uk/product/carbon-monoxide-4-7-10?ref=0`, accessed on 24.07.2020.

[170] LEEDpat, Version 4.2, utility by K.E. Hermann (FHI) and M.A. Van Hove (HKBU), Berlin / Hong Kong, 2014; see also `www.fhi-berlin.mpg.de/KHsoftware/LEEDpat/index`.

[171] Z. P. Liu, P. Hu, and A. Alavi. “Catalytic role of gold in gold-based catalysts: A density functional theory study on the CO oxidation on gold”. *Journal of the American Chemical Society* 124 (2002), 14770–14779.

[172] A. A. Phatak, W. N. Delgass, F. H. Ribeiro, and W. F. Schneider. “Density functional theory comparison of water dissociation steps on Cu, Au, Ni, Pd, and Pt”. *Journal of Physical Chemistry C* 113 (2009), 7269–7276.

[173] J. L. Fajín, M. N. D. Cordeiro, and J. R. Gomes. “Water adsorption and dissociation on the Au(321) stepped surface”. *Journal of Molecular Structure: THEOCHEM* 946 (2010), 51–56.

[174] J. Liu, X. M. Cao, and P. Hu. “Density functional theory study on the activation of molecular oxygen on a stepped gold surface in an aqueous environment: A new approach for simulating reactions in solution”. *Physical Chemistry Chemical Physics* 16 (2014), 4176–4185.

[175] X. Deng, B. K. Min, A. Guloy, and C. M. Friend. “Enhancement of O_2 dissociation on Au(111) by adsorbed oxygen: Implications for oxidation catalysis”. *Journal of the American Chemical Society* 127 (2005), 9267–9270.

[176] M. Gajdoš, A. Eichler, and J. Hafner. “CO adsorption on close-packed transition and noble metal surfaces: Trends from ab initio calculations”. *Journal of Physics Condensed Matter* 16 (2004), 1141–1164.

[177] J. Pischel and A. Pucci. “Low-Temperature Adsorption of Carbon Monoxide on Gold Surfaces: IR Spectroscopy Uncovers Different Adsorption States on Pristine and Rough Au(111)”. *Journal of Physical Chemistry C* 119 (2015), 18340–18351.

[178] F. M. Hoffmann, J. Hrbek, S. Ma, J. B. Park, J. A. Rodriguez, D. J. Stacchiola, and S. D. Senanayake. “Enhancing the reactivity of gold: Nanostructured Au(111) adsorbs CO”. *Surface Science* 650 (2016), 17–23.

[179] L. Piccolo, D. Loffreda, F. J. S. Aires, C. Deranlot, Y. Jugnet, P. Sautet, and J. C. Bertolini. “The adsorption of CO on Au(111) at elevated pressures studied by STM, RAIRS and DFT calculations”. *Surface Science* 566-568 (2004), 995–1000.

[180] D. Boden. “Structural Characterisation of a TiO_2/Au(111) Catalyst Under CO Oxidation Conditions”. MA thesis. Leiden University, 2018.

[181] U. Diebold, J. Lehman, T. Mahmoud, M. Kuhn, G. Leonardelli, W. Hebenstreit, M. Schmid, and P. Varga. “Intrinsic defects on a TiO_2(110)(1 x 1) surface and their reaction with oxygen: A scanning tunneling microscopy study”. *Surface Science* 411 (1998), 137–153.

[182] M. D. Rasmussen, L. M. Molina, and B. Hammer. “Adsorption, diffusion, and dissociation of molecular oxygen at defected TiO_2(110): A density functional theory study”. *Journal of Chemical Physics* 120 (2004), 988–997.

[183] N. Saliba, D. H. Parker, and B. E. Koel. “Adsorption of oxygen on Au(111) by exposure to ozone”. *Surface Science* 410 (1998), 270–282.

[184] B. K. Min, X. Deng, D. Pinnaduwage, R. Schalek, and C. M. Friend. “Oxygen-induced restructuring with release of gold atoms from Au(111)”. *Physical Review B - Condensed Matter and Materials Physics* 72 (2005), 1–4.

[185] L. Huang, P. Zeppenfeld, J. Chevrier, and G. Comsa. “Surface morphology of Au(111) after exposure to oxygen at high temperature and pressure”. *Surface Science* 352-354 (1996), 285–289.

[186] J. Chevrier, L. Huang, P. Zeppenfeld, and G. Comsa. “Characterization by scanning tunneling microscopy of the oxygen induced restructuring of Au(111)”. *Surface Science* 355 (1996), 1–12.

[187] Y. Uchida, X. Bao, K. Weiss, and R. Schlögl. “Oxygen-induced restructuring of Au(111) observed by reflection electron microscopy”. *Surface Science* 401 (1998), 469–475.

[188] R. L. Kuittinen and K. Laasonen. “Coadsorption of CO and O_2 on Pd(111)”. *Chemical Physics* 314 (2005), 19–24.

[189] B. Shan, N. Kapur, J. Hyun, L. Wang, J. B. Nicholas, and K. Cho. “CO-coverage-dependent oxygen dissociation on Pt(111) surface”. *Journal of Physical Chemistry C* 113 (2009), 710–715.

[190] H. Ulbricht, G. Moos, and T. Hertel. “Physisorption of molecular oxygen on single-wall carbon nanotube bundles and graphite”. *Physical Review B - Condensed Matter and Materials Physics* 66 (2002), 1–7.

[191] P. Giannozzi, R. Car, and G. Scoles. “Oxygen adsorption on graphite and nanotubes”. *Journal of Chemical Physics* 118 (2003), 1003–1006.

[192] D. J. Miller, H. Øberg, S. Kaya, H. Sanchez Casalongue, D. Friebel, T. Anniyev, H. Ogasawara, H. Bluhm, L. G. Pettersson, and A. Nilsson. “Oxidation of Pt(111) under near-ambient conditions”. *Physical Review Letters* 107 (2011), 1–5.

[193] J. M. Hawkins, J. F. Weaver, and A. Asthagiri. “Density functional theory study of the initial oxidation of the Pt(111) surface”. *Physical Review B - Condensed Matter and Materials Physics* 79 (2009), 1–13.

[194] D. E. Starr, E. M. Pazhetnov, A. I. Stadnichenko, A. I. Boronin, and S. K. Shaikhutdinov. “Carbon films grown on Pt(111) as supports for model gold catalysts”. *Surface Science* 600 (2006), 2688–2695.

[195] Y. Baskin and L. Meyer. “Lattice constants of graphite at low temperatures”. *Physical Review* 100 (1955), 544.

[196] R. E. Stallcup, L. M. Villarreal, S. C. Lim, I. Akwani, A. F. Aviles, and J. M. Perez. “Atomic structure of the diamond (100) surface studied using scanning tunneling microscopy”. *Journal of Vacuum Science and Technology B: Microelectronics and Nanometer Structures* 14 (1996), 929–932.

[197] T. Frauenheim, U. Stephan, P. Blaudeck, D. Porezag, H. G. Busmann, W. Zimmermann-Edling, and S. Lauer. “Stability, reconstruction, and electronic properties of diamond (100) and (111) surfaces”. *Physical Review B* 48 (1993), 18189–18202.

[198] T. Hom, W. Kiszenick, and B. Post. “Accurate Lattice Constants from Multiple Reflection Measurements II. Lattice Constants of Germanium, Silicon and Diamond”. *Journal of Applied Crystallography* 8 (1998), 457–458.

[199] F. Maier, M. Riedel, B. Mantel, J. Ristein, and L. Ley. “Origin of surface conductivity in diamond”. *Physical Review Letters* 85 (2000), 3472–3475.

[200] K. A. Chiu, P. H. Wu, C. Y. Peng, J. S. Tian, and L. Chang. “Homoepitaxial growth and stress analysis of (111) diamond film with embedded gold islands”. *Vacuum* 118 (2015), 104–108.

[201] S. Ikeda and M. Yoshio. “Investigation of oriented diamond films on noble metal”. *Journal of the Ceramic Society of Japan* 109 (2001), 542–549.

[202] I. Motochi, N. W. Makau, and G. O. Amolo. “Metal-semiconductor ohmic contacts: An ab initio Density Functional Theory study of the structural and electronic properties of metal-diamond (111)-(1x1) interfaces”. *Diamond and Related Materials* 23 (2012), 10–17.

[203] B. Westenfelder, J. Biskupek, J. C. Meyer, S. Kurasch, X. Lin, F. Scholz, A. Gross, and U. Kaiser. “Bottom-up formation of robust gold carbide”. *Scientific Reports* 5 (2015), 1–6.

[204] For EU regulations see for example `ec.europa.eu/growth/sectors/automotive/environment-protection/emissions_en`, accessed on 29.03.2021.

[205] F. Fischer and H. Tropsch. “The Synthesis of Petroleum at Atmospheric Pressures from Gasification Products of Coal”. *Brennstoff-Chemie* 7 (1926), 97–104.

[206] E. I. Koytsoumpa, C. Bergins, and E. Kakaras. “The CO_2 economy: Review of CO_2 capture and reuse technologies”. *Journal of Supercritical Fluids* 132 (2018), 3–16.

[207] Z. Zhang, S. Y. Pan, H. Li, J. Cai, A. G. Olabi, E. J. Anthony, and V. Manovic. “Recent advances in carbon dioxide utilization”. *Renewable and Sustainable Energy Reviews* 125 (2020), 109799.

[208] H. Sajjad, H. H. Masjuki, M. Varman, M. A. Kalam, M. I. Arbab, S. Imtenan, and S. M. Rahman. “Engine combustion, performance and emission characteristics of gas to liquid (GTL) fuels and its blends with diesel and bio-diesel”. *Renewable and Sustainable Energy Reviews* 30 (2014), 961–986.

[209] M. A. Bassiony, A. Ibrahim, and M. M. El-Kassaby. “An experimental study on the effect of using gas-to-liquid (GTL) fuel on diesel engine performance and emissions”. *Alexandria Engineering Journal* 55 (2016), 2115–2124.

[210] see for example `www.sasol.com/innovation/gas-liquids/overview`, accessed on 29.03.2021.

[211] see for example `www.shell.com/energy-and-innovation/natural-gas/gas-to-liquids`, accessed on 29.03.2021.

[212] M. E. Dry. "The Fischer-Tropsch process: 1950-2000". *Catalysis Today* 71 (2002), 227–241.

[213] Q. Zhang, J. Kang, and Y. Wang. "Development of Novel Catalysts for Fischer-Tropsch Synthesis: Tuning the Product Selectivity". *ChemCatChem* 2 (2010), 1030–1058.

[214] F. G. Botes, J. W. Niemantsverdriet, and J. Van De Loosdrecht. "A comparison of cobalt and iron based slurry phase Fischer-Tropsch synthesis". *Catalysis Today* 215 (2013), 112–120.

[215] Z. Gholami, N. Asmawati Mohd Zabidi, F. Gholami, O. B. Ayodele, and M. Vakili. "The influence of catalyst factors for sustainable production of hydrocarbons via Fischer-Tropsch synthesis". *Reviews in Chemical Engineering* 33 (2017), 337–358.

[216] N. E. Tsakoumis, M. Rønning, Ø. Borg, E. Rytter, and A. Holmen. "Deactivation of cobalt based Fischer-Tropsch catalysts: A review". *Catalysis Today* 154 (2010), 162–182.

[217] M. D. Argyle and C. H. Bartholomew. "Heterogeneous catalyst deactivation and regeneration: A review". *Catalysts* 5 (2015), 145–269.

[218] C. J. Weststrate, I. M. Ciobîcă, A. M. Saib, D. J. Moodley, and J. W. Niemantsverdriet. "Fundamental issues on practical Fischer-Tropsch catalysts: How surface science can help". *Catalysis Today* 228 (2014), 106–112.

[219] D. J. Moodley, J. van de Loosdrecht, A. M. Saib, M. J. Overett, A. K. Datye, and J. W. Niemantsverdriet. "Carbon deposition as a deactivation mechanism of cobalt-based Fischer-Tropsch synthesis catalysts under realistic conditions". *Applied Catalysis A: General* 354 (2009), 102–110.

[220] M. Ehrensperger and J. Wintterlin. "In situ scanning tunneling microscopy of the poisoning of a Co(0001) Fischer-Tropsch model catalyst by sulfur". *Journal of Catalysis* 329 (2015), 49–56.

[221] J. Barrientos, V. Montes, M. Boutonnet, and S. Järås. "Further insights into the effect of sulfur on the activity and selectivity of cobalt-based Fischer-Tropsch catalysts". *Catalysis Today* 275 (2016), 119–126.

[222] J. van de Loosdrecht, B. Balzhinimaev, J. A. Dalmon, J. W. Niemantsverdriet, S. V. Tsybulya, A. M. Saib, P. J. van Berge, and J. L. Visagie. "Cobalt Fischer-Tropsch synthesis: Deactivation by oxidation?" *Catalysis Today* 123 (2007), 293–302.

[223] A. M. Saib, D. J. Moodley, I. M. Ciobîcă, M. M. Hauman, B. H. Sigwebela, C. J. Weststrate, J. W. Niemantsverdriet, and J. Van De Loosdrecht. "Fundamental understanding of deactivation and regeneration of cobalt Fischer-Tropsch synthesis catalysts". *Catalysis Today* 154 (2010), 271–282.

[224] K. H. Cats, I. D. Gonzalez-Jimenez, Y. Liu, J. Nelson, D. van Campen, F. Meirer, A. M. Van der Eerden, F. M. de Groot, J. C. Andrews, and B. M. Weckhuysen. "X-ray nanoscopy of cobalt Fischer-Tropsch catalysts at work". *Chemical Communications* 49 (2013), 4622–4624.

[225] P. J. Van Berge, J. Van De Loosdrecht, S. Barradas, and A. M. Van Der Kraan. "Oxidation of cobalt based Fischer-Tropsch catalysts as a deactivation mechanism". *Catalysis Today* 58 (2000), 321–334.

[226] C. H. Wu, B. Eren, H. Bluhm, and M. B. Salmeron. "Ambient-Pressure X-ray Photoelectron Spectroscopy Study of Cobalt Foil Model Catalyst under CO, H_2, and Their Mixtures". *ACS Catalysis* 7 (2017), 1150–1157.

[227] S. Turczyniak, W. Luo, V. Papaefthimiou, N. S. Ramgir, M. Haevecker, A. Machocki, and S. Zafeiratos. "A Comparative Ambient Pressure X-ray Photoelectron and Absorption Spectroscopy Study of Various Cobalt-Based Catalysts in Reactive Atmospheres". *Topics in Catalysis* 59 (2016), 532–542.

[228] V. Papaefthimiou, T. Dintzer, V. Dupuis, A. Tamion, F. Tournus, A. Hillion, D. Teschner, M. Hävecker, A. Knop-Gericke, R. Schlögl, and S. Zafeiratos. "Nontrivial redox behavior of nanosized cobalt: New insights from ambient pressure X-ray photoelectron and absorption spectroscopies". *ACS Nano* 5 (2011), 2182–2190.

[229] A. C. Kizilkaya, J. W. Niemantsverdriet, and C. J. Weststrate. "Oxygen Adsorption and Water Formation on Co(0001)". *Journal of Physical Chemistry C* 120 (2016), 4833–4842.

[230] M. E. Grass, P. G. Karlsson, F. Aksoy, M. Lundqvist, B. Wannberg, B. S. Mun, Z. Hussain, and Z. Liu. "New ambient pressure photoemission endstation at advanced light source beamline 9.3.2". *Review of Scientific Instruments* 81 (2010), 053106.

[231] S. Zhu, M. Scardamaglia, J. Kundsen, R. Sankari, H. Tarawneh, R. Temperton, L. Pickworth, F. Cavalca, C. Wang, H. Tissot, J. Weissenrieder, B. Hagman, J. Gustafson, S. Kaya, F. Lindgren, I. Källquist, J. Maibach, M. Hahlin, V. Boix, T. Gallo, F. Rehman, G. D'Acunto, J. Schnadt, and A. Shavorskiy. "HIPPIE: a new platform for ambient-pressure X-ray photoelectron spectroscopy at the MAX IV Laboratory". *Journal of Synchrotron Radiation* 28 (2021), 624–636.

[232] J. Knudsen, J. N. Andersen, and J. Schnadt. "A versatile instrument for ambient pressure x-ray photoelectron spectroscopy: The Lund cell approach". *Surface Science* 646 (2016), 160–169.

[233] Product information provided by Praxair: `www.lindeus.com/-/media/corporate/praxairus/documents/specification-sheets-and-brochures/gases/hydrogen/hydrogen-h2-spec-sheet-ss-p4604.pdf?la=en`, accessed on 09.01.2021.

[234] Product information provided by Air Liquide: `specialty.airliquide.co.uk/product/hydrogen-5-0-501/?category=pures`, accessed on 11.01.2021.

[235] Product information provided by Praxair: `https://www.lindeus.com/-/media/corporate/praxairus/documents/specification-sheets-and-brochures/gases/carbon-monoxide-co-spec-sheet-ss-p4576.pdf?la=en`, accessed on 14.04.2021.

[236] Product information provided by Air Liquide: `specialty.airliquide.co.uk/product/carbon-monoxide-3-7-10/?category=pures`, accessed on 09.01.2021.

[237] B. W. Lee, R. Alsenz, A. Ignatiev, and M. A. Van Hove. "Surface structures of the two allotropic phases of cobalt". *Physical Review B* 17 (1978), 1510–1520.

[238] N. S. Mcintyre and M. G. Cook. "X-Ray Photoelectron Studies on Some Oxides and Hydroxides of Cobalt, Nickel, and Copper". *Analytical Chemistry* 47 (1975), 2208–2213.

[239] Casa Software Ltd, `www.casaxps.com`.

[240] A. Lebugle, U. Axelsson, R. Nyholm, and N. Mårtensson. " Experimental L and M Core Level Binding Energies for the Metals 22 Ti to 30 Zn ". *Physica Scripta* 23 (1981), 825–827.

[241] M. C. Biesinger, B. P. Payne, A. P. Grosvenor, L. W. Lau, A. R. Gerson, and R. S. C. Smart. “Resolving surface chemical states in XPS analysis of first row transition metals, oxides and hydroxides: Cr, Mn, Fe, Co and Ni”. *Applied Surface Science* 257 (2011), 2717–2730.

[242] I. Groot et al. In preparation.

[243] B. Böller, K. M. Durner, and J. Wintterlin. “The active sites of a working Fischer-Tropsch catalyst revealed by operando scanning tunnelling microscopy”. *Nature Catalysis* 2 (2019), 1027–1034.

[244] J. Lahtinen, J. Vaari, and K. Kauraala. “Adsorption and structure dependent desorption of CO on Co(0001)”. *Surface Science* 418 (1998), 502–510.

[245] C. J. Weststrate, J. van de Loosdrecht, and J. W. Niemantsverdriet. “Spectroscopic insights into cobalt-catalyzed Fischer-Tropsch synthesis: A review of the carbon monoxide interaction with single crystalline surfaces of cobalt”. *Journal of Catalysis* 342 (2016), 1–16.

[246] C. J. Weststrate, A. C. Kizilkaya, E. T. Rossen, M. W. Verhoeven, I. M. Ciobîcă, A. M. Saib, and J. W. Niemantsverdriet. “Atomic and polymeric carbon on Co(0001): Surface reconstruction, graphene formation, and catalyst poisoning”. *Journal of Physical Chemistry C* 116 (2012), 11575–11583.

[247] B. Böller, M. Ehrensperger, and J. Wintterlin. “In Situ Scanning Tunneling Microscopy of the Dissociation of CO on Co(0001)”. *ACS Catalysis* 5 (2015), 6802–6806.

[248] L. Xu, Y. Ma, Z. Wu, B. Chen, Q. Yuan, and W. Huang. “A photoemission study of ethylene decomposition on a Co(0001) surface: Formation of different types of carbon species”. *Journal of Physical Chemistry C* 116 (2012), 4167–4174.

[249] L. Xu, Y. Ma, Y. Zhang, B. Chen, Z. Wu, Z. Jiang, and W. Huang. “Water adsorption on a Co(0001) surface”. *Journal of Physical Chemistry C* 114 (2010), 17023–17029.

[250] W. Jiawei, J. Chen, Q. Guo, H. Y. Su, D. Dai, and X. Yang. “H_2O and CO coadsorption on Co (0001): The effect of intermolecular hydrogen bond”. *Surface Science* 663 (2017), 56–61.

[251] As it can be found with different nomenclature in standard literature such as S. Hofmann. *Auger- and X-Ray Photoelectron Spectroscopy in Materials Science.* Springer-Verlag Berlin Heidelberg, 2013.

[252] `vuo.elettra.eu/services/elements/WebElements.html`, last acccessed on 29.03.2021.

[253] C. J. Powell and A. Jablonski. *NIST Electron Inelastic-Mean-Free-Path Database - Version 1.2.* Gaithersburg, MD: National Institute of Standards and Technology, 2010.

[254] J. Yang, J. J. Ma, S. H. Ma, and X. Q. Dai. “Theoretical study of direct versus oxygen-assisted water dissociation on Co(0001) surface”. *Chemical Physics Letters* 681 (2017), 29–35.

[255] D. Eom, D. Prezzi, K. T. Rim, H. Zhou, M. Lefenfeld, S. Xiao, C. Nuckolls, M. S. Hybertsen, T. F. Heinz, and G. W. Flynn. “Structure and electronic properties of graphene nanoislands on Co(0001)”. *Nano Letters* 9 (2009), 2844–2848.

[256] J. Lahtinen, P. Kantola, S. Jaatinen, K. Habermehl-Cwirzen, P. Salo, J. Vuorinen, M. Lindroos, K. Pussi, and A. P. Seitsonen. “LEED and DFT investigation on the (2x2)-S overlayer on Co(0001)”. *Surface Science* 599 (2005), 113–121.

[257] `www.webelements.com/cobalt/crystal_structure.html`, accessed on 14.01.2021.

[258] J. Van Elp, J. L. Wieland, H. Eskes, P. Kuiper, G. A. Sawatzky, F. M. De Groot, and T. S. Turner. “Electronic structure of CoO, Li-doped CoO, and $LiCoO_2$”. *Physical Review B* 44 (1991), 6090–6103.

[259] M. Lee, Y. Youn, K. Yim, and S. Han. “High-throughput ab initio calculations on dielectric constant and band gap of non-oxide dielectrics”. *Scientific Reports* 8 (2018), 1–8.

[260] C. Chen, Q. Wang, R. Zhang, B. Hou, D. Li, L. Jia, and B. Wang. “High coverage CO adsorption and dissociation on the Co(0001) and Co(100) surfaces from DFT and thermodynamics”. *Applied Catalysis A: General* 523 (2016), 209–220.

[261] K. Pussi, M. Lindroos, J. Katainen, K. Habermehl-Ćwirzeń, J. Lahtinen, and A. P. Seitsonen. “The $(\sqrt{7}x\sqrt{7})R19.1°-C_6H_6$ adsorption structure on Co(0001): A combined tensor LEED and DFT study”. *Surface Science* 572 (2004), 1–10.

[262] B. Hulsken, J. W. Gerritsen, and S. Speller. “Measuring the Au(111) surface state at the solid-liquid interface”. *Surface Science* 580 (2005), 95–100.

[263] `pubchem.ncbi.nlm.nih.gov/compound/Tetradecane`, last accessed on 26.03.2021.

[264] Personal communication from Surface Preparation Laboratory, Zaandam.

[265] D. Potoczna-Petru. “The interaction of model cobalt catalysts with carbon”. *Carbon* 29 (1991), 73–79.

[266] B. Li, Q. Zhang, L. Chen, P. Cui, and X. Pan. “Vacancy-mediated diffusion of carbon in cobalt and its influence on CO activation”. *Physical Chemistry Chemical Physics* 12 (2010), 7848–7855.

[267] P. Van Helden, J. A. Van Den Berg, and C. J. Weststrate. “Hydrogen adsorption on Co surfaces: A density functional theory and temperature programmed desorption study”. *ACS Catalysis* 2 (2012), 1097–1107.

[268] C. J. Weststrate, M. Mahmoodinia, M. H. Farstad, I. H. Svenum, M. D. Strømsheim, J. W. Niemantsverdriet, and H. J. Venvik. “Interaction of hydrogen with flat (0001) and corrugated (11-20) and (10-12) cobalt surfaces: Insights from experiment and theory”. *Catalysis Today* 342 (2020), 124–130.

[269] J. J. Ma, L. F. Wang, S. H. Ma, and J. Yang. “Interaction of water with stepped Co(0001): how is it different from flat Co(0001)?” *European Physical Journal B* 91 (2018), 1–10.

[270] M. Zhang, H. Huang, and Y. Yu. “Water Adsorption and Decomposition on Co(0001) Surface: A Computational Study”. *Catalysis Letters* 148 (2018), 3126–3133.

[271] L. Lukashuk, K. Föttinger, E. Kolar, C. Rameshan, D. Teschner, M. Hävecker, A. Knop-Gericke, N. Yigit, H. Li, E. McDermott, M. Stöger-Pollach, and G. Rupprechter. “Operando XAS and NAP-XPS studies of preferential CO oxidation on Co_3O_4 and CeO_2-Co_3O_4 catalysts”. *Journal of Catalysis* 344 (2016), 1–15.

[272] C. J. Weststrate, P. Van Helden, J. Van De Loosdrecht, and J. W. Niemantsverdriet. “Elementary steps in Fischer-Tropsch synthesis: CO bond scission, CO oxidation and surface carbiding on Co(0001)”. *Surface Science* 648 (2016), 60–66.

[273] Q. Ge and M. Neurock. “Adsorption and activation of CO over flat and stepped Co surfaces: A first principles analysis”. *Journal of Physical Chemistry B* 110 (2006), 15368–15380.

[274] B. Zijlstra, R. J. Broos, W. Chen, H. Oosterbeek, I. A. Filot, and E. J. Hensen. "Coverage Effects in CO Dissociation on Metallic Cobalt Nanoparticles". *ACS Catalysis* 9 (2019), 7365–7372.

[275] C. F. Huo, Y. W. Li, J. Wang, and H. Jiao. "Adsorption and dissociation of CO as well as CH_x coupling and hydrogenation on the clean and oxygen pre-covered Co(0001) surfaces". *Journal of Physical Chemistry C* 112 (2008), 3840–3848.

[276] G. Rattan and M. Kumar. "Carbon monoxide oxidation using cobalt catalysts: A short review". *Chemistry and Chemical Technology* 8 (2014), 249–260.

[277] A. K. Dalai and B. H. Davis. "Fischer-Tropsch synthesis: A review of water effects on the performances of unsupported and supported Co catalysts". *Applied Catalysis A: General* 348 (2008), 1–15.

[278] E. Rytter and A. Holmen. "Perspectives on the Effect of Water in Cobalt Fischer-Tropsch Synthesis". *ACS Catalysis* 7 (2017), 5321–5328.

[279] C. G. Okoye-Chine, M. Moyo, X. Liu, and D. Hildebrandt. "A critical review of the impact of water on cobalt-based catalysts in Fischer-Tropsch synthesis". *Fuel Processing Technology* 192 (2019), 105–129.

[280] M. Claeys, M. E. Dry, E. Van Steen, E. Du Plessis, P. J. Van Berge, A. M. Saib, and D. J. Moodley. "In situ magnetometer study on the formation and stability of cobalt carbide in Fischer-Tropsch synthesis". *Journal of Catalysis* 318 (2014), 193–202.

[281] C. G. Visconti, E. Tronconi, L. Lietti, P. Forzatti, S. Rossini, and R. Zennaro. "Detailed Kinetics of the Fischer–Tropsch Synthesis on Cobalt Catalysts Based on H-Assisted CO Activation". *Topics in Catalysis* 54 (2011), 786–800.

[282] R. B. Anderson, R. A. Friedel, and H. H. Storch. "Fischer-Tropsch reaction mechanism involving stepwise growth of carbon chain". *The Journal of Chemical Physics* 19 (1951), 313–319.

[283] J. J. Geerlings, M. C. Zonnevylle, and C. P. de Groot. "Studies of the Fischer-Tropsch reaction on Co(0001)". *Surface Science* 241 (1991), 302–314.

[284] R. L. Palmer and D. A. Vroom. "Mass-spectrometric measurements of enhanced methanation activity over cobalt and nickel foils". *Journal of Catalysis* 50 (1977), 244–251.

[285] J. Yang, Y. Qi, J. Zhu, Y. A. Zhu, D. Chen, and A. Holmen. "Reaction mechanism of CO activation and methane formation on Co Fischer-Tropsch catalyst: A combined DFT, transient, and steady-state kinetic modeling". *Journal of Catalysis* 308 (2013), 37–49.

[286] W. Huang, L. Sun, P. Han, and J. Zhao. "CH_4 dissociation on Co(0001): A density functional theory study". *Journal of Natural Gas Chemistry* 21 (2012), 98–103.

[287] S. M. Wetterer, D. J. Lavrich, T. Cummings, S. L. Bernasek, and G. Scoles. "Energetics and kinetics of the physisorption of hydrocarbons on Au(111)". *Journal of Physical Chemistry B* 102 (1998), 9266–9275.

[288] K. A. Fichthorn and R. A. Miron. "Thermal Desorption of Large Molecules from Solid Surfaces". *Physical Review Letters* 89 (2002), 2–5.

[289] K. Habermehl-Ćwirzeń and J. Lahtinen. "Sulfur poisoning of the CO adsorption on Co(0001)". *Surface Science* 573 (2004), 183–190.

[290] M. Armbrüster, R. Schlögl, and Y. Grin. "Intermetallic compounds in heterogeneous catalysis - A quickly developing field". *Science and Technology of Advanced Materials* 15 (2014).

[291] P. Bera and J. M. Vohs. “Reaction of CH_3OH on Pd/ZnO(0001) and PdZn/ZnO(0001) model catalysts”. *Journal of Physical Chemistry C* 111 (2007), 7049–7057.

Nederlandse Samenvatting

Katalysatoren zijn van groot belang voor ons dagelijks leven, voor energievoorziening, milieubescherming en de productie van talrijke chemicaliën en levensmiddelen. Daarom komen katalysatoren ook in zeer veel verschillende vormen voor, zoals enzymen in je eigen lichaam, moleculen in oplossingen of poeders gemaakt van metalen en oxiden. In al deze gevallen is de rol van de katalysator echter dezelfde; hij maakt een chemische reactie sneller, energiezuiniger en/of selectiever voor bepaalde uitgangsstoffen of producten. De katalysator keert daarbij terug naar zijn oorspronkelijke staat zodra de zogenaamde katalytische cyclus is voltooid. De focus van dit proefschrift ligt op een bepaalde soort heterogene katalysatoren, vaste stoffen die de reactie tussen gassen katalyseren. Om de prestaties van dergelijke katalysatoren te verbeteren, streeft de oppervlaktewetenschap naar een gedetailleerd begrip van hun werkingsmechanisme op de atomaire schaal. Standaardmethoden van de oppervlaktewetenschap zijn onder meer microscopie om het oppervlak in beeld te brengen, spectroscopie om de elementaire samenstelling te meten en diffractie om de structuur te bepalen. Deze methoden zijn het gemakkelijkst toe te passen op vlakke, éénkristallijne metalen in ultrahoog vacuüm. Omdat katalysatoren in de industrie echter bij atmosferische of zelfs significant hogere drukken worden gebruikt, spreekt men van de zogenaamde drukkloof (Engels: *pressure gap*) tussen wetenschap en toepassing. Om deze kloof te overbruggen worden steeds meer zogenaamde in situ methoden ontwikkeld. De *ReactorSTM*, die in hoofdstuk 3 en hoofdstuk 4 wordt gebruikt, is een rastertunnelmicroscoop geïntegreerd in een doorstroomreactorcel, die zich wederom in een vacuümkamer bevindt. Op deze manier kan een gecontroleerde bereiding en karakterisering van modelkatalysatoren worden gecombineerd met beeldvorming onder atmosferische druk. Laatstgenoemde geeft informatie over de structuur van het katalysatoroppervlak tijdens de reactie. Aan de andere kant kan röntgenfotoelektronenspectroscopie bij drukken dichtbij het atmosferische bereik geadsorbeerde moleculen en de chemische toestand van atomen op het oppervlak tijdens de reactie identificeren. Als de röntgenfotonen, zoals in hoofdstuk 5 van dit proefschrift, van een synchrotronbron afkomstig zijn, heeft deze methode een hoge energieresolutie, is oppervlaktegevoelig en geschikt voor snelle metingen.

Afgezien van het drukverschil, verschillen industriële katalysatoren ook door hun complexe structuur van éénkristallen, die in de traditionele oppervlaktewetenschap bestudeerd worden. Om ook deze zogenaamde materiaalkloof (Engels: *materials gap*) te overbruggen, worden modelkatalysatoren steeds complexer gemaakt: van éénkristallijne metalen, via gestapte en gekromde éénkristallen, naar oxide éénkristallen en metaal, oxide en sulfide nanodeeltjes op de verschillende éénkristallen. Dit proefschrift gaat over een metallisch éénkristal, een oxide éénkristal en een complexe modelkatalysator met nanodeeltjes.

Hoofdstuk 3 toont het eerste gebruik van een ZnO$(10\bar{1}0)$ éénkristal in de *ReactorSTM*. Zinkoxide is onderdeel van de meest bestudeerde katalysator, Cu-ZnO/Al_2O_3, voor de stoomreformering van methanol, de reactie tussen methanol en water om schone waterstof te produceren. Deze katalysator heeft het potentieel om voertuigen met waterstofbrandstofcellen veiliger en gebruiksvriendelijker te maken. Hiervoor moet de katalysator voornamelijk zeer selectief voor de productie van CO_2 in plaats van CO zijn, waarin het zinkoxide een grote rol kan spelen. Eerst beschrijf ik enkele experimentele uitdagingen die het gebruik van ZnO$(10\bar{1}0)$ in een rastertunnelmicroscoop in vacuüm met zich mee brengt. Ook kwantificeren wij de waterachtergrond in de reactorcel van de *ReactorSTM*. Als ZnO$(10\bar{1}0)$ in de reactor aan argon wordt blootgesteld, verruwt dit water het oppervlak zodat een groot aantal stappen zichtbaar wordt. Aangezien water echter ook een uitgangsstof van de stoomreformering van methanol is, moet geconcludeerd worden dat het $(10\bar{1}0)$ oppervlak van zinkoxide mogelijk niet stabiel is onder realistische omstandigheden en studies van ZnO$(10\bar{1}0)$ in vacuüm slechts beperkt geschikt zijn als model voor industriële processen.

In hoofdstuk 4 gaan we verder met de studie van een complexere modelkatalysator in de vorm van TiO_2 nanodeeltjes op goud. Katalysatoren op basis van goud zijn actief voor CO oxidatie, en dat bij lagere temperaturen in vergelijking met andere materialen. Daarom kunnen ze de uitstoot van CO tijdens het opwarmen van verbrandingsmotoren verminderen. Met betrekking tot het mechanisme van deze katalysator zijn de oxidatietoestand van het goud tijdens de reactie, de rol van het oxide en ook de rol van water in het gasmengsel onduidelijk. In de *ReactorSTM* kan de vorming van een dun laagje goudoxide op Au(111) bij atmosferische drukken van O_2 of het reactiemengsel worden gezien. De dissociatie van O_2, die hiervoor noodzakelijk is, wordt waarschijnlijk door de waterachtergrond in de gassen mogelijk gemaakt. Aangezien verontreinigingen in het goud de vorming van het oxide kunnen bevorderen en een waterachtergrond ook onder realistische omstandigheden aanwezig is, lijkt het bestaan van het oxide op industriële katalysatoren waarschijnlijk. TiO_2 nanodeeltjes op Au(111) hebben echter geen invloed op de vorming van het goudoxide. We kunnen daarom uitsluiten dat TiO_2

tijdens de CO oxidatie atomair zuurstof aan het Au(111) oppervlak levert.

In hoofdstuk 5 wordt in situ röntgenfotoelektronenspectroscopie gebruikt om een kobalt éénkristal te onderzoeken, dat als modelkatalysator voor Fischer-Tropsch synthese fungeert. Met behulp van deze reactie kunnen schonere, synthetische brandstoffen uit een mengsel van CO en H_2 geproduceerd worden. Hoewel kobalt al industrieel wordt gebruikt, onderzoekt de wetenschap een aantal deactiveringsprocessen zoals de oxidatie van kobalt en de afzetting van koolstof en producten van de reactie op het oppervlak. De oxidatie van het kobalt kan sterk van de structuur van het kobaltmonster afhangen. In het geval van onze metingen op Co(0001) lijkt het oppervlak in CO metaalachtig te blijven. In H_2 kan de waterachtergrond het oppervlak echter oxideren, zelfs als er zoveel water als mogelijk uitgefilterd wordt. Hoewel het tegenovergestelde bij zowel lagere als hogere drukken wordt gemeten, komen deze resultaten overeen met metingen op kobaltfolie bij vergelijkbare drukken. Een mogelijke verklaring hiervoor is gebaseerd op de verschillende plekken die CO, H_2 en H_2O op Co(0001) prefereren. Ook stellen wij in hoofdstuk 5 een model voor waarmee de hoeveelheid van moleculen en atomen, die tijdens de reactie op Co(0001) gedeponeerd worden, gekwantificeerd kan worden.

Over het algemeen zijn alle drie de systemen die in dit proefschrift onderzocht worden een voorbeeld van het feit dat kleine concentraties van verontreinigingen in gassen en monstermaterialen een significante invloed op de resultaten van in situ metingen kunnen hebben. Hoewel dit de interpretatie van resultaten bemoeilijkt, bevordert het ook het naderen tot meer realistische reactieomstandigheden.

Deutsche Zusammenfassung

Katalysatoren sind von großer Bedeutung für unser tägliches Leben: für nachhaltige Energieversorgung, Umweltschutz, die Produktion von zahlreichen Chemikalien und die Nahrungsmittelversorgung. Daher treten Katalysatoren auch in den verschiedensten Formen auf, als Enzyme in unserem Körper, Moleküle in Lösungen oder Puder aus Metallen und Oxiden. In all diesen Fällen ist die Rolle des Katalysators jedoch die gleiche; er macht eine chemische Reaktion schneller, energieeffizienter und/oder selektiver für bestimme Edukte oder Produkte. Hierbei kehrt der Katalysator nach der Vollendung des sogenannten katalytischen Zyklus wieder in seinen ursprünglichen Zustand zurück. Der Fokus dieser Arbeit liegt auf einer Art von heterogenen Katalysatoren, nämlich Oberflächen, die Reaktionen zwischen Gasen katalysieren. Um die Leistung solcher Katalysatoren zu verbessern, strebt die Oberflächenwissenschaft nach einem detaillierten Verständnis ihrer Wirkungsweise auf dem atomaren Niveau. Ihre Standardmethoden beinhalten Mikroskopie, um die Oberfläche abzubilden, Spektroskopie zur Messung der elementaren Zusammensetzung und Beugung zur Bestimmung der Struktur. Diese Methoden können am einfachsten auf flachen, einkristallinen Metallen in Ultrahochvakuum angewendet werden.

Da Katalysatoren in der Industrie jedoch bei atmosphärischen oder sogar signifikant höheren Drücken gebraucht werden, spricht man von der sogenannten Drucklücke (englisch: *pressure gap*) zwischen Wissenschaft und Anwendung. Um diese Lücke zu schließen, werden stets neue sogenannte in situ Methoden entwickelt. Das *ReactorSTM*, welches in Kapitel 3 und Kapitel 4 dieser Arbeit verwendet wird, ist ein Rastertunnelmikroskop, das in eine Durchflussreaktorzelle integriert ist. Letztere befindet sich wiederum in einer Vakuumkammer. Auf diese Weise kann eine kontrollierte Vorbereitung und Charakterisierung von Modellkatalysatoren mit dem Abbilden in atmosphärischen Drücken kombiniert werden. Letzteres gibt Aufschluss auf die Struktur der Katalysatoroberfläche während der Reaktion. Im Gegensatz hierzu kann Röntgenphotoelektronenspektroskopie bei Drücken nahe dem atmosphärischen Bereich adsorbierte Moleküle sowie den chemischen Zustand von Atomen der Oberfläche während der Reaktion identifizieren. Wenn die Röntgenstrahlen, wie in Kapitel 5 dieser Arbeit, aus einer Synchrotronquelle stammen, hat diese Methode eine hohe Energieauflösung, ist oberflächensensitiv und für schnelle Messungen geeignet. Außer dem Druckunterschied unterscheiden sich industrielle Katalysatoren auch durch ihre komplexe Struktur von den Einkristallen, die in der traditionellen Oberflächenwissenschaft untersucht werden. Um auch diese sogenannte Materiallücke (englisch: *materials gap*) zu überbrücken, werden Modellkatalysatoren stets komplexer gemacht: von einkristallinen Metallen, über gestufte und gekrümmte Einkristalle, zu Oxideinkristallen sowie Metall-, Oxid- und Sulfid-Nanopartikeln auf Einkristallen. Diese Arbeit behandelt einen metallischen Einkristall, einen Oxideinkristall, sowie einen komplexen Modellkatalysator mit Nanopartikeln.

Kapitel 3 zeigt die erste Verwendung eines ZnO($10\bar{1}0$)-Einkristalls im *ReactorSTM*. Zinkoxid ist Teil des am meisten untersuchten Katalysators für die Dampfreformierung von Methanol, Cu-ZnO/Al_2O_3. Dieser Katalysator hat das Potenzial, Fahrzeuge mit Wasserstoffbrennzellen sicherer und ihren Gebrauch einfacher zu machen. Hierfür muss der Katalysator jedoch äußerst selektiv für die Produktion von CO_2 statt CO sein, wofür das Zinkoxid eine große Rolle spielen könnte. Zunächst stellen wir einige experimentelle Herausforderungen dar, die der Gebrauch von ZnO($10\bar{1}0$) im Rastertunnelmikroskop in Vakuum mit sich bringt. Außerdem quantifizieren wir den Wasserhintergrund in der Reaktorzelle des *ReactorSTM*. Wenn ZnO($10\bar{1}0$) in der Zelle Argon ausgesetzt wird, raut dieses Wasser die Oberfläche auf, sodass eine große Anzahl an Stufen sichtbar ist. Da Wasser jedoch auch ein Edukt der Dampfreformierung von Methanol ist, muss der Schluss gezogen werden, dass die ($10\bar{1}0$)-Oberfläche von Zinkoxid unter realistischen Bedingungen eventuell nicht stabil ist und Studien von ZnO($10\bar{1}0$) in Vakuum nur bedingt als Modell für den industriellen Prozess geeignet sind.

In Kapitel 4 gehen wir zur Studie eines komplexeren Modellkatalysators in der Form von TiO_2/Au(111) über. Katalysatoren, die auf Gold basieren, sind aktiv für CO-Oxidation, und das bei niedrigeren Temperaturen im Vergleich zu anderen Materialien. Daher könnten sie die Emission von CO während des Warmlaufens von Verbrennungsmotoren reduzieren. Bezüglich des Mechanismus auf diesem Katalysator sind jedoch der Oxidationszustand des Goldes während der Reaktion, die Rolle des Oxids und auch die Rolle von Wasser in der Gasmischung unklar. Im *ReactorSTM* kann die Bildung eines oberflächlichen Goldoxids auf Au(111) in atmosphärischen Drücken von O_2 oder der Reaktionsmischung beobachtet werden. Die hierzu notwendige Dissoziation von O_2 wird wahrscheinlich durch den Wasserhintergrund in den Gasen möglich gemacht. Da auch Kontaminierungen im Gold die Bildung des Oxids fördern können und der Wasserhintergrund unter realistischen Umständen ebenfalls vorhanden ist, scheint die Existenz des Oxids auf industriellen Katalysatoren wahrscheinlich. TiO_2-Nanopartikel auf Au(111) haben jedoch keinen Einfluss auf die Bildung des Goldoxids. Wir können damit ausschließen, dass TiO_2 während der CO-Oxidation atomaren Sauerstoff an die Au(111)-Oberfäche liefert.

Kapitel 5 zeigt die Anwendung von in situ Röntgenphotoelektronenspektroskopie zur Untersuchung eines Kobalt-Einkristalls, der als Modellkatalysator für Fischer-Tropsch-Synthese dient. Mit Hilfe dieser Reaktion können sauberere, synthetische Brandstoffe aus einer Mischung von CO und H_2 hergestellt werden. Obwohl Kobalt schon industriell verwendet wird, beschäftigt sich die Wissenschaft mit einigen Deaktivierungsprozessen wie der Oxidation des Kobalts und der Ablagerung von Kohlenstoff sowie Produkten der Reaktion. Die Oxidation des Kobalts kann stark von der Struktur der Kobaltprobe abhägen. Im Fall von unseren Messungen auf Co(0001) scheint die Oberfläche in CO metallisch zu bleiben. In H_2 kann der Wasserhintergrund die Oberfläche jedoch oxidieren, selbst wenn so viel Wasser wie möglich herausgefiltert wird. Obwohl das Gegenteil sowohl in niedrigeren als auch in höheren Drücken beobachtet wird, stimmen diese Ergebnisse mit Messungen auf Kobaltfolie in ähnlichen Drücken überein. Eine mögliche Erklärung hierfür basiert auf den unterschiedlichen Positionen, die CO, H_2 und H_2O auf Co(0001) bevorzugen. Außerdem stellen wir in Kapitel 5 ein Modell vor, mit dem die Menge an Materialien, die während der Reaktion auf Co(0001) abgelagert werden, quantifiziert werden kann.

Allgemein gesprochen sind alle drei Systeme, die in dieser Arbeit untersucht wurden, ein Beispiel dafür, dass kleine Konzentrationen von Kontaminierungen in Gasen und Probenmaterialien einen signifikanten Einfluss auf die Ergebnisse von in situ Messungen haben können. Obwohl dies die Interpretation von Ergebnissen erschwert, fördert es auch die Annäherung an realistischere Reaktionskonditionen.

Acknowledgments

Irene Groot supervised the research presented in this thesis. Apart from providing the much needed chemist's overview for the interpretation of results, Irene always has an open ear and supports individual personal development. I am especially thankful for the opportunity to expand my skill set by taking on the NAP-XPS project. **Rik Mom** introduced me to the ins and outs of the ReactorSTM setup while supervising my master's project. Thank you for the confidence to let me work so independently in the lab and for allowing me to experience my first beamtime for the SXSTM project. Although we worked together less than originally planned for my PhD project, **Ludo Juurlink** allowed me to participate in an interesting side project that was quite different from my main projects.

Preparing and performing the beamtimes for my last project would not have been possible without **Richard van Lent**, **Dajo Boden**, **Mahesh Prabhu**, **Hamed Achour**, and **Elahe Motaee**. Of course we were greatly supported by **local contacts**: Monika Blum, Andrey Shavorskiy, Mattia Scardamaglia, Yifan Ye, Suyun Zhu, and Slavomir Nemsak. For our group meeting discussions I am also thanking the rest of the **Groot group** and many from the larger **CASC group** under the leadership of **Marc Koper**. **Marcel Rost**, thank you for teaching me, among other things, how to use the capacitive approach, which saved so many valuable lab hours. I want to thank **Francesco Carlà** for taking much time for explanations during our SXRD beamtimes and for input on the discussion of XPS data.

The experimental work performed in Leiden heavily depends on the **fine mechanics department**, who are not only extremely skilled but also great to work with. Although, I probably received help from every employee at the FMD one time or another, I want to especially thank **Mirthe Bergman** for her work on the ReactorSTM and uplifting conversations during the first years of my PhD, **Freek Groenewoud**, **Fred Schenkel**, and **Robin Schrama** for taking over work for our group, **Emiel Wiegers** for quite some spot welding, and **Thijs Hoogenboom** for his help with other projects. Our lab work also depends on the fast repairs and the development

of new electronics and software by the **electronics department** in Leiden, where I especially want to thank **Bert Crama**, **Raymond Koehler**, **Martin Moene**, and **Peter van Veldhuizen**. In other areas I was supported by **José Dijkzeul**, **Wilfred van der Geest**, **Wen Tian Fu**, the **BHV**, the **reception staff** in the Huygens building, and **facility services**. Additionally, many companies supply us with parts and maintenance. I especially want to thank **Leiden Probe Microscopy** for their advice regarding gas delivery systems.

My students in the lab, **Yanick Monk**, **Laurens de Jong**, and many **LO students**, did not only give me the opportunity to teach content but to learn teaching as well. I also want to thank **Edgar Blokhuis** for teaching advice and motivating words while I assisted in his courses. I am thankful to **Esther Groeneveld**, **Peter Berben**, **Toine Cents**, **Xander Nijhuis**, **Evgeny Pidko**, **Leon Lefferts**, **Guido Mul**, and **Annemarie Huijser** for discussions and motivating words during the CatC1Chem progress meetings. Sharing our frustrations with the other PhD candidates in the program, **Devin O'Neill**, **Robert Franz**, and **Rolf Postma**, could be quite helpful.

Not underestimating the personal support network, I first want to thank my father **Klaus** for motivating me to understand the world around me and to make good use of the possibilities for education I was given, as well as for always having advice. Mama **Elke**, thank you for all those warm woolen socks and the great care during my stays in Darmstadt. **Ulrike & Devran**, I always enjoy those conversations about our jobs and lives. Thank you for making me an aunt twice in the last four years. My parents, grandparents, and godparents, **Eric & Tina Knop**, supported me financially during my bachelor and master studies.

Blandine, you are not only a good friend, but also gave me a fun place to stay for a while. **Guido**, thank you for the truly amazing experience of traveling through Japan. Together with **Alberico** and **Eduardo** we have the most fun evenings discussing science, society, and life. **Andrea**, thank you for meeting me at the sports center for much needed breaks from the lab. I also want to thank the employees, volunteers, and four-legged residents at the **Haags Dierencentrum** for needed distractions and a chance to practice my Dutch. Although I was not always the best at keeping in contact after moving to the Netherlands, I am glad to still call fellow students from my bachelor studies my friends today. Thank you, **Steffen**, **Laura**, **Victor**, **Barbara**, and **Mona**. I also want to thank those that have and are making the measurement hall a brighter place: **Gesa**, **Norman**, **Sabine**, **Tim**, **Peter**, **Tobias**, **Martin**, **Irene**, **Tjerk**, **Tjerk**, **Jaimy**, **Tycho**, **Sergi**, and many more.

Last but definitely not least, **Werner & Loki**, I feel so lucky that I met the two of you. You are unbelievably supportive in many different ways and gave me so much more reason not to stay in the lab or on the computer for too long (on most days).

About the Author

Sabine Wenzel was born in Darmstadt, Germany, in 1992. She graduated from high school at the Edith-Stein-Schule in 2010 with a special focus on mathematics and physics. Sabine performed her bachelor studies in physics, with a minor in philosophy, at the Technische Universität Darmstadt. This included a bachelor project participating in the setup of a quantum key distribution system in the laser and quantum optics group of Prof.dr. Thomas Walther.

After spending some months in Spain for travel and volunteer work, Sabine moved to the Netherlands in 2014 to continue her studies at the Universiteit Leiden. Here she combined the master in physics with the science-based business track. For the scientific master project Sabine joined the group of Dr. Irene Groot, focusing on operando research in heterogeneous catalysis, which is part of the catalysis and surface chemistry group. While investigating the physical vapor deposition of rhenium oxide and tungsten oxide on Au(111), this project ultimately led to the research on surface gold oxide presented in this thesis. The business part of the study was concluded with a six-month internship in the department of new business development at cosine measurement systems, Warmond.

In 2017 Sabine returned to the Groot group for her PhD research, which first focused on the use of in situ scanning tunneling microscopy on zinc oxide and titania on gold. Additionally, Sabine took on the first near-ambient pressure X-ray photoelectron spectroscopy project performed in the Groot group, which included leading beamtimes at the ALS in Berkeley, US and at Max IV in Lund, Sweden. During her time in the Groot group she also participated in multiple beamtimes at the ESRF in Grenoble, France, performing in situ surface X-ray diffraction as well as in situ synchrotron X-ray assisted scanning tunneling microscopy. The PhD position in Leiden included presenting results at conferences and following a number of courses of scientific as well as transferable content. Additionally, Sabine supervised student research projects and assisted in the teaching of bachelor courses on calculus and statistical thermodynamics.